2019

Performance and Stability of CaCl2·6H2O-Based Phase Change Materials

Joshua Charles
Lehigh University, joshuamcharles@gmail.com

Performance and Stability of $CaCl_2 \cdot 6H_2O$-Based Phase Change Materials

by

Joshua M. Charles

Presented to the Graduate and Research
Committee of Lehigh University in Candidacy for
the Degree of Doctor of Philosophy

in

Mechanical Engineering

Lehigh University

January 2019

Approved and recommended for acceptance as a dissertation in partial fulfillment of the requirements for the degree of Doctor of Philosophy.

_____
Date

_____
Arindam Banerjee, PhD
Dissertation Advisor

_____
Accepted Date

Committee Members:

_____
Arindam Banerjee, PhD
Committee Chairman

_____
Sudhakar Neti, PhD

_____
Justin Jaworski, PhD

_____
Carlos Romero, PhD

_____
Kemal Tuzla, PhD

_____
Richard Bonner, PhD

Acknowledgments

I would like to express my sincere thanks to my committee chairmen professors Sudhakar Neti and Arindam Banerjee, who have supported me in this work for the past three years and have offered suggestions and guidance as I assembled this dissertation. I would also like to thank Dr. Carlos Romero for the oversight he gave to this project and for providing me with the atmosphere, funding, and time required to complete this work. Truly, this dissertation would not have been possible without his support. In addition, I extend a special thank you to the remainder of my doctoral committee members: Professors Kemal Tuzla, and Justin Jaworski and Dr. Richard Bonner. Thank you for your willingness to take the time to sit on my doctoral committee. Your questions and guidance offered at our various meetings have contributed greatly to my understanding of the research presented herein. The breadth of perspectives brought by my committee members has been very helpful as I approached the multi-faceted and expansive problems associated with phase change material development.

I also want to express my thanks to the fellow students and visiting scholars who have assisted me in this work. I would like to thank my colleagues Xingchao Wang and Chunjian Pan for their help in various areas of this project. Chunjian, in particular, helped me better understand the heat transfer dynamics of PCM solidification and melting and how it could be analyzed using models. I'd also like to thank Georgios Pilitsis and Arunachalam Subramanian for their assistance with the hundreds of calorimeter tests conducted. Much of the corrosion work presented was conducted through the hard work of Shaojun Ren, Fengziang Nie, He Yun, Anika Chakravarti, and Guanrong Song. I am also grateful for Elif Eker Kahveci's assistance in better understanding the issues surrounding the separation of calcium chloride hexahydrate.

A special thank you and acknowledgement goes out to my collaborators at Advanced Cooling Technologies (ACT): Richard Bonner, Sean Hoenig, Ying Zheng, Chien-Hua Chen, and Fangyu Cao. I truly enjoyed working with the entire ACT team and always enjoyed our meetings and the time spent together working on this project.

Last but surely not least, I would like to express my thanks to my wonderful and loving wife Megan, who has been very understanding and supportive over the past three years of work. Thanks for understanding when I had to spend all my free evenings at Starbucks writing this dissertation.

The information, data, or work presented herein was funded in part by the Advanced Research Projects Agency – Energy (ARPA-E), U.S. Department of Energy, under Award Number DE-AR0000582.

The information, data, or work presented herein was funded in part by an agency of the United States Government. Neither the United States Government nor any agency thereof, nor any of their employees, makes any warranty, express or implied, or assumes any legal liability or responsibility for the accuracy, completeness, or usefulness of any information, apparatus, product, or process disclosed, or represents that its use would not infringe privately owned rights. Reference herein to any specific commercial product, process, or service by trade name, trademark, manufacturer, or otherwise does not necessarily constitute or imply its endorsement, recommendation, or favoring by the United States Government or any agency thereof. The views and opinions of authors expressed herein do not necessarily state or reflect those of the United States Government or any agency thereof.

Index

List of Tables

List of Figures

Nomenclature

A	Heat transfer surface area
ACC	Air cooled condenser
ACT	Advanced Cooling Technologies, Inc.
Al 5086	Aluminum alloy 5086
Al 6061	Aluminum alloy 6061
ARPA-E	Department of Energy Advanced Research Project-Energy
α	Rate of change of data smoothing about current discrete data point
β	Corrosion rate conversion factor
C_A	Arrhenius constant
CC	$CaCl_2$ (Calcium chloride)
CC4	$CaCl_2 \cdot 4H_2O$ (Calcium chloride tetrahydrate)
CC6	$CaCl_2 \cdot 6H_2O$ (Calcium chloride hexahydrate)
CC6+	$CaCl_2 \cdot 6H_2O$ in water solution
CC6+KN	$CaCl_2 \cdot 6H_2O$ + KNO_3 mixture
CC6+MC6	$CaCl_2 \cdot 6H_2O$ + $MgCl_2 \cdot 6H_2O$ mixture
Cp	Specific heat
CS	A36 Carbon steel
CSV	Comma-separated value file
Cu	Copper
DSC	Differential scanning calorimetry
Δm	Change in mass of coupon during corrosion
ΔT	Temperature change
E_a	Arrhenius equation apparent activation energy
Ex. H_2O	Excess water above the stoichiometric hexahydrate composition
γ	Data smoothing range about current discrete data point
h	Convective heat transfer coefficient
HCl	Hydrochloric acid
HF_{aq}	Hydrofluoric acid
H_f	Latent heat of fusion
HXC	Hydroxyethyl cellulose
j	Current discrete data point
k	Thermal conductivity

K	Corrosion rate
KCl	Potassium chloride
KF	Potassium fluoride
KN	KNO_3 (Potassium nitrate)
l	Integer value above or below current discrete data point
L	Calorimeter bottle wall thickness
LDC	Large dehydration cell
m	Mass
M	Molar mass
m_{add}	Mass of water to be added to anhydrous $CaCl_2$
MCCC12	$2MgCl_2 \cdot CaCl_2 \cdot 12H_2O$ (Tachyhydrite)
MC6	$MgCl_2 \cdot 6H_2O$ (Magnesium chloride hexahydrate)
$m_{T\ loss}$	Slope of calorimeter temperature loss/gain
n	Moles
N	Data smoothing weight normalization parameter
N_{cyc}	Number of cycles
NS10	$Na_2SO_4 \cdot 10H_2O$ (Sodium sulfate decahydrate; Glauber's Salt)
PCM	Phase change material
q	Heat flux
Q	Thermal energy transferred
Q_{hyd}	Heat of hydration/dehydration of salt
R	Gas constant
R^2	Coefficient of determination for linear curve fit
R_c	PCM cooling rate in °C/hr
$R_{f\text{-}b}$	Convective thermal resistance between calorimeter fluid and inner bottle wall
R_b	Conductive thermal resistance through calorimeter bottle wall
$R_{b\text{-}a}$	Convective thermal resistance between calorimeter outer bottle wall and air
RMS	Root mean squared error
RTD	Resistance temperature detector
ρ	Density of corrosion test metal
S	Corrosion test coupon surface area
SC2	$SrCl_2 \cdot 2H_2O$ (Strontium chloride dihydrate)
SC6	$SrCl_2 \cdot 6H_2O$ (Strontium chloride hexahydrate)
SS 304	Stainless steel 304
step(i)	Discrete temperature data point step size (2Hz sampling rate unless otherwise noted)

σ	Population standard deviation
t	Cycling rate
t_c	Corrosion test duration
T	Temperature
T_f	PCM freeze temperature
TGA	Thermogravimetric analysis
T_m	PCM melt temperature
$T_{m(l)}$	Temperature in slight excess of PCM melt temperature (liquid state PCM)
T_o	DSC peak onset temperature
T_p	DSC heat flux peak temperature
VBA	Microsoft Excel Visual Basic for Applications
$V_o[]$	Unsmoothed array-based data point
$V_{sm}[]$	Smoothed array-based data point
w	Mass fraction
wt%	Weight percentage (mass percentage)
xH_2O	Moles of water per mole of salt

Subscripts

1	Initial state
2	Secondary state
4*	$4H_2O$ (tetrahydrate) layer after separation
6*	$6H_2O$ (hexahydrate) layer after separation
a	Air
bottle	Drop calorimeter bottle
cal	Drop calorimeter system minus PCM, ENC, and fluid
CC	$CaCl_2$ (Calcium chloride)
CC+w	Anhydrous $CaCl_2$ plus entrained moisture
CC4	$CaCl_2 \cdot 4H_2O$ (Calcium chloride tetrahydrate)
CC4*	$CaCl_2$ in CC4 layer of PCM after separation
CC6	$CaCl_2 \cdot 6H_2O$ (Calcium chloride hexahydrate)
CC6*	$CaCl_2$ in CC6 layer of PCM after separation
Cu	Copper
cyl	Calorimeter calibration cylinder

cyl RTD	Calorimeter calibration cylinder RTD
ENC	PCM encapsulation used for drop calorimetry and rapid cycling
ew	Entrained moisture in anhydrous $CaCl_2$
eye	Stainless steel eye used to hang Cu/SS calorimeter calibration cylinder
f	Fluid
f-a	Difference between fluid and air
fluid	Fluid
H_2O	Water
i	Discrete calorimeter time step
j*	Arbitrary layer after PCM segregation
KCl	Potassium chloride
l	Supernatant liquid
L	Liquid state
l*	Supernatant liquid layer after separation
LDC	Large dehydration cell
lid	Test cap for drop calorimeter
loss	Calorimeter losses
PCM	Phase change material
RTD	Drop calorimeter resistance temperature detector and hanger
s	Solid state
Salt	Salt
SC6	$SrCl_2 \cdot 6H_2O$ (Strontium chloride hexahydrate)
SS	Stainless steel 304
stir bar	Magnetic stir bar in drop calorimeter bottle
t	Time
T	Phase transition state
tot	Total
w	Water

Abstract

Thermal energy storage is receiving increased attention as the world transitions away from fossil fuels and seeks to improve the efficiency of existing energy production systems. While higher-temperature thermal energy storage has received the majority of attention in the field, thermal energy storage at temperatures close to ambient conditions may also have some practical applications. Hydrated salt phase change materials (PCMs) store thermal energy in this temperature range and can have high gravimetric and volumetric energy storage capacities while having a very low cost. Despite the benefits of these salts, they generally suffer from supercooling, phase segregation during cycling, and a high corrosion potential. In the current work, these inorganic salts were characterized and tested by a variety of laboratory methods; including: differential scanning calorimetry, drop calorimetry, rapid and slow thermal cycling, thermogravimetric analysis, and a large dehydration cell. Through these methods, the following parameters or conditions could be measured or observed: the melt temperature, the heat of fusion of melting, the material's water content, supercooling, and phase separation during cycling.

After initial characterization of the thermal performance of several hydrated salt candidate materials, three calcium chloride hexahydrate ($CaCl_2 \cdot 6H_2O$)-based salts were selected for additional testing. For the first of these salts, $CaCl_2 \cdot 6H_2O$ + magnesium chloride hexahydrate ($MgCl_2 \cdot 6H_2O$) a new eutectic composition was found along with a modeled phase diagram, which agrees well with the experimental findings. This salt was cycled for over two thousand seven hundred cycles with minimal changes in the heat of fusion or melt temperature as measured by drop calorimetry. A second material, $CaCl_2 \cdot 6H_2O$ + potassium nitrate (KNO_3), was also fully characterized and cycled with good long-term performance during cycling. When $CaCl_2 \cdot 6H_2O$ was similarly characterized and cycled, it was found to experience phase segregation during cycling.

Potassium chloride (KCl) was found to stabilize $CaCl_2 \cdot 6H_2O$, although this stabilizing effect was only realized after a supernatant liquid was removed from the frozen PCM. The ternary phase diagram of the $CaCl_2$-H_2O-KCl system suggests that several stable mixtures are possible at different H_2O weight percentages, which was verified through experimentation. It was also found that $CaCl_2 \cdot 6H_2O$, which has separated, can be restored to a homogenous state through heating to temperatures above 45°C. In addition, a clear relationship between the PCM cooling rate and the rate at which separation progresses was found; with faster cooling resulting in less separation.

Several common metals were tested for corrosion resistance when in direct contact with the three $CaCl_2 \cdot 6H_2O$-based PCMs. Test were conducted under isothermal (molten) and cycling conditions, where metal coupons were immersed in the PCM test samples for test periods of up to a year. For the $CaCl_2 \cdot 6H_2O$ and $CaCl_2 \cdot 6H_2O$ + $MgCl_2 \cdot 6H_2O$ PCMs, an aluminum alloy and carbon steel were found to have good corrosion resistance under both isothermal and cyclic testing. An anodized aluminum was found to provide superior corrosion resistance. If the $CaCl_2 \cdot 6H_2O$ + KNO_3 PCM is used, aluminum samples were found to deteriorate very quickly and either carbon steel or stainless steel are recommended for containment.

Medium-scale (100-1000 kg) batches of industrial-grade $CaCl_2 \cdot 6H_2O$ with additives were prepared and cycled in a prototype cold storage system. When tested by drop calorimetry, these materials showed good thermal performance and stability, although there appears to be a slight decrease in latent energy as the number of cycles was increased. Additional testing of industrial-grade materials is required in order to determine if they maintain their stability and performance at greater than a hundred cycles. This work has resulted in a demonstrably stable, low-temperature PCM with good thermal performance, low cost, and good material compatibility with several common, inexpensive metals.

1 Introduction

Thermal energy storage is essential for life. Every day the earth absorbs and stores solar energy from the sun. Some of this energy is stored as sensible heat in the oceans and land and a portion is stored as latent energy in the form of clouds. Sensible heat stored by the oceans, land, and atmosphere during the day maintains the dark side of the planet at comfortable temperatures throughout the night. Latent heat energy stored in gaseous water is released as clouds precipitate moisture. Truly the earth is a marvelously-balanced thermal energy system with the energy being stored more or less perfectly matching that radiated to space. On a small scale, thermal energy storage has influenced human design for centuries. For instance, as presented by Butti et al. in their book "A Golden Thread", ancient Greek homes were designed to absorb heat from the sun during winter days. This heat would be released from the earthen floors and adobe walls of the house during the night, maintaining inside temperatures without the need for a furnace [B20]. With the later advent of glass, thermal energy storage within structures became much more efficient as the glass prevented heat absorbed by the materials or air inside the structure from escaping. Glass heat "traps", such as greenhouses have been used since the 18th century to maintain plants at moderate temperatures even during the coldest months of the year [B20]. Throughout history, heated stones or bricks have been used to maintain temperatures in the region immediately surrounding an individual. Some examples of this are foot or bed warmers, which were little more than fire-heated stones. These heated stones could be used to keep feet warm during long wagon rides or could be swept through the covers of a bed in order to pre-heat it on cold nights. Truly, thermal energy storage is everywhere if one only looks for it.

After over a century of rapid industrial progress, the world has realized the importance of energy efficiency as overconsumption of natural resources threatens our way of life. While much of the recent research has focused on electricity production and storage, thermal energy storage has

also enjoyed a renaissance, particularly as it relates to solar-thermal energy storage. In the current work, a thermal energy storage material utilizing the latent heat of a solid/liquid phase transition was developed. This material is designed to have a phase transition temperature of around 30°C with a relatively high latent heat of fusion (>150 J/g). Since this phase change material (PCM) is made from hydrated salts, materials costs are very low (~ $\$_{USD}$ 0.10/kg). These three conditions of a phase transition temperature around 30°C, a high heat of fusion, and low cost pave the way for some interesting use cases for this material. Two of these use cases are presented herein – supplemental cooling of air-cooled main steam condensers and building thermal regulation.

1.1 Supplemental Cooling of Air-Cooled Condensers

Fossil power plants currently account for 63% of annual U.S. electricity production, with production split almost equally between coal and natural gas [E2]. Over the past decade, the percentage of electricity generated by natural gas plants has risen dramatically due to a combination of low natural gas prices and increasing regulation of coal-fired plants. Many of these new gas plants have chosen to use air-cooled main steam condensers (ACCs) due to either limited water resources or hot water discharge limits. It should be noted that ACCs have also been installed at several U.S. coal-fired plants in order to reduce water usage. While ACCs do provide benefits in reducing water usage, they introduce plant efficiency constraints as their cooling performance is strongly tied to ambient conditions. Thermodynamics dictate that the efficiency of a Rankine-cycle fossil plant is limited by the maximum temperature difference between the hot and cold reservoirs. With hot-side steam temperatures limited by metallurgical constraints, a low condenser temperature is crucial for maximum plant efficiency. Despite good condenser design, on hot days an ACC may not be capable of cooling the condensate to the desired temperature. As condenser temperature rises, backpressure on the final turbine stage

rises accordingly, reducing generation at a given steam flow rate. According to the U.S. Department of Energy's (DOE) Advanced Research Project Agency – Energy (ARPA-e), a 3°C rise in steam condensate temperature is known to result in a 1% reduction in power output [A9]. Such a reduction in power output will have a direct negative impact on the economics of plant operation as lost generation is lost energy to sell. Compounding this problem is the fact that the hottest days are typically periods of high electricity demand. Since high demand usually corresponds to a higher electricity selling price, lost demand during these periods of time can be particularly harmful to a plant's bottom line.

One potential technology that could improve ACC performance is through the use of a PCM, which can be melted during the day, absorbing heat from the steam. Such a solution has been proposed and developed by Advanced Cooling Technologies (ACT), Lehigh University, and the University of Missouri, with project funding and oversight provided by ARPA-E. This cooling system utilizes a hydrated salt phase change material with a melt temperature between the average daytime and nighttime temperatures. When the heat load exceeds the limits of the ACC, the PCM is available to be melted, removing heat from the steam. As the ambient air temperature falls during the night and the ACC is capable of maintaining lower condensate temperatures, the PCM is frozen (regenerated), with heat transferred to the air through fins at the top of the system. Once frozen, the PCM is ready to remove heat from the steam the following day. An illustration of this ACC cooling system is presented in Figure 1.1.

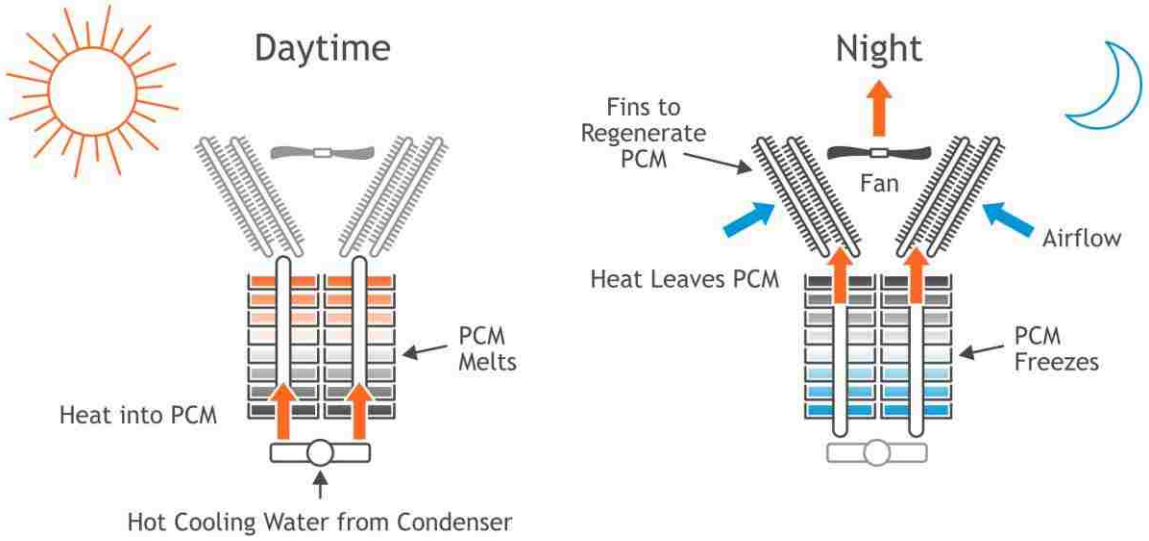

Figure 1.1: Proposed PCM-Based Supplemental Condenser Cooling System

1.2 Building Thermal Regulation

According to the U.S. Energy Information Administration (EIA), in 2015 heating and cooling were together responsible for 51.3% of residential energy usage in the U.S. [E1]. The use of low-temperature phase change materials to offset this energy demand was examined by Dr. Maria Telkes in the late 1940's. In 1949 she constructed a house, which was entirely heated by solar energy in Dover, Massachusetts (Figure 1.2). Solar energy entered the house through large second story windows, behind which were located solar hot air collectors. Hot air from these collectors was circulated through rooms filled with barrels of Glauber's salt ($Na_2SO_4 \cdot 10H_2O$), which would absorb the thermal energy and melt at a temperature of 32°C (90°F). During the night or poor weather days, heat from the cans would be used to heat the house, freezing the Glauber's salt in the process [H20]. Unfortunately, during the third winter of operation, the Glauber's salt separated into salt and supernatant liquid layers – rendering it useless from a latent energy storage perspective [L7]. This separation is an inherent quality of Glauber's salt, although in subsequent work Telkes claimed to have eliminated it [T5].

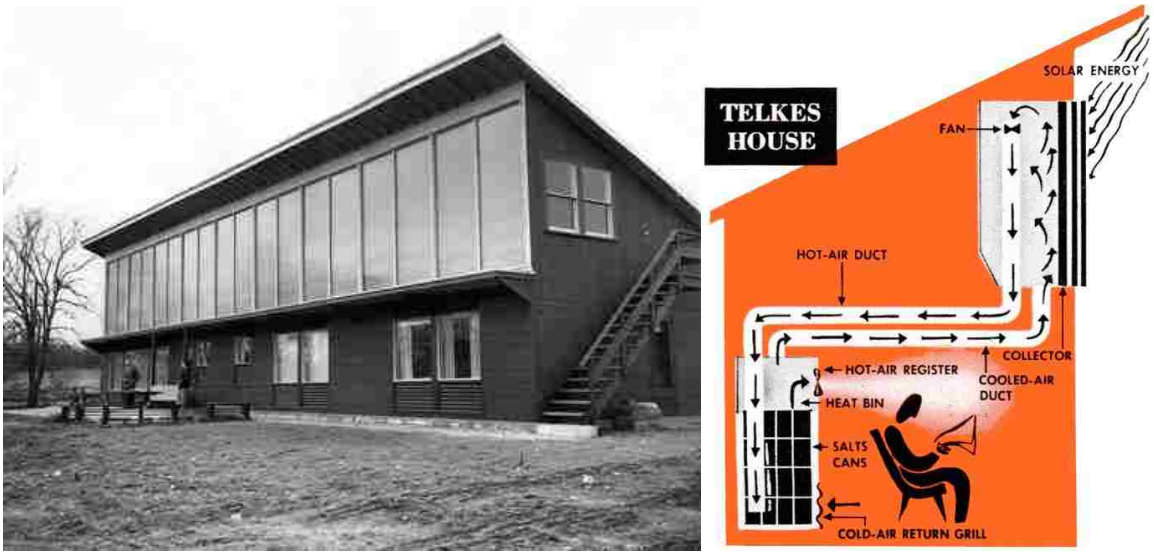

Figure 1.2: The Dover House as Constructed by Dr. Maria Telkes [B20,H20]

Despite this failure by Telkes, PCM-based thermal energy storage is still of interest in space heating applications. For instance, recent experimental work by Barzin et al. has considered the use of paraffin-based PCMs embedded into common construction materials, such as gypsum wallboard [B4,B5]. Although thermal energy could be stored using a sensible heat-based storage system, a PCM-based storage system is preferable due to the high volumetric energy density of PCMs. To illustrate this, cubes representing the volume of five common materials required to store 1 kJ of thermal energy between 25 and 35°C are presented in Figure 1.3. For each of these five materials, thermal energy storage in the specified temperature range is purely sensible energy storage. If a PCM, such as calcium chloride hexahydrate ($CaCl_2 \cdot 6H_2O$, or CC6) is used to store this energy, it can be seen that a much smaller volume of material is required! CC6 has a phase transition temperature (T_m) of 29°C and latent heat of fusion (H_f) of 170 kJ/kg. This smaller volume is not only important as it requires less space for comparable thermal energy storage, but it may also result in reduced containment costs. For instance, liquid water is a common thermal energy store and it is virtually free. However, as seen in Figure 1.3, storing a comparable

quantity of thermal energy in water will require an order of magnitude larger containment vessel relative to CC6. It should be noted that these cost and volume savings can only be realized if the PCM is very low in cost – as is the case for CC6.

Figure 1.3: Volume of Material Required for 1 kJ of Storage Between 25 & 35°C

One potential application of PCMs to building temperature regulation is embedding of the PCM into floor tiles. The PCM can be embedded into the tiles in one of two ways. A method by which a paraffin-based PCM was mixed with the tile material and binder was presented by Hittle [H18]. This method is not recommended for use with hydrated salt PCMs due to their volume change during freezing and melting. Instead, it is recommended that the tile be constructed in such a way that voids within the tile be filled with PCM, while leaving a slight air gap to allow for expansion and contraction. A basic illustration of this configuration is presented in Figure 1.4. With this method, the structural integrity of the tiles must be fully evaluated to ensure they are as durable as standard tile.

Two proposed applications for the PCM embedded floor tile are presented in Figure 1.5. First is coupling of the tile with a solar heated radiant floor system. Such systems are known to be capable of offsetting a portion of a home's heating demand, even in climates far from the equator, such as the north eastern region of the U.S. While hot water from the solar collectors

could be directly used to store heat for nighttime use, a significant volume of water would be required if large quantities of thermal energy were to be stored. Instead, it is proposed that a layer of PCM embedded tile be placed on the floor above the radiant heating pipes. During the day this tile will absorb thermal energy from the solar collector, melting the PCM. At night, the PCM will solidify, maintaining the room at a comfortable temperature close to the phase transition temperature of the PCM.

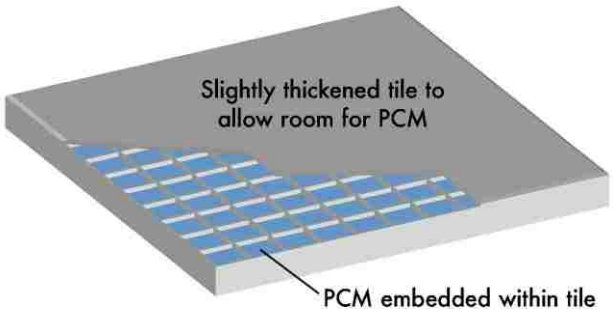

Figure 1.4: Floor Tile with Embedded PCM

A second, entirely passive configuration for solar heating with PCM floor tile thermal storage is presented on the righthand side of Figure 1.5. The building is designed such that during the day solar radiation enters the structure through large windows. This solar radiation is absorbed by the PCM tiles, melting the PCM. At night the PCM solidifies, releasing heat to the air in the building. A secondary benefit of this storage system is that it prevents overheating of the structure during times when maximum sunlight is entering through the windows. Instead of heating the air and other building materials, the incident radiation is absorbed by the melting PCM, preventing high room temperatures.

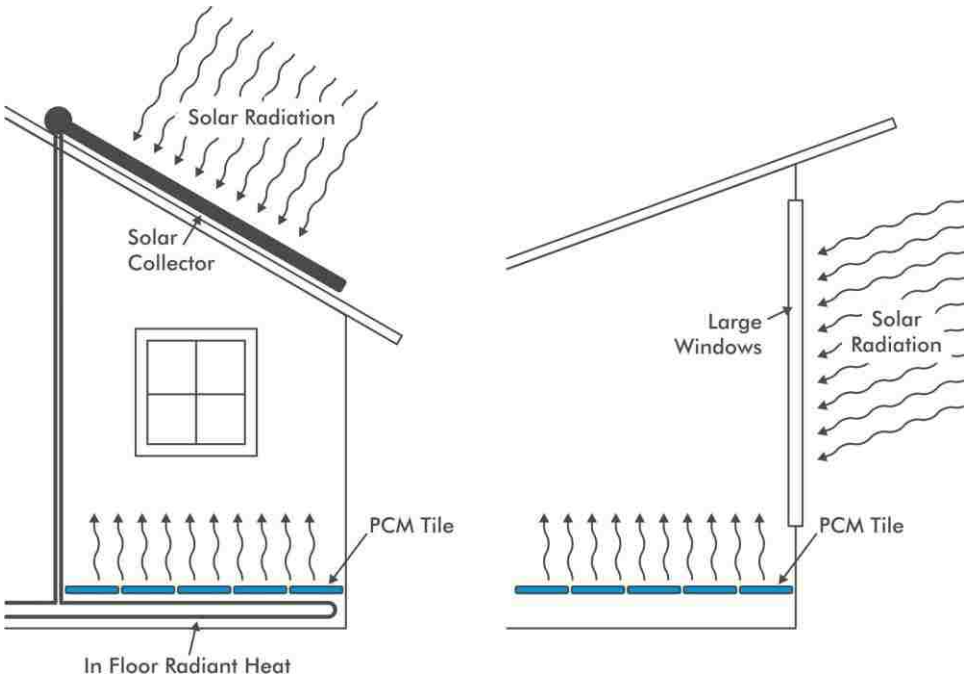

Figure 1.5: Usage Examples for PCM Embedded Floor Tile

The two presented applications for thermal storage only scratch the surface of potential thermal energy storage applications in the temperature range about 30°C. There are additional applications in smart clothing, the automotive industry, space systems, and weapons; anywhere where temperature regulation and/or thermal load shifting is required. However, before considering practical applications an inexpensive, durable, PCM with both the required phase change temperature and latent heat must be developed and demonstrated. This research is the focus of the present study.

A comprehensive search for PCMs in the temperature range between 15 and 35°C is conducted in Chapter 2, with a handful of hydrated salts selected for additional characterization and testing. Test methods for PCM testing and characterization are presented in Chapter 3 before being used to characterize the previously-selected PCMs in Chapter 4. Three CC6-based PCMs were selected for in-depth testing and characterization, which uncovered significant issues

related to supercooling and phase separation. Supercooling was largely eliminated through the addition of a small percentage of strontium chloride hexahydrate ($SrCl_2 \cdot 6H_2O$ or SC6) to the salts. Separation of CC6 is addressed in detail in Chapter 5, where it was found that the addition of a small percentage of potassium chloride (KCl) eliminated separation if specific PCM preparation procedures were followed. Phase equilibria models are presented to assist in explaining the role KCl plays in the stabilization of CC6. The use of hydrated salt PCMs raises corrosion concerns with regard to any structural metals they are contained in or come in contact with. Corrosion testing between three CC6-based PCMs and a handful of common metals is presented in Chapter 6. Despite initial corrosion concerns, carbon steel was found to have a low corrosion rate when in contact with all three of the CC6-based PCMs. A second metal, aluminum alloy 5086, also had good corrosion performance in two of the three PCMs. Finally, industrial-grade CC6 was prepared in quantities of up to 200 liters for testing in a 10 kWh prototype cold-storage system. A summary of the specifics of this preparation and the thermal performance of the resulting PCM are presented in Chapter 7.

2 Phase Change Thermal Energy Storage

As discussed in Section 1, the two primary forms of thermal energy storage are sensible and latent energy storage. On the macro scale, sensible energy storage is quite straightforward with a given unit of thermal energy raising the temperature of a mass by a specified quantity [P11]:

$$Q = \int_{T_1}^{T_2} mC_p dT = mC_p(T_2 - T_1) \quad (1)$$

where, m is the mass under consideration, C_p is the specific heat of the material, and T_2 and T_1 are the final and initial temperatures respectively. On the atomic level, sensible energy storage directly relates to the motion of sub-atomic particles, with higher energy corresponding to a greater degree of motion and lower energy reduced motion. While sensible thermal energy storage is quite effective, its relatively low storage density is a considerable limitation for many applications.

Latent thermal energy storage overcomes the limitation of low storage density by utilizing the energy released or absorbed during a material's phase transition. This phase transition can be between a solid and liquid, liquid and gas or solid and gas. Since there is a large volume change when transitioning between a solid and gas or liquid and gas, these transitions are not typically considered for practical energy storage and will not be considered here. There is also a class of latent energy storage materials, which utilize solid to solid conversions between crystal types. Once again, these materials are outside the scope of this report and the term "phase transition" will exclusively be used in referring to the liquid/solid transition. The equation describing latent heat energy storage is as follows [P11]:

$$Q = \int_{T_1}^{T_m} mC_p dT + m\alpha H_f + \int_{T_m}^{T_2} mC_p dT \quad (2)$$

Where T_m is the phase change temperature, α is the fraction of phase change completed, and H_f is the latent heat of melting or freezing. Equation (2) consists of three parts. The two integrals detail sensible heat storage of the material in the temperature regions before and after the phase change. Note that the specific heat (C_p) of the melted and frozen material are often different. During a phase transition, a large quantity of heat is released or absorbed from the material despite a negligible or very small temperature difference. The magnitude of heat transferred during this process is described by the center term of Equation (2), where the material's latent heat of fusion is multiplied by the fraction of mass having undergone the phase change.

Like sensible energy, latent thermal energy corresponds to an increase or decrease in motion of atoms and/or molecules. However, it differs in the magnitude of this change. For instance, during melting of a solid, a threshold has been reached where the energy of the atoms and/or molecules exceeds that of the crystalline bonds holding them together. This causes the atoms and/or molecules to break free of the crystalline structure and reach the higher energy state referred to as a liquid. A similar process occurs for the transition from liquid to gas although the energies involved are often much greater. When looked at macroscopically, this disparity in energies is striking. To illustrate this, the sensible heat storage capacity of water and ice are presented alongside their latent heat of melting in Figure 2.1.

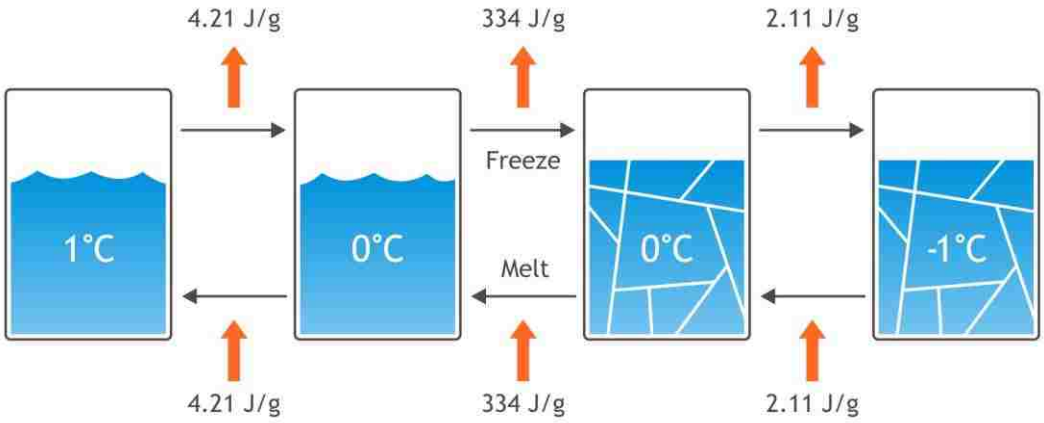

Figure 2.1: Sensible vs. Latent Heat Storage in Water and Ice

As seen, 4.21 J/g of thermal energy must be removed from the water to cool it from 1 to 0°C. From 0°C, removing 334 J/g of energy is required to fully freeze the water, despite no change in temperature. Once frozen at 0°C, the ice can be cooled an additional 1°C by removal of 2.11 J/g of thermal energy. This process and associated energy flows are reversed in the case where water is absorbing thermal energy. It is clear from this example, that the 334 J/g of thermal energy associated with the phase transition far outweighs the sensible heat storage capacity of either the water (4.21 J/g°C) or ice (2.11 J/g°C). If the system can tolerate a very large temperature swing of the storage medium, or if the quantity of the medium is very large (as is the case with the oceans), sensible heat storage may make sense. However, since most practical systems do not have either of these luxuries, the benefit of latent heat stores is evident.

2.1 Phase Change Material Classes

Latent heat storage is not without its drawbacks. Primary among these is that a material with an appropriate phase transition temperature must be used. While the melting of ice to water works well for cooling foods and drinks, it is obvious why this phase change is completely ineffective

at storing heat from a solar thermal collector operating at 700°C. Fortunately, there are many different phase change materials, which have widely different transition temperatures. Figure 2.2 presents T_m vs. H_f for a subset of PCM classes with melting temperatures in the range between 0 and 300°C. These PCMs consist of the organic paraffins and sugar alcohols and the inorganic hydrated salts and their eutectics. Since there is considerable overlap in these PCM classes in both T_m and H_f, additional selection criteria are needed to arrive at the optimal PCM for a given application.

The following is a list of the primary parameters, which influence PCM selection:

- Phase transition temperature (T_m).
- Liquid/solid enthalpy of fusion (H_f).
- PCM material cost and availability.
- Thermal conductivity (k).
- Safety and environmental concerns.
- Containment requirements and corrosiveness.
- Long-term thermal stability of H_f during repeated cycling.
- Supercooling.
- Volume change during phase change.

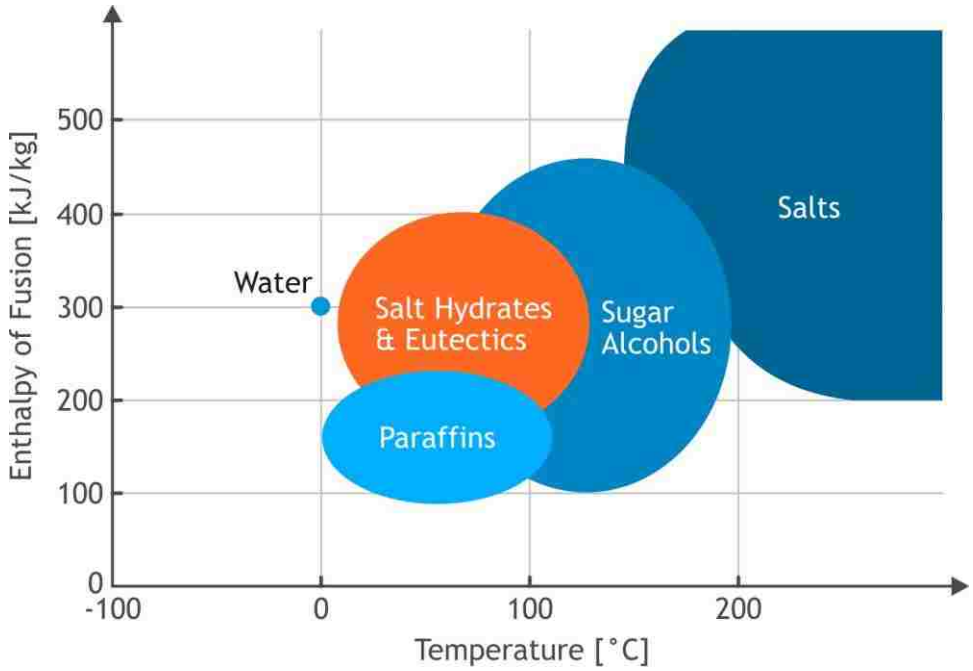

Figure 2.2: Melting Temperature & Latent Heat of Fusion of Various PCMs [P11,G2]

Selection of the correct phase change temperature is highly application dependent and the PCM should be selected such that the system being heated or cooled by the PCM can be operated at the desired temperature. For most applications, a higher heat of fusion is desired as this not only minimizes the quantity of PCM required but can also result in a smaller mass and/or volume of PCM. PCM costs are critical to any application, but especially to those that require many tons of material and are competing against mature technologies, such as the ACC supplemental cooling system presented in Section 1.1. Most PCMs are known to have low thermal conductivities, which greatly impact the rate at which thermal energy can be transferred into and out of the PCMs. Even a marginally higher conductivity can result in significant overall system-level costs as the required heat transfer area is reduced. Some PCMs have either safety or environmental concerns that are considerable barriers to their widespread use – especially in large quantities. Fortunately, most inorganic PCMs are quite benign to both the environment and humans. Corrosion of containment materials by the PCMs must be addressed as many PCMs are known to

be highly corrosive, which can result in catastrophic material failures over very short timescales. Thermal stability of a PCM during decades of repeated cycling is critical for material success in most applications. For instance, if the material begins to lose its thermal storage capacity over time, it may fail to provide the needed thermal energy storage capacity. PCM supercooling refers to the phenomenon where the PCM must be cooled to a temperature below its freezing temperature before crystallization begins. Supercooling can be a considerable barrier to the practical use of a PCM if the temperature must be significantly decreased below the actual freezing temperature. Finally, the volume change of the PCM during a phase transition must be considered in order to prevent stresses on the container housing the PCM.

While the importance of these parameters is dependent on the specific application, they should all be considered to ensure maximum performance of the PCM. Each class of PCMs tends to have an advantage in several of these areas, while other PCMs perform better in others.

2.1.1 Paraffins

The organic PCMs consist of the paraffin, fatty acids, and sugar alcohol classes. Of these, the paraffins are the most widely used class of PCMs. Paraffin waxes behave very well as PCMs as they melt and freeze congruently in the very desirable temperature range of between 0-110°C. Congruent melting and freezing is important as it means the PCM does not undergo what is known as phase segregation. Phase segregation (also referred to as phase separation, or separation) can result in significantly degradation of the latent heat storage capacity after numerous thermal cycles. Paraffins are also known to be non-toxic, non-corrosive, do not supercool, and can have a high heat of fusion (> 200 J/g). The major drawbacks to the use of paraffin PCMs is their order of magnitude higher price, relative to hydrated salt PCMs, and their very low thermal conductivity [C15,H3]. This low thermal conductivity is normally addressed by providing additional heat transfer surface area to help move thermal energy into and out of the paraffin.

The advantages and disadvantages of paraffin wax PCMs are summarized in Table 2.1. Finally, in general, paraffins have a lower volumetric storage density than hydrated salt PCMs. While this may not be an issue for many applications, there are some applications, such as the floor tile presented in Section 1.2, where the thermal storage volume is at a premium.

Table 2.1: Advantages and Disadvantages of Paraffins Used as PCMs [S21]

Advantages	Disadvantages
No Separation	
Stable	Higher Cost
High Latent Heat	Low Thermal Conductivity
No Supercooling	Flammable
Safe	Wide Melting Temp. Range
Non-corrosive	

An exhaustive literature review of paraffin-based PCMs with melt temperatures in the range of interest (15 – 30°C) was conducted. These paraffin-based PCMs are presented in Table 2.2. It is interesting to note that Table 2.2 shows that melt temperature directly correlates with the number of carbon atoms in the paraffin. For all PCMs, the latent heat of fusion is close to or exceeds 200 J/g, which is a very good thermal storage capacity on a mass-basis.

Table 2.2: Paraffin PCMs with Phase Change Temperature in the Considered Range

Paraffins (Alkanes)	T_m [°C]	H_f [kJ/kg]	Cp_L [kJ/kg°C]	Cp_S [kJ/kg°C]	d_L [kg/m^3]	d_S [kg/m^3]	k_L [W/m°C]	k_S [W/m°C]	Sources
Paraffin 16 Carbons (n-Hexadecane) [$C_{16}H_{34}$]	16.7 - 20.0	200 - 252	2.19 - 2.25	1.65 - 2.11	770 - 780	830 - 835	0.150		[B1,B2,B16,F8,H3,H16, L8,L18,M4,N1,S18]
Paraffin C16-C18	20.0 - 22.0	152							[J2,T17,Z1]
Paraffin 17 Carbons (n-Heptadecane) [$C_{17}H_{36}$]	20.8 - 22.6	164 - 214	2.93	2.57	775 - 778			0.240	[B1,B2,G4,H3,H16,L8, S18,Y2]
Paraffin C13-C24	22.0 - 24.0	189	2.10	2.90	760	900		0.210	[A1,B11,C11,J2,T13, T17,Z1]
Paraffin 18 Carbons (n-Octadecane) [$C_{18}H_{38}$]	27.5 - 28.4	200 - 244	2.16 - 2.22	1.75	771 - 780	814 - 850	0.148 - 0.150	0.150 - 0.360	[B1,B2,H3,H16,J2,L8, N1,S8,S18,Z1]
Paraffin 19 Carbons (n-Nonadecane) [$C_{19}H_{40}$]	23.3 - 32.0	131 - 222		1.97	785				[B1,B2,H3,H16,L8,S18]

2.1.2 Non-Paraffin Organics

The non-paraffin organics are a large category of PCMs. Materials include fatty acids and their eutectic mixtures, esters, sugar alcohols, and glycols. In general, these PCMs are known to melt/freeze congruently and are chemically stable. They normally have a low corrosiveness and are non-toxic [C10]. In the case of fatty acids, there are minimal supply issues as they are derived from vegetable or animal sources, which are not only widely available, but are also highly renewable [F10]. Another advantage inherent to fatty acids is a minimal volume change between the liquid and solid state, which minimizes containment issues which arise due to a change in volume. The primary drawbacks to the use of non-paraffin organics are their flammability and very low thermal conductivity. Costs also tend to be higher than inorganics, and even paraffins [F10]. Odor can also be a concern for some organics. For example, Lane mentioned that capric acid (T_m = 30 to 36°C) smells like a wet goat [L7]. Despite these drawbacks, it was pointed out by Feldman et al. that the lower corrosivity and good chemical stability preclude the use of the more expensive encapsulations, which are required when using inorganic, hydrated salt PCMs [F11]. Table 2.3 presents the non-paraffin organic PCMs found in the literature, while the advantages and disadvantages of these non-paraffin organics are summarized in Table 2.4. As was the case for paraffins, an increase in the number of carbon atoms in the non-paraffin, organic PCMs corresponds to an increase in the melt temperature [Z2].

Table 2.3 (a): Non-Paraffin Organic PCMs in the Considered Temperature Range

Non-Paraffin Organics	T_m [°C]	H_f [kJ/kg]	Cp_L [kJ/kg°C]	Cp_S [kJ/kg°C]	d_L [kg/m³]	d_S [kg/m³]	k_L [W/m°C]	k_S [W/m°C]	Sources
Caprylic Acid [$C_8H_{16}O_2$]	16.0 - 16.7	149			862 - 901	881 - 1033	0.145 - 0.149	0.148	[A1,C10,L4,S18,Z1]
Propyl Palmitate [$C_{19}H_{38}O_2$]	16.0 - 20.0	186 - 190							[C1,F8,H11,Z1]
Acetic Acid [$C_2H_4O_2$]	16.6 - 16.7	184 - 187	1.96	2.04	1050		0.180		[H3,S18]
Glycerin [$C_3H_8O_3$]	17.9 - 18.2	199 - 200			1260		0.289	0.143	[C9,H3,N1,S18]
Butyl Stearate [$C_{22}H_{44}O_2$]	19.0	120 - 200							[F11]
Alfol 12 (1-dodecanol) [$C_{12}H_{26}O$]	20.0	200							[F8]
Polyethylene Glycol 600 (E600) [$(OC_2H_2)_nOH_2$]	20.0 - 25.0	127 - 146		2.26	1100 - 1126	1232	0.160 - 0.189		[F8,H3,L4,S18]
Dimethyl Sebacate [$C_{12}H_{22}O_4$]	21.0	120 - 135							[F11]
Lithium Chloride Ethanolate [$LiClC_2H_5O$]	21.0	188							[H3]
Octadecyl 3-Mercaptopropionate [$C_{21}H_{42}O_2S$]	21.0	141 - 143							[F11,K10]
Iodohexadecane [$C_{16}H_{33}I$]	22.2	131							[B1,B2]
Allyl Palmitate [$C_{19}H_{36}O_2$]	22.6	173							[B1,B2]
Ethyl Palmitate [$C_{18}H_{36}O_2$]	23.0	122 - 182							[K9,S35]
Dodecanol [$C_{12}H_{26}O$]	23.8 - 26.0	184 - 200							[B1,B2,H11]

Table 2.3 (b): Non-Paraffin Organic PCMs in the Considered Temperature Range

Non-Paraffin Organics	T_m [°C]	H_f [kJ/kg]	Cp_L [kJ/kg°C]	Cp_S [kJ/kg°C]	d_L [kg/m^3]	d_S [kg/m^3]	k_L [W/m°C]	k_S [W/m°C]	Sources
Undecylenic Acid [$C_{11}H_{20}O_2$]	24.6	141							[B1,B2]
Octadecyl Acrylate [$C_{21}H_{40}O_2$]	25.7	115							[B1,B2]
Phorone [$C_9H_{14}O$]	25.8	124							[B2]
d-Lactic Acid [$C_3H_6O_3$]	26.0	184			1249				[H3,S18]
Vinyl Stearate [$C_{20}H_{38}O_2$]	27.0 - 29.0	122							[F11,Z1]
Diphenyl Oxide [$C_{12}H_{10}O$]	28.0				1073				[H3]
Hexadecyl Decanoate (Cetyl Caprate) [$C_{26}H_{52}O_2$]	29.4	186	2.08	2.81					[A12]
Methyl Palmitate [$C_{17}H_{34}O_2$]	29.0	199 - 205							[H3,S18,S35]
1-3 Methyl Pentacosane [$C_{26}H_{54}$]	29.0	197							[H3]
Ethyl Stearate [$C_{20}H_{40}O_2$]	33.0	188							[S35]
Capric [$C_{10}H_{20}O_2$]	30.0 - 36.0	150 - 163	1.60 - 2.10	1.90 - 1.95	878 - 886	1004	0.149 - 0.153	0.150 - 0.160	[A1,C10,D5,F10,K3,L4,P6, S1,S18,S19,Y2]
Lauric [$C_{12}H_{24}O_2$]	41.0 - 52.5	160 - 212	1.53 - 2.27	1.70 - 2.81	862 - 870	1007	0.147	0.150 - 0.170	[A1,C10,D5,F10,H10,K3,L4,P6, S1,S4,S7,S18,S19,T16,Y2,Z1]
Palmitic [$C_{16}H_{32}O_2$]	54.1 - 64.3	163 - 212	2.37 - 2.94	1.90 - 2.20	847 - 862	942 - 989	0.162 - 0.165	0.160	[A1,C10,F10,H10,K3,L4,P6, S1,S7,S17,S18,S19,T16,Z1]
Myristic Acid [$C_{14}H_{28}O_2$]	49.0 - 58.0	168 - 228	2.26 - 3.67	1.60 - 3.29	844 - 861	989 - 990	0.150	0.170	[A1,C10,H3,K3,L4,P6,S1, S7,S17,S18,S19,Y2,Z1]
Stearic Acid [$C_{18}H_{36}O_2$]	54.0 - 70.0	155 - 210	2.10 - 2.38	1.59 - 2.86	847 - 1150	940 - 1080	0.172 - 0.290	0.290 - 0.300	A1,C10,F10,H3,K3,L4,P6, S1,S18,S19,S20,Z1]

Table 2.4: Advantages and Disadvantages of Non-Paraffin Organics Used as PCMs [F11,L7]

Advantages	Disadvantages
No Separation Stable High Latent Heat No Supercooling Safe Non-corrosive Insoluble in Water	Higher Cost Low Thermal Conductivity Flammable Lower Density Wide Melting Temp. Range Foul Odors

2.1.3 Hydrated Salts

Hydrated salts are the most widely researched type of inorganic PCMs. The general chemical form of these salts is a salt bonded to a quantity of water according to the following relationship:

$$Salt \cdot nH_2O$$

Where, n is the number of moles of water relative to a singular mole of the salt. Hydrated salt PCMs are desirable due to their very low cost, while maintaining high heats of fusion. Advantages for most salts include minimal health and safety concerns, wide availability, and the potential for tuning of their melt/freeze temperature through the use of additives, mixtures with other salts, or variations in the quantity of water (hydration level). Although hydrated salts have low thermal conductivities, they still tend to have several times greater conductivities than organic PCMs. In addition, as pointed out by Farid et al., hydrated salt PCMs have a high volumetric energy storage density [F3]. The major disadvantages of hydrated salt PCMs include a propensity to supercool and either incongruent or semi-incongruent melting and freezing. Researchers have demonstrated different nucleation agents, which are capable of eliminating or greatly reducing supercooling of hydrated salts. For instance, strontium chloride hexahydrate ($SrCl_2 \cdot 6H_2O$ or SC6)

is a well-known additive, which eliminates nearly all of the supercooling of calcium chloride hexahydrate. Semi-incongruent melting and freezing of hydrated salts is generally addressed through the use of thickening agents or the addition of other additives, which form a congruently melting/freezing eutectic with the base salt. Corrosion is another issue inherent to the use of hydrated salts as it impacts containment of the salts. Containment is all the more critical, when it is understood that hydrated salts must be perfectly encapsulated throughout their lifetime in order to prevent a change in hydration. This is due to the fact that hydrated salts either behave as a desiccant or humectant at ambient conditions [F11]. Calcium chloride and its hydrates up to 6 moles of water are well-known desiccants [N4]. Sodium sulfate decahydrate ($Na_2SO_4 \cdot 10H_2O$) is a humectant under typical ambient conditions, meaning it releases moisture to the atmosphere [K8]. Some common hydrated salt PCMs in the temperature range 15-35°C are summarized in Table 2.5.

The hydrated salt mixtures and eutectics found in the literature are summarized in Table 2.6. A eutectic mixture corresponds to the mixture ratio of two salts which results in the lowest melting point. At the eutectic mixture, both salts undergo a phase change at the same temperature, making the phase transition process congruent. It is interesting to note that several of the mixtures show a variation in the phase change temperature as the mixture changes. This phenomenon appears to be an effective method for slight adjustments of the phase change temperature of these hydrated salt mixtures. The advantages and disadvantages of hydrated salt PCMs are summarized in Table 2.7.

Table 2.5: Salt Hydrate Inorganic PCMs in the Considered Temperature Range

Hydrated Salts	T_m [°C]	H_f [kJ/kg]	Cp_L [kJ/kg°C]	Cp_S [kJ/kg°C]	d_L [kg/m^3]	d_S [kg/m^3]	k_L [W/m°C]	k_T [W/m°C]	k_S [W/m°C]	Sources
$NaOH \cdot 3.5H_2O$	15.0 - 15.5	219								[B11,C1,N2,S26,Z1]
$Na_2CrO_4 \cdot 10H_2O$	18.0									[B11,Z1]
$KF \cdot 4H_2O$	18.0 - 20.0	230 - 246	2.39 - 2.47	1.62 - 1.84	1447 - 1456	1437 - 1455	0.479		0.608	[H12,N2,S15,S28]
$LiClO_4 \cdot 3H_2O$	20.0									[K10]
$FeBr_3 \cdot 6H_2O$	21.0 - 27.0	105								[S18]
$Mn(NO_3)_2 \cdot 6H_2O$	25.0 - 26.0	126 - 148			1728	1600 - 1795				[C11,D3,J2,N1,S18,S28, T17,Z1]
$LiBO_2 \cdot 8H_2O$	25.7	289								[G4]
$CaCl_2 \cdot 6H_2O$	27.0 - 29.9	160 - 201	2.13 - 2.32	1.44 - 1.46	1496 - 1562	1690 - 1802	0.539 - 0.561	0.700	1.09 - 1.10	[A1,C6,C11,E5,F5,G4,H3, H12,L4,L9,L18,N2,T6]
$Na_2HAsO_4 \cdot 12H_2O$	28.0				1736					[H3]
$LiNO_3 \cdot 3H_2O$	29.9 - 30.2	189 - 296	2.76	1.73	1425 - 1430	1550 - 1575	0.584		0.820	[H3,H12,S14,S18]
$Na_2SO_4 \cdot 10H_2O$	31.1 - 32.5	222 - 254	3.26 - 3.31	1.76 - 1.93	1330 - 1410	1458 - 1485	0.544 - 0.589		0.514	[A1,C3,C14,G5,G6,H3,K10, K14,N2,P12,S1,S18,T2,T5,T6]
$Na_2CO_3 \cdot 10H_2O$	32.0 - 36.0	247 - 267			1440 - 1442					[H3,H12,N2,S18,T6]
$KFe(SO_4)_2 \cdot 12H_2O$	33.0	173								[S18]
$CaBr_2 \cdot 6H_2O$	34.0	116 - 138			1956	2194				[L4,N2,S18,S28]
$LiBr_2 \cdot 2H_2O$	34.0	124								[S18]
$Na_2HPO_4 \cdot 12H_2O$	35.0 - 36.1	279 - 280	1.93 - 2.51	1.55 - 1.68		1552 - 1520	0.589		2.93	[H12,L18,S1]

Table 2.6 (a): Salt Hydrate Mixtures in the Considered Temperature Range

Hydrated Salt Mixtures			Eut.	Type	T_m [°C]	H_f [kJ/kg]	Cp_L [J/g°C]	Cp_S [J/g°C]	Sources
$Mn(NO_3)_2 \cdot 6H_2O$ (96%)	$MnCl_2 \cdot 4H_2O$ (4%)			wt%	15.0 - 25.0	126	2.78	2.34	[C1,K9]
$Mn(NO_3)_2 \cdot 6H_2O$ (99%)	$MnCl_2 \cdot 4H_2O$ (1%)			wt%	22.1	121			[N1]
$Cu(NO_3)_3 \cdot 6H_2O$ (51-55%)	$LiNO_3 \cdot 3H_2O$ (49-45%)			wt%	16.5	250			[K10]
$LiNO_3 \cdot 3H_2O$ (52-45%)	$Zn(NO_3)_2 \cdot 6H_2O$ (48-55%)			wt%	17.2	220			[C1,K10]
$Na_2SO_4 \cdot 10H_2O$ (50%)	NaCl (50%)			mol %	18.0	286	3.26	1.76	[D8,N1]
$CaCl_2 \cdot 6H_2O$ (90%)	$MgCl_2 \cdot 6H_2O$ (10%)			wt%	26.0				
$CaCl_2 \cdot 6H_2O$ (85%)	$MgCl_2 \cdot 6H_2O$ (15%)			wt%	25.0				
$CaCl_2 \cdot 6H_2O$ (80%)	$MgCl_2 \cdot 6H_2O$ (20%)			wt%	23.5				
$CaCl_2 \cdot 6H_2O$ (75%)	$MgCl_2 \cdot 6H_2O$ (25%)			wt%	21.0				
$CaCl_2 \cdot 6H_2O$ (66.6%)	$MgCl_2 \cdot 6H_2O$ (33.3%)		X	wt%	23.0 - 25.0	127	2.74		[C11,H12,Z3]
$CaCl_2 \cdot 6H_2O$ (50%)	$MgCl_2 \cdot 6H_2O$ (50%)			wt%	25.0	95			[S18]
$Co(NO_3)_2 \cdot 6H_2O$ (41.5-52.5%)	$LiNO_3 \cdot 3H_2O$ (37.8-52.7%)	H_2O (5.8-9.7%)		wt%	22.3	265			[K10]
$CaCl_2 \cdot 6H_2O$ (95%)	$Mg(NO_3)_2 \cdot 6H_2O$ (5%)			wt%	22.8	162	2.74	3.54	[G2]
$Na_2SO_4 \cdot 10H_2O$ (75.1%)	H_2O (24.9%)			wt%	24.0	159			[K10]
$Na_2SO_4 \cdot 10H_2O$ (79.9%)	H_2O (20.1%)			wt%	27.0	178			[K10]
$Na_2SO_4 \cdot 10H_2O$ (84.9%)	H_2O (15.1%)			wt%	29.0	199			[K10]
$Na_2SO_4 \cdot 10H_2O$ (90.4%)	H_2O (9.6%)			wt%	32.0	214			[K10]
$Na_2SO_4 \cdot 10H_2O$ (94.7%)	H_2O (5.3%)			wt%	32.0	237			[K10]
$LiNO_3 \cdot 3H_2O$ (65-55%)	$Ni(NO_3)_2 \cdot 6H_2O$ (35-45%)		X	wt%	24.2	230			[K10]
$Ca(NO_3)_2 \cdot 6H_2O$ (45%)	$Zn(NO_3)_2 \cdot 6H_2O$ (55%)		X	wt%	25.0	130			[L15]
$Ca(NO_3)_2 \cdot 4H_2O$ (47%)	$Mg(NO_3)_2 \cdot 6H_2O$ (53%)		X	wt%	30.0	134 - 136			[L6,S18]
$Ca(NO_3)_2 \cdot 4H_2O$ (67%)	$Mg(NO_3)_2 \cdot 6H_2O$ (33%)		X	wt%	30.0	136			[L15]
$Ca(NO_3)_2 \cdot 4H_2O$ (72%)	$Al(NO_3)_3 \cdot 9H_2O$ (28%)		X	wt%	35.0	139			[L15]
$CaCl_2 \cdot 6H_2O$ (93%)	KNO_3 (7%)			wt%	25.0	120			
$CaCl_2 \cdot 6H_2O$ (95.3%)	NaCl (4.3%)	KCl (0.4%)	X	wt%	26.0 - 26.8	188 - 189	1.44	1.35	[A1,G4,H12,S1]
$Mg(NO_3)_2 \cdot 6H_2O$ (18%)	$Zn(NO_3)_2 \cdot 6H_2O$ (82%)		X	wt%	32.0	130			[L15]

Table 2.6 (b): Salt Hydrate Mixtures in the Considered Temperature Range

Hydrated Salt Mixtures			d_L [kg/m^3]	d_S [kg/m^3]	k_L [W/m°C]	k_S [W/m°C]	Sources
$Mn(NO_3)_2 \cdot 6H_2O$ (96%)	$MnCl_2 \cdot 4H_2O$ (4%)		1728 - 1738	1795			[C1,K9]
$CaCl_2 \cdot 6H_2O$ (66.6%)	$MgCl_2 \cdot 6H_2O$ (33.3%)		1590				[C11,H12,Z3]
$Co(NO_3)_2 \cdot 6H_2O$ (41.5-52.5%)	$LiNO_3 \cdot 3H_2O$ (37.8-52.7%)	H_2O (5.8-9.7%)					[K10]
$CaCl_2 \cdot 6H_2O$ (95%)	$Mg(NO_3)_2 \cdot 6H_2O$ (5%)			1481	0.752	0.911	[G2]
$Ca(NO_3)_2 \cdot 6H_2O$ (45%)	$Zn(NO_3)_2 \cdot 6H_2O$ (55%)		1931				[L15]
$Ca(NO_3)_2 \cdot 4H_2O$ (67%)	$Mg(NO_3)_2 \cdot 6H_2O$ (33%)		1676				[L15]
$Ca(NO_3)_2 \cdot 4H_2O$ (72%)	$Al(NO_3)_3 \cdot 9H_2O$ (28%)		1727				[L15]
$CaCl_2 \cdot 6H_2O$ (95.3%)	NaCl (4.3%)	KCl (0.4%)		1640	0.540	1.09	[A1,G4,H12,S1]
$Mg(NO_3)_2 \cdot 6H_2O$ (18%)	$Zn(NO_3)_2 \cdot 6H_2O$ (82%)		1915				[L15]

Table 2.7: Advantages and Disadvantages of Hydrated Salts Used as PCMs

Advantages	Disadvantages
Low Cost Widely Available Higher Thermal Conductivity High Volumetric Storage Density Tuning of Phase Change Temp. Safe	Instabilities / Phase Separation Supercooling Large Volume Change Corrosive Require Sealed Container

2.2 PCM Selection

For the purposes of the work considered in this study, hydrated salts were the only PCM type selected for additional study. The primary reason for this was PCM cost and availability as thermal energy storage systems, such as those presented in Chapter 1, would require large quantities of the selected PCM. If paraffins were used instead of hydrated salts, the order of magnitude higher price would likely render a large-scale thermal energy storage system immediately uncompetitive from a cost perspective. Therefore, hydrated salt PCMs became the only viable option despite their significant drawbacks of phase instability, supercooling, and corrosiveness.

A short list of hydrated salt PCMs from Table 2.5 and Table 2.6 were selected for characterization. This list of PCMs was primarily prepared by only considering those PCMs with the lowest possible cost, wide availability, and appropriateness of T_m and H_f to the desired application. This short list of PCMs is presented in Table 2.8.

Table 2.8: Hydrated Salt PCMs Selected for Characterization

PCM	T_m [°C]	H_f [J/g]	Sources
Sodium Hydroxide 3.5 Water [$NaOH \cdot 3.5H_2O$]	15.0 - 15.5	219	[B11,C1,N1,S26,Z1]
Potassium Fluoride Tetrahydrate [$KF \cdot 4H_2O$]	18.0 – 20.0	230 - 246	[H12,N2,S15,S28]
Calcium Chloride Hexahydrate + Magnesium Chloride Hexahydrate [$CaCl_2 \cdot 6H_2O$ + $MgCl_2 \cdot 6H_2O$ (33 wt%)]	23.0 - 25.0	127	[C11,H12,Z3]
[$CaCl_2 \cdot 6H_2O$ + $MgCl_2 \cdot 6H_2O$ (50 wt%)]	25.0	95	[S18]
Calcium Chloride Hexahydrate [$CaCl_2 \cdot 6H_2O$]	27.0 – 29.9	160 - 201	[A1,C6,C11,E5,F5,G4,H3, H12,L4,L18,N2,T6]
Sodium Sulfate Decahydrate [$Na_2SO_4 \cdot 10H_2O$] (Glauber's Salt)	31.1 – 32.5	222 - 254	[A1,C3,C14,G5,G6,H3, K10,K14,N2,P12,S1,S18, T2,T5,T6]

3 Experimental Methods

There are several different test methods used to quantify the performance, supercooling, and long-term stability of PCM samples. Some of these test methods, such as differential scanning calorimetry (DSC) or thermogravimetric analysis (TGA) are well established and utilize widely-available equipment. In addition to these methods, several additional methods and pieces of equipment were developed to address the specific analysis needs of the PCM development presented in this work. This equipment includes a drop calorimeter, an automated thermal cycling system, and a PCM dehydration cell.

3.1 Differential Scanning Calorimetry

Differential scanning calorimetry (DSC) has been widely demonstrated as an effective method for evaluating both the phase change temperature and latent heat of PCMs [S20,R9,T19,A12]. DSC testing has several advantages. First, numerous tests can be conducted quite rapidly; on the order of 45 minutes per test. In addition, the process is standardized, repeatable, and utilizes widely-available equipment. However, there are some disadvantages inherent to DSC testing of PCMs. First, the sample size is very small (< 25 mg), which prevents it from accurately examining large, non-homogenous PCM samples. This is of particular importance with regard to phase separation and supercooling of the PCM. Phase separation is known to be more pronounced in deeper, and consequently larger, samples of PCM. This is due to irreversible separation largely being driven by density differences in the different phases after they have separated. If the separated phases remain in close proximity to one another after separation, the probability they will re-combine into a homogenous mixture is increased. The second significant limitation of DSC testing is accurate measurements of supercooling. While at first glance supercooling appears to be an atomic/micro-scale phenomenon, it is known that there are macroscopic methods, which

work to prevent supercooling. For instance, as will be shown in Section 4.6.2, supercooling can be effectively suppressed by adding inert nucleation surfaces (FeO, wood chips) to the PCM. These materials have quite large dimensions; on the order of 0.01 to 1 mm. While these materials can be added to the DSC samples, their large size relative to the total sample size makes it difficult to ensure sample uniformity. As will be shown, the DSC is capable of detecting (and even measuring) supercooling. However, in nearly all samples tested, the DSC overpredicted supercooling by 50 to 100% relative to larger-scale supercooling tests. For these reasons, nucleating agents were not added to DSC samples and any measured supercooling values were not taken to be accurate.

3.1.1 DSC Test Method

A TA Instruments Q2000 DSC (Figure 3.1) equipped with an auto sampler was used for all DSC tests. 15 to 25 mg PCM samples were placed into hermetically sealed aluminum pans individually loaded into the DSC's autosampler tray. Nitrogen was used as a purge gas at a flow rate of 50 mL/min. During each test, the PCM sample pan is loaded into the test chamber alongside an identical, empty reference pan. The DSC continually measures the heat flow into and out of the test sample and reference pan throughout sample heating and/or cooling. By plotting this heat flux against the sample temperature, both the phase transition temperature and latent heat of melting can be calculated. Figure 3.2 presents a typical DSC heat flow curve during a test. The following test procedure was used for all DSC tests:

1. Hold sample isothermal at -30°C for 2 minutes
2. Heat sample to 50°C at 7°C/min
3. Hold sample isothermal at 50°C for 1 minute
4. Cool sample to -20°C at -7°C/min

Figure 3.1: TA Instruments Q2000 DSC

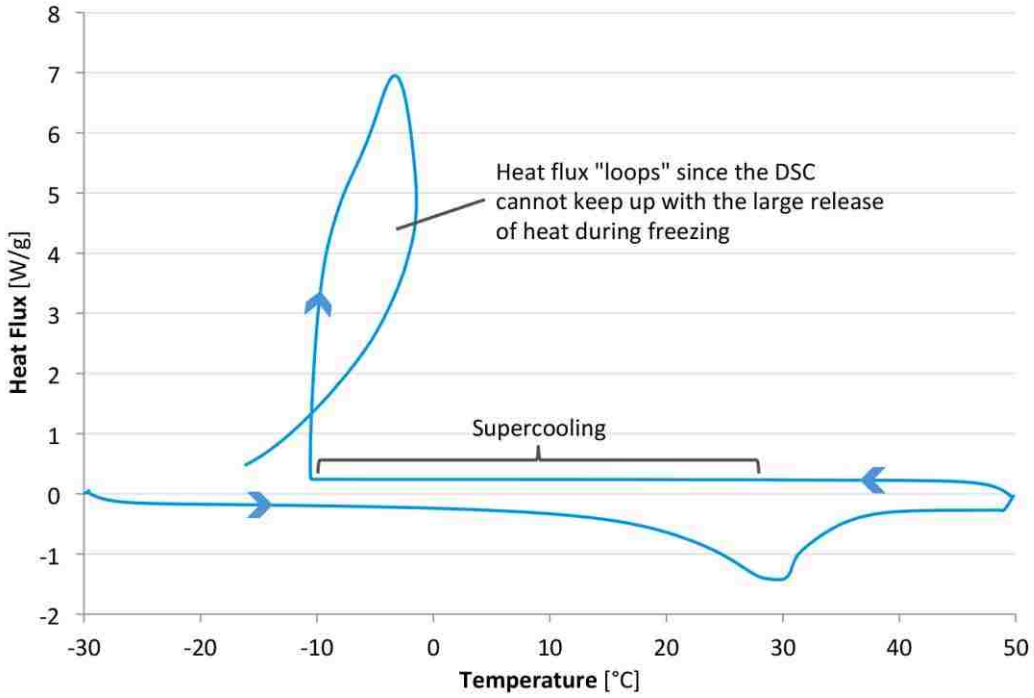

Figure 3.2: DSC Test Heat Flux Curve Example

As seen in Figure 3.2, during melting of the PCM, a defined (negative) peak is found in the heat flux curve. A similar peak is not typically encountered during freezing of a hydrated salt PCM due to supercooling. Since the PCM does not freeze at the actual freezing temperature, there is a built-up "potential" which releases the latent heat of freezing very quickly when the PCM finally freezes at a temperature well below the freezing temperature. This rapid release of energy overwhelms the cooling mechanism of the DSC, allowing the sample temperature to rise slightly, resulting in a loop in the cooling curve. Because of this abnormality during freezing, only the melting peak is considered in examining the thermal properties of hydrated salt PCMs.

The melting peak is examined by first drawing a line across the base of the peak such that it lies tangent to the heat flux curve before and after the peak (see Figure 3.3). The area enclosed by this line and the peak of the heat flux curve is equivalent to the latent heat of the PCM (H_f). Two critical temperature values are evaluated using the melting peak. First, the temperature at point of maximum heat flux is defined as the peak temperature (T_p). Second, a line can be drawn tangent to the heat flux curve at the point of maximum slope on the cold side of the peak temperature. The temperature at which this line intersects the line across the base of the peak is defined as the onset temperature (T_o). This onset temperature can be thought of as the temperature at which melting of the PCM begins. Since this temperature has been found to be closer to the actual PCM melting temperature than the peak temperature, it is defined as T_m for all of the DSC PCM tests.

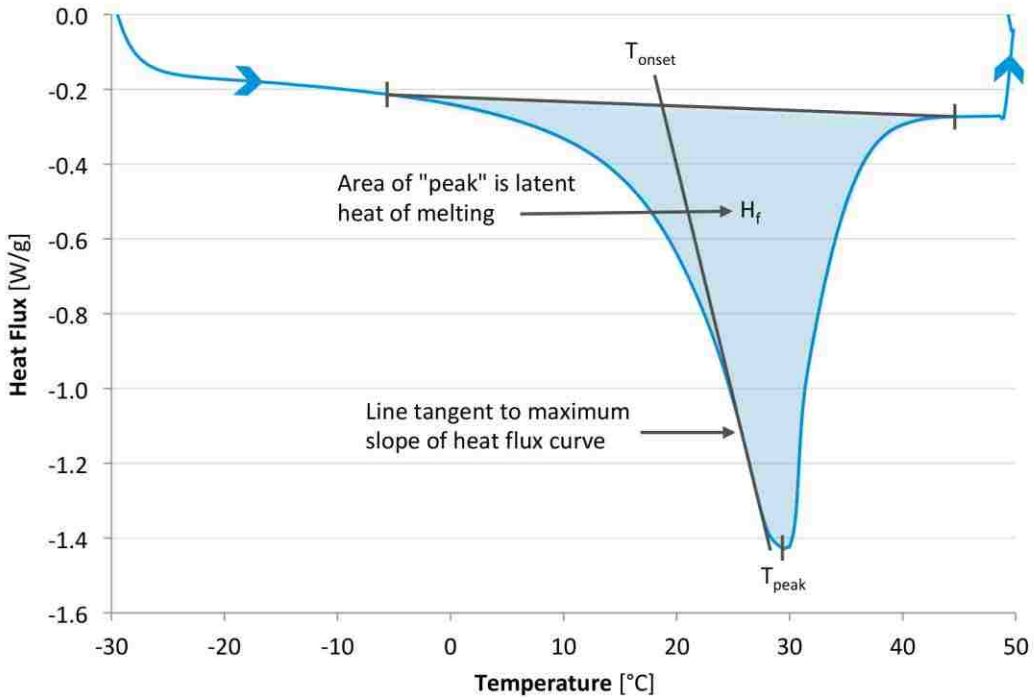

Figure 3.3: Analysis of Melting Peak of DSC Result

3.2 PCM Thermal Cycling System

Repeated thermal cycling of PCM candidates is essential to ensure long-term performance of the materials. This is especially important with most hydrated salt PCMs as they are known to undergo phase separation during cycling. If even a small percentage of the PCM changes phase during each cycle, over the course of years (assuming a daily cycle), a large percentage of the PCM will transition into a phase which does not undergo a phase change at the desired temperature. This can severely lower the thermal storage capacity of the system. In order to test PCM stability over several thousand cycles, an automated system for thermal cycling of PCM samples was developed.

To allow for several thousand thermal cycles to be completed within a reasonable period of time (~1 year), it was decided that the thermal cycling system should be capable of freezing or melting ~200 g samples of PCM once every hour. This requires that the heat transfer rate into or out of the PCM samples be sufficient to allow for complete melting or freezing within the desired time. Since conduction within the PCM is fixed by the PCM properties (~0.5 W/m·K in the case of hydrated salts), high convective heat transfer between the PCM samples and their surroundings is essential in meeting the one-hour freeze/melt time. After some experimentation, it was found that immersion of the ~200 g PCM samples in a water bath allowed for melting/freezing within the required time. In order to minimize cycling time, the time required to change the temperature of the water bath between hot and cold at the end of each half-cycle must be minimized. In order to accomplish this, the water in the bath was designed to be drained at the end of each hour and would be replaced by water already at the opposite temperature extreme. In this way, the time required to heat and cool the mass of water in the bath would not translate into additional melting or freezing time.

A custom cycling system was designed around these criteria, with the principles of its operation being presented in Figure 3.4. This system is composed of three vertically-stacked tanks with the ~200 g PCM samples placed in the top two tanks. Both of these two tanks are fitted with both a heating and cooling system, which can be turned on and off as required. The heating system is composed of water heating elements in the bottom of each tank, while the cooling system employs a separate chiller, which circulates chilled glycol through coils located around the inside walls of the tanks. As illustrated in Figure 3.4, there are four operational steps of this system. Step 4 is defined as the step when both of the PCM tanks are filled with water with one of the tanks being heated and the other being cooled. This step lasts for around an hour and is the step during which the PCM samples in the tanks undergo a phase change. After an hour, the valve beneath PCM Tank 2 opens, allowing the water in this tank to drain into the Drain Tank during

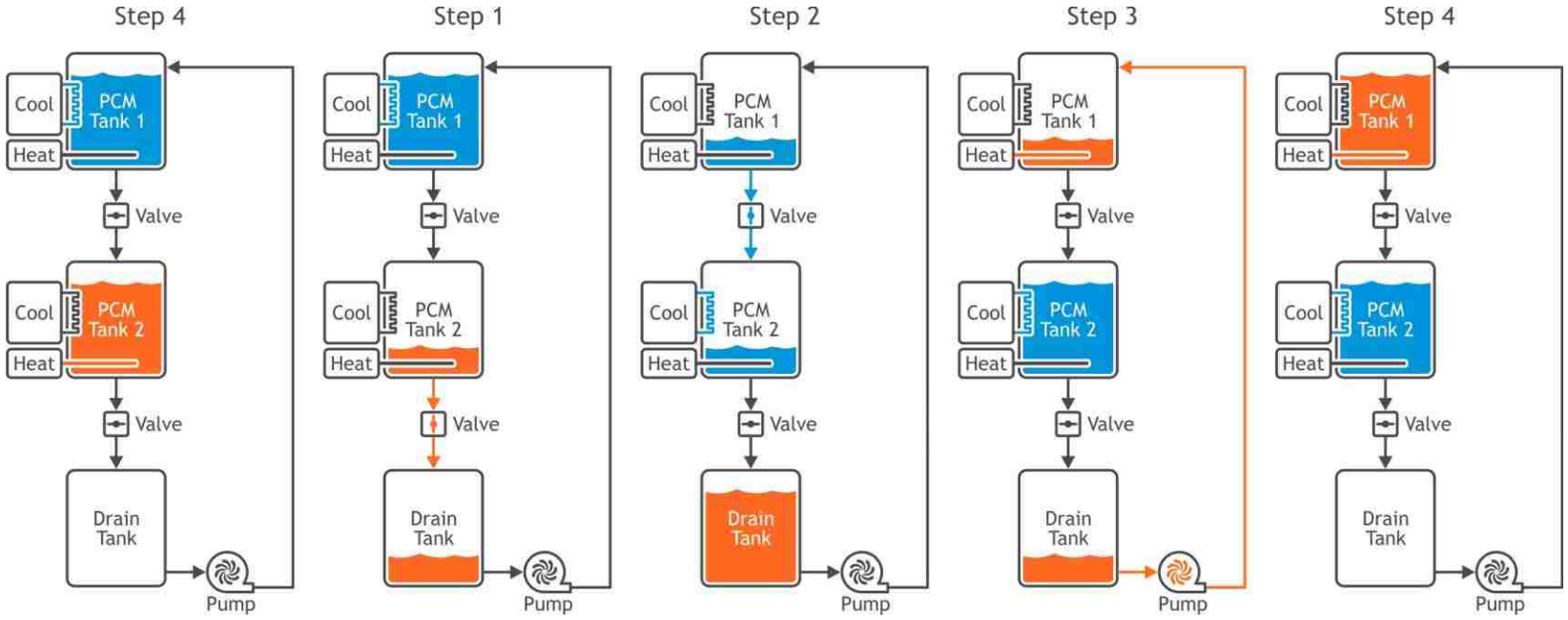

Figure 3.4: Thermal Cycling System Operational Steps

Step 1. During Step 2, the Tank 2 valve closes, while the valve beneath PCM Tank 1 simultaneously opens, draining the water from PCM Tank 1 into PCM Tank 2. Since this water is at the opposite temperature extreme with respect to the samples in PCM Tank 2, the PCM in this tank begins to be heated or cooled immediately. As the water flows into PCM Tank 2, the heater or chiller in this tank is activated to maintain the temperature of the new water. In Step 3, the water in the Drain Tank is pumped from this tank into PCM Tank 1, where it begins to heat or cool the PCM samples in that tank. As before, either the heater or chiller activates in PCM Tank 1 to maintain the temperature of the new water in the tank. With both tanks filled with water, a new Step 4 begins, but with the water in both PCM tanks at the opposite temperature extreme. The benefit of this design is that the hot water is always being heated and the cold water is constantly being cooled. Therefore, once the one-hour phase transition step is complete (Step 4), water at the opposite temperature extreme is instantly available to begin the following phase transition in the opposite direction.

The physical thermal cycling system was designed to accommodate up to thirty-two ~200 g PCM samples split evenly between the two heating/cooling tanks. The following equation was used to find the required heating and cooling loads (Q) of the system due to the latent and sensible heat of the PCM and the sensible heat of the stainless-steel encapsulations:

$$Q = n\frac{m_{PCM}\left(H_f + Cp_{PCM}\Delta T\right) + m_{ENC}Cp_{SS}\Delta T}{t} \tag{3}$$

Where n is the number of samples, m_{PCM} is the mass of PCM per sample, Cp_{PCM} is the PCM specific heat, ΔT is the temperature change of the PCM during melting or freezing, m_{ENC} is the mass of a single stainless-steel encapsulation, Cp_{SS} is the specific heat of stainless steel, and t is the time during which the PCM either melts or freezes. Assuming an n of 32, m_{PCM} of 200 g, H_f of 170 J/g, Cp_{PCM} of 2.5 J/g°C, ΔT of 45°C, m_{ENC} of 300 g, Cp_{SS} of 0.5 J/g°C, and t of 3,600 seconds, a Q of

562 W is found. Because of unknown thermal losses from the tanks and piping of the cycling system, the system was designed around a higher Q of 1,000 W, providing significant operational margin.

Heat was supplied to the heating/cooling tanks through two 1,500 W water heater elements placed into the bottom of the two 11.4 liter tanks. Only one of these heaters was operated at a time with the second being used as a backup in the event of a heater failure. A Polyscience 6100 series, 1 hp chiller was used to provide up to 1,200 W of cooling at temperatures approaching 0°C. This coolant was circulated through 15-circuits of copper coils around the inside of the top two tanks. A 50:50 water/glycol mixture was used as the heat transfer fluid to prevent localized freezing at the chiller setpoint temperature of 1.5°C. A completed heating/cooling tank is presented in Figure 3.5.

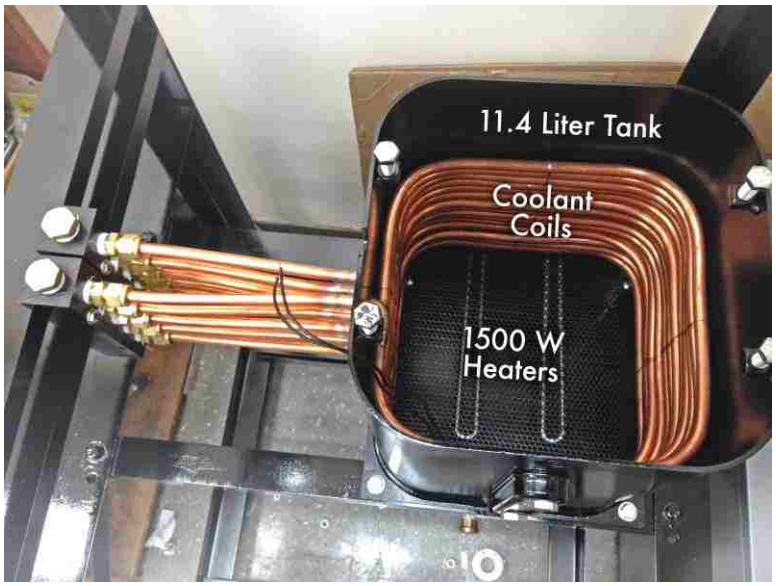

Figure 3.5: Heating/Cooling Tank of Thermal Cycling System

Threaded, ½ inch brass piping was used to connect the three tanks and pump. Brass solenoid valves were used to control the water flow out of both of the heating/cooling tanks and to direct coolant to the tank being cooled. A 30 W pump was used to raise water from the drain tank at the bottom of the system to the top heating/cooling tank. The entire system was controlled using Intel's Edison computer-on-module system running Arduino software. Figure 3.6 presents the overall system design and finished construction of the automated thermal cycling system.

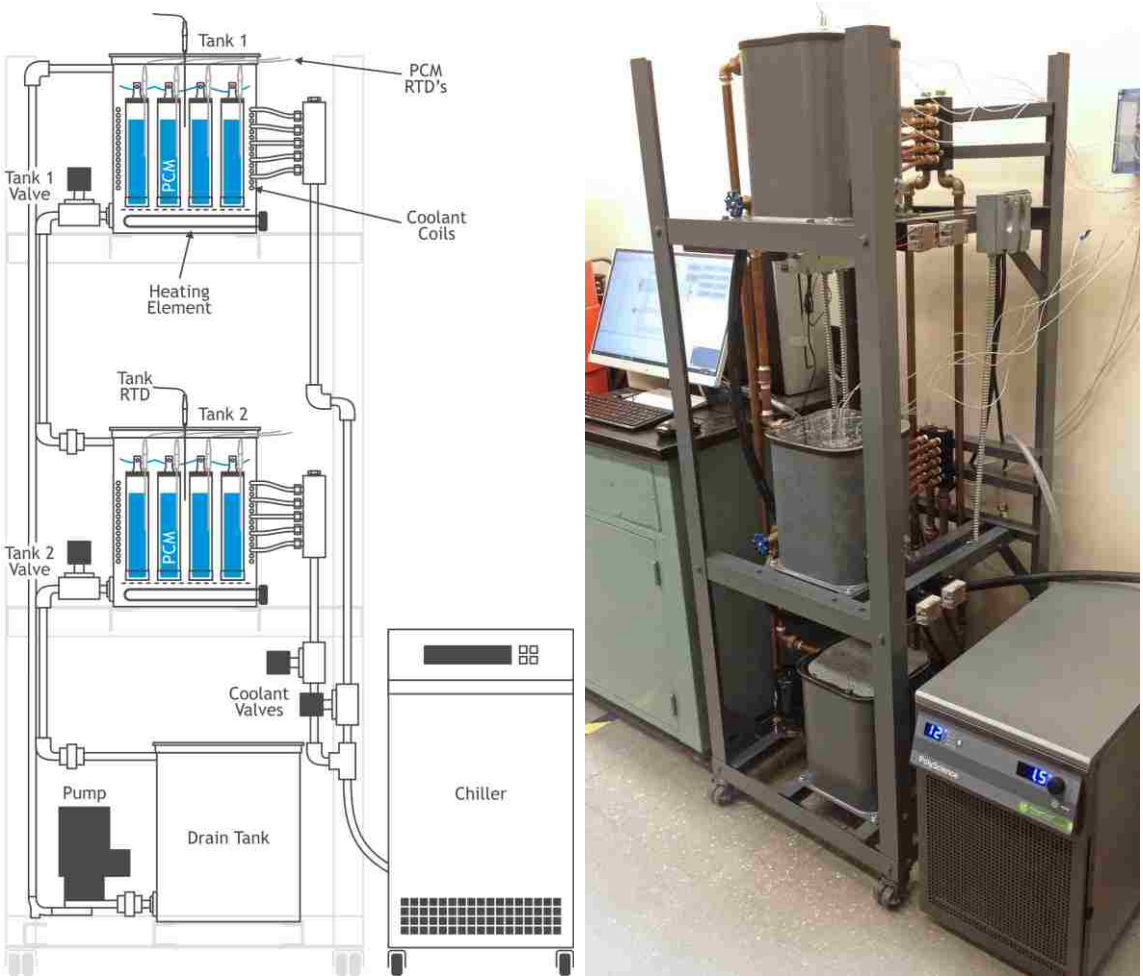

Figure 3.6: Thermal Cycling System Design & Completed System

Measurement Computing's USB-Temp data acquisition boxes were used for temperature collection during cycling. Tank water temperatures were recorded along with internal temperatures for each PCM sample. Four and three-wire 100 Ω resistance temperature detectors (RTDs) were used for all temperature measurements. Temperature data was written to a file using DASYLab data acquisition software. Typical operation of the cycling system was at water temperatures of 5 and 50°C for the cold and hot tank respectively. Although a cooling and heating period of 60 minutes was targeted, this time was later increased to 75 minutes to ensure complete freezing of all of the samples tested. This system has operated for more than 11,000 complete heating/cooling periods (Over 1.5 years) without major equipment failure and with only short shutdowns for scheduled and unexpected laboratory power outages.

3.3 Drop Calorimeter

While DSC testing is capable of measuring the heat of fusion and phase change temperature of a PCM sample, as mentioned above, it is limited in its use due to the small size of the samples (< 25 mg). In addition, while the DSC can thermal cycle a PCM sample, it is impractical for long-term thermal cycling (> 100 cycles). To overcome these issues, a method for analyzing the thermal properties of large PCM samples was needed. These large samples would be the ~200 g samples cycled in the rapid cycling system, improving on the cycling limitation of the DSC. A drop calorimeter was designed and constructed, which was capable of measuring the heat of fusion, phase change temperature, and supercooling of up to 200 g samples of PCM.

3.3.1 Calorimeter Design

A drop calorimeter consists of a liquid bath into which a sample at a different temperature is immersed. Both the temperature of the bath and sample are measured throughout the test. During the test, heat is transferred between the sample and bath until a thermal equilibrium is

reached. If the specific heat of the liquid is known, the latent thermal energy storage capacity of the sample can be calculated.

While this concept is simple, difficulties arise in the implementation of such a calorimeter. The most significant difficulty is that of heat losses between the liquid bath and its surroundings. In order to minimize these losses, it was decided to use a vacuum insulated, 1.18 L, stainless steel bottle for the bath container. This bottle was sized based on the size of the ~200 g samples to be tested. The design of this bottle-based calorimeter is presented in Figure 3.7.

A high accuracy (±0.15°C at 0°C), 4-wire, 100 Ω RTD supplied by Omega was placed inside the bottle to measure the fluid temperature. A magnetic stir bar was also added inside the bottle to allow for mixing of the fluid. The insulated bottle lid is used to support the PCM sample immersed in the fluid. An RTD inside this sample records the temperature of the PCM during the test. Although the outer wall of the insulated bottle is considered the edge of the calorimeter control volume, the bottle was placed inside a larger insulated container to reduce convective heat transfer from the surface of the bottle to the air. This outer container can be thought of as blocking the calorimeter from breezes. RTDs located both inside and outside of this container measure the temperature of the air surrounding the calorimeter and that of the surrounding room. A magnetic stirrer placed into the bottom of the outer container is used to rotate the stir bar in the bottom of the calorimeter bottle.

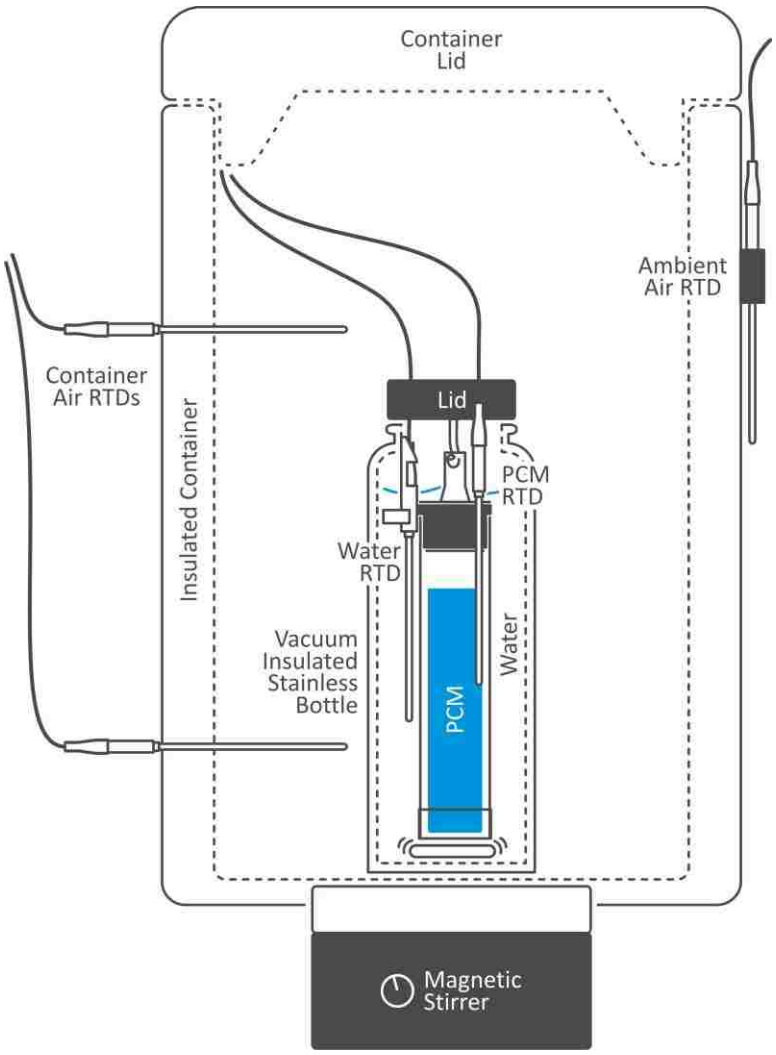

Figure 3.7: Drop Calorimeter Design

3.3.2 Calorimeter Energy Balance

As in any energy balance analysis, the control volume of the drop calorimeter must be clearly defined. The left side of Figure 3.8 presents the control volume as defined for a PCM sample test in the drop calorimeter. The following equation, Equation (4), must hold true to satisfy the energy balance of the test case presented in Figure 3.8:

$$(m_{bottle} + m_{lid} + m_{RTD} + m_{stir\ bar})\mathbf{Cp_{cal}}\Delta T_{fluid} + m_{fluid}Cp_{fluid}\Delta T_{fluid} + m_{ENC}Cp_{ENC}\Delta T_{PCM} + m_{PCM}(Cp_{PCM}\Delta T_{PCM} + \mathbf{H_{f\ PCM}}) = 0 \quad (4)$$

Variables highlighted in bold (Cp_{cal} and $H_{f\ PCM}$) are the unknowns to be solved for, with the subscripts defined as follows:

bottle:	stainless steel, vacuum insulated bottle without lid
lid:	insulated bottle lid with hook for hanging samples
RTD:	RTD and hanger in bottle used to measure fluid temperature
stir bar:	magnetic stir bar for fluid mixing
cal:	calorimeter system minus PCM, sample encapsulation (ENC), and fluid
fluid:	fluid in the calorimeter bottle
ENC:	container for PCM including RTD for temperature measurements
PCM:	the PCM being tested

ΔT refers to a change in temperature of the parameter considered. Before Equation (4) can be used to calculate H_f of the PCM, the second unknown, Cp_{cal}, must be solved for. Cp_{cal} is a constant dependent on the material properties of the bottle, lid, fluid RTD, and stir bar. Calculation of Cp_{cal} is conducted by first defining a calorimeter calibration control volume; presented on the right side of Figure 3.8.

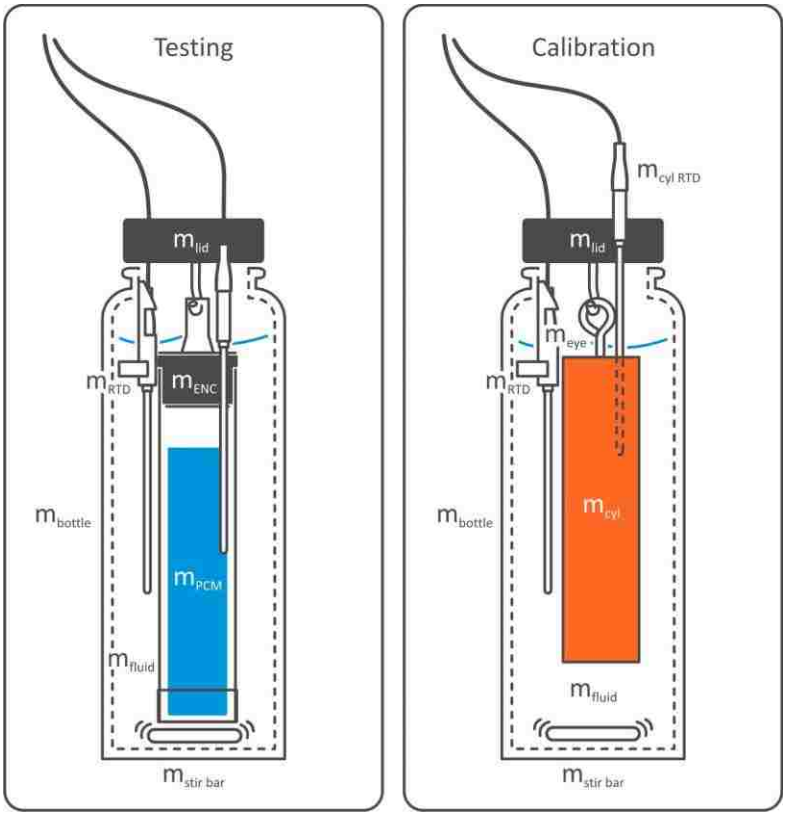

Figure 3.8: Control Volumes for Testing and Calibration States of Drop Calorimeter

For a calorimeter calibration test, the PCM sample is replaced with a 38 mm diameter x 152 mm long cylinder of pure copper or stainless steel 304. This cylinder is suspended from the calorimeter lid by a stainless steel eye threaded into the top of the cylinder. A stainless steel RTD placed into a hole in the cylinder monitors its internal temperature. The following equation governs the energy balance for a calibration test:

$$(m_{bottle} + m_{lid} + m_{RTD} + m_{stir\ bar})\mathbf{Cp_{cal}}\Delta T_{fluid} + m_{fluid}Cp_{fluid}\Delta T_{fluid} + \left(m_{cyl}Cp_{cyl} + (m_{eye} + m_{cyl\ RTD})Cp_{SS}\right)\Delta T_{cyl} = 0 \quad (5)$$

The cylinder is designated by the subscript “cyl”, the subscript “eye” is the stainless steel eye used to hang the cylinder, “SS” is stainless steel 304, and “cyl RTD” is the RTD used for temperature measurement of the cylinder. Since Cp_{cal} is the only unknown in Equation (5), it can be solved for through calibration tests of the calorimeter.

3.3.3 Calorimeter Calibration

A drop calorimeter was constructed according to the design presented in Figure 3.7. Figure 3.9 shows the calorimeter bottle along with the copper cylinder used for calibration and a ~200 g PCM sample encapsulation. Prior to each calibration test, the bottle was filled with between 885 and 940 g of distilled water. It was found that this quantity of water was sufficient for covering a submerged sample, while not overflowing the bottle. Once the bottle was filled with water, it was covered with an uninsulated cap and placed into either a 5°C refrigerated box or a heated box at 50°C. Meanwhile, the calibration cylinder was placed in the opposite temperature box. After letting the water and cylinder equilibrate to the temperatures of their respective boxes, the bottle was removed from its box, re-weighed to determine the weight of water, covered with the test cap, and placed into the outer container of the calorimeter. The magnetic stirrer was turned on and this capped bottle was let set for an hour to allow the outer surface of the bottle to equilibrate with the surrounding air. After an hour, the calibration cylinder was removed from its temperature-controlled box, hooked onto the test cap, and dropped into the bottle. Temperatures of the cylinder, water, air surrounding the bottle, and ambient room air were recorded using Measurement Computing’s USB-Temp data acquisition box, with data written to a file using Measurement Computing’s DAQami software package. Temperature readings were taken at the rate of 2 Hz.

Figure 3.9: Calorimeter Bottle, Copper Calibration Cylinder, and PCM Sample Encapsulation

Figure 3.10: Inside of Calorimeter Bottle

The temperature traces for a copper calibration test are presented in Figure 3.11. After each calibration test, changes in the temperature traces of the cylinder, water, and air surrounding the calorimeter bottle were discretized over a specified time period, t_i. These discrete ΔT values are defined as $(\Delta T_{cyl})_i$, $(\Delta T_f)_i$, and $(\Delta T_a)_i$ for the cylinder, water, and air respectively. Equation (5) can be applied to each of these discrete ΔT values; resulting in Equation (6).

$$\begin{aligned} &\sum_{i=0}^{n}(m_{bottle} + m_{lid} + m_{RTD} + m_{stir\ bar})Cp_{cal}(\Delta T_f)_i + \\ &\sum_{i=0}^{n} m_f\left(Cp_f\right)_i(\Delta T_f)_i + \\ &\sum_{i=0}^{n}\left(m_{cyl}\left(Cp_{cyl}\right)_i + \left(m_{eye} + m_{cyl\ RTD}\right)\left(Cp_{SS}\right)_i\right)\left(\Delta T_{cyl}\right)_i = 0 \end{aligned} \tag{6}$$

Equation (6) adequately closes the energy balance for the idealized calorimeter (presented in Equation (5)) across each discretized time period, t_i. However, the actual calorimeter is not ideal as there are thermal energy transfers into and out of the control volume. In other words, there are either heat losses or gains across the bottle wall. Interestingly, it was found that the calibration tests themselves provided a method for accounting for these energy flows into and out of the calorimeter control volume.

Heat transfer between the calorimeter fluid and the surrounding air (Q_{loss}) can be thought of as a thermal resistance problem. This problem has three distinct resistances; that of the convective heat transfer between the fluid and inner bottle wall ($R_{f\text{-}b}$), conductive heat transfer through the wall of the bottle (R_b), and convective heat transfer between the outer wall of the bottle and the surrounding air ($R_{b\text{-}a}$).

$$R_{tot} = R_{f\text{-}b} + R_b + R_{b\text{-}a} = \frac{1}{h_f A} + \frac{L}{kA} + \frac{1}{h_a A} \tag{7}$$

Where h_f and h_a are the convective heat transfer coefficients of the fluid and air respectively, L is the bottle wall thickness, k is the bottle wall conductivity, and A is the surface area of the inside or outside of the bottle (assumed to be equal for this simple analysis). Using Equation (7), the total heat flux (q) through the bottle wall can be solved for:

$$q = \frac{T_f - T_a}{R_{tot}} = \frac{A\,(T_f - T_a)}{\frac{1}{h_f} + \frac{L}{k} + \frac{1}{h_a}} \tag{8}$$

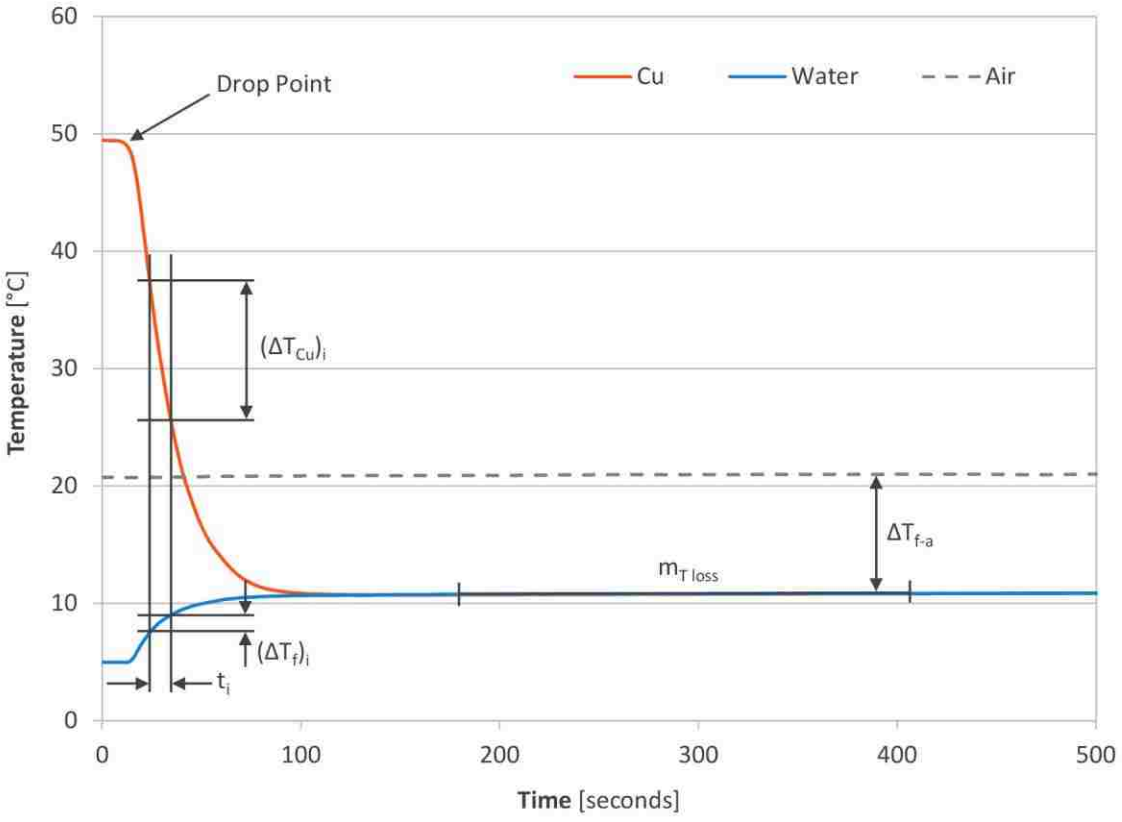

Figure 3.11: Temperature Traces and Discretizations for Cu-based Calorimeter Calibration

Assuming constant conductive and convective heat transfer coefficients, bottle wall thickness, and bottle surface area, Equation (8) shows that the heat flux through the bottle wall only

depends on the temperature difference between the fluid and surrounding air (T_f-T_a). For the purposes of this report, this temperature difference is designated by $\Delta T_{f\text{-}a}$.

Although Equation (8) provides an estimate of heat flux across the bottle wall, the heat transfer variables are unknown, meaning the relationship between $\Delta T_{f\text{-}a}$ and Q needed to be solved for empirically. In order to find this relationship, each calibration test was allowed to run for at least an hour after the cylinder and fluid temperatures reached equilibrium. During this hour, the temperature of the fluid rises or falls very slowly toward the temperature of the air surrounding the bottle. For instance, in Figure 3.11, the equilibrium temperature is seen to slowly rise towards the warmer air temperature. The slope of this gradual temperature rise ($m_{T\ loss}$) was calculated by performing a linear regression of the temperature data (with respect to the discrete data steps, i) before being plotted against $\Delta T_{f\text{-}a}$ for numerous calibration tests (Figure 3.12).

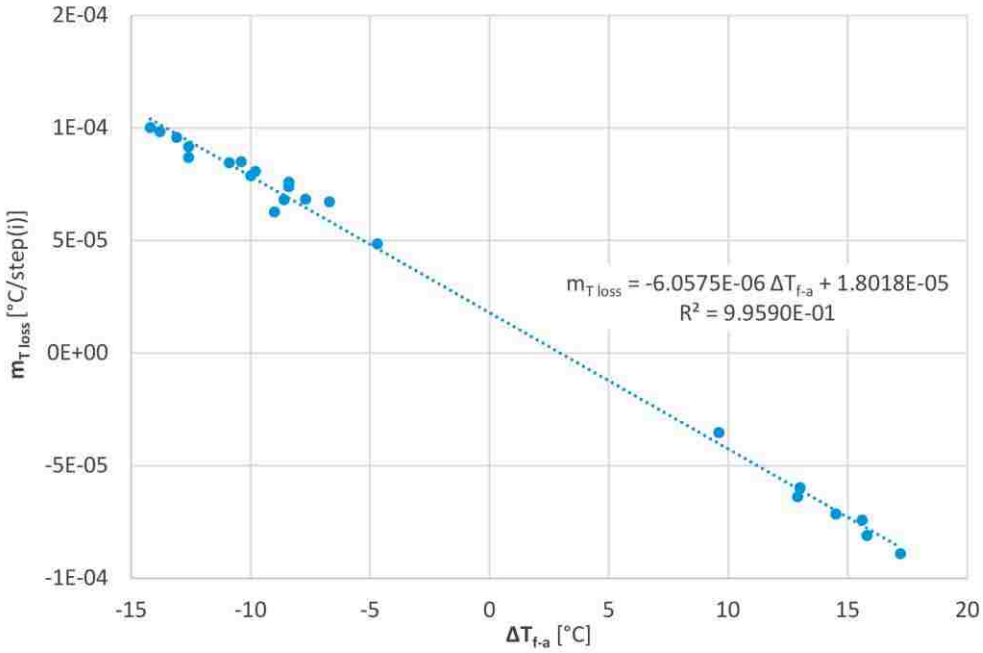

Figure 3.12: $m_{T\ loss}$ vs $\Delta T_{f\text{-}a}$ for Various Calorimeter Calibration Tests

Figure 3.12 shows that a linear regression curve fit has a good match with the $m_{T\ loss}$ data points; the root mean squared (RMS) error is 99.59%. It should be noted that this curve fit lies slightly above $m_{T\ loss}$ = 0°C/step(i) at $\Delta T_{f\text{-}a}$ = 0°C. While this was not initially expected, it should be noted that a small amount of energy is added to the water by way of the magnetic stir bar spinning in the bottom of the calorimeter bottle. This method of measuring $m_{T\ loss}$ accounts for any energy added to the system by the stir bar, which shifts the $m_{T\ loss}$ line to greater than 0°C/step(i) at a $\Delta T_{f\text{-}a}$ of 0°C. With the linear relationship between $m_{T\ loss}$ and $\Delta T_{f\text{-}a}$ quantitatively found, Equation (6) can be re-written to account for $m_{T\ loss}$. In the discrete form, $m_{T\ loss}$ can be thought of as a correction to the calorimeter system temperatures during the time between two measurements. In other words, $m_{T\ loss}$ is subtracted from ΔT_f and ΔT_{cyl} at each discrete step i:

$$\begin{aligned}&\textstyle\sum_{i=0}^{n}(m_{bottle} + m_{lid} + m_{RTD} + m_{stir\ bar})\mathbf{Cp_{cal}}(\Delta T_f - m_{T\ loss})_i + \\ &\textstyle\sum_{i=0}^{n} m_f(Cp_f)_i(\Delta T_f - m_{T\ loss})_i + \\ &\textstyle\sum_{i=0}^{n}\left(m_{cyl}\left(Cp_{cyl}\right)_i + (m_{eye} + m_{cyl\ RTD})(Cp_{SS})_i\right)(\Delta T_{cyl} - m_{T\ loss})_i = 0\end{aligned} \tag{9}$$

Letting $m_{T\ loss}$ = -6.0575 x 10^{-6}/step(i) $\Delta T_{f\text{-}a}$ + 1.8018 x 10^{-5}°C/step(i), as seen in Figure 3.12, Equation (9) becomes:

$$\begin{aligned}&\textstyle\sum_{i=0}^{n}(m_{bottle} + m_{lid} + m_{RTD} + m_{stir\ bar})\mathbf{Cp_{cal}}(\Delta T_f + 6.06 \times 10^{-6}\Delta T_{f\text{-}a} - 1.80 \times 10^{-5})_i + \\ &\textstyle\sum_{i=0}^{n} m_f(Cp_f)_i(\Delta T_f + 6.06 \times 10^{-6}\Delta T_{f\text{-}a} - 1.80 \times 10^{-5})_i + \\ &\textstyle\sum_{i=0}^{n}\left(m_{cyl}\left(Cp_{cyl}\right)_i + (m_{eye} + m_{cyl\ RTD})(Cp_{SS})_i\right)(\Delta T_{cyl} + 6.06 \times 10^{-6}\Delta T_{f\text{-}a} - 1.80 \times 10^{-5})_i = 0\end{aligned} \tag{10}$$

In order to calculate Cp_{cal}, numerous tests with both copper and stainless steel calibration cylinders were conducted. Tests were conducted with the cylinder beginning the tests at close to 5 or 50°C. The water temperature always began the test at the opposite temperature extreme. For each test, the temperature of both the cylinder and water were recorded at a 2 Hz sampling

rate, resulting in temperature traces similar to that seen in Figure 3.11. A Microsoft Visual Basic for Applications (VBA) code was implemented in Microsoft Excel to first smooth these temperature traces to remove any small perturbations in the temperature between adjacent data points. Smoothing was accomplished using a weighted average method about each discrete temperature data value. Weighted average smoothing assigns a weight to each data point within a given range (γ) of the current data point (j). The weight of the current data point is set to the highest value with the weight decreasing as a function of $1/\alpha^{|j-l|}$; where α controls the rate of change in the weight, and l is the integer location above or below the current data point. A visual illustration of this weighted average method for α=1.5 and γ=4 is presented in Figure 3.13.

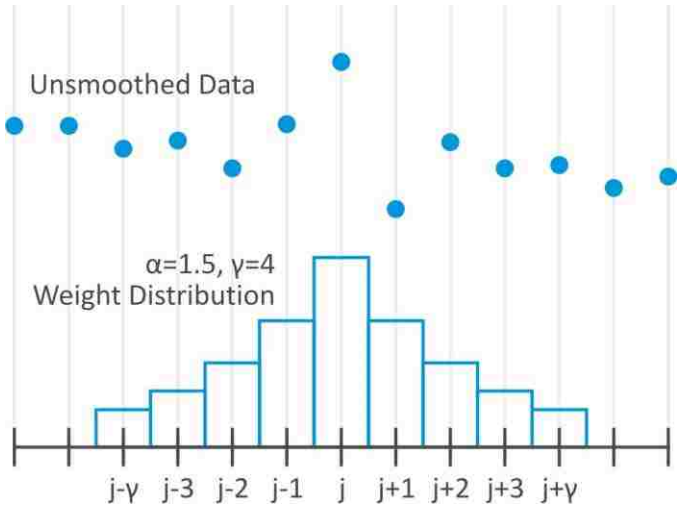

Figure 3.13: Weighted Average Smoothing of Temperature Data

Before multiplying the weights and data points, the sum of the weights should be normalized to 1. With the sum of the weights normalized to 1, the weighted average simply becomes the sum of the product of the normalized weights and corresponding data points. The following equation is used to find the weight normalization factor N:

$$N = \frac{1}{\left(\sum_{i=0}^{\gamma} \frac{2}{\alpha^i}\right) - 1} \tag{11}$$

With N found, each temperature data point can be individually smoothed through the following:

$$V_{sm}[j] = \sum_{l=j-\gamma}^{j+\gamma} V_o[j] \frac{N}{\alpha^{|j-l|}} \tag{12}$$

Where $V_o[j]$ is the unsmoothed array-based data point and $V_{sm}[j]$ is the weighted average-smoothed data point. After smoothing the data, Equation (10) was iteratively solved for with the goal of finding Cp_{cal}, when the energy balance of Equation (10) is satisfied.

It should be noted that Cp_f, Cp_{Cu}, and Cp_{SS} depend on temperature, which means they have discrete forms at the points i in Equation (10). The following curve fits were used to define these specific heat values:

$$Cp_f = 3.46 \times 10^{-13} T_f^6 - 1.37 \times 10^{-10} T_f^5 + 2.28 \times 10^{-8} T_f^4 - 2.05 \times 10^{-6} T_f^3 + 1.12 \times 10^{-4} T_f^2 - 3.35 \times 10^{-3} T_f + 4.22 \tag{13}$$

$$Cp_{Cu} = -1.00 \times 10^{-11} T_{Cu}^4 + 5.43 \times 10^{-9} T_{Cu}^3 - 1.09 \times 10^{-6} T_{Cu}^2 + 2.10 \times 10^{-4} T_{Cu} + 0.38 \tag{14}$$

$$Cp_{SS} = -(6.31 \times 10^3 + 20.84 T_{SS}) / (6.63 \times 10^3 + 17.86 T_{SS}) - 0.49 \tag{15}$$

Results for the calculated Cp_{cal} values are presented in Figure 3.14. The location of these Cp_{cal} values with respect to their normal distribution curve are illustrated in Figure 3.14.

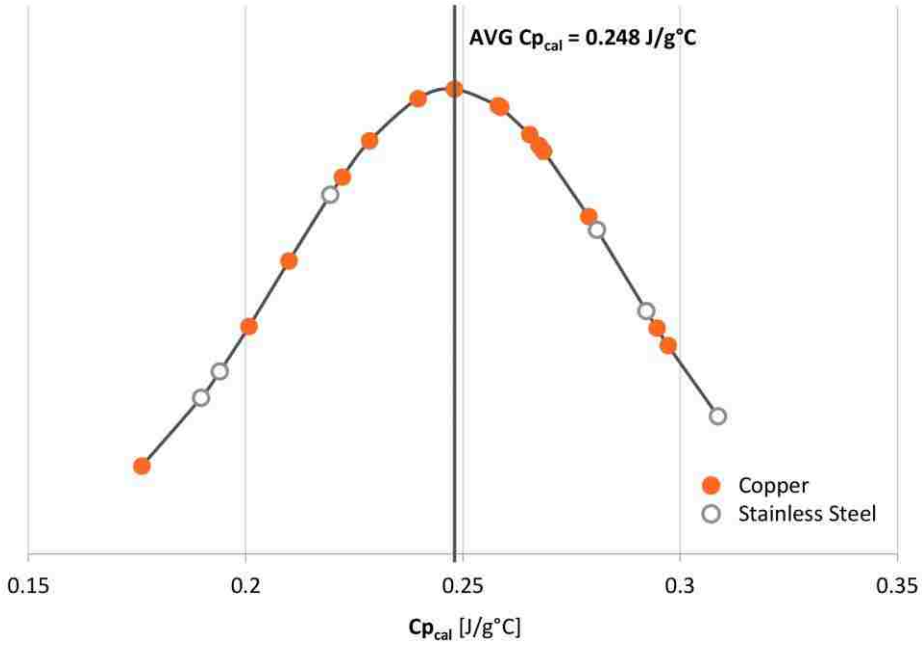

Figure 3.14: Calorimeter Calibration Cp_{cal} Normal Distribution Curve

The vacuum-insulated calorimeter bottle is constructed of stainless steel, which has a specific heat of approximately 0.5 J/g°C, twice that of the 0.248 J/g°C found for the calorimeter. However, the vacuum gap in the bottle effectively causes around half of the bottle mass to be outside of the calorimeter system control volume. This condition should cut the effective specific heat of the bottle in one half (~0.25 J/g°C). This result is virtually identical to the calculated average Cp_{cal} value of 0.248 J/g°C, lending credibility to this result.

To test the uncertainty of the calorimeter calibration constant, each calibration test was re-calculated by first calculating the left-hand-side of Equation (10) with Cp_{cal} = 0.248 J/g°C. The result of this calculation (Q) was divided by the energy change in the fluid (Q_f), resulting in the calorimeter measurement uncertainty:

$$\text{Calorimeter Measurement Uncertainty} = \left(\frac{Q}{Q_f}\right) 100\% \tag{16}$$

The calorimeter measurement uncertainty results are presented in Figure 3.15. It was found that 2 standard deviations (2σ) (95% confidence) fall at ±1.152%.

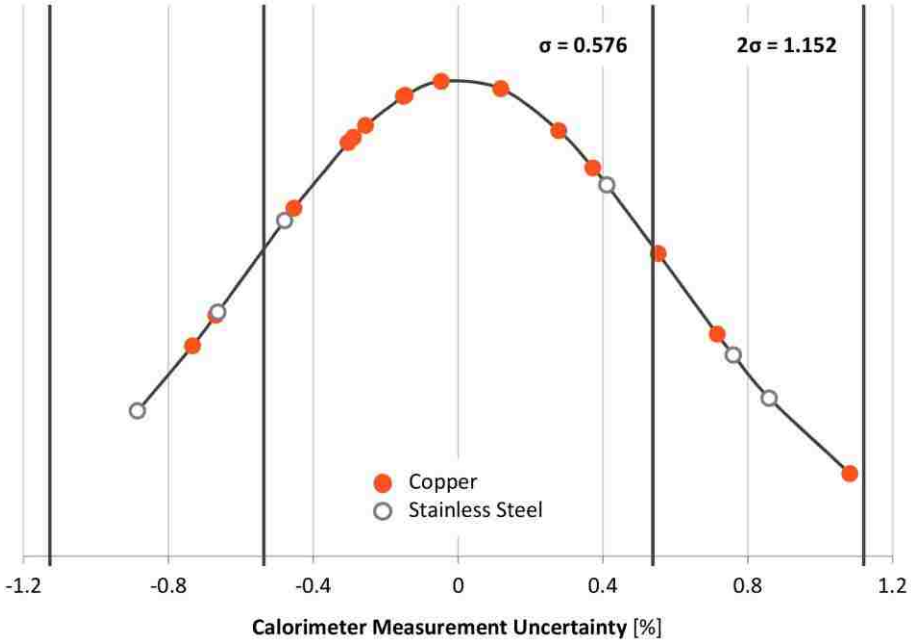

Figure 3.15: Calorimeter Measurement Uncertainty Normal Distribution Curve

3.3.4 Calorimetry of PCM Samples

With the drop calorimeter calibrated (Cp_{cal} = 0.248 J/g°C), the VBA code was modified to allow for drop calorimetry of the ~200 g PCM test samples. As was the case for the calibration tests, the thermal loss term ($m_{T\,loss} = -6.0575 \times 10^{-6}\,\Delta T_{f\text{-}a} + 1.8018 \times 10^{-5}$) was subtracted from the terms of Equation (4), resulting in the following discretized equation for the calorimeter/sample control volume:

$$\sum_{i=0}^{n}(m_{bottle} + m_{lid} + m_{RTD} + m_{stir\ bar})Cp_{cal}\left(\Delta T_f + 6.06 \times 10^{-6}\Delta T_{f\text{-}a} - 1.80 \times 10^{-5}\right)_i +$$
$$\sum_{i=0}^{n} m_f\left(Cp_f\right)_i\left(\Delta T_f + 6.06 \times 10^{-6}\Delta T_{f\text{-}a} - 1.80 \times 10^{-5}\right)_i +$$
$$\sum_{i=0}^{n} m_{ENC}\left(\mathbf{Cp_{ENC}}\right)_i\left(\Delta T_{PCM} + 6.06 \times 10^{-6}\Delta T_{f\text{-}a} - 1.80 \times 10^{-5}\right)_i + \quad (17)$$
$$\sum_{i=0}^{n} m_{PCM}\left(\left(\mathbf{Cp_{PCM}}\right)_i\left(\Delta T_{PCM} + 6.06 \times 10^{-6}\Delta T_{f\text{-}a} - 1.80 \times 10^{-5}\right)_i + \mathbf{H_{f\ PCM}}\right) = 0$$

There are three unknowns in Equation (17); Cp_{ENC}, Cp_{PCM}, $H_{f\ PCM}$. Fortunately, Cp_{ENC} and Cp_{PCM} can be easily solved for using the calorimeter itself. Cp_{ENC} is the specific heat of the stainless steel cylinder used to house the PCM. This is calculated using the control volume presented in Figure 3.16, and Equation (18). Note that the cylinder is filled with water (subscript w) in order to improve the heat transfer to the sample RTD.

$$\sum_{i=0}^{n}(m_{bottle} + m_{lid} + m_{RTD} + m_{stir\ bar})Cp_{cal}\left(\Delta T_f + 6.06 \times 10^{-6}\Delta T_{f\text{-}a} - 1.80 \times 10^{-5}\right)_i +$$
$$\sum_{i=0}^{n} m_f\left(Cp_f\right)_i\left(\Delta T_f + 6.06 \times 10^{-6}\Delta T_{f\text{-}a} - 1.80 \times 10^{-5}\right)_i +$$
$$\sum_{i=0}^{n} m_{ENC}\left(\mathbf{Cp_{ENC}}\right)_i\left(\Delta T_w + 6.06 \times 10^{-6}\Delta T_{f\text{-}a} - 1.80 \times 10^{-5}\right)_i + \quad (18)$$
$$\sum_{i=0}^{n} m_w\left(\left(Cp_f\right)_i\left(\Delta T_w + 6.06 \times 10^{-6}\Delta T_{f\text{-}a} - 1.80 \times 10^{-5}\right)_i\right) = 0$$

Cp_{PCM} for the PCM samples is found by setting $H_{f\ PCM}$ in Equation (17) to 0 and conducting drop calorimetry such that the PCM remains completely solid or liquid throughout the test. For instance, to measure Cp_L of $CaCl_2 \cdot 6H_2O$ (T_m = 29°C), the initial fluid temperature was set to 29°C with the initial sample temperature held at 50°C. This system equilibrates to a temperature several degrees above T_m of the PCM, ensuring the PCM remains liquid throughout the test. Similar tests can be conducted to find Cp_s for the PCM samples, where the initial water and sample temperatures are below T_m of the PCM. With Cp_L and Cp_s found for the PCM samples, $(Cp_{PCM})_i$ in Equation (17) was set for each discrete i, based on whether $(\Delta T_{PCM})_i$ is above or below the phase transition temperature.

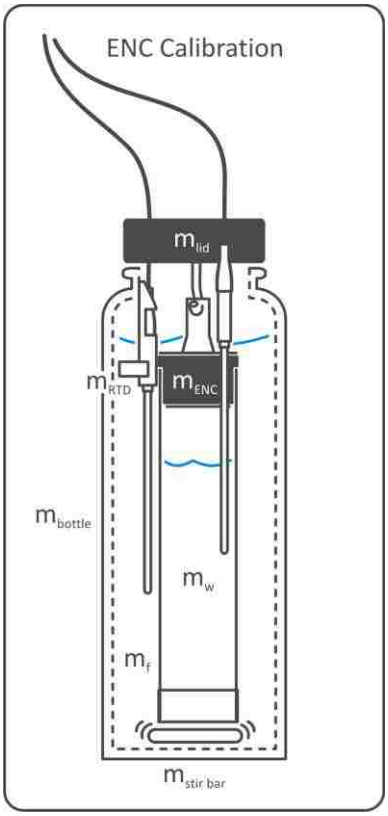

Figure 3.16: Control Volume for Calculation of Cp_{ENC}

Interestingly, if drop calorimetry is only being used to quantify changes in H_f with cycling, a precise value for the specific heats is not required as the specific heat component is not known to change appreciably with cycling. As long as comparable test temperatures are used, the specific heat contribution to the change in H_f between two tests will be identical. This approach is limited as the calculated magnitude of H_f is dependent on the Cp values used. Ideally, both liquid and solid Cp's should be calculated for each PCM tested.

With $(Cp_{ENC})_i$ and $(Cp_{PCM})_i$ found, Equation (17) can finally be used to solve for H_f. The method used is similar to that used for calibration, where a VBA code smooths the temperature traces of the PCM sample and calorimeter fluid (water) before using these temperatures are used to calculate H_f. The temperature traces of a typical PCM melting latent heat test are presented in

Figure 3.17. It can be seen that the PCM undergoes a melting phase change at around 29°C, which corresponds to the point where the PCM temperature curve flattens.

In order to find the uncertainty inherent with this calorimetry technique during testing of PCM samples, H_f was repeatedly calculated during both melting and freezing of a single sample. This process was repeated for four samples with a population standard deviation (σ) being computed individually for each sample. These values of σ are presented in Figure 3.18 alongside the average standard deviation value, which was found to be ±2.64%. This value of σ was defined as the calorimeter uncertainty during testing of PCM samples.

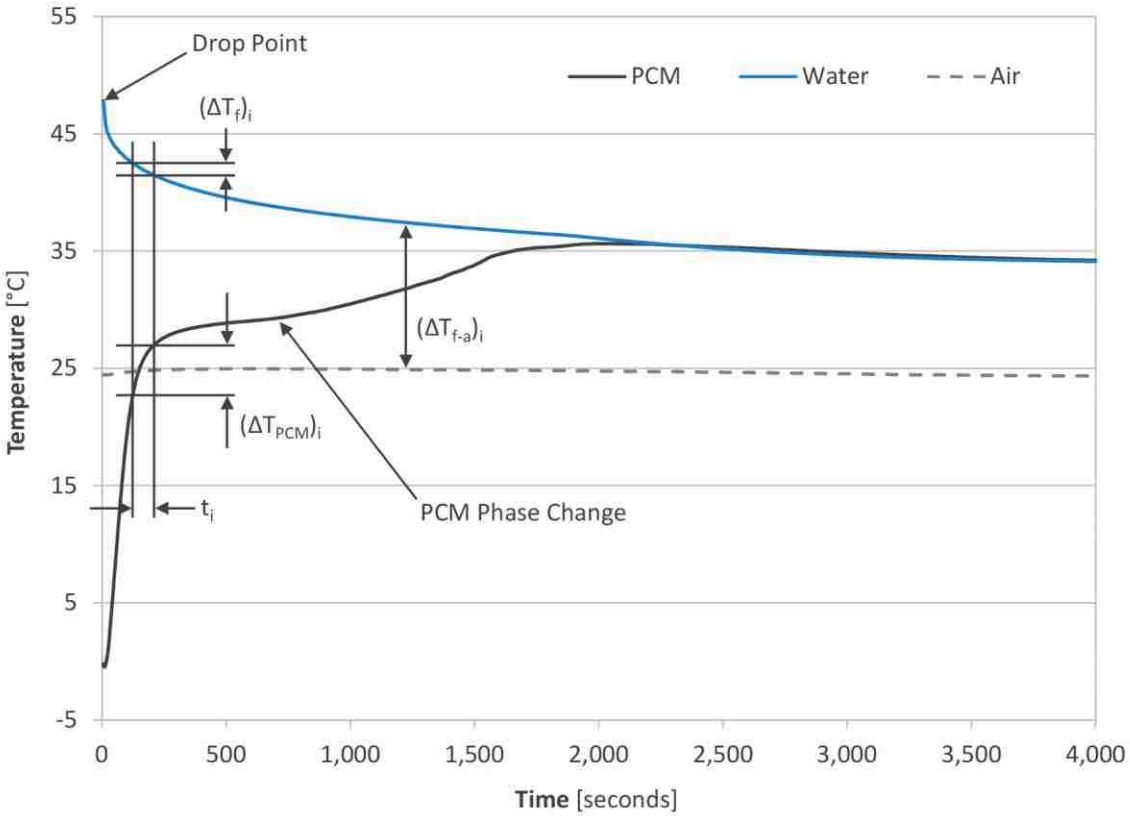

Figure 3.17: Temperature Traces for Typical PCM Calorimeter Test

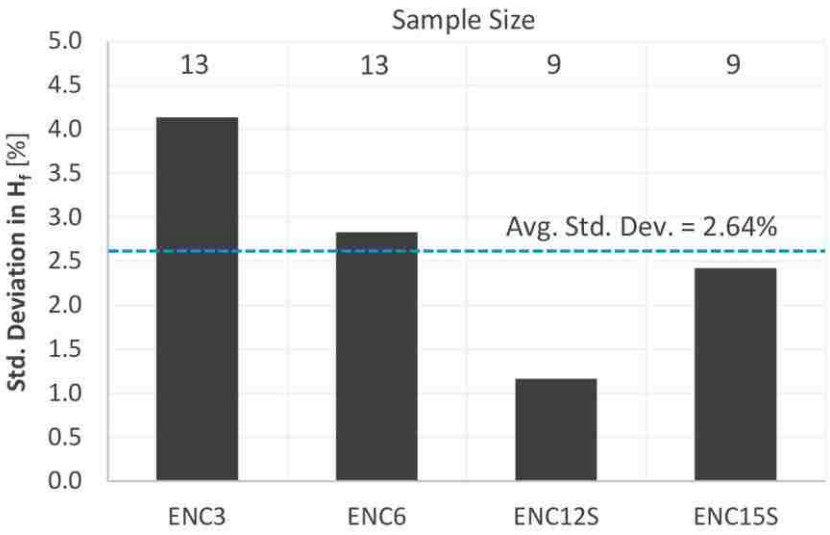

Figure 3.18: Standard Deviation in H_f as Calculated by Drop Calorimeter Across 4 Samples

3.4 Water Bath Testing

While the PCM cycling system presented in Section 3.2 was used for rapid, long-term PCM cycling, a programable water bath was used for short-term cycling at slower cycling rates. This water bath is illustrated in Figure 3.19. The water bath used for this testing was a Polyscience 7-liter low profile, refrigerated water bath with programmable controller and a temperature set range between -20 and 200°C. The programmable controller is capable of an unlimited number of programs with unlimited numbers of steps. For the purposes of this research, simple linear temperature ramps and holds were programed using the controller.

Due to the height limitations of the bath, the stainless steel cylinders used for the ~200 g samples were cut shorter, and smaller (~80 g) PCM samples were prepared. Up to 12 of these samples can be simultaneously placed into the bath. Samples containing an RTD were connected to a computer using Measurement Computing's USB-TEMP data acquisition device. Measurement

Computing's DAQami software package was used to collect the temperature information, which was written to a comma-separated value (CSV) file.

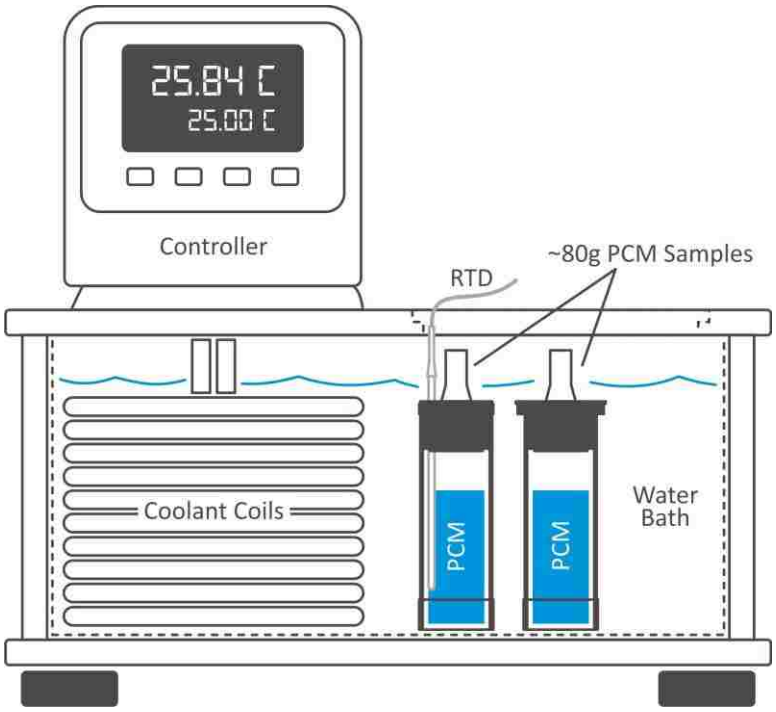

Figure 3.19: Polyscience Programmable Water Bath with ~80 g PCM Samples

3.4.1 Motivation for Water Bath Testing of $CaCl_2 \cdot 6H_2O$-Based PCMs

Because of the ability for precise temperature ramps, the water bath was able to simulate repeated, gradual cooling and heating of the PCM. A typical water bath cycle consists of maintaining the PCM at 35°C for 2 hours, followed by linear cooling to 25°C over the course of 10 hours. After cooling, the PCM was maintained at 25°C for 2 hours. The cycle is completed by heating to 35°C during another 10 hour period. This 24 hour cycle allows for study of the PCM under a slower cycling rate with a very small temperature difference between the environment (water) and the PCM. Feilchenfeld et al. has noted that PCM separation (instability) increases as

the cooling rate is slowed [F6]. Carlsson described a similar phenomenon by saying that, “phase change cycling does not result in (separation) if the driving temperature difference at repeated melting and crystallization relative to the melting point is comparably high” [C5]. Because of this, it was critical to test the PCM under a slower cycling rate to ensure the rapid cycling results were not positively biasing the PCM stability results. In addition, while supercooling can be estimated during rapid cycling, the PCM’s low thermal conductivity results in considerable temperature non-uniformities throughout the PCM, which introduces significant error in the measured supercooling. By cooling slowly with a small driving temperature difference, PCM temperature non-uniformities are virtually eliminated, allowing for accurate measurements of supercooling.

3.4.2 Alternate Water Bath Test Setup for PCM Visualization

An alternate configuration of the water bath was developed to allow for photographic or video visualization of the phase change process. In order to capture the phase change, a GoPro camera was fitted into a small glass enclose, which was lowered into the water bath. While the GoPro is water resistant, the glass enclosure was used so that the camera could be connected to a power cord instead of relying on the internal battery. An opaque cover was fitted to the top of the glass enclosure to prevent reflections on the internal surface of the glass. To reduce the focal length of the camera, a small macro lens was fitted to the front of the camera, which allowed for the test sample to be placed within 2-5 cm of the lens. A light was placed above the water bath to adequately illuminate the sample. This water bath configuration is presented in Figure 3.20.

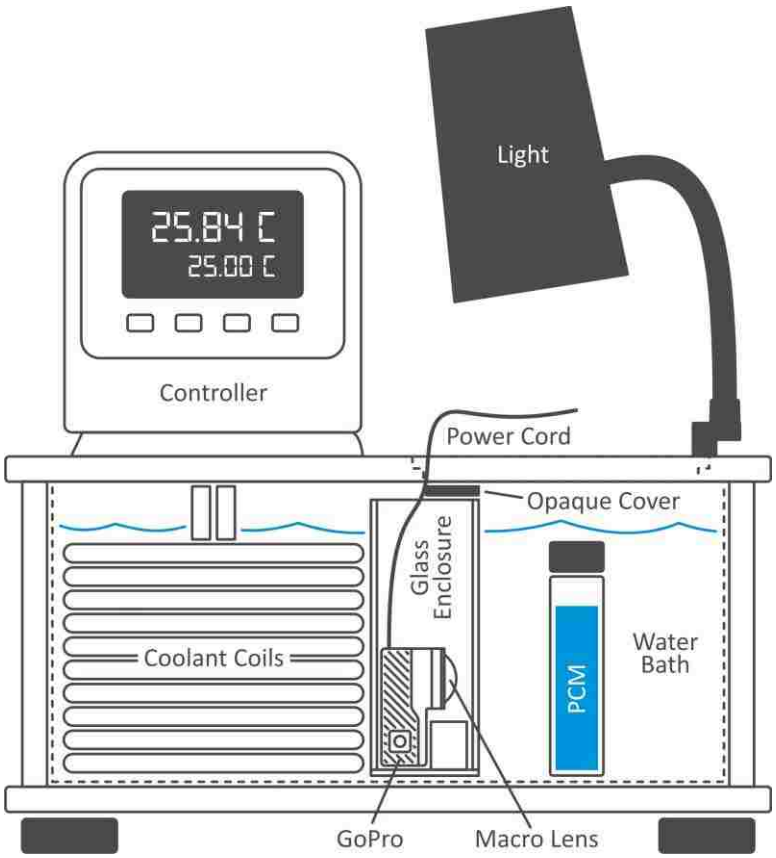

Figure 3.20: Water Bath Fitted with GoPro for Sample Visualization

This visualization technique is useful for examining the freezing and melting process of the PCM. For instance, the moment of initial crystallization is important for an understanding of supercooling and the processes (and additives) which reduce it. Figure 3.21 presents images from two different freeze tests at the moment of initial crystallization. Visualization is also important for providing a positive determination of the point at which the PCM fully melts and/or solidifies. If the camera is set to take a picture at a regular interval (every 1 or 2 seconds for instance), the phase transition time can be measured by multiplying the capture interval by the number of frames until the phase transition is complete.

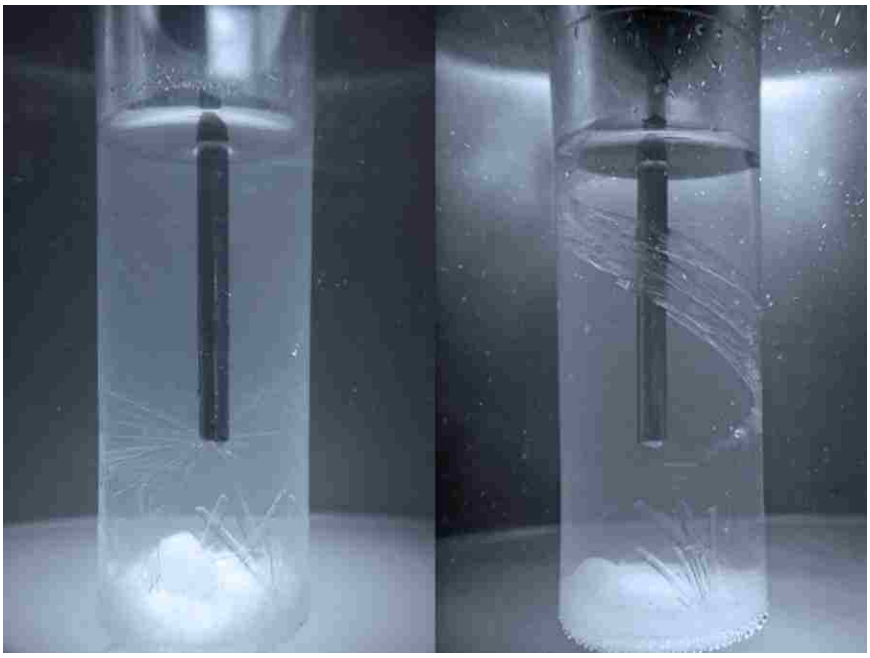

Figure 3.21: Initial Freeze for Two Samples as Captured Using GoPro in Water Bath

3.5 Thermogravimetric Analysis of Hydrated Salt PCMs

Thermogravimetric analysis (TGA) was used to determine the hydration of the hydrated salt PCMs. A TA Instruments Q500 TGA was used for all analyses (Figure 3.22). The TGA operates by dehydration of a small PCM sample (~50 mg) in a controlled furnace with nitrogen gas purge. A basic chiller allows the sample to begin the test at temperatures slightly below ambient conditions. For the work presented herein, TGA tests began at room temperature and concluded at 400°C with a linear temperature ramp rate of 10°C/min. The nitrogen purge rate was maintained at 40 ml/min. During dehydration, the sample mass is continuously recorded, allowing sample dehydration to be observed throughout the entire test. Once the sample mass no longer changes with increasing temperature, the sample can be assumed to be fully dehydrated. A typical TGA mass loss plot is presented in Figure 3.23.

Figure 3.22: TA Instruments Q500 TGA

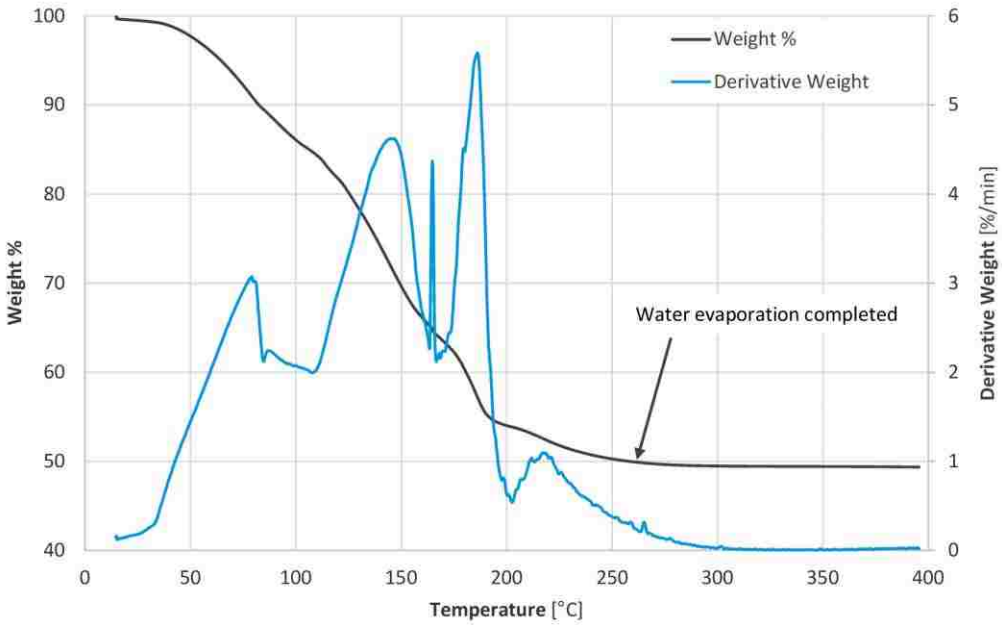

Figure 3.23: TGA Weight Loss Curve Example

TGA weight loss curves contain critical information about the disassociation of the salt-water bonds within the PCM. This can be seen in the derivative weight curve, where the peaks correspond to the relative locations where specific hydrates are dehydrated. For instance, $6H_2O$ dehydrates to $4H_2O$, followed by dehydration to $2H_2O$ at even higher temperatures.

Although the TGA was found to be capable of measuring the weight percentage of water in the PCM through dehydration, a significant challenge was encountered during most of these tests. During TGA testing, step changes in the measured weight change were detected, with the final measured H_2O weight percentage being well below that predicted. Two of these discontinuities are presented in Figure 3.24, which show wt% jumps of between 7 and 13%.

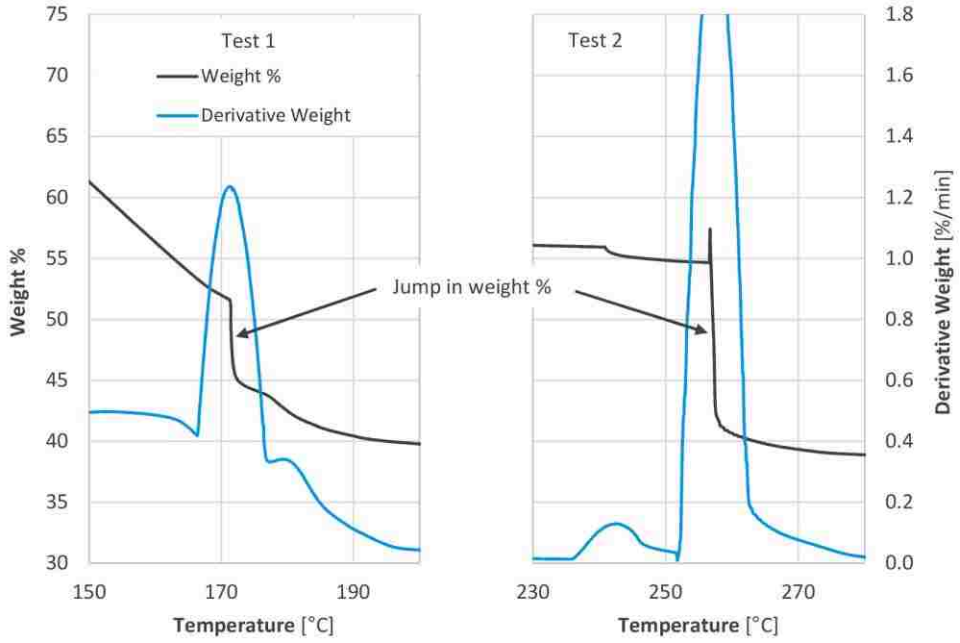

Figure 3.24: Jump in Weight Percentage During PCM Dehydration

The reason for the jumps became apparent upon removal of the TGA sample pans. After drying, the dehydrated PCM was found to have dramatically expanded and fragmented. As a hydrated

salt PCM is heated, its uppermost surface is dried first, resulting in a dried crust across the top surface of the PCM. Initially this crust is thin and quite porous, but as additional water is evaporated, it thickens and can form a continuous vapor barrier over the still moist salt beneath. If this continuous layer forms, the evaporating water beneath the layer builds pressure until the layer ruptures – spewing PCM from the sample pan. Since the TGA is a very delicate instrument, measuring mass changes on the order of fractions of a mg, if even a very small quantity of PCM falls from the sample pan, it will register as a discontinuity in the measured weight %. The platinum samples pans used in the Q500 TGA aggravated this phenomenon as they were open with only a low circumferential lip (~1 mm) to contain the sample. While the TGA was effectively used to measure the water content of several hydrated salt samples, its success rate was sufficient low and the potential for damage of the TGA sufficiently high to prevent additional TGA testing of the hydrated salt PCMs. It is suggested that closed (with vent), deep sample pans be used when testing hydrated salt PCMs via TGA.

3.6 Large Dehydration Cell

In order to get around the TGA limitations outlined in the proceeding section, a new method for measuring the hydration of PCM samples was developed. This method is referred to as the Large Dehydration Cell (LDC) method. The LDC method is a very simple method, which consists of a 38.1 mm diameter stainless steel cylinder, which is capped at the bottom end. Over the top (open) end of the cylinder is fitted a loose-fitting stainless steel cap, with two small vent holes. This cylinder and cap are pictured in Figure 3.25. During dehydration of the PCM sample, the cap ensures that no PCM is ejected from the LDC.

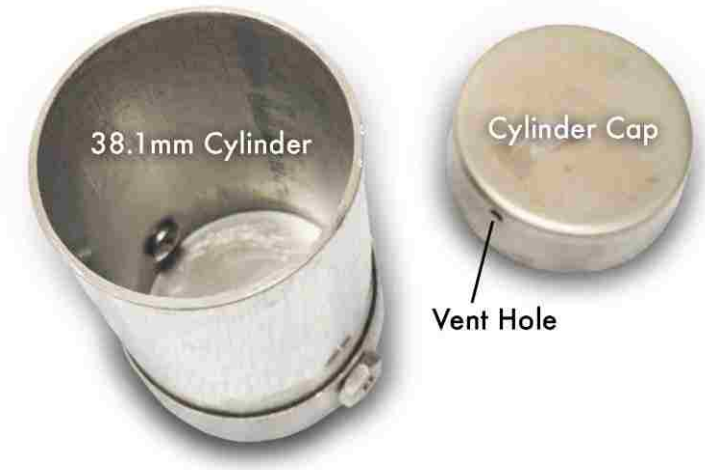

Figure 3.25: LDC Cylinder & Cap

Like its name suggests, the LDC is simply a container for dehydration of relatively large (5-10 g) samples of hydrated salts. Prior to each test, the empty cylinder and cap are weighed using a sensitive balance (accurate to ±1 mg). After PCM is placed into the cylinder, the combined PCM/cylinder system is re-weighed to determine the mass of PCM. PCM can be added to the cylinder in either the solid or liquid form. Next, the capped LDC with PCM is placed onto a hot plate, which is maintained at 310°C. At 5-10 minute intervals during heating, the LDC is removed from the hot plate and immediately re-weighed, with its weight being recorded. After being weighed, the LDC is returned to the hot plate for continued heating. Once the weight change between subsequent mass measurements is within ±1 mg, the LDC is removed from the hot plate and allowed to cool. By subtracting these final mass measurements from the mass of the LDC and PCM being heating, the mass of water evaporated (m_{H2O}) can be found:

$$m_{H2O} = m_1 - m_2 \tag{19}$$

Where m_1 and m_2 are the mass of the LDC plus PCM before and after dehydration respectively. The mass of salt (m_{Salt}) in the PCM is given by the following:

$$m_{Salt} = m_{PCM1} - m_{H2O} = m_1 - m_{LDC} - m_{H2O} \quad (20)$$

Where m_{PCM1} is the mass of PCM before dehydration and m_{LDC} is the mass of the cylinder and cap. With the mass of salt and water known, the mass fraction of either salt (w_{Salt}) or water (w_{H2O}) can be easily found:

$$w_{Salt} = \frac{m_{Salt}}{m_{PCM1}} = \frac{m_{Salt}}{m_1 - m_{LDC}} = \frac{m_1 - m_{LDC} - m_{H2O}}{m_1 - m_{LDC}} \quad (21)$$

$$w_{H2O} = \frac{m_{H2O}}{m_{PCM1}} = \frac{m_{H2O}}{m_1 - m_{LDC}} = \frac{m_1 - m_2}{m_1 - m_{LDC}} \quad (22)$$

Conversion of the masses of salt and H_2O to the hydration level (xH_2O) in moles of water per mole of salt is conducted through use of Equation (23).

$$xH_2O = \frac{m_{H2O}}{m_{Salt}} \frac{M_{Salt}}{M_{H2O}} \quad (23)$$

Where M_{Salt} and M_{H2O} are the molar mass of salt and water respectively. In order to test the repeatability of the LDC, similar PCM samples were consecutively dehydrated with samples sizes of between 7 and 10.5 g. Results of these tests are presented in Table 3.1. Although only four tests were run due to time limitations, they show good agreement with one another. A population standard deviation for xH_2O was found to be only 0.08 moles. While this is not accurate enough for very precise determination of the hydration level (on the order of 0.01 moles), it is sufficient to determine if there are significant differences in water content between samples. For instance, the LDC can be used to determine if a sample has a slight excess or deficit of water relative to its purported hydration level. This can be beneficial in explaining phenomenon specific to that sample. Additional repeatability tests with identical samples have found results to be even more repeatable than those presented in Table 3.1.

Table 3.1: LDC Repeatability Tests

Sample	m_{H2O} [wt%]	xH_2O
10s (1)	48.34	5.76
10s (2)	49.14	5.95
10s (3)	48.26	5.75
10s (4)	48.65	5.84
σ	0.35	0.08

4 Characterization of Select Hydrated-Salt PCMs

Thermal characterization of the selected hydrated salt PCMs presented in Table 2.8 was conducted using the methods outlined in Section 3. The following sections present the characterization results for these PCMs.

4.1 Sodium Hydroxide 3.5 Hydrate ($NaOH \cdot 3.5H_2O$)

Sodium hydroxide 3.5 hydrate ($NaOH \cdot 3.5H_2O$) has been presented in the literature as a congruently-melting PCM with the thermal characteristics as presented in Table 4.1. This PCM is not only desirable due to congruent-melting/freezing, but also its high heat of fusion (218 J/g). Its melt temperature is at the bottom of the examined range (15 – 35°C).

Table 4.1: Thermodynamic Properties of $NaOH \cdot 3.5H_2O$ as Presented in the Literature

T_m [°C]	H_f [J/g]	Source
15.0		[B11,C1,Z1]
15.4	218	[C1,N2,S26]

A major concern with the use of this PCM is that of aggressive corrosion. In addition, this salt is known to vigorously react with certain metals; with aluminum being one of these metals. NaOH hydrates are known to react with aluminum, producing sodium aluminate ($NaAlO_2$) and hydrogen gas in a highly exothermic reaction. During DSC testing, it is believed that this reaction proceeded between the $NaOH \cdot 3.5H_2O$ and the aluminum sample pan. The heat released during the reaction made reliable DSC testing of this material impossible. Because of this and the known high corrosiveness of this salt, $NaOH \cdot 3.5H_2O$ was eliminated from additional testing.

4.2 Potassium Fluoride Tetrahydrate ($KF{\cdot}4H_2O$)

Potassium fluoride tetrahydrate ($KF{\cdot}4H_2O$) is a congruently-melting PCM with its thermal characteristics presented in Table 4.2. This PCM is desirable due to congruent-melting/freezing as well as a high latent heat (> 230 J/g). Potassium fluoride (KF) does have some safety concerns as it ranks as a Category 3 in oral, inhalation, and dermal toxicity according to the 2012 OSHA Hazard Communication Standard (29 CFR 1910.1200) [T10]. The OSHA standard rates chemical hazards between 1 and 4 with 1 being the most hazardous.

Table 4.2 (a): Thermodynamic Properties of $KF{\cdot}4H_2O$ as Presented in the Literature

T_m [°C]	H_f [J/g]	Cp_L [J/g·K]	Cp_s [J/g·K]	ρ_L [kg/m^3]	ρ_s [kg/m^3]	Source
18.0						[N2]
18.5	230	1.72		1480		[H12]
18.5	246	2.47	1.62	1456	1437	[S15]
18.5	231			1447	1455	[S28]

Table 4.2 (b): Transport Properties of $KF{\cdot}4H_2O$ as Presented in the Literature

k_L [W/m·K]	k_s [W/m·K]	η [cP]	ν [m^2/s]	Source
0.479	0.608	4.32	2.97×10^{-6}	[S15]

4.2.1 DSC Testing of $KF{\cdot}4H_2O$

Despite the safety concerns, a small quantity of $KF{\cdot}4H_2O$ was prepared by adding the appropriate quantity of distilled water to laboratory-grade KF. This $KF{\cdot}4H_2O$ was tested by DSC using the procedure outlined in Section 3.1.1. A heat flux curve for this testing is presented in Figure 4.1 and Figure 4.2 with the results summarized in Table 4.3. Supercooling of this PCM was estimated

my looking at the cooling curve of the DSC test as presented in Figure 4.2. As the PCM was cooled, its heat flux curve remained flat until around -4.5°C, at which point it rapidly rose as the PCM froze. By subtracting this supercooled "freezing temperature" from the melting temperature, it was found that $KF{\cdot}4H_2O$ tends to supercool by approximately 22.5°C. It should be noted that due to a relatively high cooling rate (7°C/min), DSC results are known to overpredict supercooling. This is because the degree of supercooling depends strongly on the cooling rate, with a high cooling rate increasing supercooling [L7]. For this reason, DSC supercooling estimates should only be used as rough estimates of supercooling and not as actual supercooling measurements. For a more in-depth understanding of supercooling see Section 4.3.4 below.

Table 4.3: DSC Test Results of $KF{\cdot}4H_2O$

T_m [°C]	T_p [°C]	H_f [J/g]	Supercooling [°C]
17.8 – 18.1	21.0 – 22.7	203 – 217	~ 22.5

Although $KF{\cdot}4H_2O$ performed well throughout DSC testing, it was decided to terminate testing of this material due to safety concerns. Most notable was the concern that fluorine ions would react with the hydrogen ions introduced through the addition of water – forming hydrofluoric acid (HF_{aq}). HF_{aq} is extremely hazardous with Class 1 and 2 toxicity according to the 2012 OSHA Hazard Communication Standard (29 CFR 1910.1200) [T9].

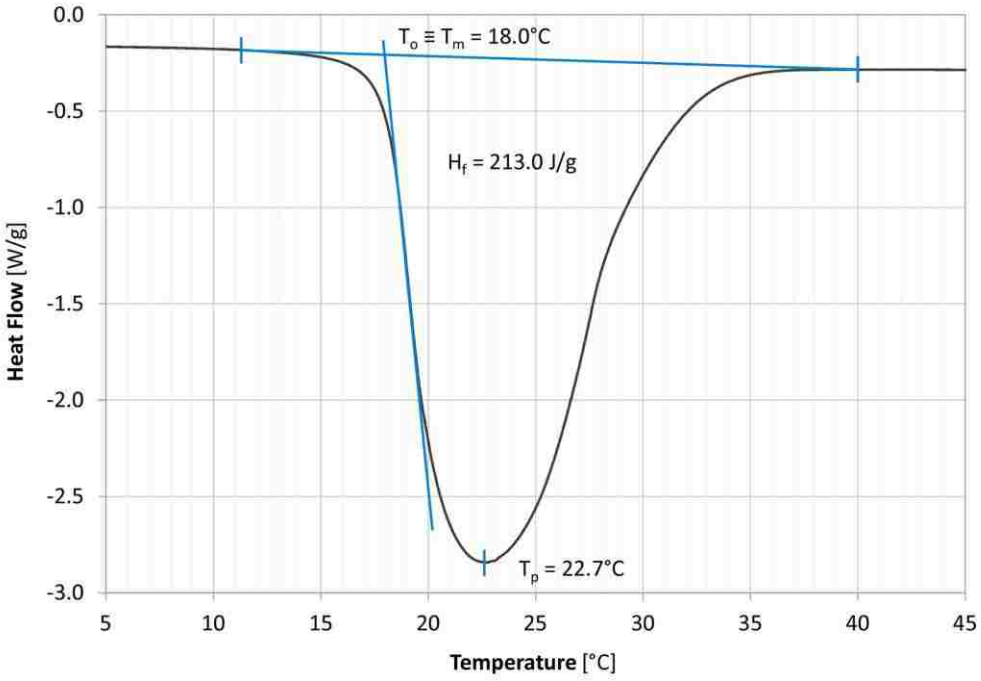

Figure 4.1: $KF{\cdot}4H_2O$ DSC Melting Results

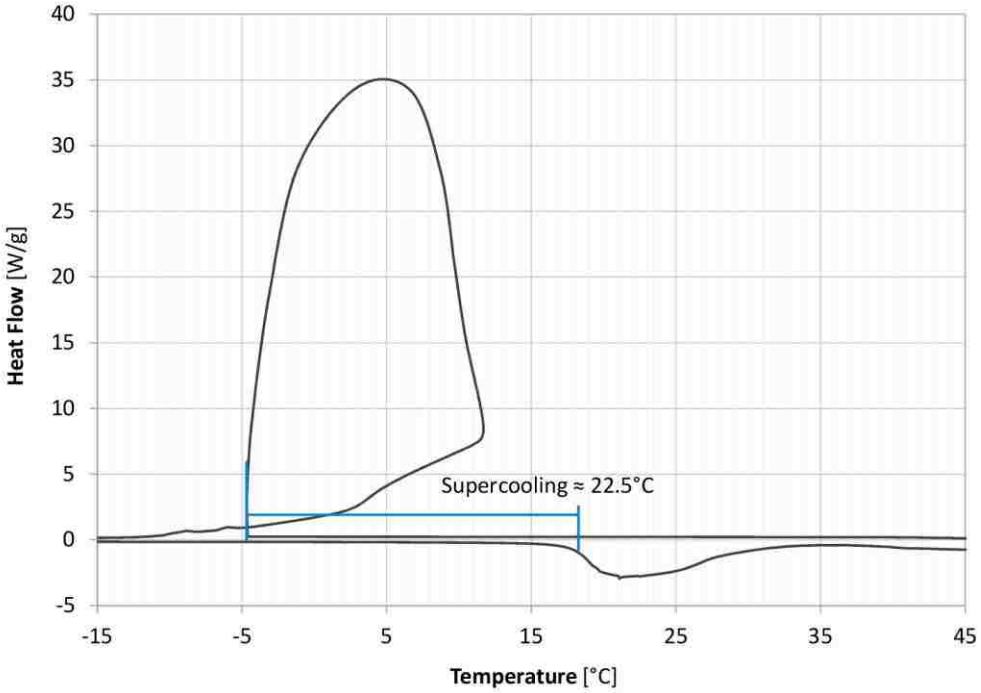

Figure 4.2: $KF{\cdot}4H_2O$ DSC Supercooling Results

4.3 $CaCl_2 \cdot 6H_2O + MgCl_2 \cdot 6H_2O$

A mixture of Calcium Chloride Hexahydrate and Magnesium Chloride Hexahydrate ($CaCl_2 \cdot 6H_2O$ + $MgCl_2 \cdot 6H_2O$ or CC6+MC6) is widely discussed in the literature as a viable low-temperature PCM [H12,Z1,L13]. Typically, a ratio of 66% $CaCl_2 \cdot 6H_2O$ to 33% $MgCl_2 \cdot 6H_2O$ (66:33) by weight is stated to be the eutectic ratio of these two salts. The eutectic mixture of two salts is the mixture composition where both salts melt/freeze at the same temperature, meaning that both phases simultaneously undergo the phase transition. This point corresponds to the lowest melting temperature across the range of possible mixture percentages. Literature thermodynamic properties of the 66:33 ratio is presented in Table 4.4.

Table 4.4: Thermodynamic Properties of 66:33 CC6+MC6 from the Literature

T_m [°C]	H_f [J/g]	Cp [J/g·K]	ρ [kg/m^3]	Source
23				[Z3]
25	127	2.74	1590	[C11,H12,Z1]

Li et al. examined mixtures of CC6+MC6 with weight ratios of 90:10, 85:15, 80:20 and 75:25 [L13]. Their testing found that increasing the percentage of $MgCl_2 \cdot 6H_2O$ decreased the phase change temperature, with a minimum phase change temperature of 21.4°C found at the 75:25 ratio. A latent heat of fusion of 101.5 J/g was measured for this PCM using DSC. It should be noted that these results are for the aforementioned PCM with 3 wt% $SrCl_2 \cdot 6H_2O$ added as a nucleating agent, which reduced supercooling to 2.1°C [L13]. He et al. conducted similar testing at the 80:20 wt. ratio with 1% SC6 added to minimize supercooling [H14]. A summary of these published results is presented in Table 4.5 below.

Table 4.5: Thermodynamic Properties of CC6+MC6+SC6

CC6+MC6 [wt ratio]	SC6 [wt%]	T_m [°C]	H_f [J/g]	Source
75:25	3	21.4	102	[L13]
80:20	3	23.5		[L13]
	1	27.3	123	[H14]
85:15	3	25.0		[L13]
90:10	3	26.0		[L13]

Initial characterization of the CC6+MC6 mixtures was conducted using DSC. Results for the 66:33 mixture are presented in Table 4.6 and Figure 4.3. These results agree well with those presented in the literature for this mixture (Table 4.4). Examining the DSC cooling curve in Figure 4.4, DSC-predicted supercooling was found to be considerable at approximately 43°C; although actual supercooling is known to be less than this.

Table 4.6: DSC Test Results of 66:33 CC6+MC6

CC6+MC6 [wt ratio]	T_m [°C]	T_p [°C]	H_f [J/g]	Supercooling [°C]
66:33	19.7 – 21.1	23.7 – 26.9	95.1 – 127	~ 43

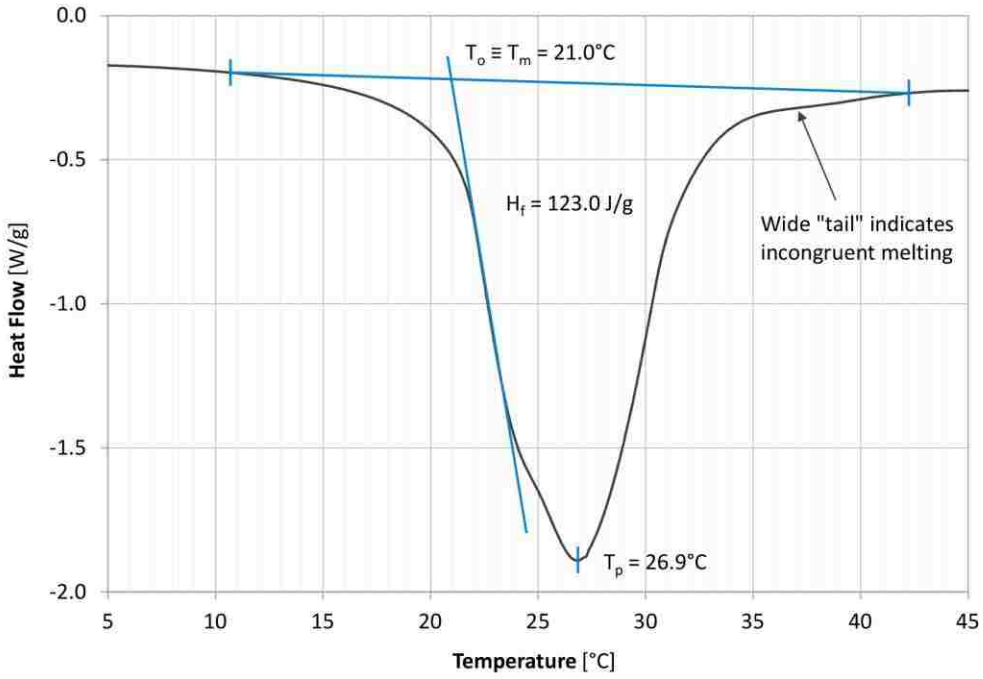

Figure 4.3: 66:33 CC6+MC6 DSC Melting Results

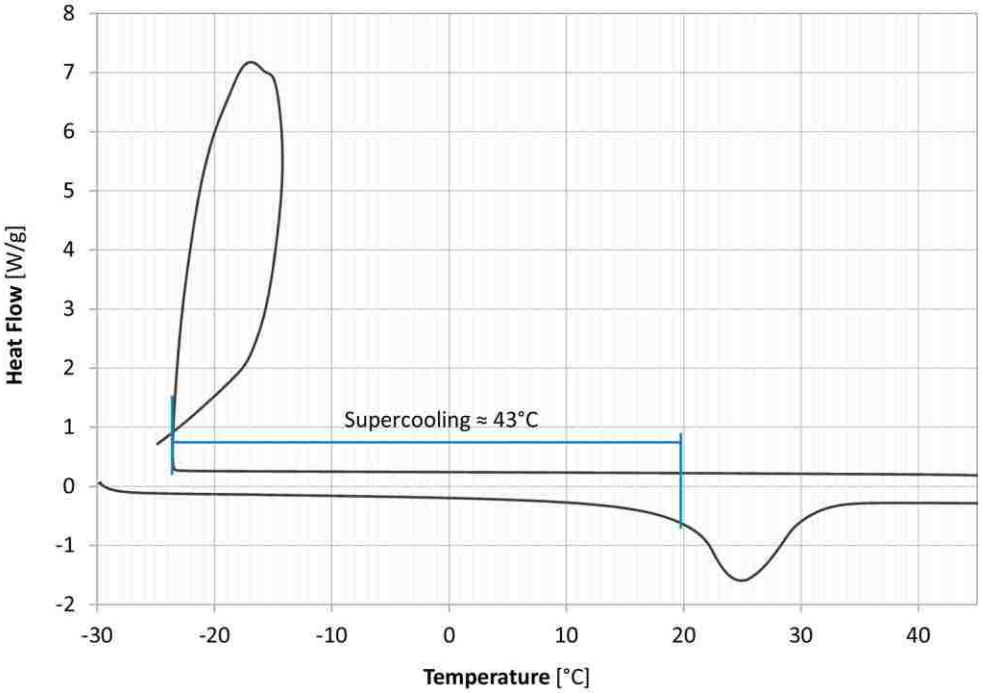

Figure 4.4: 66:33 CC6+MC6 DSC Supercooling Results

4.3.1 Finding the CC6+MC6 Eutectic Composition

While the T_m and H_f results found during DSC tests of 66:33 CC6+MC6 showed good agreement with those presented in the literature, it was noted that this PCM did not melt and freeze congruently. When frozen to a temperature slightly below the predicted phase transition temperature, a small percentage of the PCM was found to remain liquid. Likewise, after melting at a temperature just above the melting temperature, a portion of the PCM was found to remain solid. Because of these incongruent phase transitions, it was determined that the 66:33 CC6+MC6 mixture does not result in a congruently melting/freezing eutectic.

With the mixture of CC6+MC6 corresponding to the eutectic point unknown, various mixture percentages of the two salts were prepared and visually observed for congruent melting/freezing. Photos of these mixtures are presented in Figure 4.5, where the four bottles on the left are for CC6+MC6 mixtures between 75:25 and 85:15 in the liquid state and on the righthand side of Figure 4.5 are mixtures between 80:20 and 95:5 in the solid state. Two phenomena were noticed during this testing. First, for the liquid samples with CC6 concentrations below approximately 82 wt%, a crystal of PCM would remain when the sample was melted to a temperature slightly above the melt temperature. Secondly, if the CC6 concentration was greater than approximately 82 wt%, a liquid layer would be formed on the top of the frozen solid at temperatures slightly below the freezing point. If these PCM mixtures were frozen to a temperature below 0°C, this liquid layer would solidify, forming a lighter colored solid layer on top of the PCM. Both of these phenomena are illustrated in Figure 4.5. Although not explicitly seen in Figure 4.5, a CC6+MC6 mixture of 82:18 was found to result in congruent freezing and melting and was therefore proposed as the true eutectic mixture of CC6+MC6. This eutectic mixture of CC6+MC6 should hold regardless of sample size as it is based on the steady-state

equilibria conditions between the two salts. The exact eutectic composition may shift slightly if the salts contain sufficient impurities.

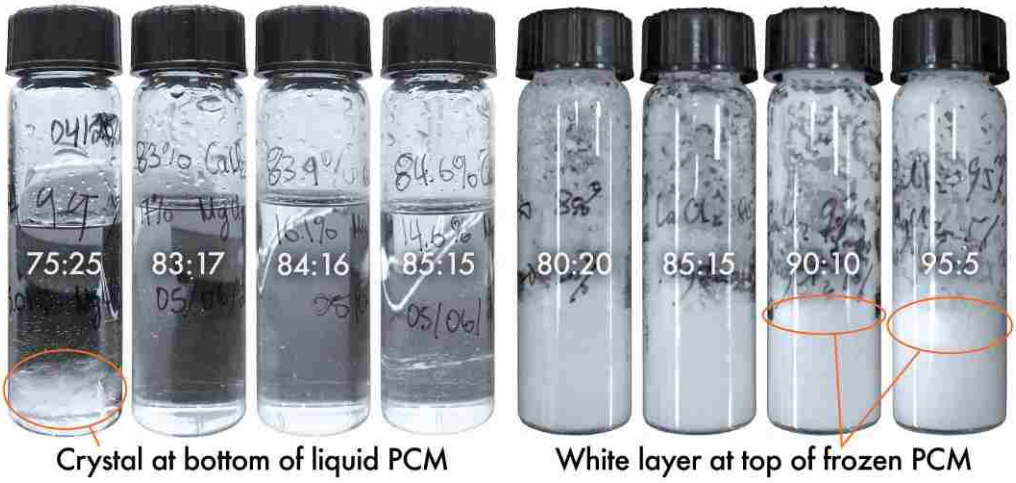

Figure 4.5: Separation of Varying Concentrations of CC6+MC6 During Melting and Freezing

4.3.2 A CC6+MC6 Phase Diagram

A binary phase diagram for the CC6+MC6 system was found using an Extended UNIQUAC thermodynamic model-based software package developed by Thomsen [T12]. The Extended UNIQUAC model is based on excess Gibbs energy, with an added Debye-Hückel law term and a term corresponding to the UNIQUAC equation. More information about this model can be found in work by Thomsen et al. [T11] and Iliuta et al. [I1]. Thomsen's software package allows for modeling of binary, ternary, and quaternary phase diagrams of aqueous salt solutions. The program includes ions for Na^+, H^+, Cl^-, Ca^{2+}, Mg^{2+}, and OH^- along with many others and is primarily designed for use in oil field and geothermal applications. As a demonstration of the program's ability to accurately model phase diagrams, Thomsen plotted the software's prediction of the $CaCl_2/H_2O$ binary phase diagram alongside experimental data (Figure 4.6). These results show good agreement between the modeled results and experimental data.

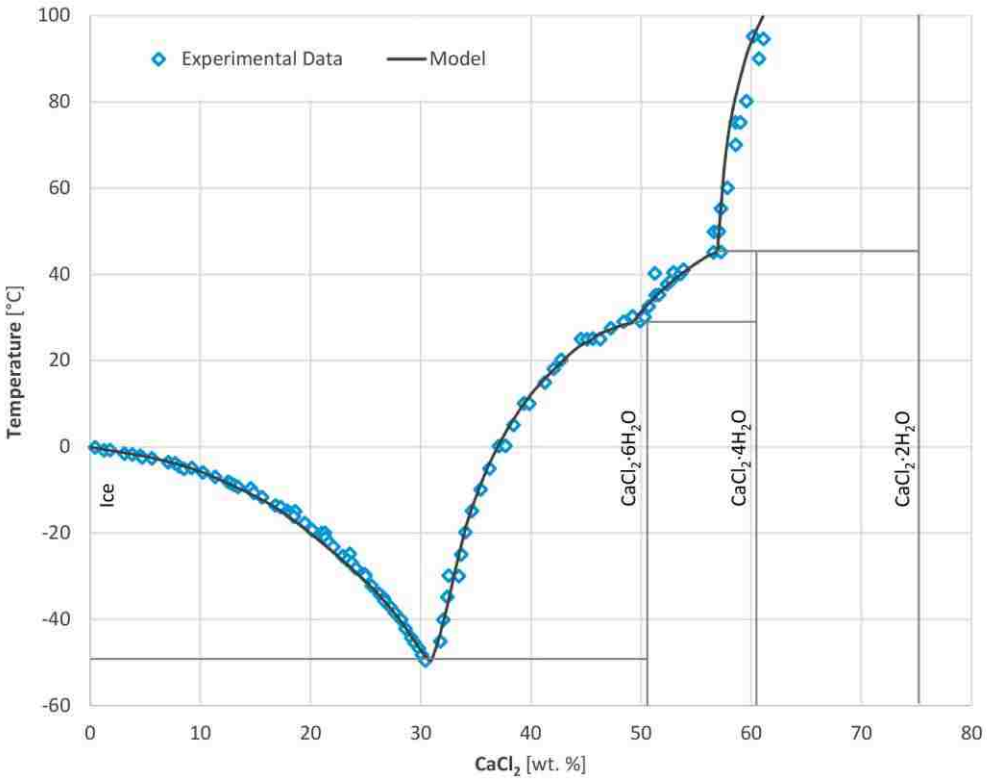

Figure 4.6: Modeled and Experimental Results for $CaCl_2/H_2O$ Phase Diagram [T12]

Thomsen's model was used to find a binary phase diagram for the CC6/MC6 system (Figure 4.7). Figure 4.7 shows that there are four primary phases as the MC6 wt% varies between 0 and 100%: $CaCl_2{\cdot}6H_2O$, $MgCl_2{\cdot}6H_2O$, $MgCl_2{\cdot}4H_2O$ (MC4), and $2MgCl_2{\cdot}CaCl_2{\cdot}12H_2O$ (MCCC12). The lines in Figure 4.7 correspond to the solid/liquid equilibrium lines (liquidous curves) for each phase. Eutectic concentrations between two phases are found at the intersection points between the phases' liquidous curves. In order to find the eutectic point of all of the phases, the uppermost liquidous curve should be considered across the MC6 wt% range. Figure 4.7 shows that at low MC6 concentrations, the CC6 phase forms the uppermost liquidous curve. At around 15 wt% MC6, the MCCC12 phase forms the uppermost liquidous curve. In excess of 90 wt% MC6, the MC4 phase melts at the highest temperature. The intersection point of the CC6 and MCCC12 phase denotes a eutectic concentration between CC6 and MC6 of approximately 15 wt% MC6. This is very close

to the eutectic composition suggested by the visual observations discussed above (18 wt% MC6). This finding lends credibility to the suggestion that 82:18 is the true eutectic composition for the CC6+MC6 mixture.

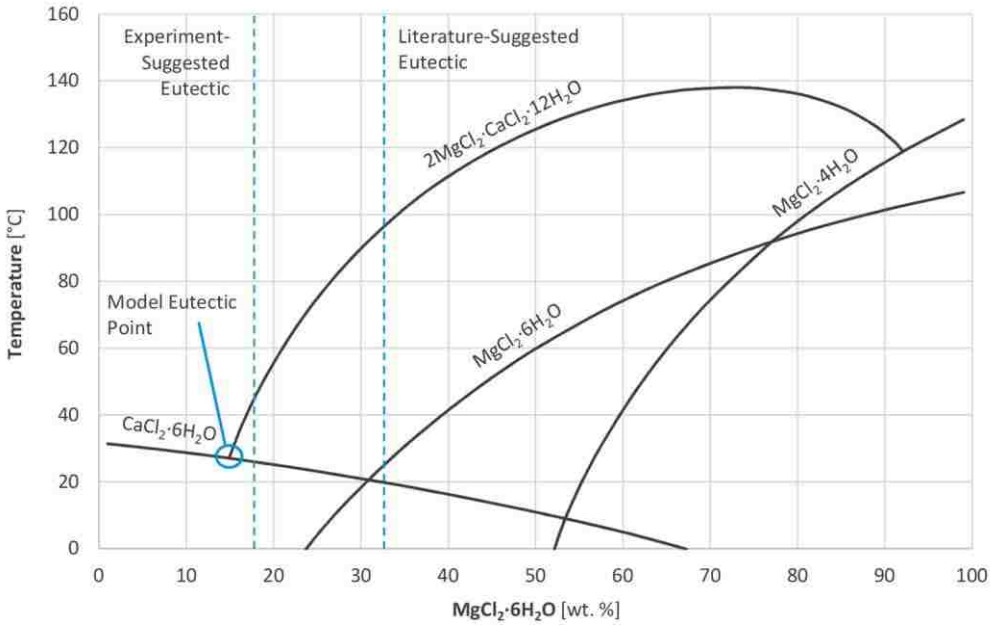

Figure 4.7: Binary CC6/MC6 Phase Diagram as Calculated by Thomson's Software Package

Figure 4.7 also reveals the probable reason for why the 66:33 composition is often suggested as the eutectic composition. As seen, the CC6 and MC6 liquidous curves intersect at approximately 31 wt% MC6, which forms a eutectic point between these two curves. Given the proximity of this point to the oft suggested eutectic composition of 33 wt% MC6, the intersection of the CC6 and MC6 curves explains the current confusion over the true eutectic point of CC6+MC6. However, if 66:33 CC6+MC6 is taken to be the eutectic concentration, Figure 4.7 shows that upon melting of the CC6 and MC6, a portion of the PCM will remain in the MCCC12 phase, which remains a solid until the temperature exceeds 90°C. This explains the solid crystal, which was observed after the bulk of the PCM was melted (as seen in Figure 4.5). Figure 4.7 suggests that as the percentage

of MC6 decreases from 31 wt%, the melting temperature of the solid MCCC12 decreases until it reaches that of the CC6 at 15 wt% MC6.

A ternary $CaCl_2$-$MgCl_2$-H_2O phase diagram was also calculated using Thomson's Extended UNIQUAC model (Figure 4.8). The primary liquidous curves for four equilibrium temperatures were plotted (20, 25, 27, and 30°C). Eutectic concentrations at each temperature can be seen as the inflection points (corners) in these curves. When the concentration of the commonly-assumed eutectic wt% concentration of 66:33 CC6+MC6 is plotted on Figure 4.8, it can be seen that this concentration does not correspond to a eutectic point. Rather, for all modeled temperatures, this concentration lies beneath (in the solid region) the MCCC12 curve, which explains the occurrence of the solid precipitate in the otherwise liquid PCM samples (Figure 4.5). The story is different when the proposed eutectic concentration of 82:18 CC6+MC6 is plotted on Figure 4.8. This concentration lies very close to the suggested eutectic point between the MC6 and MCCC12 liquidous curves at 27°C.

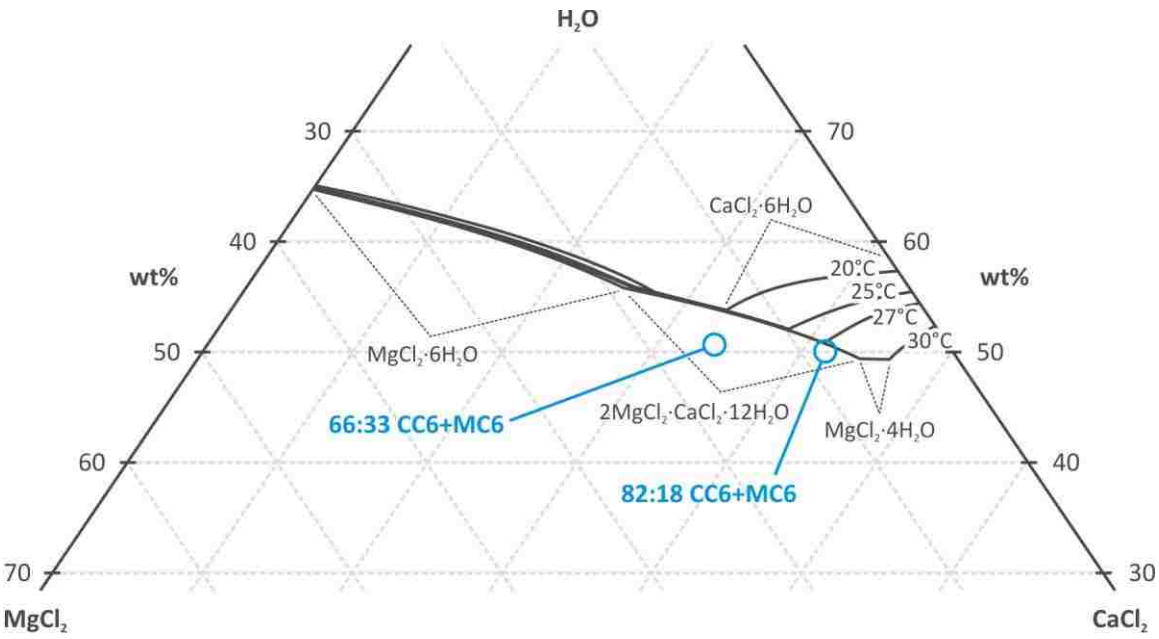

Figure 4.8: Ternary $CaCl_2$-$MgCl_2$-H_2O Phase Diagram Calculated by Thomson's Program

The visualization of CC6+MC6 samples and the modeled binary and ternary phase diagrams suggest that the 82:18 mixture of CC6+MC6 is the true eutectic concentration of this mixture. At this concentration, CC6+MC6 melts and freezes congruently at a temperature of between 25 and 27°C. It is suggested that this work be confirmed and expanded through experimental testing of the modeled $CaCl_2$-$MgCl_2$-H_2O phase diagrams.

4.3.3 DSC Testing of CC6+MC6 Mixtures

DSC melting curves for several mixture percentages of CC6+MC6 are presented in Figure 4.9, with their thermal results summarized in Table 4.7. As the concentration of MC6 increased, the melting temperature and latent heat were found to decrease until reaching a temperature of 19.9°C and latent heat of melting of 64.4 J/g at a mixture weight ratio of 50:50. Throughout the mixture range considered, the DSC melt tests always resulted in a single heat flow peak; although the width, height, and shape of this peak varied. At high concentrations of CC6, a wide peak was found, which may indicate incongruencies about the melt point. As the 50:50 ratio was approached, the peaks were found to skew towards the higher temperatures, indicating potential incongruencies on the cold side of the peak. At the intermediate mixture ratios (66:33 to 83:17), the melting heat flow peaks were found to be symmetric and relatively narrow with minimal "tailing" on either side of the peak. This is consistent with the visual observation of melting/freezing in Figure 4.5, although the visual observations were found to provide a more reliable method of ascertaining if the phase change was congruent. Given the results of the visualization tests and phase diagram modeling, the 82:18 CC6+MC6 mixture was selected as the true CC6+MC6 eutectic concentration and was tested more closely by DSC. These 82:18 CC6+MC6 DSC results are presented in Figure 4.10.

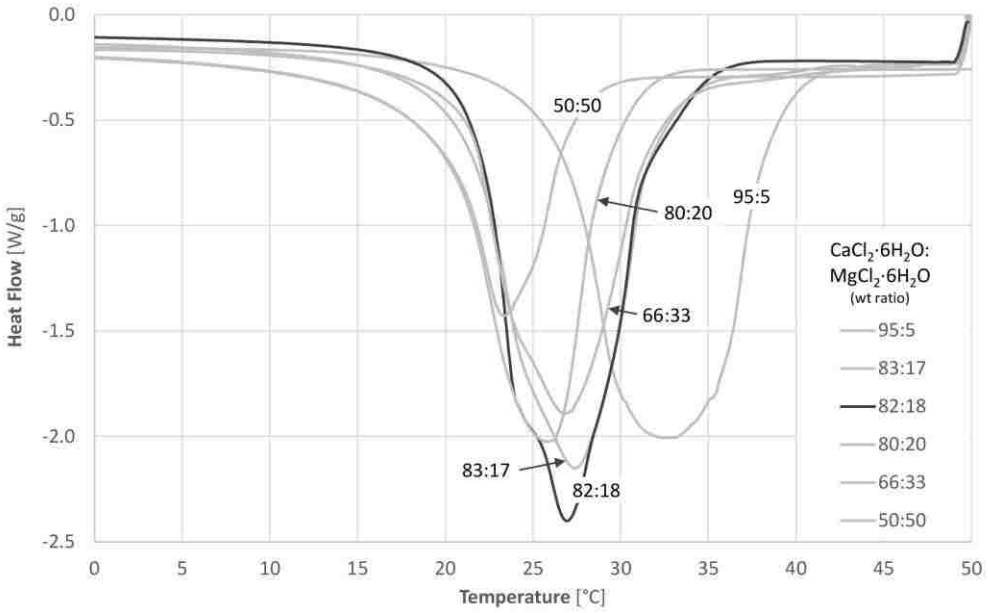

Figure 4.9: DSC Melting Curves for CC6+MC6 System at Varying Concentrations

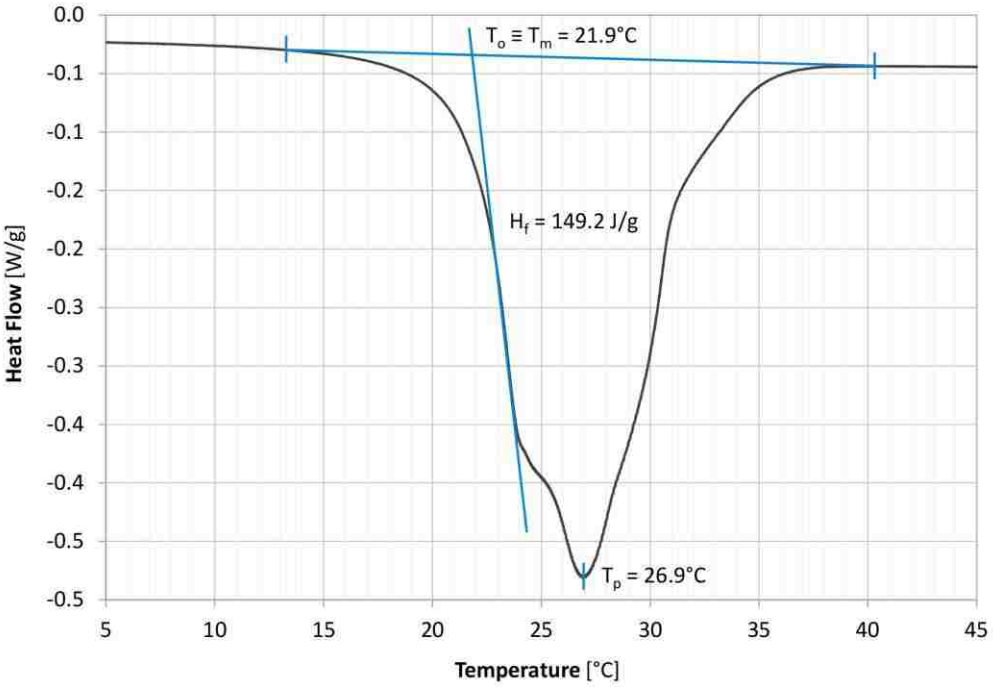

Figure 4.10: $CaCl_2 \cdot 6H_2O$ + 18% $MgCl_2 \cdot 6H_2O$ DSC Melting Results

Table 4.7: DSC Results for CC6+MC6 Mixtures

CC6+MC6 [wt ratio]	T_m [°C]	T_p [°C]	H_f [J/g]	Supercooling [°C]
50:50	19.9	23.3	64.4	~ 26
66:33	19.7 - 21.1	23.7 - 26.9	95.1 – 126.8	~ 43
80:20	19.9	25.8	118.7	
82:18	21.9	26.9	149.2	
83:17	21.0	27.4	146.7	~ 28
95:5	26.5	32.5	151.6	~ 26

4.3.4 Supercooling Suppression of 82:18 CC6+MC6

Supercooling (also called subcooling or undercooling) is a phenomenon experienced by a freezing PCM, where the temperature must be lowered well below the freezing temperature before crystallization begins. As the temperature is decreased down to the supercooling temperature, the hydrated salt will remain in the liquid state. Eventually, the PCM supercools to a temperature far enough below the phase change temperature that freezing begins. The difference between the actual freezing temperature and the temperature at which freezing begins is defined as the supercooling of the PCM. Kimura et al. reported that supercooling is due to an increase in the chemical potential when moving from the melted to crystalized state. This increase in potential can be thought of as a barrier preventing the formation of the initial nucleation sites required for crystallization [K13]. Supercooling can also be thought of as an energy barrier resulting from the surface energy effects inherent in the formation of the initial nucleation sites [M10]. A third way of thinking about this is presented by Yamaguchi et al., who suggests that structural differences between the liquid and crystallized salt are responsible for supercooling [Y1]. Supercooling results when the energy barrier preventing this conversion must be overcome in order for freezing to begin.

As seen in Table 4.7, DSC testing of CC6+MC6 mixtures suggested considerable supercooling (26 to 43°C); although the DSC is known to over-predict supercooling. Since this degree of supercooling raises considerable issues for the practical use of this PCM, several additives for the prevention of supercooling were tested. While it is generally believed that these additives should have a similar crystalline structure to that of the crystallized PCM, it is also known that impurities, dust, or container surface imperfections can also lead to the formation of the initial nucleation sites required for crystal growth. Because of this, selection of a suitable nucleation additive is often an empirical pursuit with significant trial and error involved. Fortunately, although the supercooling suppression of CC6+MC6 mixtures has not been directly addressed in the literature, there has been extensive research considering the primary compound of these mixtures; $CaCl_2 \cdot 6H_2O$. As early as 1983, Lane [L7] presented strontium chloride hexahydrate ($SrCl_2 \cdot 6H_2O$, or SC6) as a promising nucleating agent for $CaCl_2 \cdot 6H_2O$. This was later confirmed through work by Feilchenfeld et al. [F6].

To test the supercooling suppression performance of potential additives, the following procedure was adopted. First a small sample of PCM (20 to 25 g) would be equilibrated at 35°C in the programable water bath. Next, the water temperature was linearly decreased to 5°C at the rate of 0.267°C/min. RTDs recorded temperatures of the water and PCM throughout the tests.

The first test was a baseline test with 82:18 CC6+MC6 prepared without any supercooling additives. This PCM was cooled the entire way to 5°C with no freezing observed, indicating supercooling of greater than 20°C. Next, the following four additives were tested at approximately 3 wt% of the total PCM weight including the additive:

- $Ca(OH)_2$
- Iron (III) Oxide (aka. rust. May be oxides or oxide-hydroxides)

- Graphite Powder
- $SrCl_2 \cdot 6H_2O$

The results of these supercooling tests are presented in Figure 4.11. Supercooling for each additive was measured as the temperature difference between the dip prior to freezing and the subsequent peak resulting during freezing. This peak corresponds to the phase transition temperature of the PCM. $SrCl_2 \cdot 6H_2O$ was found to result in the best supercooling performance with only 2.0°C of measured supercooling, followed by rust at 3.8°C of supercooling. The graphite and $Ca(OH)_2$ performed poorly with 15.5 and 16.0°C of supercooling respectively.

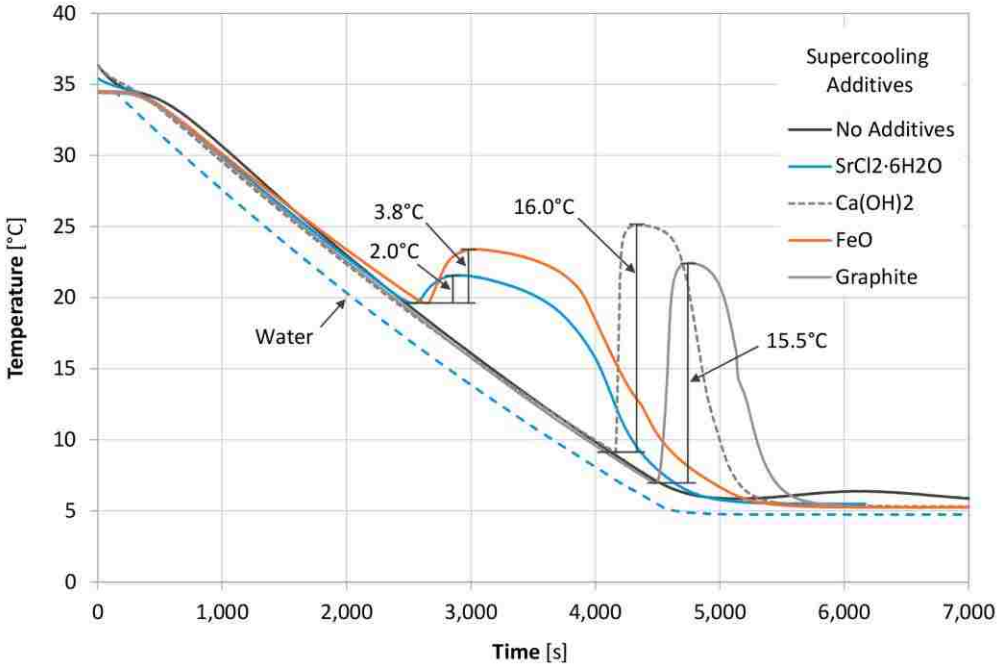

Figure 4.11: Additives Tested for $CaCl_2 \cdot 6H_2O$ + $MgCl_2 \cdot 6H_2O$ Supercooling Suppression

It is not required that all of the supercooling be eliminated for practical use of a PCM. For instance, if the PCM is frozen using a low-temperature source of only 5°C below the phase transition temperature, this source should still be capable of overcoming 2-3°C of supercooling

if the heat transfer system is properly designed. Since the 2°C of supercooling found for CC6+MC6+SC6 is within the acceptable range for most PCM applications, additional testing with supercooling additives was not conducted. Because of this good supercooling performance, 3 wt% SC6 was added to all CC6+MC6 samples prepared for long-term cycling and drop calorimetry testing.

4.3.5 82:18 CC6+MC6 Thermal Cycling

Six, ~200 g PCM samples of 82:18 CC6+MC6 were prepared for long-term cycling in the thermal cycling system presented in Section 3.2 (Table 4.8). These samples were prepared using the encapsulations presented in Section 3.3.3, which allows for drop calorimetry of the samples. To minimize supercooling, 3 wt% SC6 was added to each sample after the 82:18 mixture was mixed, resulting in 79.5, 17.5, and 3 wt% CC6, MC6, and SC6 respectively.

Table 4.8: 82:18 CC6+MC6 Samples for Thermal Cycle Testing

Sample #	m_{ENC} [g]	m_{PCM} [g]	$CaCl_2 \cdot 6H_2O$ [wt%]	$MgCl_2 \cdot 6H_2O$ [wt%]	$SrCl_2 \cdot 6H_2O$ [wt%]
15	326.1	200.3	79.6%	17.5%	3.0%
16	334.1	197.7	79.5%	17.5%	3.0%
17	316.9	194.7	79.5%	17.5%	3.0%
18	329.6	188.7	79.5%	17.5%	3.0%
19	326.1	188.8	79.6%	17.4%	3.0%
22	331.0	190.6	79.5%	17.5%	3.0%

Before beginning cycling, each of the six samples in Table 4.8 were tested by drop calorimetry to determine their initial latent heat of fusion. On average, the samples were found to have an initial H_f of approximately 150.2 J/g. After this initial characterization, the six samples were cycled between 5 and 50°C for up to 2,700 complete cycles. A complete cycle is comprised of

one melt and freeze. During cycling, the samples were removed from the cycling system at intervals of approximately 500 cycles in order to conduct drop calorimetry. After completing at least 2,700 cycles, all of the samples were removed from the cycling system and tested by drop calorimetry one final time. Calorimetry H_f results throughout thermal cycling of the CC6+MC6 PCM are presented in Figure 4.12. While there are slight variations in H_f with cycling, nearly all of the variations fall within ±4% of 150 J/g. These variations are not significant as the average standard deviation for calorimeter measurements of H_f for a single sample at a given cycle number is ±2.6%. Tabular values of H_f before and after cycling to 2,700 cycles is presented in Table 4.9. The average change in H_f after 2,700 cycles is only a decrease of 0.8 J/g.

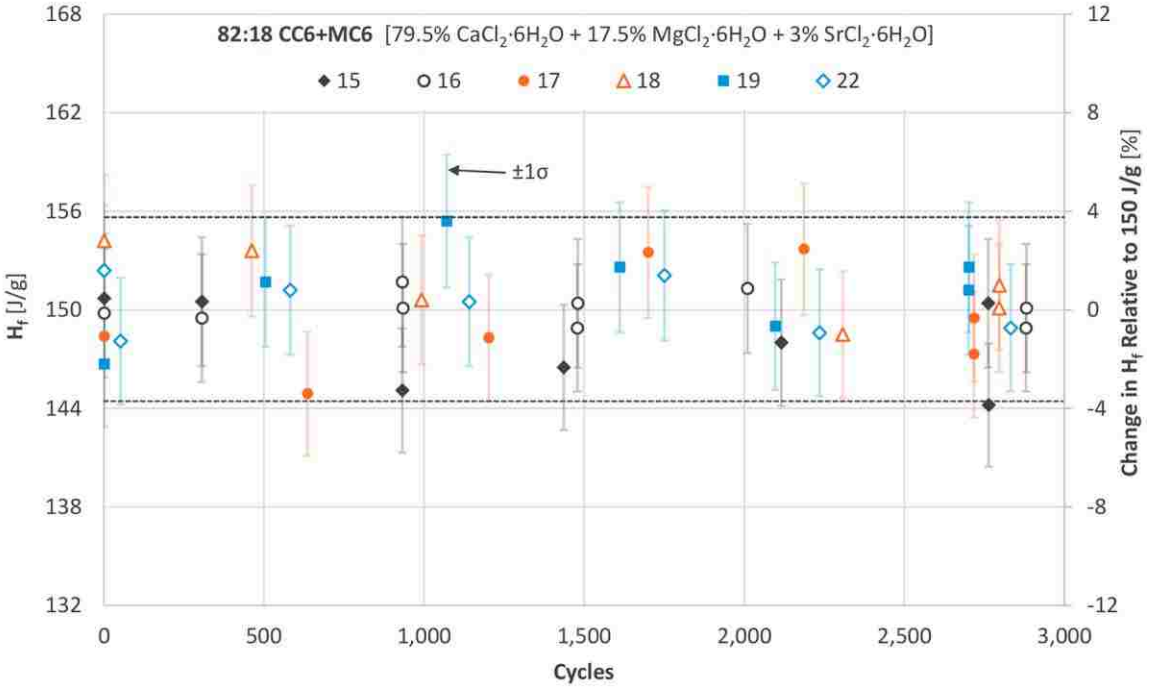

Figure 4.12: H_f During Long Term Cycling of 82:18 CC6+MC6

The flat response of H_f with thermal cycling to 2,700 cycles suggests that this PCM is stable during long-term cycling. In addition to a stable H_f within a given sample, very little variation in

measured H_f was found between samples. This is significant as it suggests that the 82:18 CC6+MC6 mixture forms a self-equilibrating PCM mixture, which maintains a well-defined structure despite small composition or hydration changes within the bulk PCM.

Table 4.9: H_f Measured by Calorimetry Before and After 2,700 Cycles of CC6+MC6

Sample #	H_f [J/g] (0 Cycles)	H_f [J/g] (2,700 Cycles)
15	149.5	147.3
16	147.8	149.5
17	149.2	148.4
18	155.5	150.8
19	146.8	151.9
22	152.6	148.9
AVG	150.2	149.5

4.4 $Na_2SO_4 \cdot 10H_2O$

Sodium sulfate decahydrate ($Na_2SO_4 \cdot 10H_2O$ or NS10), also known as Glauber's Salt, is one of the most widely-studied low-temperature PCMs. The history of this PCM goes back to the 19th century with notable early researchers being Cohen [C12] and Leenhardt et al. [L9]. In 1935 Kobe et al. published their own thermal research into this material, presenting it alongside previously-published results [K14]. By 1948, Telkes et al. had constructed a solar heated house in Dover, Massachusetts utilizing NS10 as a thermal storage medium [T4]. Initial results from this project were promising. However, as later related by Butti et al., by the third winter the salt had deteriorated and separated into two distinct layers, one remaining liquid while the other was solid [B20]. Telkes continued to experiment with NS10 finding that this PCM contains 44% anhydrous Na_2SO_4 with the remainder being H_2O by weight. At the phase transition temperature of 32.4°C, approximately 85 wt% of the PCM forms a saturated solution with the water as

$Na_2SO_4 \cdot 10H_2O$, while the remaining 15% remains in the solid, anhydrous form, settling to the bottom of the container due to the higher density of the anhydrous solid. To prevent this phase separation, Telkes introduced thickening agents, which prevented the anhydrous solid from settling out of the NS10 solution. Thickened NS10 was cycled 1,000 times without a significant change in thermal performance [T6]. Other researchers have considered this PCM, resulting in a plethora of thermal information for this hydrated salt. A summary of this information (dating back to the 1800's) is presented in Table 4.10 and Table 4.11.

Table 4.10: Thermodynamic Properties of NS10 as Presented in the Literature

T_m [°C]	H_f [J/g]	Cp_L [J/g·K]	Cp_s [J/g·K]	ρ_L [kg/m^3]	ρ_s [kg/m^3]	Source
31.4	238					[L9]
31.7	253			1330	1458	[T6]
32.0	245					[C3]
32.0	251	3.26	1.92	1330	1460	[G6,S1]
32.2	251					[T3]
32.4		3.34	2.52			[P12]
32.4	241					[S18]
32.4	243	3.32				[K14,T2]
32.4	251	3.31	1.76	1410	1460	[G5]
32.4	253				1460	[H3]
32.4	254		1.93		1485	[A1]
32.5	251					[K10]
32.8	214					[C12]

Table 4.11: Transport Properties of NS10 as Presented in the Literature

k_L [W/m·K]	k_s [W/m·K]	Source
0.544		[A1]
0.589	0.514	[G6,S1]

4.4.1 DSC of $Na_2SO_4 \cdot 10H_2O$

NS10 was tested by DSC to find its melt temperature and latent heat of melting (Figure 4.13). The measured T_m of 33.2°C is slightly above that presented in the literature, while the measured H_f of 190.6 J/g is considerably lower than the published data. Upon examination of the melting curve, it is apparent that a second melting peak occurs at -0.7°C. Since this salt is known to disassociate into a solution and anhydrous Na_2SO_4, this behavior is not unexpected. As the frozen solution and PCM is heated, the solution reaches its melting point first, at a temperature close to 0°C. Upon further heating, the still frozen PCM eventually melts at the PCM's phase transition temperature. Since a portion of the bulk PCM has disassociated (indicated by the second peak near 0°C), the lower H_f value is not unexpected. These results are consistent with findings by Furbo, who stated that at temperatures below the phase transition temperature an incongruently melting PCM will consist of three district layers [F15]. From top to bottom, these layers are a saturated salt solution, a layer of crystalized PCM, and a sedimentary layer of anhydrous PCM. Supercooling for NS10 was also estimated using the DSC cooling curve, with the results presented in Table 4.12. Since incongruencies were encountered so early in the testing phase of NS10, and since this material's melting temperature was slightly above that desired for the cold storage system being developed, further testing with this PCM was not conducted.

Table 4.12: DSC Results for NS10

T_m [°C]	T_p [°C]	H_f [J/g]	Supercooling [°C]
33.2	36.5	190.6	~ 45

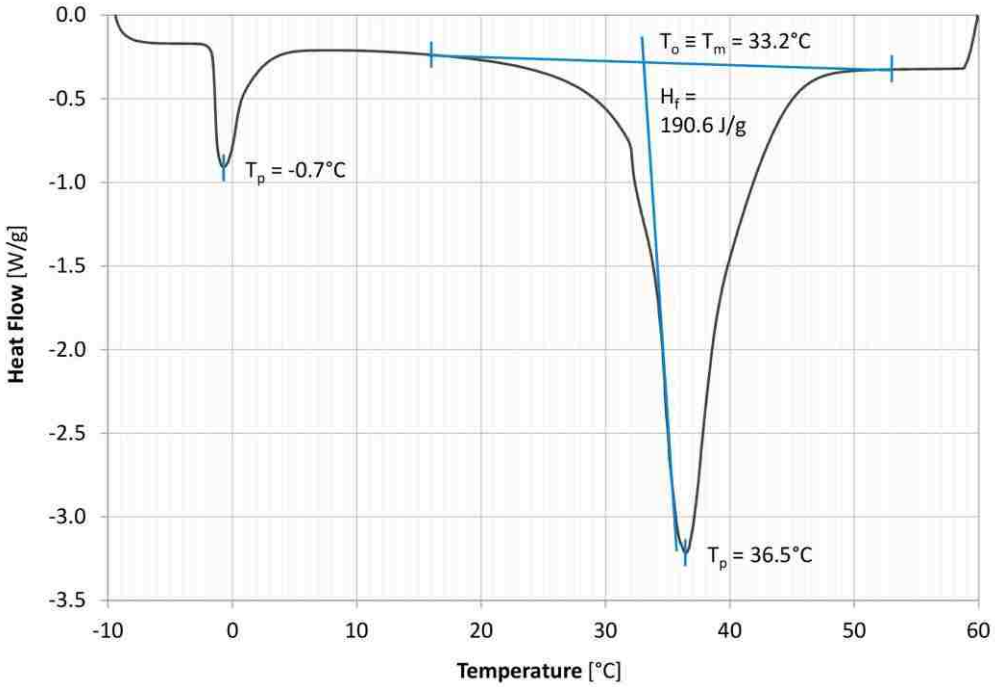

Figure 4.13: NS10 DSC Melting Results

4.5 $CaCl_2 \cdot 6H_2O + KNO_3$

During DSC testing of various PCMs within the required phase transition temperature range, a new PCM mixture was uncovered. It was found that the addition of a small quantity of potassium nitrate (KNO_3 or KN) to CC6 lowered the phase change temperature of CC6, while still resulting in a congruently melting PCM. While this PCM has not been characterized or tested in the literature, a similar composition is mentioned in a Chinese patent [W3]. The motivation for examining this PCM was to find a PCM with a phase transition closer to 25°C than plain CC6.

4.5.1 DSC of CC6+KN

Samples of $CaCl_2 \cdot 6H_2O$ + KNO_3 (CC6+KN) were prepared with between 3.6 and 10.8 wt% KNO_3. These samples were tested by DSC to note any differences in T_m and H_f. Several of these DSC

curves are plotted alongside the curve for CC6 (0% KN) in Figure 4.14. It is evident that as the concentration of KNO_3 increases, both the melting temperature and the latent heat of melting decrease. This is beneficial if a PCM with a slightly lower melt point is desired. However, this decrease in temperature comes at the cost of PCM thermal storage potential. The T_m and H_f decrease are plotted with respect to KNO_3 percentage in Figure 4.15. As seen, the change in both temperature and latent heat was found to obey a linear relationship with respect to KNO_3 percentage. Since these results indicate a relatively low H_f (<100 J/g) for KNO_3 concentrations greater than 10 wt%, it is recommended that this concentration be set as an upper-limit for this mixture.

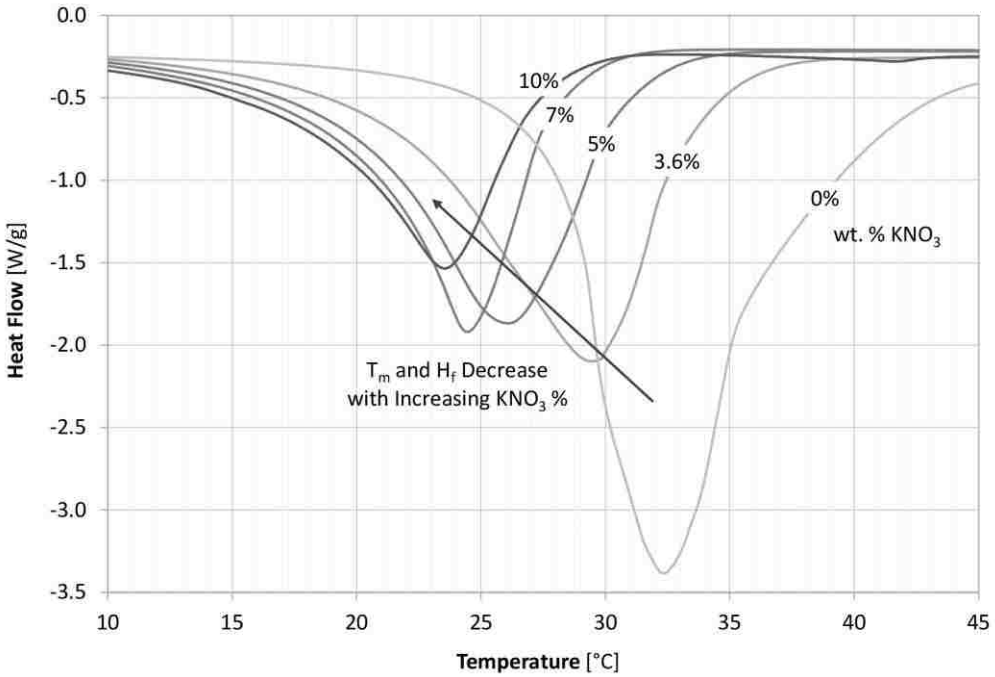

Figure 4.14: Change in CC6+KN DSC Curves with Varying Concentrations of KN

The absence of sharp peaks, double peaks, and the smoothness of the DSC curves in Figure 4.14 indicate congruent melting of all CC6+KN mixtures. However, as the percentage of KNO_3 increases, significant asymmetry of the heat flux peak is seen, with the cold-side of the peak

being stretched. While this results in a lower onset temperature, it also indicates a widening of the phase transition temperature range. This is problematic if the PCM driving temperature difference for freezing fails to fall below the lower bound of the phase transition temperature. DSC test results for the CC6+KN mixtures are summarized in Table 4.13. Supercooling information was estimated for several of the mixtures using DSC; showing a consistent 24 to 25°C of supercooling. Given the temperature requirements of the thermal energy storage system being developed, a CC6+KN mixture ratio of 93:7 was selected for all further testing. At this ratio, the phase transition temperature was depressed to 19.6°C, while maintaining a latent heat of fusion of 120 J/g.

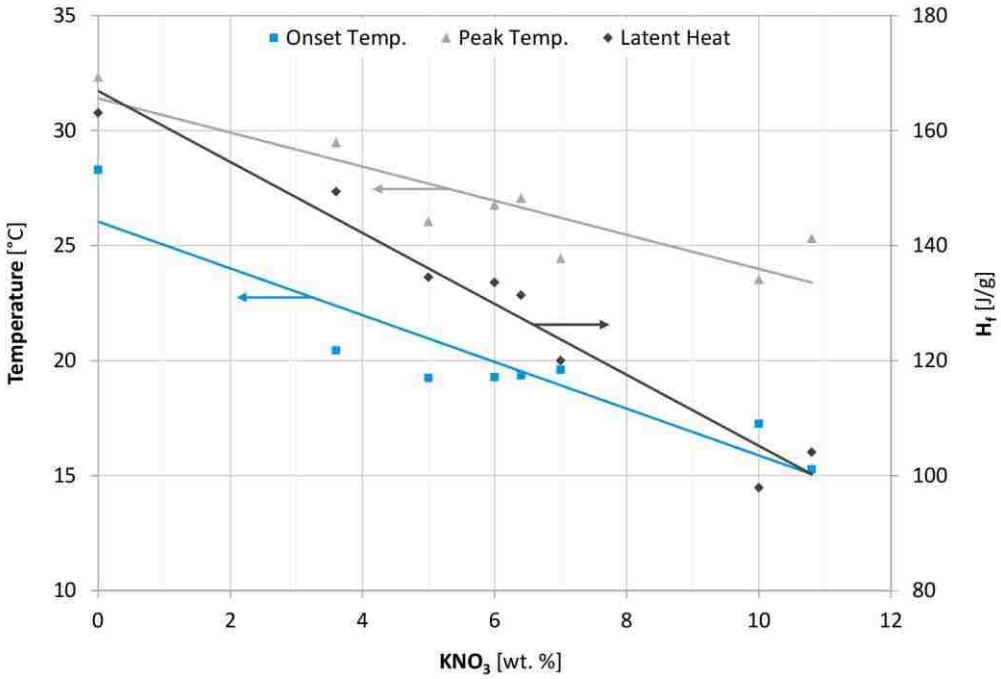

Figure 4.15: Impact of KNO_3 Percentage on T_o, T_p, and H_f for the CC6+KN Mixture

Table 4.13: DSC Results for CC6+KN Mixtures

CC6+KN [wt ratio]	T_m [°C]	T_p [°C]	H_f [J/g]	Supercooling [°C]
89.2:10.8	15.3	25.3	104.1	~24.4
90:10	17.3	23.5	97.9	
93:7	19.6	24.5	120.0	
93.6:6.4	19.4	27.1	131.4	~25.2
95:5	19.3	26.1	134.5	
96.4:3.6	20.4	29.5	149.4	~24.8
100:0	28.3	32.3	163.1	~28.3

4.5.2 Supercooling Suppression of CC6+KN

As shown in Table 4.13, supercooling of the CC6+KN mixtures is significant. It was hypothesized that additives, which suppress supercooling in the base PCM (CC6) would help eliminate it in the mixture. Since SC6 is known to largely eliminate supercooling in CC6 [L7,K13], it was tested in the 93:7 CC6+KN mixture. When tested by cooling in a water bath, this PCM showed good supercooling mitigation performance with approximately 2.1°C of supercooling (Figure 4.16).

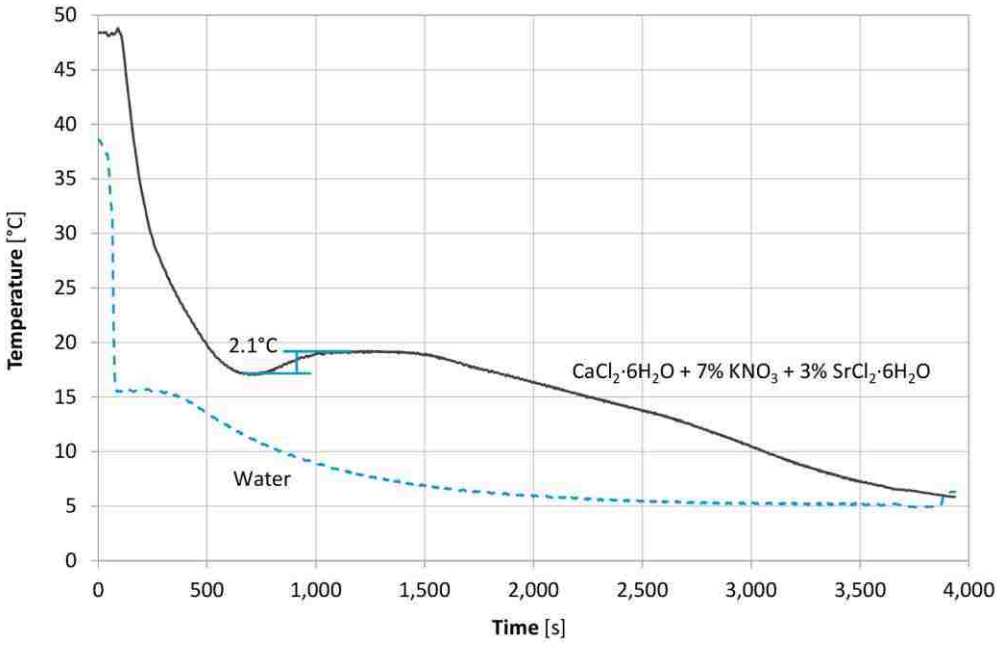

Figure 4.16: Supercooling of 93:7 CC6+KN with 3 wt% SC6 Added

4.5.3 93:7 CC6+KN Thermal Cycling

As with the CC6+MC6 mixture, six, identical, ~200 g samples of 93:7 CC6+KN were prepared for long-term cycling (Table 4.16). 3 wt% SC6 was added to each sample to minimize supercooling. Note that the 3% SC6 is added after the CC6+KN is mixed at the 93:7 ratio, meaning the actual mixture is 90.2, 6.8, and 3 wt% for CC6, KN, and SC6 respectively.

Table 4.14: 93:7 CC6+KN Samples for Thermal Cycle Testing

Sample #	m_{ENC} [g]	m_{PCM} [g]	$CaCl_2 \cdot 6H_2O$ [wt%]	KNO_3 [wt%]	$SrCl_2 \cdot 6H_2O$ [wt%]
10	329.1	205.0	90.2%	6.8%	3.0%
11	319.4	204.3	90.2%	6.8%	3.0%
12	319.6	203.5	90.2%	6.8%	3.0%
13	320.1	214.0	90.2%	6.8%	3.0%
14	319.3	196.7	90.2%	6.8%	3.0%
21	330.1	192.9	90.4%	6.7%	3.0%

Initial drop calorimeter of these six samples found an average heat of fusion of 128.6 J/g, which is comparable to that found using DSC. These six samples were cycled between 5 and 50°C for at least 2,700 complete cycles (150 min. per cycle) with the samples being removed for calorimetry at regular intervals of approximately 500 cycles. Calorimetry H_f results before, during and after thermal cycling of the CC6+KN PCM are presented in Figure 4.17. With the exception of Sample 14, H_f is seen to remain relatively constant during cycling with nearly all of the data falling within ±10% of the average initial H_f value. Furthermore, given the typical standard deviation for calorimeter PCM measurements, most of the data lies within the calorimeter's ±2σ sample uncertainty range of ±5.2%. Sample 14 was found to increase in H_f through approximately 1,200 cycles, at which point its H_f value began to drop slightly. While this deviation appears large, it should be noted that it is still within + 12% from the average initial H_f value of 128.6 J/g. The reason for this increase is not known but is thought to be due to a small compositional difference in Sample 14. Tabular values of H_f before and after cycling to 2,700 cycles are presented in Table 4.15. The average decrease in H_f after 2,700 cycles is only 2.1 J/g.

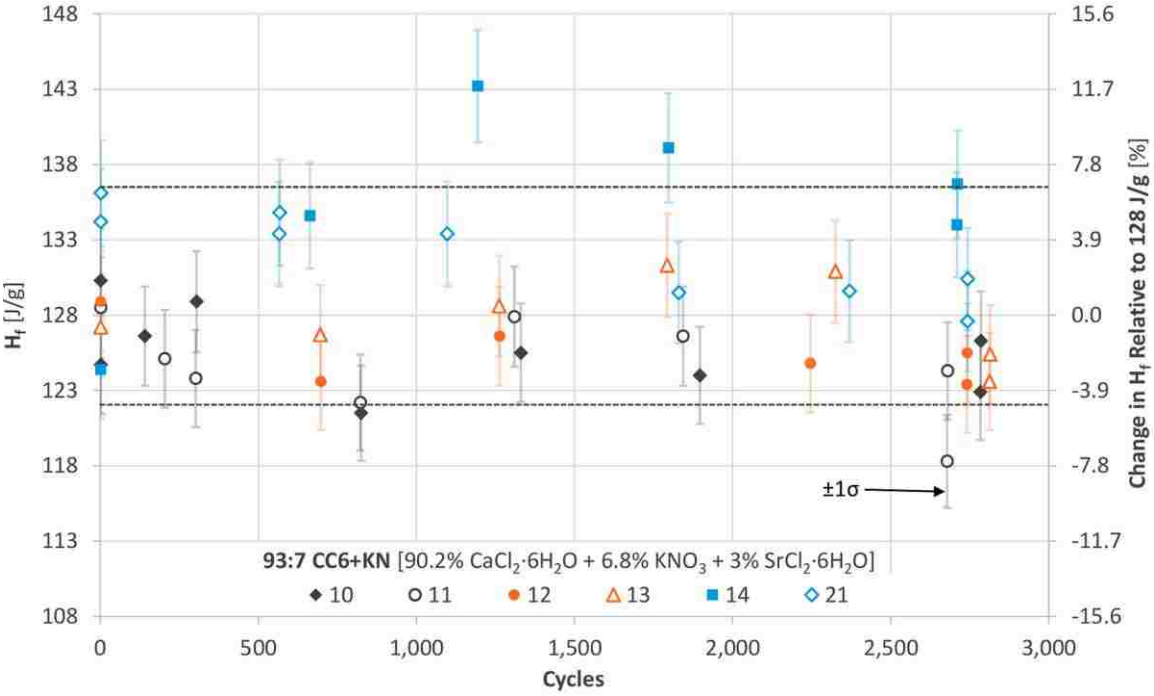

Figure 4.17: H_f During Long Term Cycling of 93:7 CC6+KN

Table 4.15: H_f Measured by Calorimetry Before and After 2,700 Cycles of CC6+KN

Sample #	H_f [J/g] (0 Cycles)	H_f [J/g] (2,700 Cycles)
15	127.5	124.6
16	128.5	121.3
17	128.9	124.5
18	127.2	124.5
19	124.4	135.4
22	135.2	129.0
AVG	128.6	126.5

Given the minimal decrease in H_f after cycling, it is proposed that the 93:7 CC6+KN PCM is thermally stable during long-term cycling. If the PCM were not thermally stable with cycling, H_f

would decline considerably as the cycle number was increased. Good agreement between all six samples lends confidence to these findings.

4.6 $CaCl_2 \cdot 6H_2O$

Calcium chloride hexahydrate ($CaCl_2 \cdot 6H_2O$ or CC6) is perhaps the most widely studied hydrated salt PCM with a phase transition temperature in the 30°C range. Initial work into this PCM dates back to the 19th century with Roozeboom considering the hydrates of calcium in 1889 [R10]. In Hale et al's. work for NASA in the 1970's, CC6's melt temperature and latent heat of fusion were recorded [H3]. In 1975, Telkes [T6] and Lorsch et al. [L18] touched on CC6 as a promising hydrated salt PCM, although there was little discussion on any of the challenges associated with its use. Carlsson et al's work in 1979 represents the first information considering the stability and/or modification of CC6 to ensure long-term thermal performance. During the 1980's, the first detailed work looking at CC6 was conducted. Abhat conducted DSC testing of CC6 [A1]. Feilchenfeld et al. experimented with CC6 thickening and the extra-water principle in order to promote phase stability [F6]. Also considered by Feilchenfeld et al. was the impact of additives, such as KCl, on reducing CC6's melt temperature [F5,F7]. Brandstetter outlined the reasons for phase instability in CC6 alongside a potential solution in the extra water principle [B19]. Perhaps the most seminal work of the period was conducted by George Lane, while working as a researcher at Dow Chemical Co. Lane considered the addition of $SrCl_2 \cdot 6H_2O$ and other additives to CC6 as nucleating and stabilization agents [L2,L8]. In addition, Lane et al. found that the addition of small quantities of KCl and NaCl could have a positive impact on CC6 phase stability [L6,L8]. This work on CC6 phase stability will be discussed in more detail in Chapter 5. Since 1990, work by Heckenkamp et al. [H12], Esen et al. [E5], Shahbaz et al. [S12] and Carlsson [C5] have expanded the knowledge-based for this PCM. More recently, researchers such as Yuan et al. [Y3], and Li et al. [L17] have considered the addition of expanded graphite and nanoparticles to

CC6 in order to improve both supercooling, stability, and thermal conductivity. Thermodynamic and transport properties for CC6 from the literature are presented in Table 4.16 and Table 4.17.

Table 4.16: Thermodynamic Properties of CC6 From the Literature

T_m [°C]	H_f [J/g]	Cp_L [J/g·K]	Cp_s [J/g·K]	ρ_L [kg/m^3]	ρ_s [kg/m^3]	Source
27 - 29	191	1.56	1.80			[L4]
28.9	174					[T3,T6]
29.0	160		1.45	1496	1710	[A1]
29.0	170					[L18]
29.0	201					[F5]
29.4	170					[H3]
29.6	189		1.45		1620	[H12]
29.6	191	2.10	1.42	1562	1802	[L8]
29.7	170	2.13	1.46			[G4]
29.7 - 29.9	188	2.13	1.46		1710	[E5]
29.8	173					[C6]

Table 4.17: Transport Properties of CC6 From the Literature

k_L [W/m·K]	k_T [W/m·K]	k_s [W/m·K]	η [cP]	Source
0.539	0.700	1.088		[E5]
0.540				[G4]
0.540 – 0.561		1.088	11.8	[L4,L8]

4.6.1 DSC of $CaCl_2 \cdot 6H_2O$

As with the preceding PCMs, CC6 was tested by DSC to find its melt temperature and heat of fusion of melting. A typical DSC melting test of CC6 is presented in Figure 4.18. CC6 was found to melt at 28.1°C with a latent heat of fusion of 187.1 J/g. These values compare well with the

literature, although the measured T_m value is a bit below the average literature value, while H_f is slightly above. By considering the DSC freezing curve (Figure 4.19), a rough estimate of supercooling at between 28 and 38°C was made. A summary of $CaCl_2 \cdot 6H_2O$ DSC thermal and supercooling results is presented in Table 4.18.

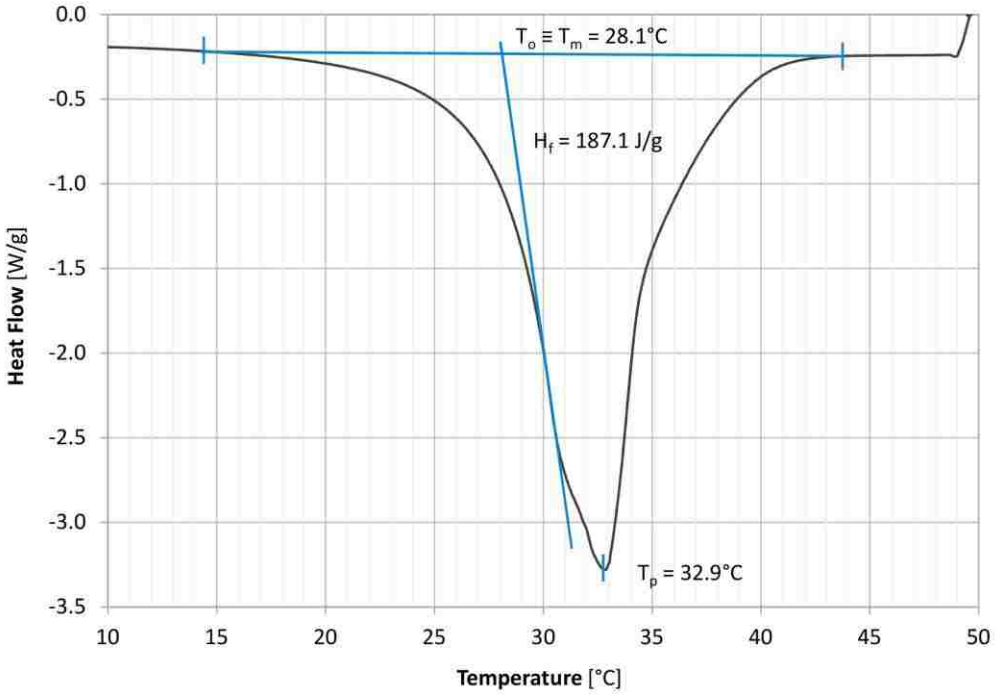

Figure 4.18: CC6 DSC Melting Results

Table 4.18: DSC Test Results of CC6

T_m [°C]	T_p [°C]	H_f [J/g]	Supercooling [°C]
28.1 – 28.8	32.3 – 33.7	163.1 – 199.5	~28 - 38

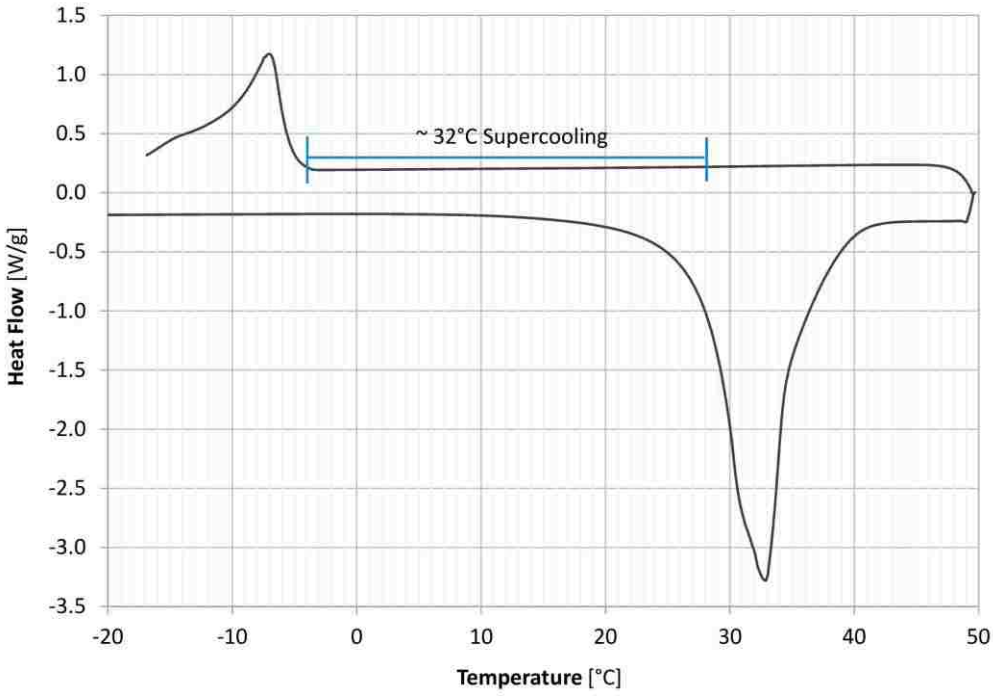

Figure 4.19: CC6 DSC Melting and Freezing Curve with Estimated Supercooling

4.6.2 Supercooling of $CaCl_2 \cdot 6H_2O$

As seen in Table 4.18, supercooling of CC6 is a significant issue, which must be solved if this PCM is to be practically used. Given the overprediction of supercooling during the DSC testing, CC6 was slowly cooled in the programable water bath from 35°C to 5°C at a cooling rate of 0.375°C/min. Results from this testing are presented in Figure 4.20. Supercooling of 17.5°C was measured for CC6 without any nucleation additives. It should be noted that this is an underestimation of supercooling as the water temperature could not be lowered below 5°C in order to prevent freezing. This is why once the PCM reached 5°C, it maintained this temperature until an unknown factor initiated freezing. Since the CC6 was maintained at 5°C for some time before freezing, it is likely that cooling (supercooling) was not the only factor which precipitated crystallization. For instance, crystallization is known to be initiated by motion of the supercooled

PCM. Four nucleation additives were examined for their supercooling performance in CC6, $SrCl_2 \cdot 6H_2O$, wood chips, rust (FeO), and graphite powder.

As seen in Figure 4.20, SC6 and rust are the best performing additives, with supercooling measured at 2.7°C for both. While it is thought that SC6 suppressed supercooling through having a crystal structure similar to CC6, the FeO does not have this property. The best explanation for the good nucleation performance of the rust is that of epitaxy, where the FeO particles provide a surface on which the crystals of CC6 can begin to grow. This may also be the catalyst driving nucleation with SC6, as SC6 remains in the solid form within the liquid CC6 and both the solid SC6 and FeO have similar particle sizes.

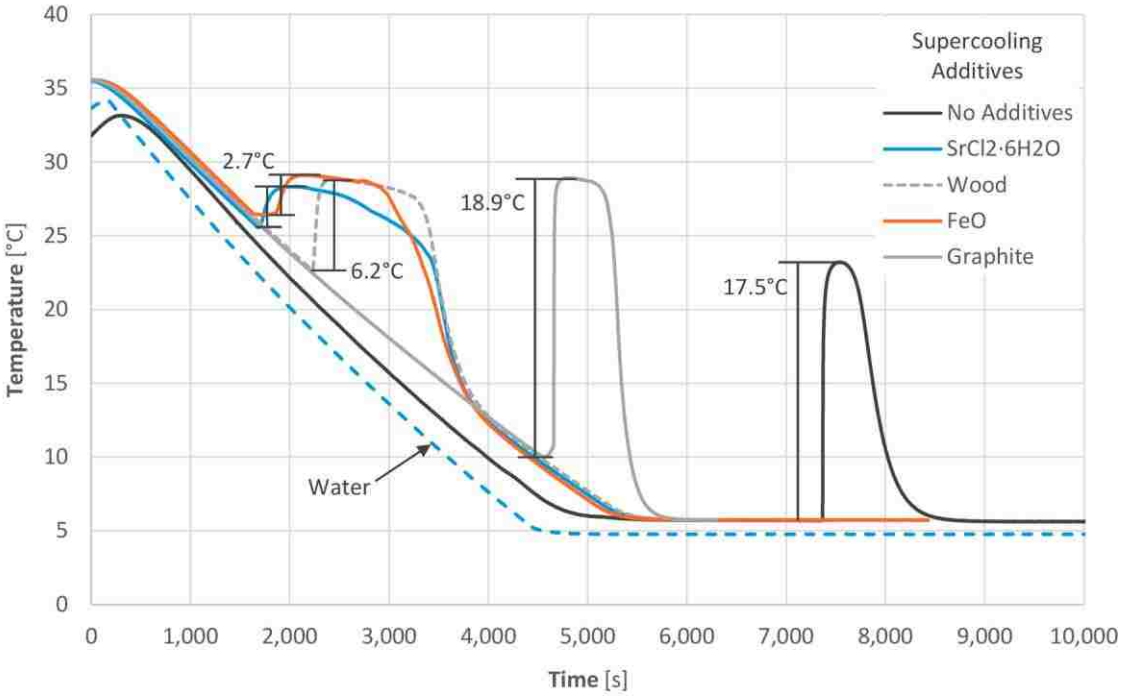

Figure 4.20: Supercooling of CC6 With and Without Nucleation Additives

Lane states that when nucleation additives are added to a material, if both the additive and bulk material have a similar crystal structures or if the lattice planes have very similar structures or periodicities, then additive-promoted nucleation will work very well [L7]. The crystal structures of CC6 and potential nucleating additives were studied extensively by Lane. Since CC6 forms a hexagonal lattice structure, several nucleation additives with similar hexagonal structures were considered (Table 4.19). When these additives were tested, Lane found that both $SrCl_2 \cdot 6H_2O$ and $BaI_2 \cdot 6H_2O$ virtually eliminated supercooling of CC6. All other additives had considerably worse performance. This work illustrates that despite similarities in crystal structure, nucleation additives may or may not work in suppressing supercooling; leaving the selection of a suitable additive largely an empirical exercise. It should be noted, and was expressed by Lane, that although one or two of the additives in Table 4.19 were shown to minimize supercooling, their long-term performance during repeated cycling was not demonstrated [L5,L7].

Table 4.19: Crystal Structures of CC6 and Tested Nucleating Additives [L5,L7]

Compound	Additive [wt%]	Angstrom Units [AU]*		Supercooling [°C]
		a	c	
$CaCl_2 \cdot 6H_2O$		7.860	3.87	22.5
$CaBr_2 \cdot 6H_2O$	0.5	8.138	4.015	17.4
$CaI_2 \cdot 6H_2O$	0.5	8.4	4.25	24.2
$SrCl_2 \cdot 6H_2O$	1.0	7.940	4.108	0.0
$SrBr_2 \cdot 6H_2O$	1.0	8.2051	4.146	2.1
$SrI_2 \cdot 6H_2O$	1.0	8.51	4.29	11.9
$BaI_2 \cdot 6H_2O$	0.5	8.9	4.6	0.0

* 1 AU = 1 x 10^{-10} m

Feilchenfeld et al. used 2 wt% SC6 to suppress supercooling in CC6 [F6]; as did Shahbaz et al. with supercooling of less than 2°C, measured after 100 thermal cycles [S12]. Because of the

positive nucleation performance of SC6, it was added to CC6 at 1, 3, and 5 wt%. It was expected that a higher percentage of SC6 would reduce supercooling to a greater degree, although a higher percentage of SC6 was also hypothesized to reduce H_f. Therefore, a minimum wt% of SC6 which results in adequate suppression of supercooling was sought. Six, ~200 g samples of CC6 at the three SC6 wt% concentrations (two samples at each SC6 concentration) were prepared and tested by drop calorimetry to note any differences in T_m and H_f. The change in H_f with increasing percentage of SC6 is presented in Figure 4.21. On average, the samples with 1 wt% SC6 were found to have a latent heat of fusion of 181.3 J/g. Increasing SC6 to 3 wt% resulting in a 5.4% decrease in H_f to 171.5 J/g. At 5 wt% SC6, H_f was found to decrease further to 165 J/g, which is 3.8% below H_f at 3 wt% SC6. These results confirm the hypothesis that the minimal quantity of SC6 required for effective long-term nucleation should be used.

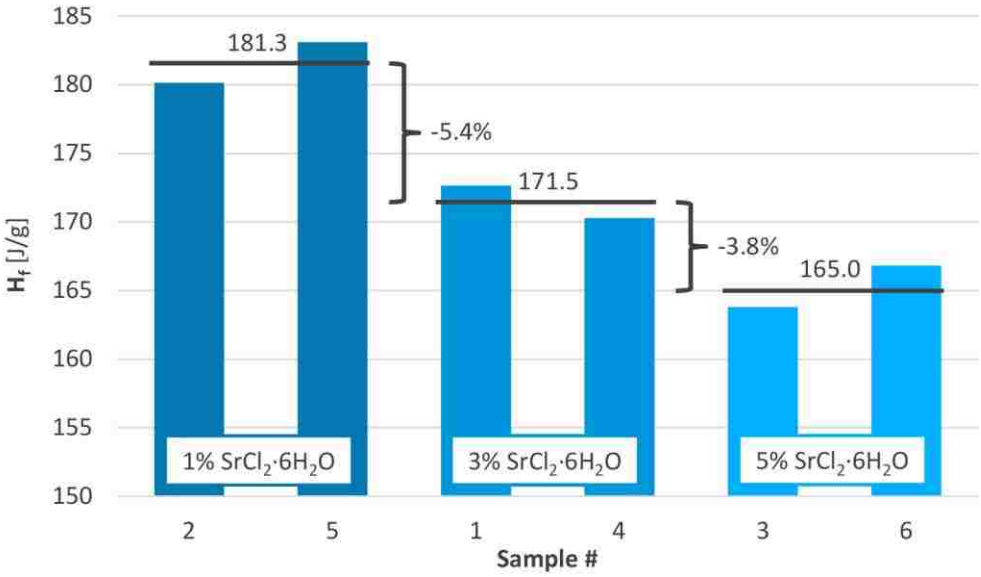

Figure 4.21: Difference in H_f with Respect to Percentage of $SrCl_2 \cdot 6H_2O$

The impact of SC6 on both the melt temperature, T_m and freeze temperature, T_f of CC6 was also considered. Phase transition temperatures for all six samples are presented in Figure 4.22. As

seen, at 1% SC6, an average T_m of 30.5°C was found. At this percentage, T_f was measured to be quite low; 25.7°C on average; a difference of 5.2°C. As SC6 is increased to 3 wt%, T_m falls to 29.2°C, with T_f rising to 28.1°C; a difference of only 1.1°C between the two.

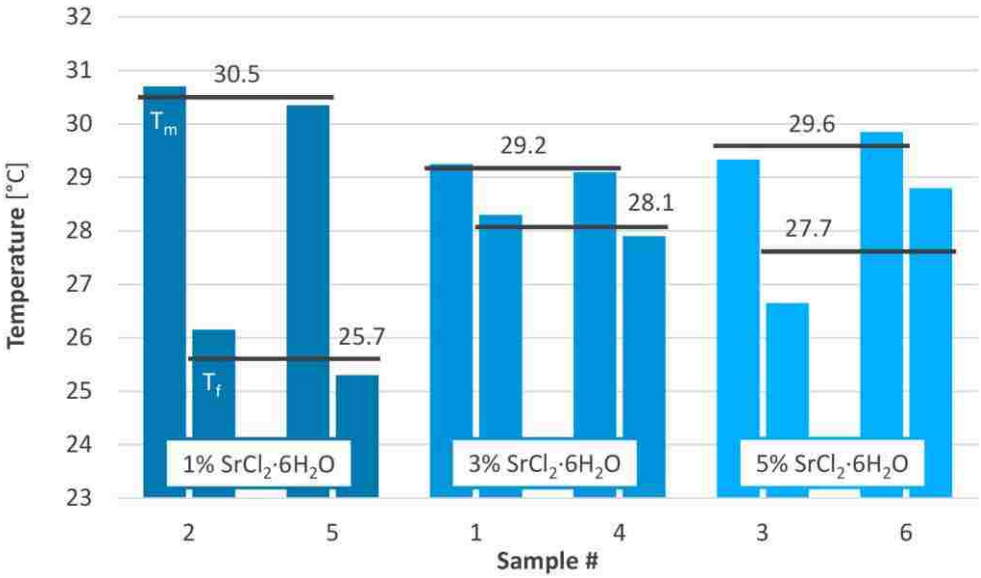

Figure 4.22: Difference in T_m and T_f with Respect to Percentage of $SrCl_2 \cdot 6H_2O$

Assarsson et al. reports that CC6 and SC6 are isomorphous and trigonal, with a unit cell of nearly identical dimensions [A10]. For concentrations greater than or equal to 3 wt% SC6, Assarsson et al. reports that at 29.5°C (the phase change temperature), $SrCl_2 \cdot 2H_2O$ (Strontium Chloride Dihydrate or SC2) is the stable solid phase within the CC6/SC6 mixture [A10]. This implies that 2/3 of the water in the added SC6 has been released into the CC6, slightly increasing its hydration level. For added SC6 concentrations less than 3 wt%, Assarsson et al. found that the solid phase at the phase change temperature was made of CC6/SC6 mixed crystals. As the concentration of SC6 increased, the crystals become progressively rich in $SrCl_2$ until a point was reached where SC6 no longer combined with CC6, but rather released water, making SC2 the dominant solid phase [A10]. Banjnóczy believed that SC2 is ineffective in the nucleation of CC6, which would

suggest that the SC6 concentration should be maintained below 3 wt% [B3]. Lane found that 0.1 wt% SC6 initially suppressed supercooling but lost its effectiveness after several cycles. 0.5 wt% SC6 eliminated supercooling for 10 cycles, while 1 wt% SC6 maintained supercooling suppression performance for more than 10 cycles [L5]. Given these results, Lane believed that SC6 must be near its saturation limit of 1.3 wt% in order for effective long-term nucleation [L7].

During the current research, the supercooling suppression of 1, 3, and 5 wt% SC6 in CC6 were tested over 1,500 rapid (~2 hr. cycle time) thermal cycles (Figure 4.23). Initially, supercooling results were identical between the three concentrations; with no measured supercooling. However, after repeated thermal cycling, substantial nucleation performance differences between the concentrations were encountered. However, after approximately 100 cycles, the 1 wt% SC6 samples began to experience significant supercooling. Additional cycling increased this supercooling, until by 1,000 cycles supercooling was virtually the same as for CC6 without SC6 (>20°C). At 3 and 5 wt% SC6, supercooling was found to remain negligible throughout all 1,500 cycles. These results agree with those by Lane suggesting that there is a minimum required concentration of SC6 to ensure long-term nucleation performance. This minimum concentration falls somewhere between 1 and 3 wt% SC6, agreeing well with Lane's suggestion that SC6 concentration should be close to 1.3 wt% to ensure good long-term nucleation performance [L7].

The excellent supercooling suppression of CC6 at greater than 3 wt% SC6, runs counter to the suggestion by Banjnóczy that SC2 (the dominant solid phase at these SC6 concentrations) is ineffective in the nucleation of CC6 [B3]. This suggests that even if SC6 releases water to form a solid phase of SC2, this solid SC2 will continue to reduce the supercooling of the CC6 – through epitaxy effects. The current work more closely agrees with Lane that a higher concentration of added SC6 promotes nucleation during repeated thermal cycles. That being said, since calorimetry results do show clear thermal advantages to limiting the concentration of SC6 (Figure

4.21) to 3 wt%, 3 wt% SC6 is suggested as the optimal concentration for effective long-term nucleation of CC6.

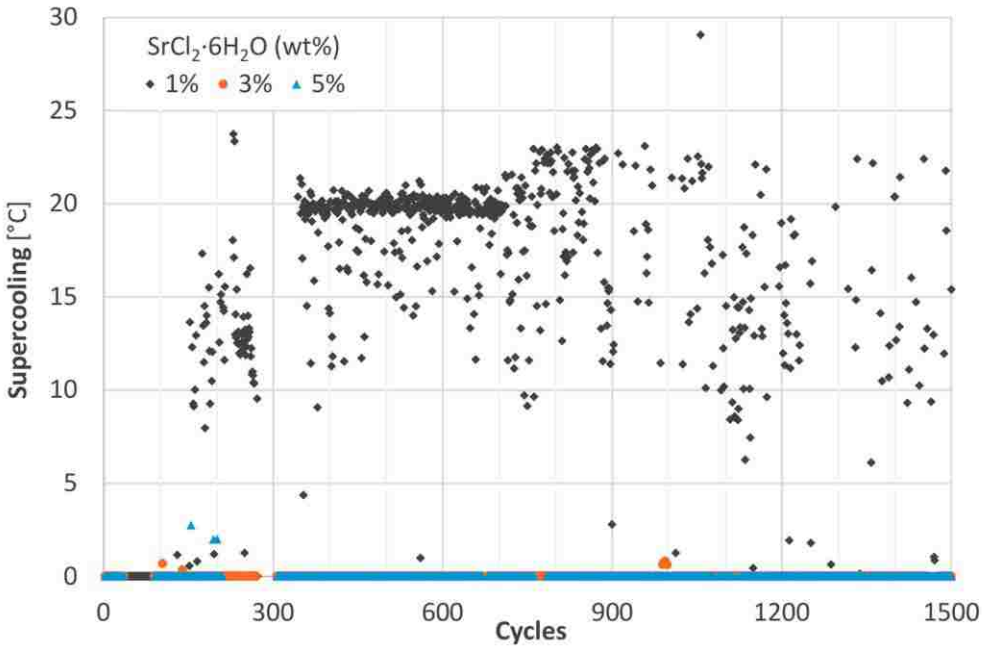

Figure 4.23: Supercooling of CC6 with Different SC6 Conc. During Long-Term Cycling

There are two potential methods by which SC6 nucleates CC6. As mentioned above, the first method is through a similar (isomorphous) crystal structure between CC6 and SC6. The second is through epitaxy, which is a fancy way of saying that a solid surface within the CC6 provides a surface on which crystalline CC6 begins to grow. In the epitaxy case, the solid surface would be solid crystals of either SC6 or SC2. Epitaxy-based nucleation of CC6 by SC6 is suggested through the good nucleation results for SC6 at concentrations greater than 3%, where SC2 is the dominant solid form. At low SC6 concentrations or low cycle numbers, added SC6 has not released water to form SC2, suggesting that isomorphous nucleation dominates in this region. This dual nature of SC6 nucleation of CC6 is further supported through imaging of the initial crystal formation of several similar samples (Figure 4.24). The images in Figure 4.24 were taken using the GoPro

water bath setup described in Section 3.4.2. For four of the samples (A, B, D, and F), it appears that initial nucleation begins on the solid $SrCl_2$ hydrate at the bottom of the bottle. This was expected and hints at epitaxy-based nucleation of the CC6. However, for samples C and E, initial crystal formation appears to begin at a point approximately ¾ of the way up the wall of the bottle. Given that the density of both SC6 and SC2 (1.930 g/cm^3 and 2.672 g/cm^3 respectively) are much greater than the density of liquid CC6 (1.5 g/cm^3), it is not believed that a solid crystal of SC hydrate is located ¾ of the way up the height of the bottle. However, given the structural similarities between CC6 and SC6, the potential for isomorphic nucleation exists. These results strengthen the finding that SC6 suppresses supercooling in CC6 through both isomorphic nucleation and epitaxy.

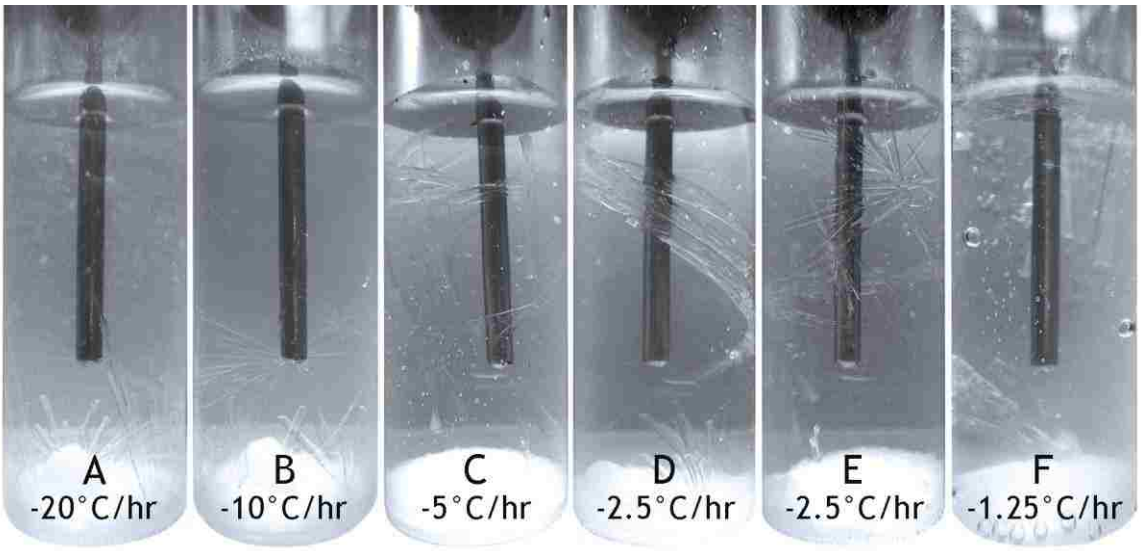

Figure 4.24: Initial Crystallization of CC6+SC6 at Different Cooling Rates

As can be seen in Figure 4.24, the CC6+SC6 samples frozen at varying cooling rates were instrumented with RTDs for PCM temperature measurement. Figure 4.25 presents temperature traces for each of these cooling rates. The key finding of this comparison is that measured supercooling is directly proportional to the cooling rate. This result is not unexpected as it is

known, for instance, that the high cooling rate of the DSC results in a large overprediction of supercooling.

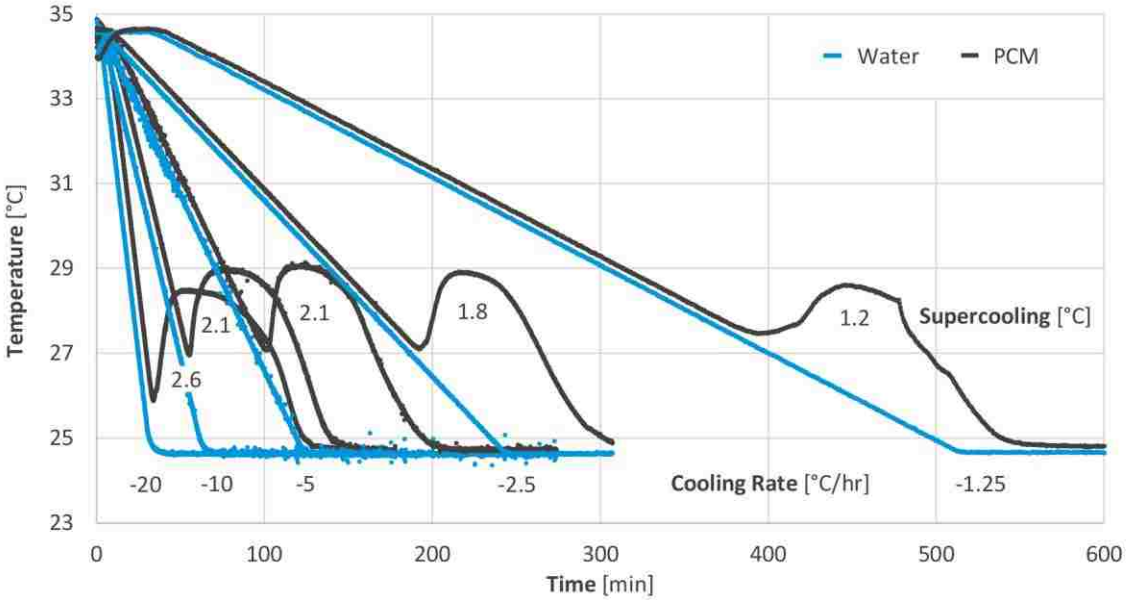

Figure 4.25: Supercooling of CC6 + 3 wt% SC6 at Different Cooling Rates

4.6.3 $CaCl_2 \cdot 6H_2O$ Thermal Cycling

Six identical, ~200 g samples of CC6 + 3 wt% SC6 were prepared for long-term cycling (Table 4.20). As was the case for the CC6+MC6 and CC6+KN PCMs, these samples were cycled for up to 2,700 complete cycles, being removed at intervals of approximately 500 cycles for drop calorimetry. Each cycle consisted of a 75-minute cooling period from 45 to 5°C immediately followed by a similar length heating period back to 45°C. Total cycle time is 150 minutes. Drop calorimetry H_f results for the six samples during 2,700 complete cycles are presented in Figure 4.26 with tabular values of H_f before and after cycling presented in Table 4.21.

Drop calorimetry measured an average H_f at 0 cycles of 172.6 J/g. As the cycle number increased, average H_f was found to slowly decrease. While there is considerable scatter in the data in Figure 4.26, most of the data falls within approximately ±13 J/g of the average (represented by the dashed lines). By the conclusion of cycling at 2,700 cycles, an average H_f of 166.0 J/g was measured; a decrease of 3.8%. This decrease in thermal performance indicates the presence of phase separation of the CC6. A complete discussion of the phase separation of CC6 will be presented in Chapter 5.

Table 4.20: CC6 Samples for Thermal Cycle Testing

Sample #	m_{ENC} [g]	m_{PCM} [g]	$CaCl_2 \cdot 6H_2O$ [wt%]	$SrCl_2 \cdot 6H_2O$ [wt%]
1	330.5	188.5	96.8	3.2
4	333.6	185.5	96.7	3.3
7	316.8	194.7	97.0	3.0
8	328.5	197.8	97.0	3.0
9	320.7	204.0	97.0	3.0
20	331.5	188.4	97.0	3.0

Table 4.21: H_f Measured by Calorimetry Before and After 2,700 Cycles of CC6

Sample #	H_f [J/g] (0 Cycles)	H_f [J/g] (2,700 Cycles)
1	173.1	158.0
4	171.8	170.9
7	173.6	163.9
8	174.0	162.3
9	168.4	166.2
20	174.7	174.8
AVG	172.6	166.0

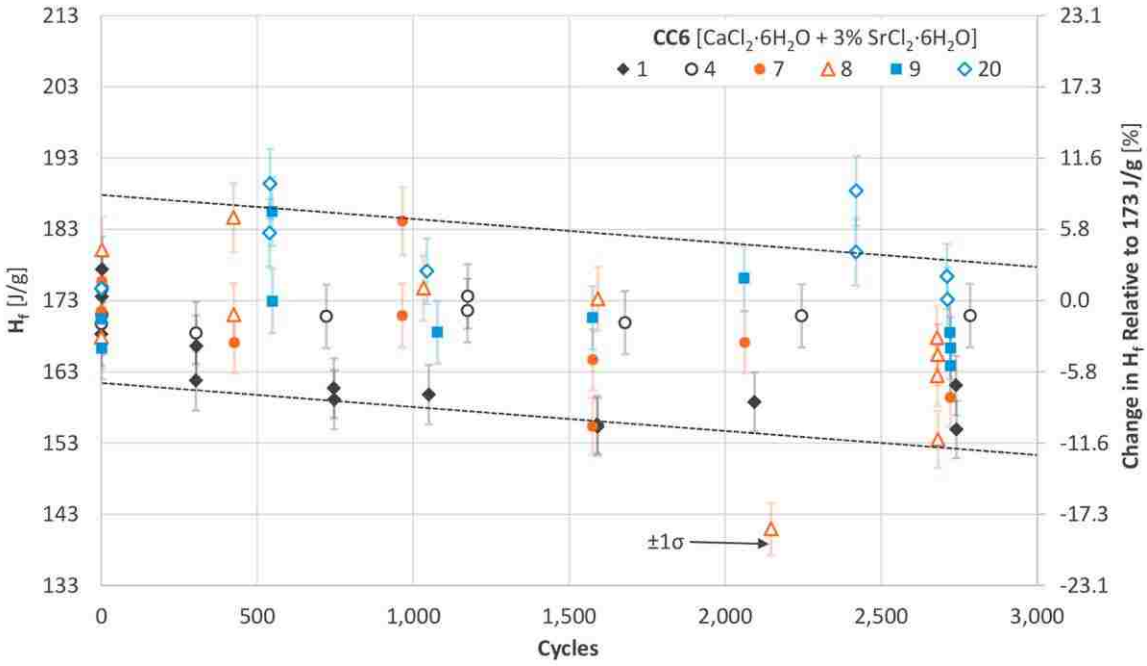

Figure 4.26: H_f During Long Term Cycling of CC6

4.7 Summary of Hydrated-Salt Characterization

The hydrated-salt PCMs presented in Table 2.8 were characterized in Chapter 4. One of the tested salts, $NaOH{\cdot}3.5H_2O$ was quickly eliminated from further testing due to its high reaction potential with the aluminum DSC test pans. Although $KF{\cdot}4H_2O$ performed well during initial DSC testing, it was eliminated from further testing due to health and safety concerns. When $Na_2SO_4{\cdot}10H_2O$ was characterized by DSC, it quickly became apparent that this salt experienced very high degrees of separation, which would prove challenging to its long-term use. In addition, its melting temperature was slightly above that desired for the ACC cooling application presented in Section 1.1.

Three $CaCl_2{\cdot}6H_2O$-based hydrated salts performed well during the initial DSC characterization and were selected for further testing: $CaCl_2{\cdot}6H_2O$, $CaCl_2{\cdot}6H_2O$ + 18% $MgCl_2{\cdot}6H_2O$ and $CaCl_2{\cdot}6H_2O$

+ 7% KNO_3. $SrCl_2 \cdot 6H_2O$ was found to reduce supercooling in all three of these PCMs to around 2°C or less. While lesser quantities of SC6 (~1 wt%) were found to initially reduce supercooling of CC6, after 100 thermal cycles the nucleation effectiveness of this additive was virtually non-existent. In order to ensure good supercooling performance after thousands of cycles, at least 3 wt% SC6 should be used. After rapid thermal cycling to 2,700 cycles, CC6 experienced on average a 3.8% decrease in H_f, while the remaining two PCMs (CC6+18% MC6 and CC6+7% KN) had a flat H_f response over a similar cycling period. These cycling results indicate that CC6 experiences phase segregation (or separation) during repeated cycling, while the CC6+MC6 and CC6+KN mixtures do not. This phase separation of CC6 during cycling will be addressed in Chapter 5.

5 Phase Stability of $CaCl_2 \cdot 6H_2O$

The foremost concern with prolonged use of $CaCl_2 \cdot 6H_2O$ is the issue of irreversible phase separation during repeated freeze-thaw cycles. As CC6 freezes it tends to form calcium chloride tetrahydrate ($CaCl_2 \cdot 4H_2O$ or CC4) in a process known as semi incongruent freezing, or "separation" for short. To help illustrate the mechanism behind separation, the binary phase diagram for the $CaCl_2$(CC)/H_2O system is presented in Figure 5.1. As liquid CC6 cools, it does not cross the liquidous curve at the point where the CC4 and CC6 curves intersect (the peritectic point). Rather, the liquidous curve is initially crossed at a point above the peritectic point—a point on the CC4 liquidous curve. Because of this, a portion of the liquid CC6 crystallizes as CC4, with the remaining, now water-rich CC6 (CC6+) remaining in the liquid state. There are three potential crystalline forms of CC4, which can form in this region, the α, β, and γ forms. Upon crossing the CC4 liquidous curve, the α CC4 phase is the most stable of the three in the relevant temperature range between 32.8 and 29.5°C [L8]. As the PCM is cooled further to the peritectic temperature, the CC6+ solution crosses the liquidous curve and solidifies. Ideally, as the CC6+ freezes, it will form a homogenous CC6 solid with the excess water in solution recombining with the crystallized CC4 to form CC6. If a homogenous, solid CC6 forms, incongruent freezing did not occur. Unfortunately, there are two factors that prevent this reversibility. First, there is a considerable density difference between solid CC4 and liquid CC6; 2.10 g/cm^3 [L8] and 1.83 g/cm^3 [N1], respectively. When CC4 freezes before CC6, the solid CC4 sinks to the bottom of the liquid CC6+, physically separating it from its liberated water. Because of this, when CC6 finally freezes at the peritectic temperature, the CC4 is physically separated from the previously liberated water, preventing it from being reconstituted into a homogeneous, crystalline CC6. The second factor preventing reversibility after the formation of CC4 is the high energy barrier which must be overcome in order for the liquid water to penetrate into and combine with the

crystalline CC4. If the CC4 were molten, this energy barrier would be reduced due to the lower bond energies at the atomic and molecular levels.

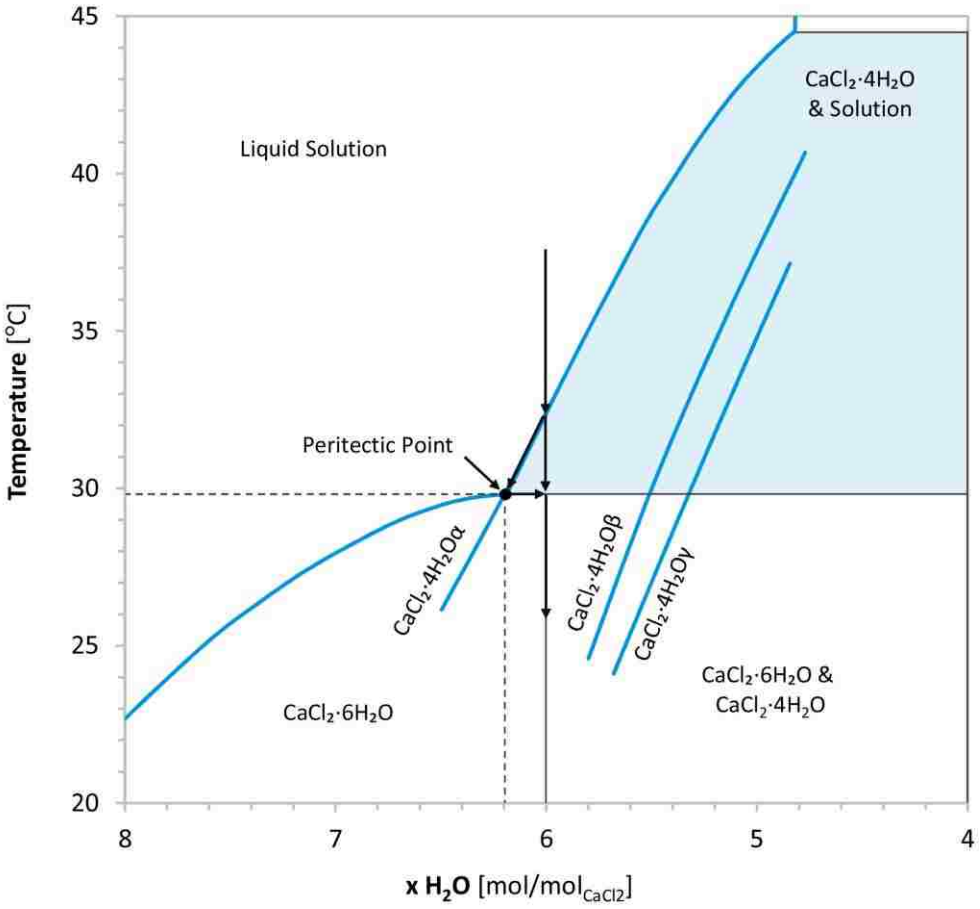

Figure 5.1: Phase Diagram of Binary $CaCl_2/H_2O$ System Near the Peritectic Point [L8]

At temperatures slightly below the freezing temperature of CC6, separation results in a stratified PCM with solid CC4 at the bottom, solid CC6 in the middle and a liquid $CaCl_2/H_2O$ solution on the top. If heating or cooling of the PCM happens quickly, the temperature range during which CC4 formation is favored is passed through more quickly, resulting in less separation. Lane has suggested that supercooling of the CC4 can also prevent separation. If the CC4 supercools, while the CC6 does not, freezing of the CC4 is delayed, reducing the time spent in the critical

temperature region where CC4 formation is favored [L8]. Alternatively, if the CC6 supercools, while CC4 does not, separation tends to increase. This section examines the methods for characterizing CC6 separation as well as solutions for preventing it.

The literature differs slightly on the true peritectic point of $CaCl_2 \cdot 6H_2O$. Brandstetter cites Mellor and Lane, who give peritectic compositions of 50.25 and 49.62 wt% $CaCl_2$ (xH_2O = 6.10 and 6.25), respectively; with corresponding temperatures of 29.8°C and 29.6°C [B19]. Despite the differences in peritectic condition, the literature consistently reports that the CC/H_2O peritectic point occurs when xH_2O is in slight excess of 6, which can be seen in Figure 5.1.

A saturated CC solution (supernatant fluid) forms on the top of frozen CC6 when CC4 forms during freezing. Saturation concentrations of CC in this supernatant fluid were presented by Brandstetter and are seen in Table 5.1. At the freezing temperature of the hexahydrate (~29.5°C), Table 5.1 suggests that the degree of hydration (xH_2O) in the supernatant liquid is close to that of the hexahydrate (6). As the temperature falls, the percentage of water in solution increases, implying that the water percentage in the solid decreased below the hexahydrate concentration [B19]. As previously discussed, this decrease in H_2O in the crystallized PCM is due to the formation of a percentage of solid CC4. The values in Table 5.1 assume that the solid hexahydrate and supernatant liquid are in equilibrium at each temperature.

Several CC6 samples were prepared and frozen with their supernatant fluid being removed and tested by TGA and DSC to find xH_2O. The frozen PCM temperature was in the range of 20-25°C. The TGA was directly used to find xH_2O of the samples by measuring the PCM mass loss as the samples were heated to 400°C. As discussed in Section 3.5, expulsion of PCM from the TGA pan makes its moisture loss results unreliable. To get around this issue, DSC test results were used to infer the moisture of the samples through the following procedure. First, the peak

temperature of the melting curve was obtained via DSC. This peak temperature was used as the input to a curve fit of the liquid/solid phase transition curve of the CC/H_2O phase diagram (Figure 5.1). Since water content in excess of the hexahydrate was expected, the curve fit was constructed using only the liquidous line to the left of the peritectic point (the CC6 curve) in Figure 5.1. The TGA and DSC-based results for xH_2O in the supernatant liquid at a temperature between 20 and 25°C are presented in Table 5.2.

Table 5.1: Saturation Values of $CaCl_2$ in Supernatant Liquid [B19]

Temperature [°C]	$CaCl_2$ [wt%]	xH_2O [mol/mol_{CaCl2}]
0	37.3	10.35
5	38.3	9.94
10	39.4	9.48
15	40.8	8.93
20	42.7	8.27
25	45.4	7.42
28	48.2	6.62
30	50.5	6.04

Table 5.2: xH_2O of Supernatant Liquid at 20-25°C Found Using TGA and DSC

Sample #	xH_2O (TGA) [mol/mol_{CaCl2}]	xH_2O (Calculated Using DSC) [mol/mol_{CaCl2}]
14	7.54	7.82
15		8.34
17	8.12	7.74
Average	7.91	

The results in Table 5.2 not only show good agreement between the TGA and DSC-calculated results, but also agree well with the saturated liquid results presented by Brandstetter in Table 5.1.

5.1 Speciation of CC6 Due to Phase Separation

The separation of CC6 with CC4 formation is illustrated in Figure 5.2. Three phases at a temperature slightly below the CC6 freezing temperature are illustrated; a supernatant liquid layer on top of an intermediate layer of solid CC6, with a layer of solid CC4 on the bottom. For the following analysis, it is assumed that only CC6 can separate to form CC4 and supernatant liquid. In other words, any CC4 or supernatant liquid initially available in the PCM will act as an inert compound during these analyses. It was also assumed that added SC6 does not impact the CC and H_2O balance. This may not always be a valid assumption as SC6 added to CC6 is known to release H_2O, forming $SrCl_2 \cdot 2H_2O$. Additional experimental information is required to determine to what extent the addition of SC6 to CC6 impacts the overall water balance of the system. In order to conduct a mass balance of this system, the total available mass of $CaCl_2$ (m_{CC}) and H_2O (m_w) in the CC6 are each divided into three variables for the three layers. These six mass variables are illustrated on the righthand side of Figure 5.2.

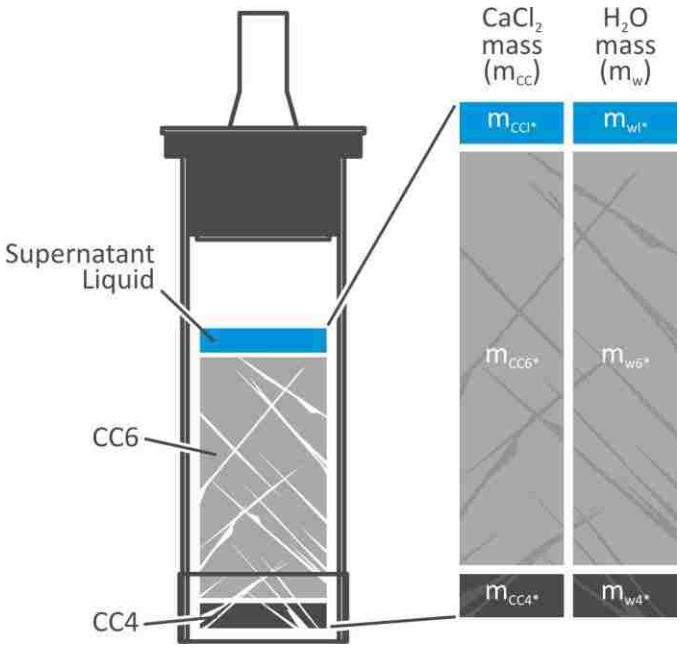

Figure 5.2: Speciation of CC6 After Separation During Freezing

Equations (24) and (25) are the governing mass balance equations for the three layer, CC/H_2O system presented in Figure 5.2.

$$m_{CC} = m_{CCl^*} + m_{CC6^*} + m_{CC4^*} \tag{24}$$

$$m_w = m_{wl^*} + m_{w6^*} + m_{w4^*} \tag{25}$$

In order to solve Equations (24) and (25), the mass fraction of $CaCl_2$ (w_{CC}) in of any of the three layers (denoted by subscript j*) is first defined using Equation (26).

$$w_{CCj^*} = \frac{m_{CCj^*}}{m_{CCj^*} + m_{wj^*}} \tag{26}$$

Where m_{CCj^*} is the mass of CC and m_{wj^*} is the mass of water. Equation (26) can be re-written in terms of the moles of CC (n_{CCj^*}) and moles of water (n_{wj^*}) in the layer j*.

$$w_{CCj^*} = \frac{n_{CCj^*}M_{CC}}{n_{CCj^*}M_{CC} + n_{wj^*}M_w} \tag{27}$$

Where M_{CC} is the molar mass of CC (110.978 g/mol) and M_w is the molar mass of water (18.015 g/mol). Letting $n_{CCj^*} = 1$, Equation (27) can be normalized to the moles of CC:

$$w_{CCj^*} = \frac{110.978\ \frac{g}{mol}}{110.978\ \frac{g}{mol} + n_{wj^*} \cdot 18.015\ \frac{g}{mol}} = \frac{6.1603}{6.1603 + n_{wj^*}} \tag{28}$$

Combining Equations (26) and (28), the mass fraction of CC can be eliminated, leaving Equation (29).

$$\frac{m_{CCj^*}}{m_{CCj^*} + m_{wj^*}} = \frac{6.1603}{6.1603 + n_{wj^*}} \tag{29}$$

After further simplification, the general equation relating m_w, m_{CC} and n_w for any layer, j*, of the PCM is found:

$$m_{wj^*}\frac{6.1603}{n_{wj^*}} = m_{CCj^*} \tag{30}$$

Equation (30) applies to the supernatant liquid region (subscript l*), the hexahydrate region (subscript 6*), and the tetrahydrate region (subscript 4*). Knowing this, Equation (30) for the hexahydrate and tetrahydrate regions can be substituted into Equation (24). Note that n_{w6^*} and n_{w4^*} are equal to 6 and 4, respectively.

$$m_{CC} - m_{CCl^*} = m_{w6^*}\frac{6.1603}{n_{w6^*}} + m_{w4^*}\frac{6.1603}{n_{w4^*}} = m_{w6^*}\frac{6.1603}{6} + m_{w4^*}\frac{6.1603}{4} \quad (31)$$

If Equation (25) is multiplied by -6.1603/6 and added to Equation (31), the mass of water in the hexahydrate (m_{w6^*}) is eliminated, allowing the mass of water in the tetrahydrate (m_{w4^*}) to be easily solved for. This summation is presented in matrix form in Equation (32) and it can be reduced to Equation (33):

$$\begin{bmatrix} \frac{6.1603}{6} & \frac{6.1603}{4} \\ -\frac{6.1603}{6} & -\frac{6.1603}{6} \end{bmatrix} \begin{bmatrix} m_{w6^*} \\ m_{w4^*} \end{bmatrix} = \begin{bmatrix} m_{CC} - m_{CCl^*} \\ -\frac{6.1603}{6}(m_w - m_{wl^*}) \end{bmatrix} \quad (32)$$

$$m_{CC} - m_{CCl^*} - \frac{6.1603}{6}(m_w - m_{wl^*}) = \frac{6.1603}{12}m_{w4^*} \quad (33)$$

Rearranging Equation (33), the mass of water in the tetrahydrate can be solved for if the mass of water (m_{wl}) and CC (m_{CCl}) in the supernatant liquid are known. Note that it is assumed that the original mass of water (m_w) and CC (m_{CC}) in the PCM are known.

$$m_{w4^*} = \frac{12}{6.1603}(m_{CC} - m_{CCl^*}) - 2(m_w - m_{wl^*}) \quad (34)$$

Plugging Equation (30) for the tetrahydrate into Equation (34), m_{CC4^*} can be solved for:

$$m_{CC4^*} = 3(m_{CC} - m_{CCl^*}) - \frac{6.1603}{2}(m_w - m_{wl^*}) \quad (35)$$

By substituting Equations (34) and (35) into Equations (24) and (25), similar equations for the mass of CC and water in the hexahydrate can be found:

$$m_{CC6^*} = -2(m_{CC} - m_{CCl^*}) + \frac{6.1603}{2}(m_w - m_{wl^*}) \quad (36)$$

$$m_{w6^*} = -\frac{12}{6.1603}(m_{CC} - m_{CCl^*}) + 3(m_w - m_{wl^*}) \quad (37)$$

For all of these equations, m_{CC} and m_w are calculated by multiplying the original CC6 mass (m) by the mass fraction of CC and H_2O originally in the CC6; w_{CC} and w_w respectively:

$$m_{CC} = w_{CC}m = \frac{6.1603}{6.1603 + n_w}m = (\text{for } n_w = 6) = 0.5066\ m \quad (38)$$

$$m_w = w_w m = \left(1 - \frac{6.1603}{6.1603 + n_w}\right)m = (\text{for } n_w = 6) = 0.4934\ m \quad (39)$$

5.2 Measuring Speciation of CC6 During Slow Cycling

Equations (34) through (39) were used to characterize the separation of CC6 during slow (1°C/hr) cycling in the programable water bath. Four identical, CC6 samples were prepared with 3 wt% SC6 added for supercooling suppression. These samples were labeled as 5S, 6S, 7S and 9S, with their compositions presented in Figure 5.3. Cycling was conducted between 35 and 25°C with a temperature ramp rate of 1°C/hr. and 2 hr. temperature holds at both the hot and cold temperatures. After 10, 25, and 40 cycles, any supernatant liquid formed on top of the frozen PCM was removed and weighed before the sample was returned to the bath for additional cycling. During this process, each time the sample was returned to the bath, the total mass of PCM was reduced by the mass of supernatant liquid, which had been removed and weighed.

Table 5.3: CC6 Samples for Slow Cycle Testing

Sample	m_{ENC} [g]	m_{PCM} [g]	$CaCl_2 \cdot 6H_2O$ [wt%]	$SrCl_2 \cdot 6H_2O$ [wt%]
5S	152.6	81.1	97.0	3.0
6S	148.3	83.5	97.0	3.0
7S	149.2	82.3	97.1	2.9
9S	153.8	76.8	97.0	3.0

After the first 10 cycles, all four samples were removed from the bath at 25°C and any supernatant liquid was dumped off and weighed. Table 5.1 was used to find the moles of water in this supernatant liquid at 25°C. To solve for m_{wl*} and m_{CCl*} using the total mass of liquid (m_l), the following relation was utilized:

$$m_l = m_{CCl*} + m_{wl*} \tag{40}$$

After dividing by m_{wl*}, Equation (40) can be rearranged with the masses of CC and water being substituted with their molar values times their molar masses:

$$\frac{m_l}{m_{wl*}} = \frac{m_{CCl*}}{m_{wl*}} + 1 = \frac{m_{CCl*} + m_{wl*}}{m_{wl*}} = \frac{n_{CCl*}M_{CC} + n_{wl*}M_w}{n_{wl*}M_w} \tag{41}$$

Letting $n_{CCl*} = 1$ with $M_{CC} = 110.978$ g/mol and $M_w = 18.015$ g/mol, Equation (41) reduces to the following for m_{wl*}:

$$m_{wl*} = \frac{n_{wl*}}{6.1603 + n_{wl*}} m_l \tag{42}$$

With m_{wl*} known, m_{CCl*} can be easily found through plugging Equation (42) into Equation (40) and solving for m_{CCl*}:

$$m_{CCl^*} = \left(1 - \frac{n_{wl^*}}{6.1603 + n_{wl^*}}\right) m_l = \frac{6.1603}{6.1603 + n_{wl^*}} m_l \quad (43)$$

Equations (42) and (43) were initially used to find m_{wl^*} and m_{CCl^*} for all four cycled samples. With the CC and water concentrations for the supernatant liquid found, Equations (34) through (37) could be used to find the concentrations of the remaining two separated PCM layers. After removing the supernatant liquid at 10 cycles, the four samples were returned to the water bath and cycled to 25 complete cycles. At 25 cycles, any supernatant liquid was removed and weighed with the speciation calculations being repeated. For these calculations, the initial mass of CC6 used (m) was that of the CC6 remaining after the initial speciation at 10 cycles. The liquid removed at 25 cycles was used to calculate the quantity of CC4, which was generated between cycles 10 and 25. This new CC4 was added to the CC4, which existed after 10 cycles to arrive at the total quantity of CC4 after 25 cycles. Similar calculations were conducted after the samples were removed from cycling at 40 cycles. Speciation results for all four samples at all cycle times are presented in Table 5.4. These results are plotted in Figure 5.3, allowing for easy visualization of CC6 speciation during cycling.

Figure 5.3 and Table 5.4 show that after 10 cycles, only a small percentage of CC6 has separated into CC4 and supernatant liquid (~1 to 2.4 wt% CC4). After 25 cycles, around 17.5% CC4 has formed in the 6S and 7S samples, while it has not significantly increased for the remaining two samples. After 40 cycles, all four samples are calculated to have CC4 levels in excess 16.6 wt%. This corresponds to around a 48-59 wt% decrease in CC6. Such a large decrease in CC6 will have a significant negative impact on the latent heat storage potential of the PCM.

Table 5.4: Speciation Results for Slow Cycling of CC6

Cycles	Sample	Liq. [g]	CC6 [g]	CC4 [g]
0	5S	0	81.10	0
	6S	0	83.50	0
	7S	0	82.30	0
	9S	0	76.80	0
10	5S	1.98	78.06	1.06
	6S	3.06	78.80	1.63
	7S	3.69	76.64	1.97
	9S	1.66	74.26	0.89
25	5S	0.67	77.11	1.42
	6S	24.08	41.69	14.43
	7S	23.63	40.44	14.53
	9S	0.50	73.45	1.16
40	5S	24.23	39.86	14.30
	6S	4.90	34.26	17.04
	7S	4.34	33.82	16.84
	9S	21.85	39.98	12.77

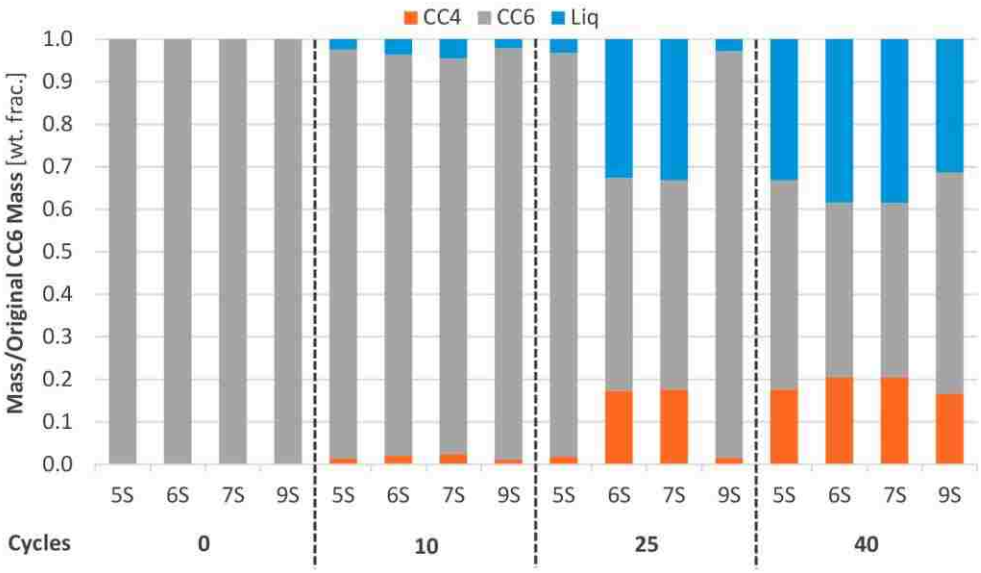

Figure 5.3: Speciation of CC6 During Slow Cycling

5.3 Thermal Cycling and Calorimetry of $CaCl_2 \cdot 6H_2O$

As outlined in Section 4.6.3, six ~200 g CC6 samples were cycled 2,700 times between 5 and 45°C. A complete cycle consisted of 75 minutes of cooling, followed immediately by 75 minutes of heating. Since the automated cycling system was designed for rapid cycling, the temperature of the water surrounding the samples was changed to the opposite extreme within several minutes at the end of each half-cycle. As shown in Figure 4.26, after 2,700 cycles, H_f was found to have decreased by only 3.8% on average. However, there are two factors, which are believed to be positively biasing these results in favor of less separation, the fast cycling rate and a melting temperature above the melting temperature of the tetrahydrate (~45°C).

5.3.1 Impact of Cycling Rate on Separation

The CC/H_2O phase diagram (Figure 5.1) suggests that any cooling CC6, which crosses the liquidous line at a $CaCl_2$ concentration to the right of the peritectic point, will experience separation. However, the phase diagram is based on equilibrium conditions between the given phases, while the separation of CC6 is in practice a reaction kinetics-limited process. Because of this, the time spent in the critical temperature region between 32.8 and 29.5°C limits the separation of CC6. In other words, if the CC6 moves through the critical temperature region more slowly (a slower cooling rate), there is more time during which CC4 can precipitate from the liquid CC6. Likewise, faster cooling rates reduce separation by minimizing the time during which CC4 can precipitate before CC6 does. Several authors, such as Lorsch et al. [L18], and Brandstetter [B19] have qualitatively commented on this phenomenon, but the impact of cooling rate on separation has not been quantitatively documented.

As shown in Section 5.2, the quantity of supernatant liquid formed above solidified CC6 directly correlates to the quantity of precipitated CC4. Therefore, by weighing the mass of supernatant

liquid after freezing, the separation of CC6 can be quantitatively measured. In order to test the impact of cycling rate on separation, freezing tests of CC6 + 3 w% SC6 were conducted at varying cooling rates using the programable water bath. SC6 was added to all samples to minimize supercooling of the CC6. For all tests, freezing began at 35°C and concluded at 25°C after a linear temperature ramp over the specified time period. The degree of separation was measured by weighing the mass of supernatant liquid on top of the frozen (at 25°C) CC6 after a single cycle. Results from this testing are presented in Figure 5.4.

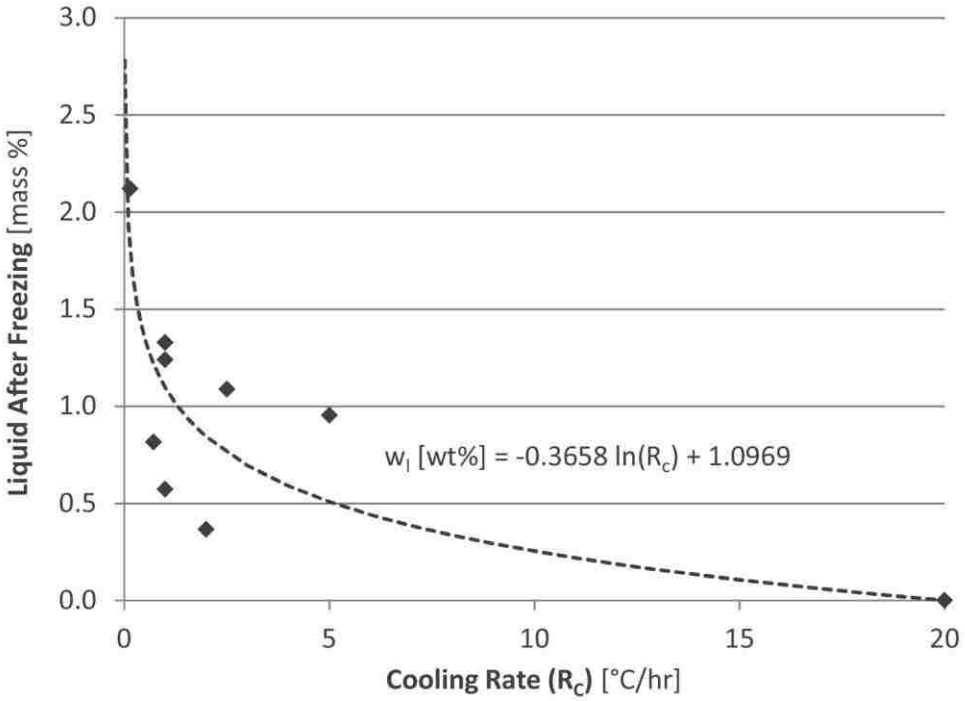

Figure 5.4: Supernatant Liquid Per Freeze vs. CC6 Freeze Rate

As expected, Figure 5.4 shows a decreasing trend in measured supernatant liquid with increasing cooling rate. The considerable scatter in the data is likely due to small differences in hydration between the samples. Despite this variability, these results can be used as a guide to predict the approximate separation of CC6 under varying cooling rates.

In order to correlate the supernatant liquid fraction in Figure 5.4 to the weight fraction of CC6 remaining in the PCM, the total weight fraction of CC6 (w_{CC6}) was defined as:

$$w_{CC6} = \frac{m_{CC6}}{m} = \frac{m_{CC6^*} + m_{w6^*}}{m} \tag{44}$$

Combining Equations (36) and (37) with Equation (44), Equation (45) results:

$$\frac{m_{CC6}}{m} = \frac{-2(m_{CC} - m_{CCl^*}) + \frac{6.1603}{2}(m_w - m_{wl^*}) - \frac{12}{6.1603}(m_{CC} - m_{CCl^*}) + 3(m_w - m_{wl^*})}{m} \tag{45}$$

Like terms can be combined, and m_{wl^*} and m_{CCl^*} are replaced with Equations (42) and (43) respectively:

$$\frac{m_{CC6}}{m} = \frac{-3.9480\left(m_{CC} - \frac{6.1603}{6.1603 + n_{wl^*}} m_l\right) + 6.0802\left(m_w - \frac{n_{wl^*}}{6.1603 + n_{wl^*}} m_l\right)}{m} \tag{46}$$

Equations (38) and (39) can be substituted into Equation (46) in order to get m_{CC} and m_w in terms of m:

$$\frac{m_{CC6}}{m} = \frac{-3.9480\left(w_{CC}m - \frac{6.1603}{6.1603 + n_{wl^*}} m_l\right) + 6.0802\left(w_w m - \frac{n_{wl^*}}{6.1603 + n_{wl^*}} m_l\right)}{m} \tag{47}$$

Equation (47) can be further reduced:

$$\frac{m_{CC6}}{m} = -3.9480\, w_{CC} + 6.0802\, w_w + 6.0802\left(\frac{4 - n_{wl^*}}{6.1603 + n_{wl^*}}\right) w_l \tag{48}$$

Where w_l is the mass fraction of supernatant liquid; or $m_l = w_l m$. Combining Equation (48) with the logarithmic curve fit in Figure 5.4, the following equation is found for the weight percentage of CC6 after cycling:

$$\frac{m_{CC6}}{m} = -3.9480\, w_{CC} + 6.0802\, w_w + 6.0802 \left(\frac{4 - n_{wl^*}}{6.1603 + n_{wl^*}} \right) (-0.3658 \ln(R_C) + 1.0969) \quad (49)$$

For CC6, Equations (38) and (39), show that w_{CC} and w_w are equal to 0.5066 and 0.4934 respectively. Substituting these values into Equation (49), the weight fraction of CC6 after cycling can be further simplified:

$$\frac{m_{CC6}}{m} = 1 + 6.0802 \left(\frac{4 - n_{wl^*}}{6.1603 + n_{wl^*}} \right) (-0.3658 \ln(R_C) + 1.0969) \quad (50)$$

Using Equation (50), the weight fraction of CC6 after a single cycle was estimated across the range of cooling rates between 0 and 20°C/hr (Figure 5.5). The secondary axis of Figure 5.5 presents the change in H_f expected if a linear inverse relationship between the CC6 mass fraction and ΔH_f is assumed. This is a reasonable assumption as only the CC6 in the PCM undergoes a phase transition at the CC6 melting temperature.

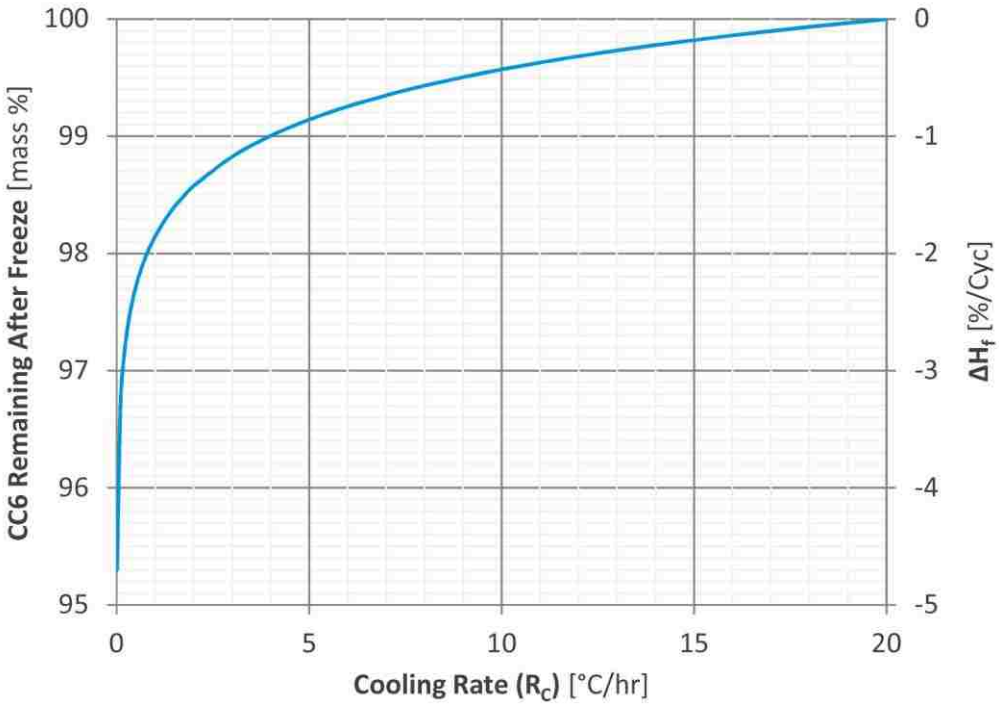

Figure 5.5: CC6 and Calculated H_f After Single Freezing vs. Cooling Rate

Figure 5.5 clearly shows that for CC6 cooling rates of less than 4°C/hr, greater than a 1% reduction in H_f can be expected per cycle. As the cooling rate approaches 0°C/hr, ΔH_f approaches -5%/cycle. It's important to note that even a small change in ΔH_f with cycling is problematic if a PCM is to be used for thousands of cycles. Figure 5.5 appears to show much better PCM stability at cooling rates approaching 20°C/hr. This Figure is not intended to be used as an exact predictor of long-term PCM stability. Rather, it is hoped that Figure 5.5 can be used as a guide in developing appropriate long-term PCM test regimes. For instance, these results clearly show that accelerated PCM cycling will under-predict actual PCM separation. Additional research should be conducted to determine how rapid cycling can be adjusted to compensate for these differences in separation with cycling speed.

5.3.2 Slow Cycling

Given the impact of cooling rate on separation, the thermal performance of CC6 during slow cycling was tested for comparison to the rapid cycling (2,700 cycle) thermal results. Four identical, ~80 g samples of CC6 + 3 wt% SC6 were prepared in stainless steel containers, which were shortened versions of the ~200 g sample cylinders presented in Figure 3.9. The compositions of these four samples are presented in Table 5.5. All samples were fitted with three-wire RTDs for temperature measurement during cycling and drop calorimeter.

Table 5.5: CC6 Samples for Slow Cycle Testing

Sample	m_{ENC} [g]	m_{PCM} [g]	$CaCl_2 \cdot 6H_2O$ [wt%]	$SrCl_2 \cdot 6H_2O$ [wt%]
8S	243.8	75.5	97.1	2.9
13S	239.0	76.2	97.0	3.0
14S	240.3	91.4	96.9	3.1
16S	240.6	88.1	96.9	3.1

Conditions for slow cycling were 24 hour cycles between 25 and 35°C with 1°C/hr. linear temperature ramps and 2 hr. holds at both the cold and hot temperatures. Samples were removed after 10 and 25 cycles for drop calorimetry, with calorimeter H_f results presented in Figure 5.6.

Figure 5.6 shows that after 10 cycles all four samples experienced a negligible change in H_f. At 25 cycles, two of the samples (13S and 16S) showed around a 35% decrease in H_f, indicating that a critical cycle number was reached somewhere between 10 and 25 cycles. Interestingly, two of the samples (8S and 14S) continued to show a negligible change in H_f at 25 cycles.

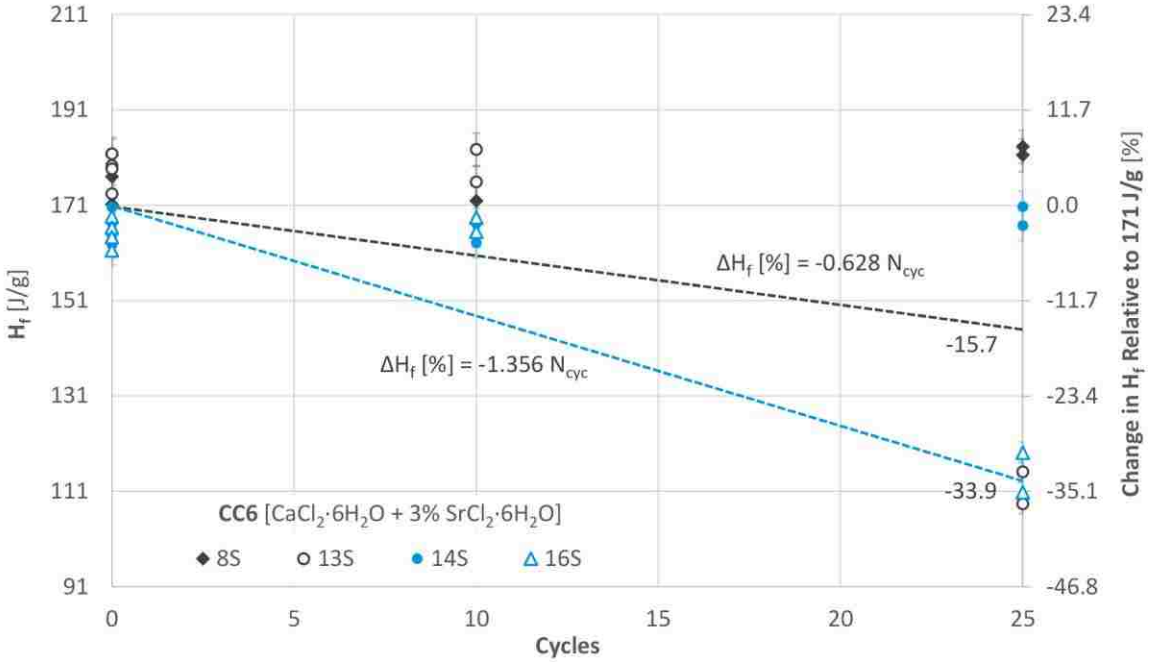

Figure 5.6: H_f of CC6 During Slow Cycling to 25 Cycles

Considering the four slow cycling samples together, it was found that after 25 cycles, ΔH_f decreased on average by 15.7%. Drawing a line between an ΔH_f of 0% at 0 cycles and this average value, a potential linear relationship between ΔH_f and the number of cycles (N_{cyc}) was found:

$$\Delta H_f[\%] = -0.628\ N_{cyc} \tag{51}$$

While enlightening, this average-based relationship is somewhat misleading as the results of Figure 5.6 show that individual CC6 samples either experience no change in ΔH_f or an average change of -33.9% at 25 cycles. In other words, there are no "average" samples. Because of this lack of data points about the mean ΔH_f at 25 cycles (-15.7%), it is recommended that only the worst-performing samples be included in the equation for ΔH_f vs. N_{cyc}. Using this methodology, the following relationship is recommended when representing the worst-case performance of CC6 during cycles with a 1°C/hr cooling rate:

$$\Delta H_f[\%] = -1.356\ N_{cyc} \quad (52)$$

While Equation (52) is valid for the first few cycles, it is unknown for how many cycles this linear relationship will hold true. It is expected that as cycle number is increased, ΔH_f will reach an asymptotic value at a point somewhere above a 100% decrease in ΔH_f. In other words, it is not expected that all of the CC6 will separate into CC4 and water, but that an equilibrium concentration between CC6, CC4 and water will eventually result in a stable mixture; albeit with a much reduced H_f value.

It should be noted that after a single cycle, Equation (52) suggests an ΔH_f value, which is of the same order as that predicted by Figure 5.5. Figure 5.5 suggests a change in H_f of -1.85%/cyc, vs. the value of -1.356 %/cyc predicted by Equation (52).

To further illustrate the difference in ΔH_f with respect to cycling speed, the rapid, long-term cycle testing of CC6 presented in Figure 4.26 is re-plotted in Figure 5.7 for ΔH_f between ±20%. Although there is considerable scatter in the data, when a linear trendline was applied to the data, a slight decrease in ΔH_f vs. the number of cycles was found:

$$\Delta H_f[\%] = -1.5 \times 10^{-3}\ N_{cyc} \quad (53)$$

These results for rapid cycling are in line with those suggested by Figure 5.4, where at the maximum cooling rate of 20°C/hr., separation was found to approach 0.

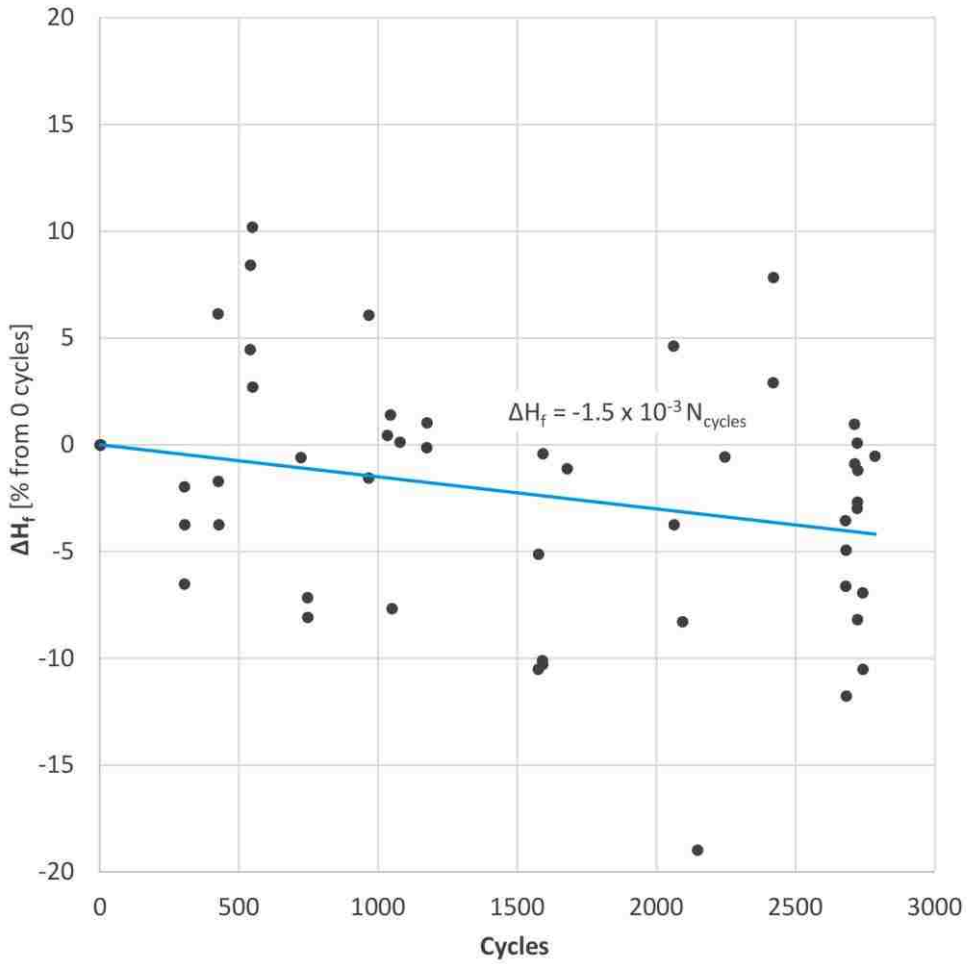

Figure 5.7: Change in H_f vs. Cycling for 45°C/hr Cooling Rate

5.3.3 Impact of High-Side Temperature on Separation

Once solid CC4 forms, an irreversible situation occurs due to CC4's melting temperature (39-45.3°C [N4]) being considerably above that of the CC6 (29.6°C [L8]). If the PCM is only heated to 35°C, solid CC6 will liquify, while CC4 remains in the solid form. As long as CC4 remains in the crystalline form, the stronger crystalline bonds largely prevent CC4 from being hydrated to CC6 by free water. It was hypothesized that if the high-side PCM temperature would rise above 39-45.3°C, both the CC6 and CC4 would liquify, allowing for a homogenous CC6 liquid to be reconstituted so long as there was sufficient free water available to increase the hydration level

of the CC4. If this hypothesis were true, increasing the temperature of a previously-separated PCM to more than 45°C, would result in a renewed, homogeneous PCM.

Testing of this hypothesis was conducted using the slow cycling test samples presented in Table 5.3. As previously shown in Figure 5.6, after 25 cycles, two of the samples (13S and 16S) experienced on average a 33.8% decrease in H_f. Up to this point in the test regime, care was taken to ensure that these samples never exceeded 40°C during cycling, storage, or calorimetry. However, after conducting the 25 cycle calorimetry tests, all four samples were heated to 50°C for a minimum of 24 hours before being re-tested by drop calorimetry. After several drop calorimetry tests, H_f was found to increase to close to its original value for Samples 13S and 16S. This result indicates that increasing the PCM temperature to greater than the melt point of the tetrahydrate is an effective method for reversing the majority of CC6 separation. Since heating to 50°C was conducted during the storage period between calorimetry tests, it is believed that the reversing of separation through heating is only dependent on temperature and not the cycling rate.

Once thermal performance was improved by heating to 50°C, all four samples were subjected to an additional 15 cycles; once again taking care to maintain the PCM at temperatures less than 40°C during cycling, storage, and calorimetry. After an additional 15 cycles, Samples 13S and 16S were again found to experience around a 30% reduction in H_f (Figure 5.8). When these samples were subsequently heated to 50°C and re-tested by drop calorimetry, virtually all of the lost latent heat capacity was recovered within a handful of calorimeter cycles.

These results demonstrate that long-term performance of CC6 can be ensured, and even recovered, through heating of the PCM to temperatures greater than the melting point of the tetrahydrate. Hot-side temperatures of greater than 40°C are not uncommon in many PCM

applications. For instance, in the supplemental condenser cooling system presented in Section 1.1, the PCM is melted via steam leaving the final low-pressure turbine in a power generation cycle. Depending on the plant, this steam can exceed 45-50°C. Accounting for modest temperature losses during heat transfer, PCM hot-side temperatures in excess of 45°C can be expected.

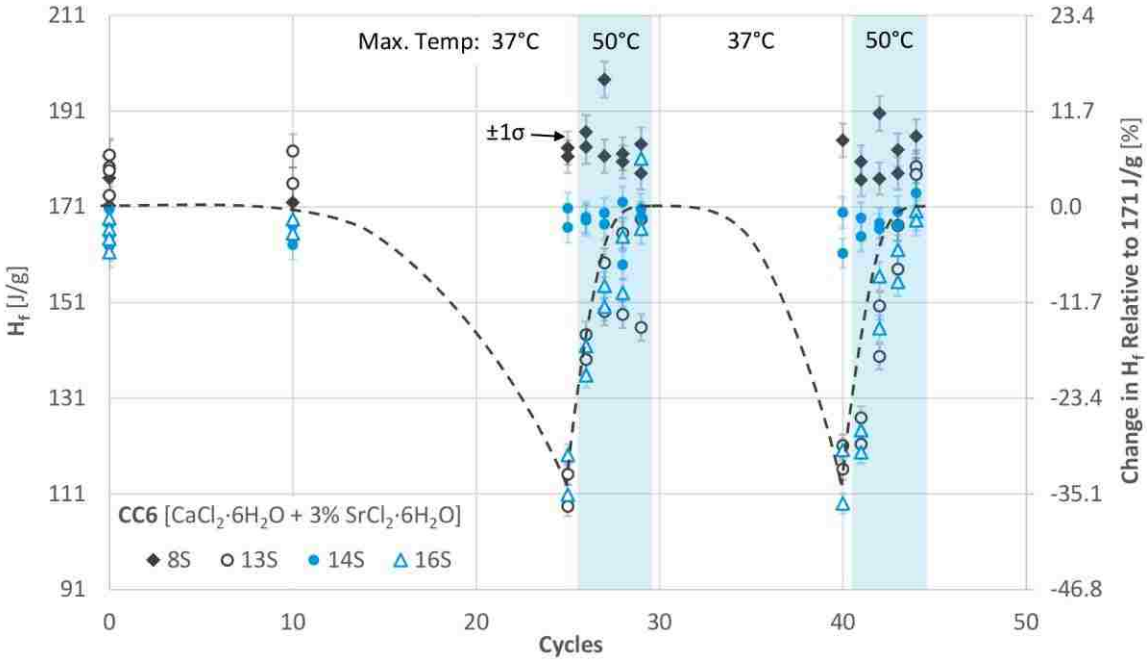

Figure 5.8: H_f During 24 Hour Cycling of CC6 with Thermal Recovery at 50°C

In order to examine the stability of CC6 in another way, temperature traces for the four instrumented CC6 samples (Figure 5.5) are presented for cycles 10, 25 and 40 in Figure 5.9. It is clear that at 10 cycles all four samples follow a similar cooling trend with around 1°C of supercooling before being frozen at a temperature of approximately 28°C. Upon heating, the deviation in sample temperature from the water temperature is an indication of melting; occurring around a temperature of 30°C. By cycle 25, Samples 13S and 16S closely follow the water temperature throughout the cooling and heating processes. This indicates a reduced heat

of fusion for both freezing and melting, which is seen in the corresponding calorimetry results at these cycle numbers (Figure 5.8).

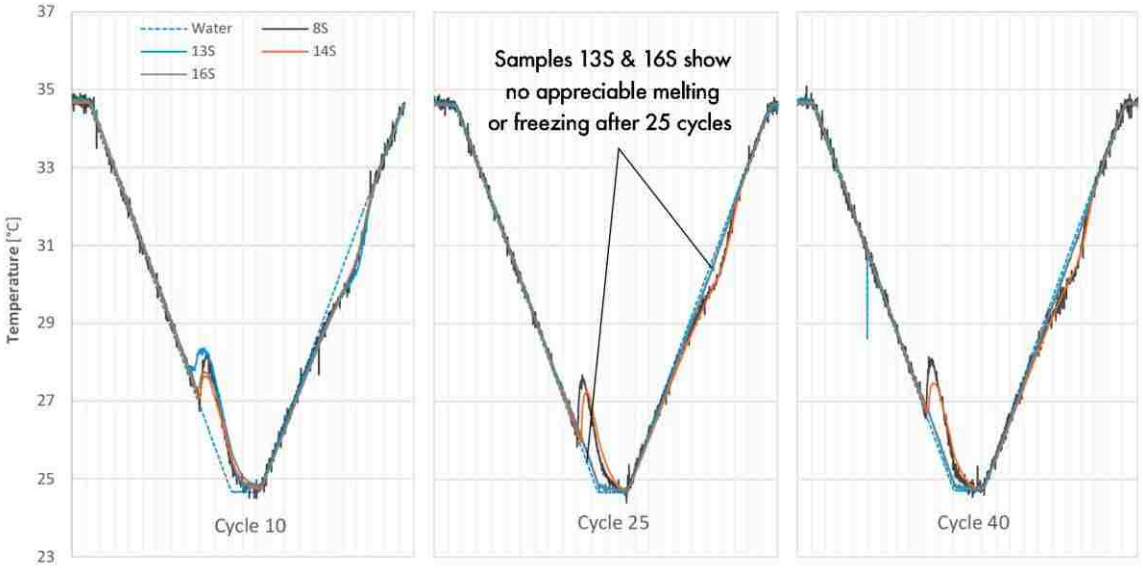

Figure 5.9: Temperature Traces of CC6 Samples During Slow Cycling

5.4 Methods for Preventing Separation of CC6

Given the poor stability results of CC6 under 24 hr. cycling, methods for preventing separation were investigated. There are three primary methods for preventing separation in hydrated salt PCMs. The most widely discussed method is through thickening of the bulk PCM, which prevents settling of solid phase (CC4 in the case of CC6) during freezing. This method was demonstrated to work for $Na_2SO_4 \cdot 10H_2O$ by Telkes, who added attapulgite clay to the salt and found that it prevented density-based separation [T7]. The second method for prevention of separation is chemical modification of the PCM through the use of an additive. For example, the addition of NaCl to CC6 has been studied by several researchers. As is often the case in hydrated salt research, little agreement is found between the literature with regard to this additive. Carlsson et al. found that NaCl shifted the $CaCl_2/H_2O$ phase diagram such that the 6-hydrate composition

was pushed away from the peritectic point. This condition would adversely affect separation [C6]. Contrary to this are findings by Kimura et al., who states that a small percentage of NaCl is essential for long-term stability [K13]. In 1986, Lane et al. [L6] patented a method of preventing separation in $CaCl_2 \cdot 6H_2O$ through the addition of potassium chloride (KCl), although this finding has not been independently verified. Carlsson et al. found that 2 wt% SC6 appeared to eliminate separation in CC6 [C6], although this conclusion was later contested by Lane. Lane suspected that Carlsson et al.'s improvement in separation was actually due to water being released from the SC6 [L2]. This leads to the third method suggested to prevent separation in CC6; the addition of excess water above the 6-hydrate concentration. The reason why excess water reduces separation is evident by considering the phase diagram of the $CaCl_2/H_2O$ system; as seen in Figure 5.1. If the CC:H_2O ratio is shifted slightly to the left of the 6-hydrate level (H_2O composition greater than $xH_2O = 6$), it can be made to correspond with the peritectic point, at which point tetrahydrate should not form during freezing. Brandstetter indicated that no separation was observed at $xH_2O = 6.14$, although he cautioned that in practice the tetrahydrate may still form due to kinetic factors [B19]. Kimura et al. found good stability at $xH_2O = 6.11$ for over 1000 cycles; although NaCl was also added to this system [K13]. Brandstetter thermal cycled CC6 with a slight excess of water. After 600 daily cycles, no tetrahydrate was found to have formed for $xH_2O = 6.14$. For excess water of less than $xH_2O = 6.10$, tetrahydrate was found to quickly form in the cycled salt, suggesting a peritectic concentration in slight excess of $xH_2O = 6.10$ [B19]. There is some disagreement on the exact peritectic concentration. Roozeboom gives the peritectic temperature and hydration level as 29.8°C and 6.10 respectively [R10]. Lane gives the peritectic point at 29.45°C at $xH_2O = 6.25$ [L8]. Kimura et al. presents the peritectic point at $xH_2O = 6.14$ [K13] and Feilchenfeld et al. gives a value of $xH_2O = 6.12$ [F6].

5.4.1 The Extra Water Approach

While the extra-water method is the simplest of the methods to implement, there was concern about the very tight moisture tolerance that the CC6 would have to be maintained at (between 6.10 and 6.14). CC6 is a desiccant at typical ambient conditions, while at higher temperatures and lower humidity, CC6 can release water. This not only necessitates careful encapsulation of the PCM, but also creates considerable challenges in ensuring the proper hydration level during material preparation. Truly anhydrous $CaCl_2$ is difficult to obtain as it readily absorbs moisture from the atmosphere. Therefore, when adding H_2O to $CaCl_2$ in order to hydrate it, the exact quantity of moisture in the "anhydrous" $CaCl_2$ must be accurately known in order to arrive at the desired hydration level. Most of the difficulties in preparation lie in the atmosphere in which the PCM is prepared. When measuring the moisture in the "anhydrous" $CaCl_2$, a nitrogen atmosphere should be maintained to ensure complete dehydration. Equipment used for this purpose, such as thermogravimetric analyzers (TGA) are typically operated with a nitrogen atmosphere over the sample pan. The real difficulty is during mixing of the water and $CaCl_2$, where an atmosphere with vapor fraction corresponding to the vapor pressure of the desired $CaCl_2$ hydrate should be maintained. This requires custom equipment with very precise humidity controls (on the order of ±0.1% relative humidity). Even if CC6 of the correct hydrate is manufactured, it must be very well encapsulated throughout its usable lifetime to prevent water from entering or exiting the PCM. Because of these challenges, the extra water method was not pursued as a practical method of CC6 stabilization.

5.4.2 The Thickening Approach

Initial work considering thickening of CC6 was conducted using hydroxyethyl cellulose (HXC). This thickening agent has a viscosity between 4,500 and 6,500 mPa·s with a solubility of 2 wt% in water at 25°C. It was added to the CC6+MC6 and CC6+KN PCMs at a mass percentage of 1-1.1%

of the water in the hydrated salts. Initially, the HXC was well-mixed in the PCMs, but within 1 hour separation between the PCM and HXC was evident; with the HXC floating on top of the PCM (Figure 5.10). This poor mixing is thought to be due to incomplete dissolution of the HXC into the hydrated salt PCMs. While there may be thickening agents, which do not exhibit this behavior, additional work with thickening agents was not conducted.

Figure 5.10: Hydrated Salt Mixture with Hydroxyethyl Cellulose

5.5 Improving the Stability of CC6 With KCl Approach

Stabilization of CC6 through the use of an additive to modify its chemical structure is believed to be the most desirable stabilization method. The reason being that this method results in a new, stable PCM with physical characteristics very similar to the original PCM. For instance, the use of thickening agents would result in a PCM, which is more gel-like in substance. While this change would likely be acceptable for many applications, it could raise new issues associated with filling of large containers, such as those proposed for the ACC cooling system. Chemical

modification of a hydrated salt also has the potential of forming a new, moisture stable eutectic between the salt and added compound. In other words, the hydration level of the new compound may be somewhat self-regulating – eliminating the need for precise atmospheric control during material preparation.

The addition of KCl to CC6 was selected for trial as a chemical stabilization technique. KCl was added to CC6 at 1, 2, and 5 wt%. Several samples of CC6 without KCl were simultaneously considered to provide baseline data. Note that all samples contained 3 wt% SC6 for supercooling suppression. Samples were tested by repeated cycling in the programable water bath according to the following procedure:

- Temperature maintained at 35°C for 4 hours
- Linear cooling from 35 to 25°C over 10 hours
- Temperature maintained at 25°C for 4 hours
- Rapid heating to 35°C to complete the cycle

After five complete cycles, samples were removed at 25°C with the supernatant liquid on top of the frozen solid being dumped off and weighed. Results of this testing are presented Figure 5.11. Data points are presented along the x-axis, with normal distribution curves for each KCl concentration plotted above the corresponding data points. The heights of the distribution curves correspond to the number of cycles completed by each sample.

Figure 5.11 clearly shows that samples without added KCl contained on average 11-12 wt% supernatant liquid after 5 cycles. Samples with KCl had much lower levels of supernatant liquid after cycling; on average around 3 wt%. What is less clear are differences between the concentrations of KCl. From these results, it can be concluded that the addition of any quantity

of KCl at or above 1 wt% will reduce the supernatant liquid after 5 cycles by approximately 75% relative to a CC6 sample without KCl.

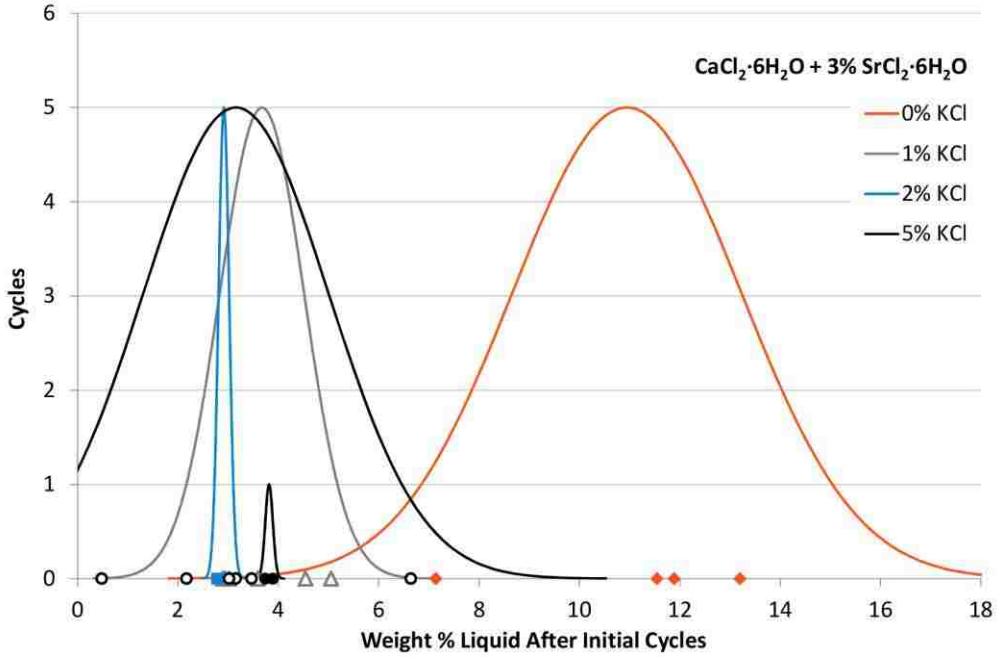

Figure 5.11: Measured Liquid After Initial Cycling of CC6 + KCl

Cycling of the samples in Figure 5.11 was continued after the initial supernatant liquid dump. This testing was conducted for two primary reasons. First, for the samples without KCl, it was assumed that the formation of supernatant liquid was due to the formation of tetrahydrate during repeated cycling. If CC4 was consistently produced during each cycle, it was expected that further cycling would result in additional supernatant liquid. The second reason for continued cycling was to test a hypothesis that the supernatant liquid for cases with KCl arose during the creation on a new, stable eutectic made up of CC6 and KCl. If this were the case, after the initial liquid dump, a significant quantity of supernatant liquid would not reappear with additional cycling. Results for the measured supernatant liquid of the samples after additional cycling are presented in Figure 5.12.

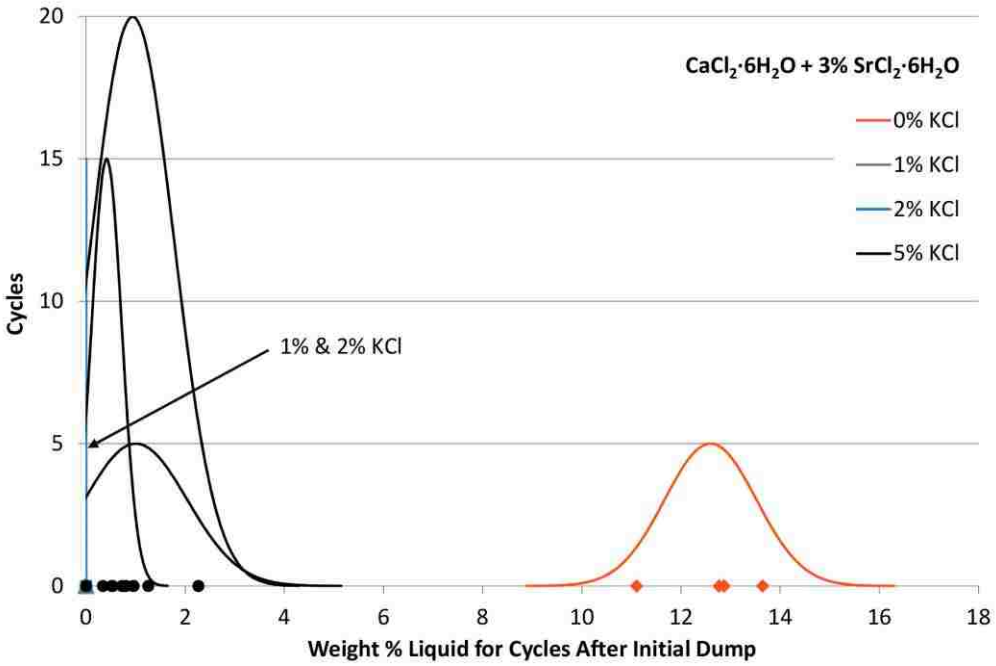

Figure 5.12: Measured Liquid After Initial Liquid Dump and Further Cycling of CC6 + KCl

Figure 5.12 shows that for the CC6 samples without KCl, around the same weight percentage (~12.5 wt%) of supernatant liquid reappeared after an additional 5 cycles. This indicates that for CC6 without KCl, supernatant liquid will continue to be produced even after it is initially removed. In other words, CC6 does not stabilize when the supernatant liquid is removed, which was expected.

For the samples with KCl, all of the samples were found to have a lower percentage of supernatant liquid formation after the initial liquid dump. Most impressively, for the 1 and 2 wt% KCl cases, no supernatant liquid was observed after 15 additional cycles. Interestingly, the 5% KCl samples experienced the formation of additional supernatant liquid, but even for these samples only one data point was greater than 2 wt% for cycle numbers of up to 20. These results strongly suggest that CC6 and KCl can form a stable, eutectic mixture at relatively low KCl weight percentages. During the formation of this compound, excess water is released and forms a

supernatant liquid on the top of the frozen PCM. If this liquid is removed, it does not re-appear even after numerous freeze-thaw cycles.

Given these positive separation results for CC6 plus 1 or 2 wt% KCl, cycling of ~80 g samples of CC6 + 2 wt% KCl was conducted. Eight samples of this composition were prepared, with four of the samples fitted with RTDs for calorimetry testing. The compositions of these eight samples are presented in Table 5.5. All eight samples were subject to 24 hr. cycling with 1°C/hr temperature ramp rates and 2 hour holds at temperatures of 25 and 35°C.

Table 5.6: CC6+KCl Samples for Slow Cycle Testing

Sample #	m_{ENC} [g]	m_{PCM} [g]	$CaCl_2 \cdot 6H_2O$ [wt%]	KCl [wt%]	$SrCl_2 \cdot 6H_2O$ [wt%]
1S	149.1	81.0	95.1	2.0	3.0
2S	151.7	80.7	95.0	2.1	2.9
3S	148.0	85.0	95.1	2.0	2.9
4S	153.1	83.2	95.1	2.0	2.9
10S	238.3*	88.2	95.2	1.9	2.8
11S	238.9*	88.5	95.1	1.9	2.9
12S	241.3*	88.6	95.1	1.9	2.9
15S	246.8*	88.0	95.1	1.9	3.0

* Includes RTD for Calorimeter Measurement

Drop calorimetry test of the later four samples were conducted before cycling with an average H_f of 162.1 J/g found. Calorimetry was repeated after 10 cycles, followed by calorimetry at 25 cycles. These results are illustrated in Figure 5.13. At 10 cycles, all four samples were found to have a negligible change in H_f. However, by 25 cycles, three of the four samples experienced on average a 32.3% drop in H_f, comparable to two of the CC6 samples without KCl (Figure 5.8). As with the samples without KCl, for up to 25 cycles the samples were maintained at less than 40°C to ensure there was no melting of any formed tetrahydrate. In order to test the thermal recovery

of the three samples with decreased ΔH_f at 25 cycles, these samples were heated to 50°C and retested in the calorimeter. Within 3 calorimeter cycles, all of the samples had recovered nearly all of their lost thermal performance.

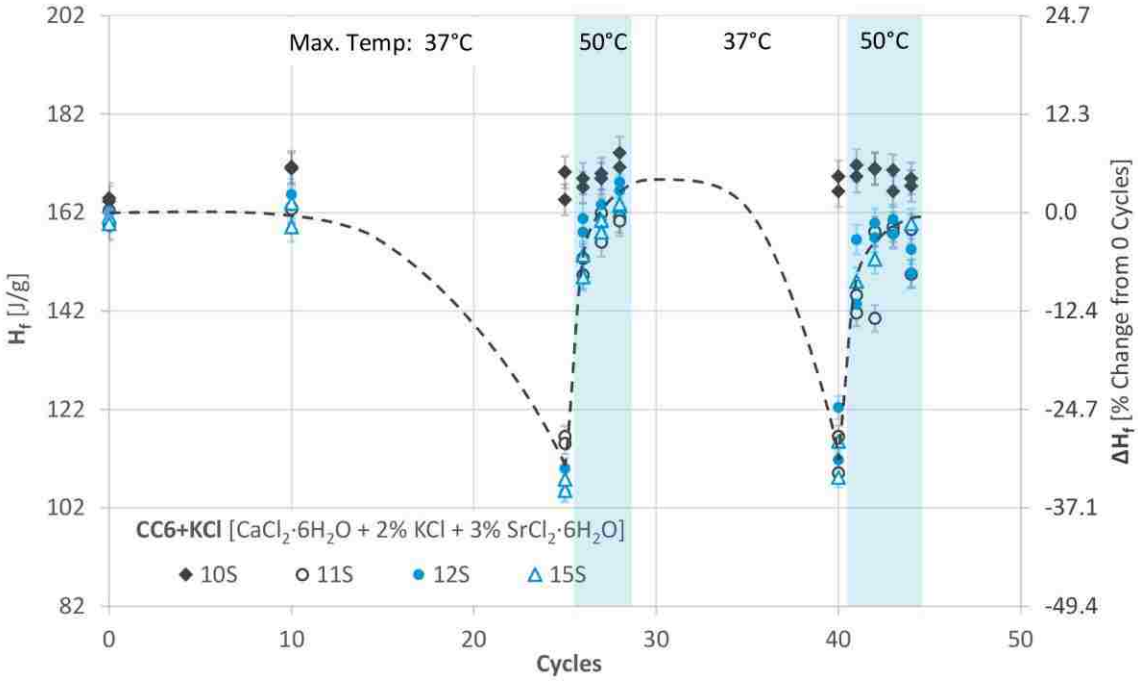

Figure 5.13: Change in H_f of CC6 + KCl During Slow Cycling

All four samples were cycled for an additional 15 cycles (a total of 40 cycles) before being tested by drop calorimetry once again. At 40 cycles, the three samples that had previously lost thermal performance (11S, 12S, and 15S) were again found to have experienced around a 30% reduction in H_f. Upon subsequent heating to 50°C, these samples once again recovered nearly all of their lost thermal performance. Comparing Figure 5.13 to Figure 5.8, it would appear that the addition of KCl has no impact on the stability of CC6. However, this was only part of the story.

While the four samples with RTDs were being cycled, the four identical samples without RTDs were cycled alongside them in order to allow for measurement of any supernatant liquid which would form. After 10 cycles, all four of these samples contained between 1 and 1.8 wt% supernatant liquid, as seen in Figure 5.14. This liquid was dumped off of the samples and weighed before the samples were returned to the water bath and cycled to 25 complete cycles. At 25 cycles, all of the samples were found to contain virtually the same quantity of liquid (~0.18 wt%). This small quantity of liquid indicated a much lower rate of separation between 10 and 25 cycles than that found for the majority of samples with RTDs (the samples where supernatant liquid was not removed). After removing this liquid and cycling to 40 cycles, an even lower percentage of liquid was found for all four samples (<0.05 wt%). Given that these four samples never exceeded 37°C, the results presented in Figure 5.14 do not agree with the calorimetry results of Figure 5.13, which raised some interesting questions. Namely, if KCl suppressed separation in all of the samples which were dumped, why was this not evident in the identical samples tested via calorimetry? It was hypothesized that the removal of supernatant liquid from the samples without RTDs was responsible for their stability. Stated another way, by not removing the supernatant liquid from the RTD-instrumented samples, any stabilizing effect due to the addition of KCl was negated.

In order to test this hypothesis, the four samples without RTDs (which had their supernatant liquid periodically dumped), which had already completed 40 cycles (1S through 4S) were instrumented with RTDs and tested by drop calorimetry. This test was performed to ensure that the low levels of supernatant liquid appearing in these samples at 40 cycles (Figure 5.14) corresponded to small decreases in their latent heat storage capacity. While these samples were not tested via calorimetry at 0 cycles, their four sibling samples with RTDs were used to provide baseline H_f values at 0 cycles. Figure 5.15 presents measured H_f for both the samples in which the supernatant liquid was periodically removed and those where it was not removed.

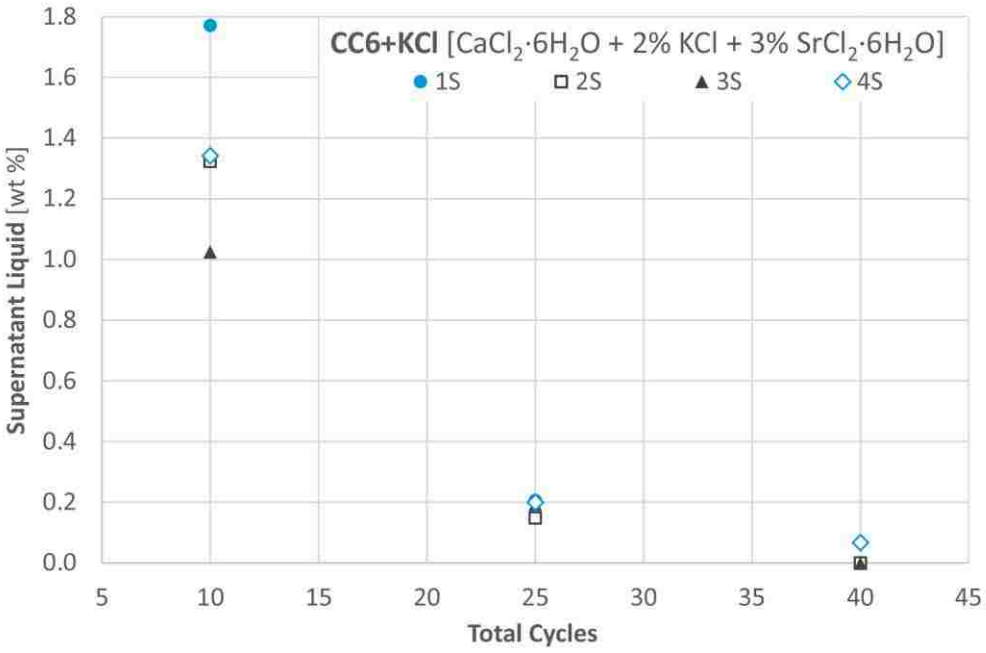

Figure 5.14: Measured Supernatant Liquid During Slow Cycling of CC6+KCl

As previously discussed, after 25 complete cycles, 3 of the 4 samples where supernatant liquid was not removed experienced a decrease in H_f of greater than 30%. This is in contrast to the four samples were supernatant liquid was periodically removed. As seen in Figure 5.15, these four samples maintained their latent energy thermal performance for up to 100 cycles. This is a significant finding as it is clearly evident that simply the addition of KCl to CC6 does not eliminate separation during repeated cycling. However, if the supernatant liquid, which appears after freezing of the CC6+KCl PCM, is removed, the PCM will remain stable. Because of this, it is critical that a procedure for supernatant liquid removal be included during PCM preparation. Additional long-term cycling should be conducted to determine if stability of the CC6+KCl PCM persists for several hundred or thousands of cycles.

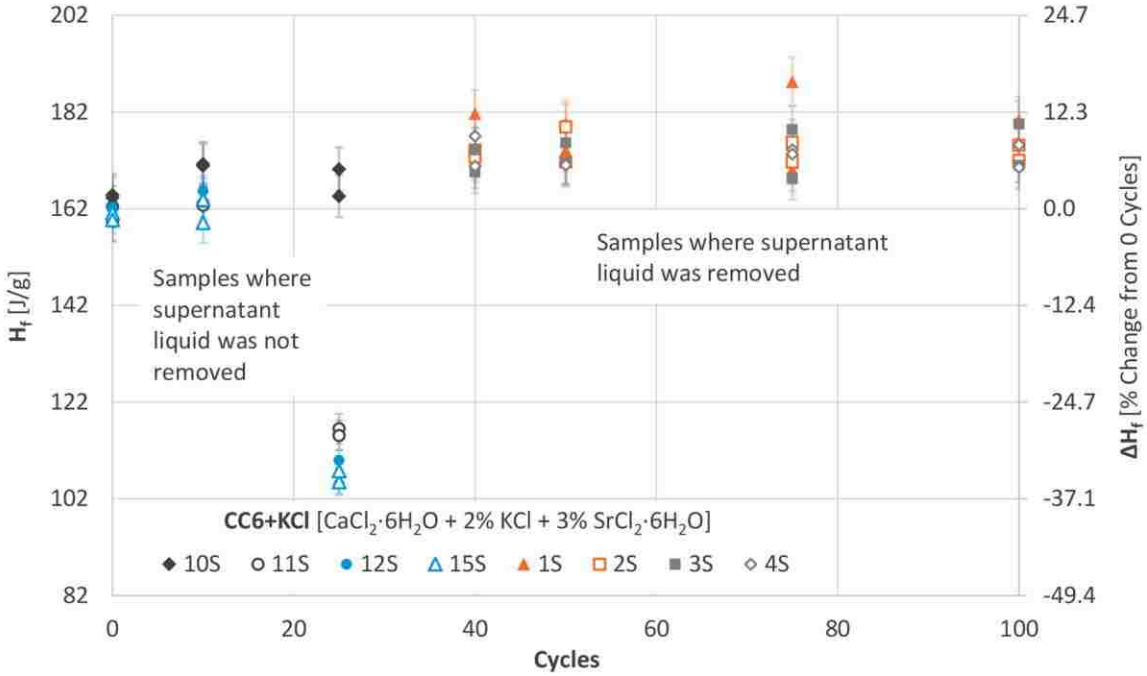

Figure 5.15: CC6+KCl Samples with and Without Supernatant Liquid Removal

5.5.1 Understanding the CC6+KCl System

In order to understand the reason for why KCl is improving the stability of $CaCl_2 \cdot 6H_2O$, changes to the $CaCl_2/H_2O$ phase diagram were modeled using software based on the extended UNIQUAC-based thermodynamic model developed by Thomsen [T12]. These modeled phase diagram results are plotted in Figure 5.16 alongside CC/H_2O phase diagrams from the literature. The modeled results are presented as the solid dark lines, while the literature values are the hashed blue lines.

Four percentages of KCl were considered for this phase diagram modeling; 0, 1, 2, and 3 wt%. Note that for the 0 wt% case, the phase diagram is equivalent to that of CC/H_2O. While the calculated 0 wt% KCl case is seen to deviate slightly (on the order of 1-3%) from the literature phase diagrams, the shape of the liquidous curves are similar and can be used to imply why KCl improves the stability of $CaCl_2 \cdot 6H_2O$. The model predicts that as the KCl concentration increases,

the peritectic point between the CC6 and CC4 liquidous curves shifts to the right and downward. As suggested by the binary CC/H_2O phase diagram (Figure 5.1), shifting the peritectic point to the right moves it closer to the xH_2O = 6 composition. The smaller the difference between the peritectic and hydrate composition, the less time freezing CC6 will spend in the critical temperature region where CC4 is produced. If the hydration level of the PCM corresponds with the peritectic composition, it is believed that a stable PCM will result.

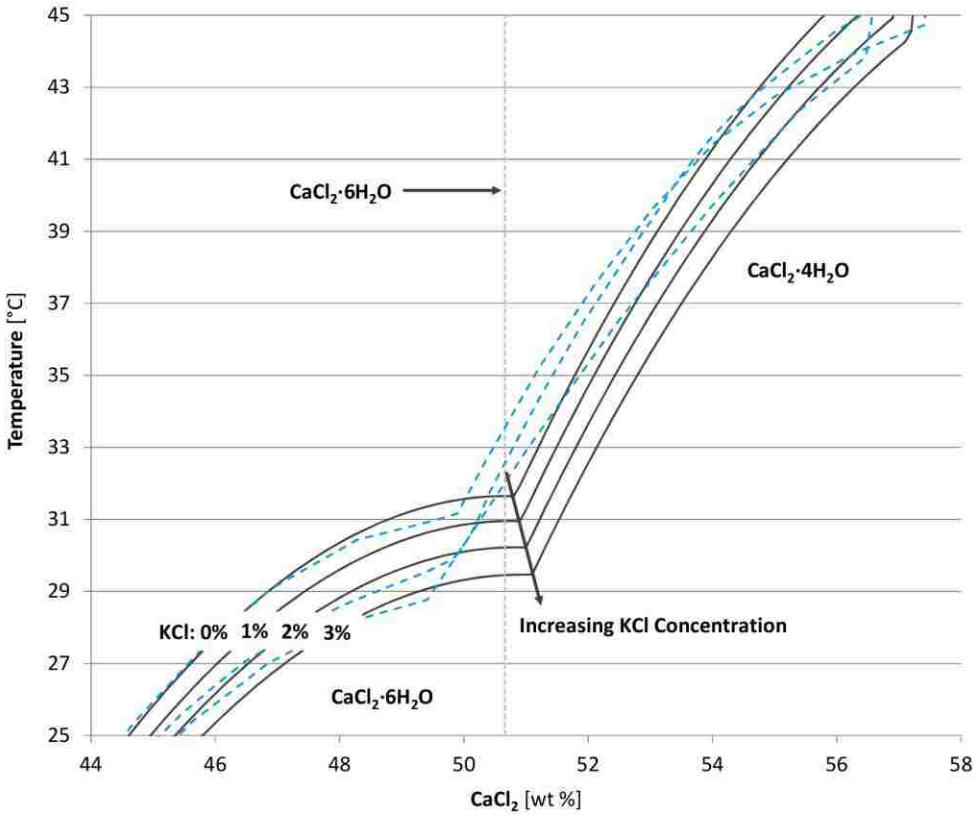

Figure 5.16: Modification of $CaCl_2/H_2O$ Phase Diagram Through the Addition of KCl

A ternary phase diagram of the $CaCl_2$-H_2O-KCl system was also modeled using Thomson's software (Figure 5.17). Four temperatures in the critical region about the PCMs phase transition temperature were considered (15, 27, 30, and 35°C). The 15 and 35°C cases were selected as

the modeled results could be compared with ternary phase diagram results presented by Deng et al. [D4]. Deng et al.'s results are presented as the filled and open circles in Figure 5.17, while the modeled results from Thomson's software package are presented as the dark gray lines. Good agreement between Deng et al.'s results and the modeled liquidous lines at 15 and 35°C were found.

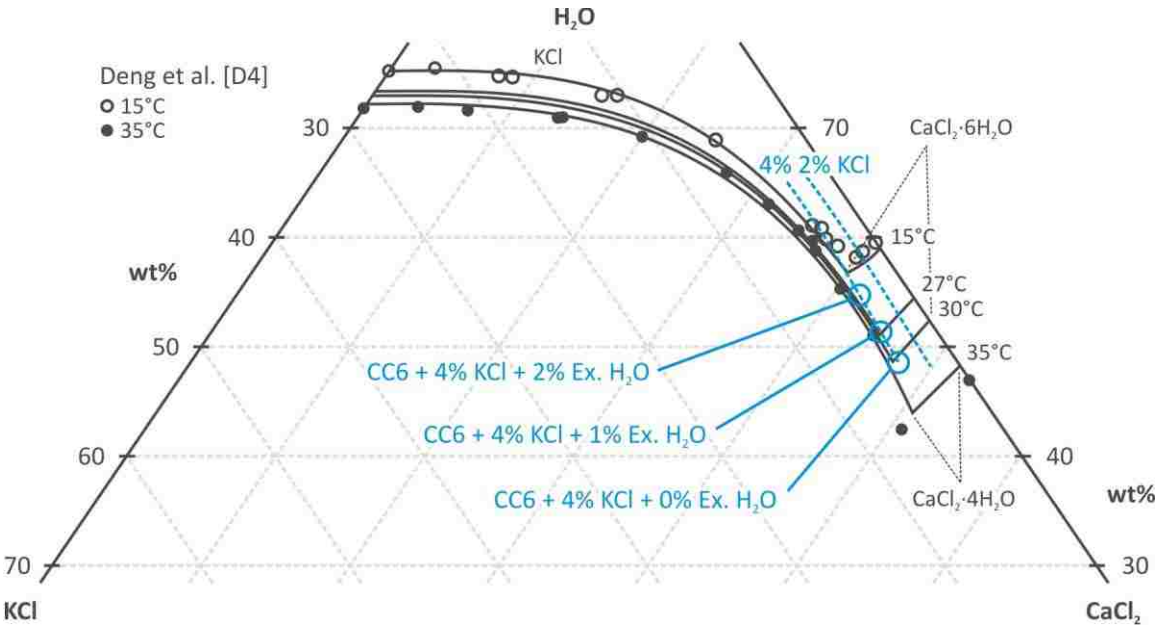

Figure 5.17: Ternary $CaCl_2$-H_2O-KCl Phase Diagram Calculated by Thomson's Program

Figure 5.17 shows two primary phases, which occur in the $CaCl_2$-H_2O-KCl system at temperatures between 15 and 35°C. At KCl concentrations greater than approximately 4 wt%, there exists a KCl phase. For KCl concentrations less than this threshold, the dominant phase is CC6, although CC4 occurs in this region at 35°C. The critical finding of Figure 5.17 is that the hydrated $CaCl_2$ phases and KCl appear to form a eutectic mixture (inflection points on liquidous curves) at KCl concentrations of approximately 4 wt%. Furthermore, Figure 5.17 shows that the position of the eutectic peak in the phase diagram varies as the quantity of water in the PCM increases above the hexahydrate composition. To help illustrate this, the PCM compositions at 4 wt% KCl and 0,

1, and 2 wt% excess water (Ex. H_2O) are denoted by open blue circles in Figure 5.17. At the hexahydrate composition (0% Ex. H_2O), the eutectic peak for the 30°C liquidous curve corresponds with the PCM composition. In other words, this indicates that CC6 + 4 wt% KCl will form a eutectic compound, which melts and freezes congruently at 30°C. If 1 wt% extra water is added to the CC6 + 4 wt% KCl PCM mixture, a eutectic composition with a phase transition temperature of 27°C results. Figure 5.17 suggests that excess moisture will continue to reduce the phase transition temperature for up to 2 wt% Ex. H_2O, where the eutectic phase transition temperature approaches 20°C. A line showing a reduced KCl concentration of 2 wt% was also plotted in Figure 5.17. It is clear that at 2 wt% KCl, the PCM composition will not correspond to a eutectic point, casting doubt on whether a stable, congruently melting/freezing PCM will result at this composition.

It should be noted that the ternary phase diagram in Figure 5.17 does not include the $SrCl_2 \cdot 6H_2O$ added to the experimental PCM mixtures tested. Sr is not an available ion in the equilibrium model by Thomson. The addition of $SrCl_2$ would likely shift the liquidous curves and corresponding eutectic points and may be the reason why stable eutectics appear to form during laboratory tests where only 2 wt% KCl has been added. Despite not containing $SrCl_2$, Figure 5.17 is put forward as an important tool in understanding the eutectic nature of $CaCl_2$-H_2O-KCl mixtures. Not only does it show that eutectics mixtures of these salts can form at low concentrations of KCl, but also that the quantity of available H_2O can directly influence the formation of these eutectics and their resulting phase transition temperatures.

5.6 Summary of CC6 Phase Stability Findings

$CaCl_2 \cdot 6H_2O$ was expected to experience phase separation after the long-term cycling in Chapter 4 uncovered a 3.8% decrease in H_f after 2,700 rapid (~2 hr.) cycles. When this separation was

examined after slower (~24 hr.) cycling, it was found that after 40 cycles around 50 wt% of the CC6 had separated into a supernatant liquid and CC4. The supernatant liquid was formed as CC6 separated into CC4 during freezing, releasing the water forming the supernatant liquid solution. If this liquid were removed from the frozen PCM, it was found to re-appear during additional slow cycling. Calorimetry testing of comparable samples at 25 cycles showed up to a ~34% decrease in H_f. Because of these results, it was determined that the separation of CC6 was much more severe than that predicted during rapid cycling and a method for minimizing this separation was sought.

The cycling rate and maximum PCM temperature were found to directly impact separation. Higher cycling rates, such as experienced by the PCM during the rapid, 2,700 cycle testing, were found to minimize separation, while maximum levels of separation per cycle occurred at slower cycling rates. Interestingly, if CC6 did experience separation, the PCM was found to be virtually restored to its original thermal performance through heating to 50°C. Heating to 50°C allowed any separated CC4 to melt, which greatly increased mixing between the CC6, CC4, and supernatant liquid. Given sufficient time at this elevated temperature, the three liquid layers mixed together reconstituting a homogenous, CC6 PCM.

By adding a small weight percentage of KCl (2 wt%) to CC6, a stable eutectic was found to result. A supernatant liquid would still form on top of this PCM when frozen, but when it was removed it would not reappear with continued cycling. When slow cycled (1°C/hr temperature ramps) and tested by drop calorimetry, this CC6+KCl PCM was found to maintain its latent heat of fusion for up to 100 cycles. It is recommended that longer-term cycling of this PCM be conducted to ensure good long-term thermal performance.

When a ternary phase diagram of the $CaCl_2$-H_2O-KCl system was modeled, it showed that eutectic mixtures form more or less along a line constant KCl concentration (~4 wt% KCl) at water concentrations close to the hexahydrate. This phase diagram suggests that different eutectic mixtures can form at water concentrations in slight excess of the hexahydrate. As the water concentration increases, the melt temperature decreases. The formation of eutectic mixtures of CC6 and KCl at low KCl concentrations helps to explain the stabilizing impact of KCl as eutectics of hydrated salts tend to be thermally stable during cycling. Finally, it was found that all of the supernatant liquid needs to be removed in order to achieve stability of the CC6+KCl PCM. If this supernatant liquid is not removed, stability is similar to that of CC6 without KCl.

6 Corrosion Testing

One of the chief concerns surrounding the use of hydrated salt PCMs is that of corrosion of any containers used to contain them. If expensive, corrosion resistant materials are required to contain the PCM, any proposed energy storage system could easily be cost limited. While some researchers have recommended the use of plastic containment for $CaCl_2 \cdot 6H_2O$ salts, in this research, metal containment options were explored due to their good structural strength and higher thermal conductivity.

The impact of corrosion on metal will eventually result in failure of the PCM containment vessel. In the most dramatic situation, sudden, catastrophic failure of the vessel could occur. Cabeza et al. [C2] have presented guidelines to predict the long-term integrity of a metal subjected to a corrosive environment. These guidelines are presented in Table 6.1, where it can be seen that only corrosion rates less than 20 μm/yr are suggested for long-term service. This 20 μm/yr corrosion rate (K) is taken as the maximum acceptable rate for all corrosion tests presented in this report.

Table 6.1: Industry Guide for Material Integrity Subject to Different Corrosion Rates [C2]

Corrosion Rate [mg/cm^2yr]	Corrosion Rate [μm/yr]	Recommendation
> 1000	> 2000	Completely destroyed within days.
100-999	200-1999	Not recommended for service greater than a month.
50-99	100-199	Not recommended for service greater than a year.
10-49	20-99	Caution recommended, based on the specific application.
0.3-9.9	-	Recommended for long term service.
< 0.2	-	Recommended for long term service; no corrosion, other than as a result of surface cleaning, was evident.

6.1 Corrosion Test Methods

The ASTM G1 [A11] method was selected as the standardized method used to conduct the corrosion tests. According to this method, corrosion test samples are prepared and weighed before being placed into the corrosive environment (immersed in PCM in this case). After the corrosion test period, the metal samples are removed from the PCM and cleaned using standard procedures. The G1 method allows for both mechanical and chemical cleaning of test samples. Cleaning is necessary as any corrosion products need to be removed from the samples before they are weighted after being corroded. With the corrosion products removed, the mass loss due to corrosion is found by subtracting the sample weight after corrosion from the initial sample weight. In order to maximize the precision of the ASTM G1 method, the chemical cleaning method was used instead of the mechanical cleaning method as the mechanical method is more prone to errors associated with operator bias. For instance, if sandpaper was used to clean away corrosion, an over-zealous researcher could inadvertently remove metal along with the corrosion.

Table 6.2: Chemicals Used to Clean Metals After Corrosion Using the ASTM G1 Method [R7]

Metal	Solution	Immersion Time	Immersion Temp.
Carbon Steel	(1) 500 ml hydrochloric acid (HCl, sp. gr. 1.19) (2) 3.5 g hexamethylene tetramine (3) Reagent water to make 1000 mL	10 min	20-25°C
Copper	(1) 500 ml hydrochloric acid (HCl, sp. gr. 1.19) (2) Reagent water to make 1000 mL	1-3 min	20-25°C
Al 6061 / 5086	(1) Nitric acid (HNO_3, sp. gr. 1.42)	1-5 min	20-25°C

The test samples used for all corrosion tests were 1.6 mm thick coupons cut to 12.7 mm by 50.8 mm. After being cut to size, the coupons were polished with a rotating wire wheel, washed, and dried before being weighed to an accuracy of ±1 mg. After being weighed, each sample was

individually immersed into a glass bottle filled with liquid PCM. Sufficient PCM was added to each bottle to ensure that the metal coupon was fully submerged.

Two corrosion test scenarios were considered for these PCM/metal samples. The first was an isothermal melted condition, where the samples were maintained at a temperature greater than the phase transition temperature (in a liquid state). Three different isothermal temperature conditions were considered; a temperature just above the phase transition temperature of each PCM ($T_{m(l)}$), 50°C and 80°C. Glass sample bottles were used for all isothermal tests. Figure 7 shows a carbon steel coupon before being immersed in the PCM-filled test bottles alongside three coupons during isothermal testing at the three temperature conditions. The isothermal test coupons were tested for periods of 2, 4, 8, 16, 24, and 48 weeks.

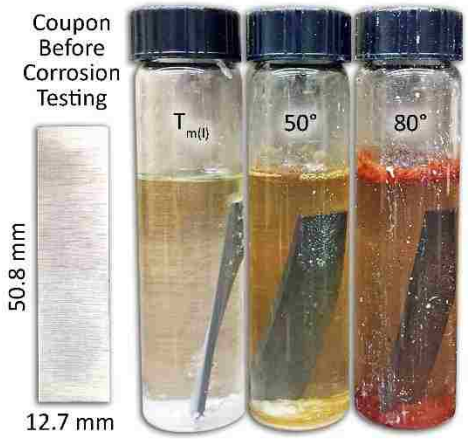

Figure 6.1: Isothermal Corrosion Test Coupon Before and During Testing

The second corrosion test condition considered was that of PCM cycling. A second PCM cycling system identical to that presented in Figure 3.6 was constructed and fitted with aluminum trays with the capacity to hold up to 168 test samples between the two cycling system tanks. The glass bottles used for the isothermal tests were replaced with plastic bottles to prevent breakage as

the freezing and melting PCM introduces considerable stresses on the containment vessel. Two cycling temperature conditions were considered. First was cycling between 5 and 50°C with 1 hr. of heating and 1 hr. of cooling (a 2 hr. cycle). The second cycling condition was cycling between 5 and 45°C with 2.5 hrs. for heating and cooling (a 5 hr. cycle). In order to increase the cycle time to 5 hrs., the PCM tanks were only filled half way with water. The PCM bottles were placed directly above the water with the bottoms of the bottles only just touching the water. This addition of an air gap effectively increased the heat transfer coefficient between the water and the PCM, decreasing the cycle time. The hot-side temperature was limited using this method, with the PCM only reaching 45°C even though the water was set at 50°C.

In order to measure the effective cycle times at the two cycling temperature conditions, RTDs were placed into samples bottles, which were frozen at both cycling rates (Figure 6.2). When the PCM and water temperatures coincide after freezing, it can be safely assumed that the PCM has been fully frozen. Using this criterion, Figure 6.2 shows that fast cycling corresponds to approximately a 0.5 hr. freeze, while the slow cycling case takes five times as long at 2.5 hrs. This freezing time is designated as “t” throughout this chapter.

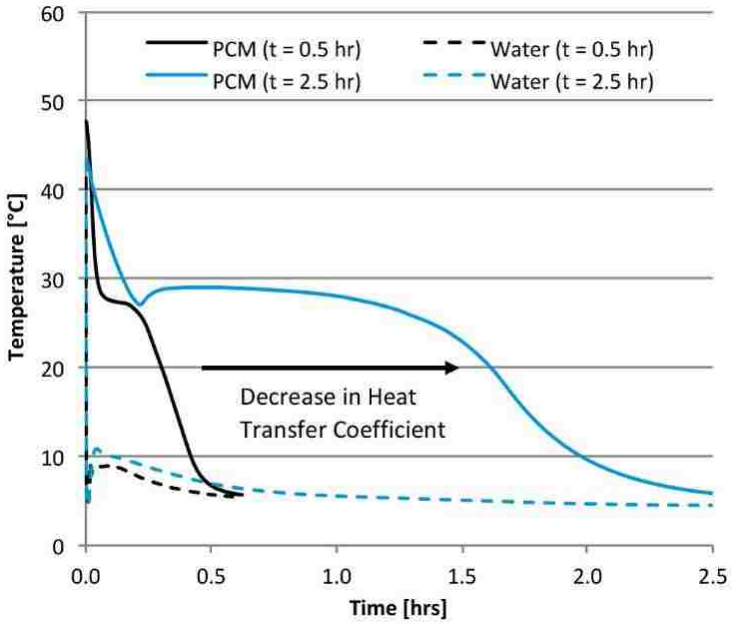

Figure 6.2: Cycling Freezing Rates for Fast and Slow Cycling

6.2 Metals Selected for Corrosion Testing

The following five metals were selected for both isothermal and cyclic corrosion testing:

- Copper (Cu)
- Stainless Steel 304 (SS 304)
- A36 Carbon Steel (CS)
- Aluminum 6061 (Al 6061)
- Aluminum 5086 (Al 5086)

Thermal and physical properties of these five metals are presented in Table 6.3, with their compositions presented in Table 6.4. With the exception of copper, which was selected for

comparison with previously published corrosion test results, these metals were selected based on the following criteria:

- Cost and Availability
- Known Corrosion Resistance
- Thermal Conductivity
- Ease of Manufacturing

Table 6.3: Thermal and Physical Properties of Metals Used in PCM Corrosion Tests [M2,M7,M8]

Metal	Cu	CS	Al 6061	Al 5086	SS 304
Thermal Cond. [W/m-K]	391	50.2	167	125	14.4
Melting Temp. [°F]	1065	1421	582	585	1316
Density [kg/m^3]	8913	7861	2768	2768	8027
Yield Strength [MPa]	228	248	241	117	207
Specification	ASTM B187	ASTM A36	ASTM B221	ASTM B209	ASTM A240
Formability	Excellent		Good	Good	Good
Machinability		Good	Good		Good
Weldability		Excellent	Good	Good	Good

Of the selected materials, CS and the two aluminums are the most desirable from both a cost, availability, and manufacturing standpoint. Al 6061 was selected due to its popularity as a general-purpose aluminum alloy. The marine-grade Al 5086 was selected as an alternative to 6061, which is known to perform better in highly corrosive environments. While CS is less desirable than aluminum from a thermal conductivity standpoint (see Table 6.3), its low cost and easy of manufacturing caused it to be selected for testing. SS 304 was selected as a highly corrosion resistant fallback material in the case where both the aluminum and CS samples had

poor corrosion resistance. Isothermal corrosion testing began with the 50°C case for all five metals immersed in the following three PCMs:

- $CaCl_2 \cdot 6H_2O$ (CC6)
- $CaCl_2 \cdot 6H_2O$ + 7 wt% KNO_3 (CC6+KN)
- $CaCl_2 \cdot 6H_2O$ + 18 wt% $MgCl_2 \cdot 6H_2O$ (CC6+MC6)

Table 6.4: Composition (wt%) of Metals Used in PCM Corrosion Tests [M7,M8]

Metal	Cu	CS	Al 6061	Al 5086	SS 304
Aluminum			95.1-98.2%	93-95.7%	
Bismuth	0-0.005%				
Carbon		0.29%			0-0.08%
Chromium			0.4-0.8%	0.05-0.25%	17.5-24%
Cobalt					0-0.29%
Copper	99.9%	>= 0.2%	0.05-0.4%	0-0.1%	0-1%
Iron		98%	0-0.7%	0-0.5%	53.48-74.5%
Lead	0-0.005%				
Magnesium			0.8-1.2%	3.5-4.5%	
Manganese		0.8 – 1.2%	0-0.15%	0.2-0.7%	0-2%
Molybdenum					0-2.5%
Nickel			0=0.05%		8-15%
Nitrogen					0-0.1%
Oxygen	0-0.04%				
Phosphorus		0.04%			0-0.2%
Silicon		0.15-0.4%	0.4-0.8%	0-0.4%	0-1%
Sulfur		0.05%			0-0.35%
Titanium			0-0.15%	0.15%	
Zinc			0-0.25%	0.25%	
Zirconium			0-0.25%		
Other			0.15%	0.15%	

For each test period, two identical test coupons were simultaneously tested to help ensure that the results were reproducible. After measuring the mass loss of each coupon, the corrosion rate was calculated using the following equation:

$$\text{Corrosion Rate (K)} = \beta \frac{\Delta m}{\rho S t_c} \tag{54}$$

Where, Δm is the change in mass of the coupon due to corrosion, ρ is the density of the metal coupon, S is the surface area of the coupon, t_c is the corrosion test duration, and β is a conversion factor to convert to the desired units. Throughout this report, the corrosion rate is expressed in μm/yr.

6.3 Isothermal Corrosion Testing

Initially, isothermal corrosion testing of the PCM/metal pairs of the five metals and three candidate PCMs was conducted. This testing was conducted at the three constant temperature conditions outlined above. By testing at three temperatures, an Arrhenius relationship between corrosion rate and temperature could be found.

6.3.1 $CaCl_2 \cdot 6H_2O$ Corrosion Testing

All five metals were corrosion tested isothermally in CC6. During testing, the PCM temperature was maintained at 30, 50 and 80°C, with the corrosion results for these conditions presented in Figure 6.3 through Figure 6.5. Note that corrosion test time is presented in $hrs^{1/2}$ as this more evenly distributes the data along the x-axis, allowing for clearer visualization in the figures. For all three temperature conditions, it can be seen that although the corrosion rate of several of the metals is quite high at short test times, as test time increases, the corrosion rate of these metals decreases considerably. The best explanation for this phenomenon is the formation of a

protective oxide layer on the surface of the coupons. During the initial corrosion test time, the corrosion rate increases up to the point where the formed oxide layer becomes thick enough to physically protect the base metal from additional oxidation. In other words, the oxide layer limits diffusion of oxygen to the base metal, greatly reducing the corrosion rate in the process.

Figure 6.3 through Figure 6.5 clearly show that SS 304 has the best corrosion resistance to CC6 at all temperatures, followed closely by Cu. At 50 and 80°C, carbon steel and Al 6061 were found to have comparable corrosion rates, with the corrosion rate of Al 6061 being approximately double that of CS at 30°C. At all temperatures, Al 5086 had the worst corrosion resistance. While the corrosion rates for most metals were initially quite high at all three temperatures, long-term corrosion resistance is considered more important when considering the long-term performance of a material in contact with the PCM. At the longest test times (48 weeks), all of the metals were found to have a low corrosion rate (<3 μm/yr) at 30°C. At 50°C, Al 5086 was the only metal with a long-term corrosion rate greater than 10 μm/yr (~15 μm/yr). When the temperature was further increased to 80°C, both of the aluminums had a corrosion rate between 10 and 15 μm/yr. Note that these corrosion rates still fall below the maximum acceptable corrosion rate of 20 μm/yr presented by Cabeza et al.in Table 6.1 [C2].

Figure 6.3 through Figure 6.5 show that for most of the tested metals the corrosion rate decreases with test time. This is due to the formation of a protective oxide layer on the surface of the metal. Only copper and SS 304 do not clearly exhibit this behavior. In the case of stainless steel, it is known that a thin, strong protective oxide layer develops very quickly and is responsible for this metal's very low corrosion rate. The rapid formation of this layer will result in a low corrosion rate even at short test periods. Interestingly, the test results in Figure 6.5 suggest that copper does not form a protective oxide layer as its corrosion rate continues to increase with increasing test time.

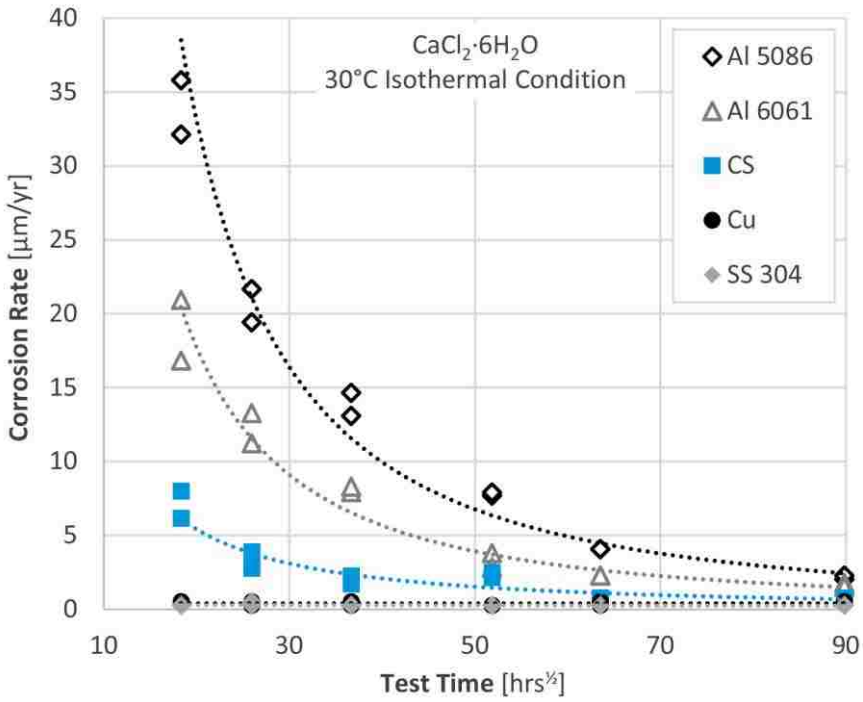

Figure 6.3: Isothermal Corrosion Test Results in CC6 at 30°C

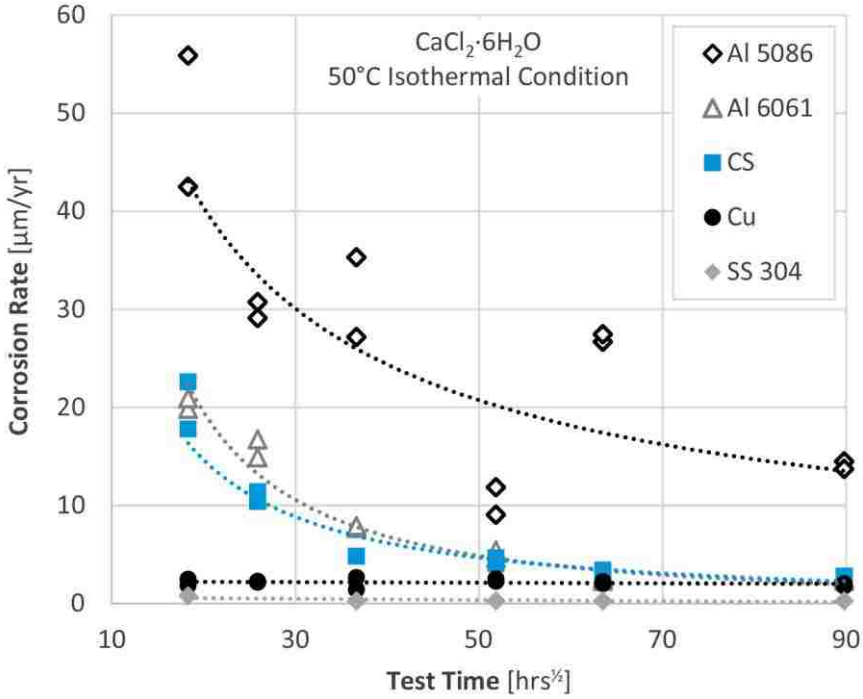

Figure 6.4: Isothermal Corrosion Test Results in CC6 at 50°C

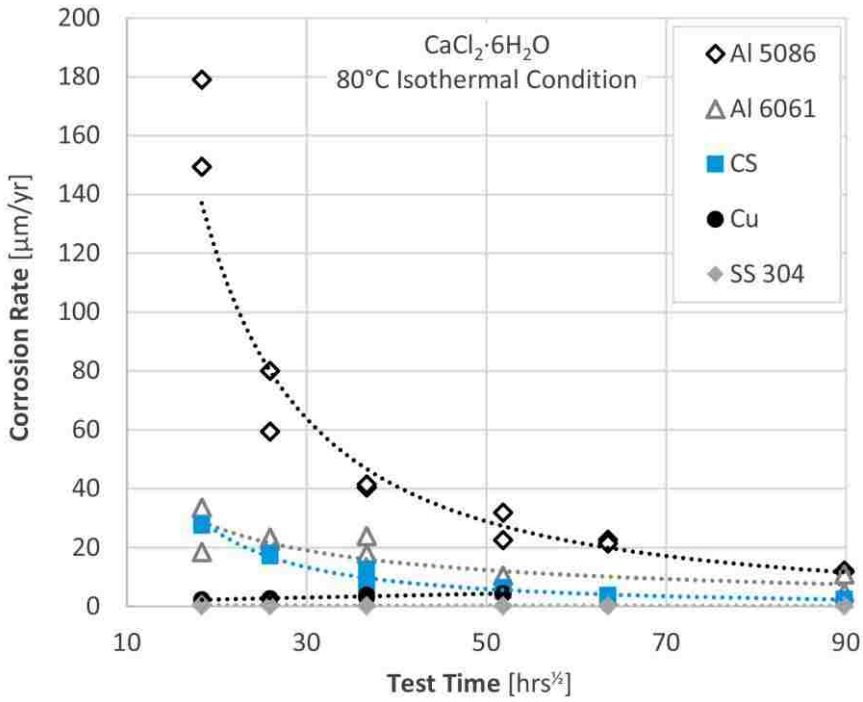

Figure 6.5: Isothermal Corrosion Test Results in CC6 at 80°C

By conducting isothermal corrosion tests at three different temperatures, the relationship between temperature and corrosion rate can be quantified for all PCM/metal pairs. As presented by Ren et al. [R7] the following pseudo Arrhenius equation can be used to correlate the corrosion rate and isothermal test temperature:

$$\ln K = -\frac{E_a}{RT} + \ln C_A \tag{55}$$

Where K is the corrosion rate, E_a is the apparent activation energy, C_A is the Arrhenius constant, R is the gas constant and T is the absolute standard temperature. By plotting ln|K| vs 1/T, linear curve fits can be made, from which E_a can be found. The Arrhenius plot for CC6 and all five metals at a 16 week test time is presented in Figure 6.6. For most of the metals, close to a linear relationship between ln|K| and 1/T was found. The equations of these linear curve fits were

used in conjunction with Equation (55) to estimate the activation energy for all five metals. Activation energy results are presented in Table 6.5 alongside the linear regression R^2 values for the linear curve fits, most of which are close to 0.9, demonstrating that the PCM/metal pairs obey an Arrhenius relationship.

Table 6.5: Activation Energy for Metals Immersed in $CaCl_2 \cdot 6H_2O$

Metal	E_a [kJ/mol]	R^2
Al 5086	6,662.691	0.896
Al 6061	6,184.996	0.955
CS	4,902.632	0.889
Copper	14,704.42	0.856
SS 304	0	N/A

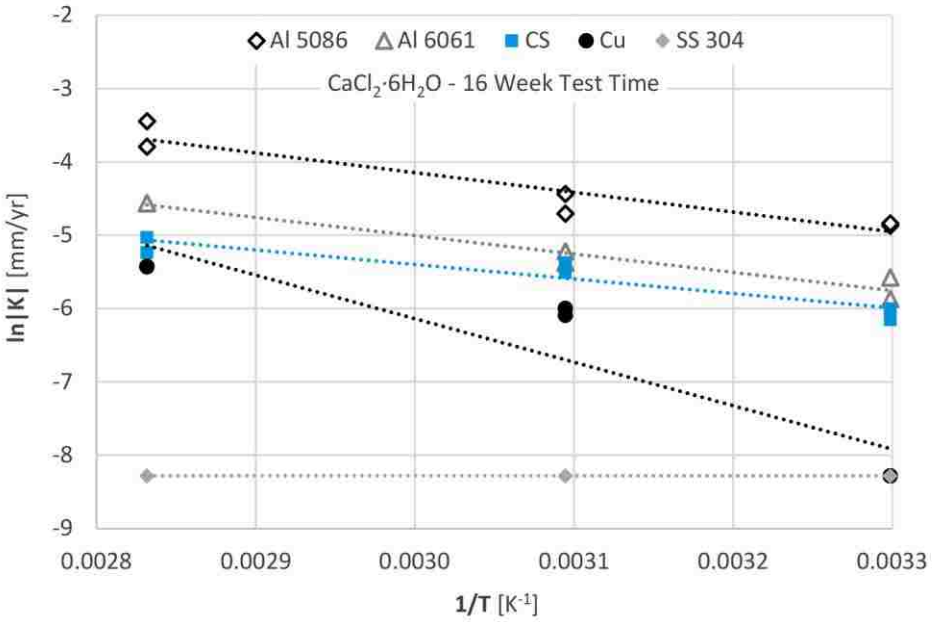

Figure 6.6: Arrhenius Curve Fits for Metals in $CaCl_2 \cdot 6H_2O$

6.3.2 $CaCl_2 \cdot 6H_2O + KNO_3$ Corrosion Testing

Similar Isothermal corrosion test results at 30, 50, and 80°C was conducted for the CC6+KN PCM. The five metals presented in Table 6.4 were tested for test periods of up to one year. These isothermal test results are presented graphically in Figure 6.7 through Figure 6.9.

Figure 6.7 through Figure 6.9 show that for nearly all of the temperatures and metals the corrosion rate decreases with time as expected. There is one exception to this rule. At 30°C, (Figure 6.7), both of the aluminum alloys do not show a clear decreasing trend in corrosion rate with increasing test time. More importantly, at the longest test time (corresponding to 1 year), the corrosion rate of Al 5086 and Al 6061 are still above the 20 µm/yr threshold.

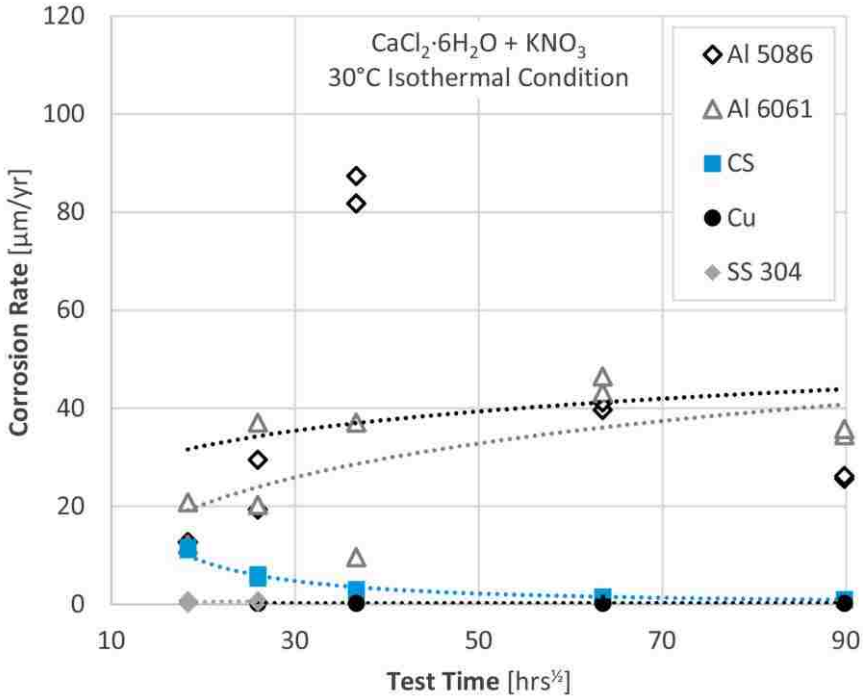

Figure 6.7: Isothermal Corrosion Test Results in CC6+KN at 30°C

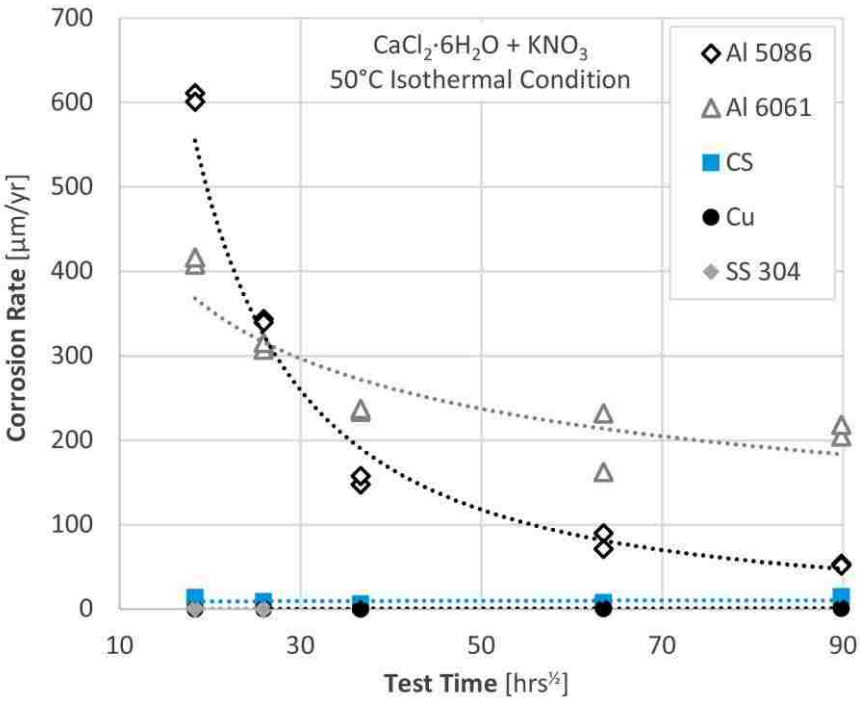

Figure 6.8: Isothermal Corrosion Test Results in CC6+KN at 50˚C

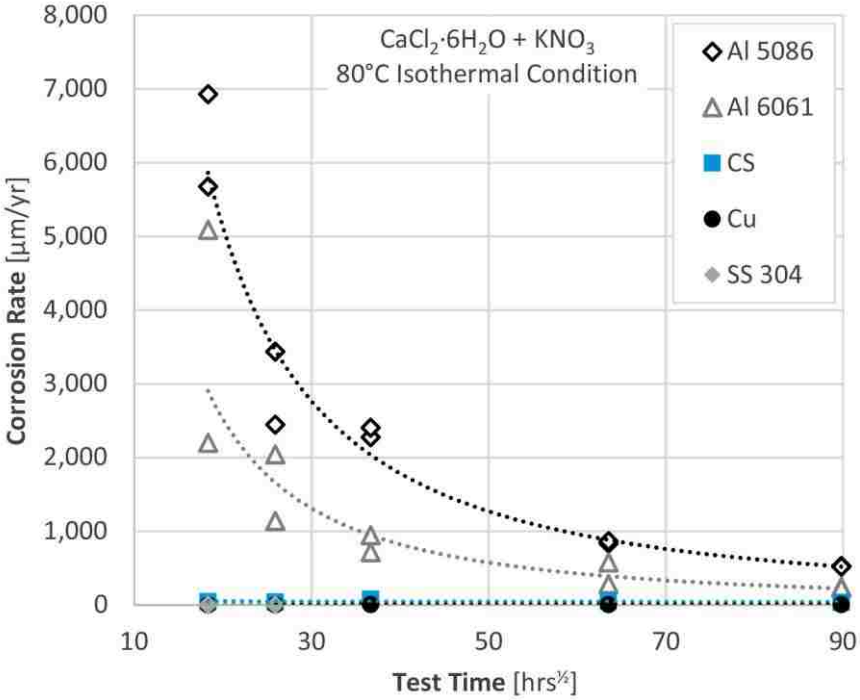

Figure 6.9: Isothermal Corrosion Test Results in CC6+KN at 80˚C

At the higher temperatures, the long-term corrosion rate of aluminum was found to be even worse, with a corrosion rate upwards of 500 μm/yr experienced by Al 5086 after 1 year of testing at 80°C (Figure 6.9). This high of a corrosion rate corresponds to dramatic corrosion of the test coupons, with large portions of the coupons being corroded away within a few weeks of the beginning of testing. The corrosion of Al 5086 and Al 6061 in CC6+KN at 30, 50, and 80°C for a two-week test period are shown in Figure 6.10. It can be clearly seen that as temperature increases, a white "froth" forms around the aluminum coupons in the bottles. This "froth" is formed from the corrosion products produced as the aluminum is oxidized. At 80°C, the "froth" is so dense that the aluminum coupon is no longer visible. Upon removal, coupon corrosion is very apparent with the lower portions of the coupons showing considerable pitting and metal loss at the higher temperatures (Figure 6.11).

These results clearly indicate that the two aluminums tested are not appropriate for use with the CC6+KN PCM. In summary, the addition of 7 wt% KNO_3 to $CaCl_2 \cdot 6H_2O$ was found to dramatically increase the corrosion rate of Al 5086 and Al 6061 – especially at temperatures greater than 25°C. Despite this poor performance on the part of the aluminum alloys, carbon steel and copper had better corrosion resistance in CC6+KN (Figure 6.12). Despite this better performance, at 80°C, even carbon steel was found to have a corrosion rate in excess of 30 μm/yr, which is well above the limit of 20 μm/yr. On average, at a given temperature, CS had an order of magnitude greater corrosion rate than copper, meaning copper easily met the 20 μm/yr criteria even at 80°C.

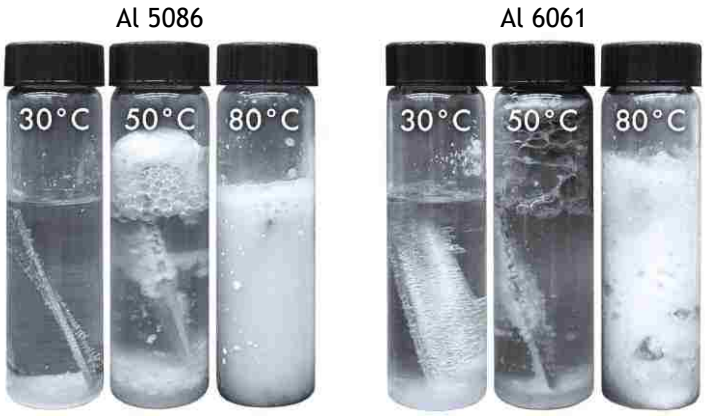

Figure 6.10: Corrosion of Al 5086 and Al 6061 in CC6+KN After 2 Weeks

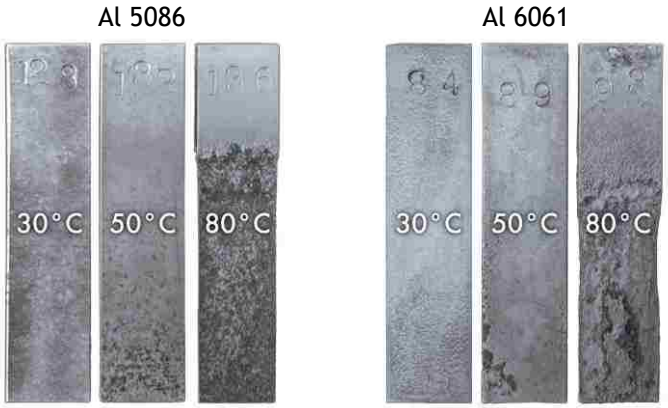

Figure 6.11: Al 5086 and Al 6061 Coupons After 2 Weeks of Corrosion in CC6+KN

Limited isothermal corrosion data for SS 304 in CC6+KN was also obtained for test periods of 2 and 4 weeks (Figure 6.13). It is clear that SS 304 is the best-performing metal in CC6+KN, with a corrosion rate of less than 1 μm/yr found for all three temperature conditions.

The temperature dependence of corrosion in CC6+KN was considered through the use of an Arrhenius plot for CC6+KN. This Arrhenius plot is presented in Figure 6.14 for a 24 week test period, with activation energies tabulated in Table 6.6. The linear regressions were found to fit the data very well with R^2 values for all four metals being greater than 0.9.

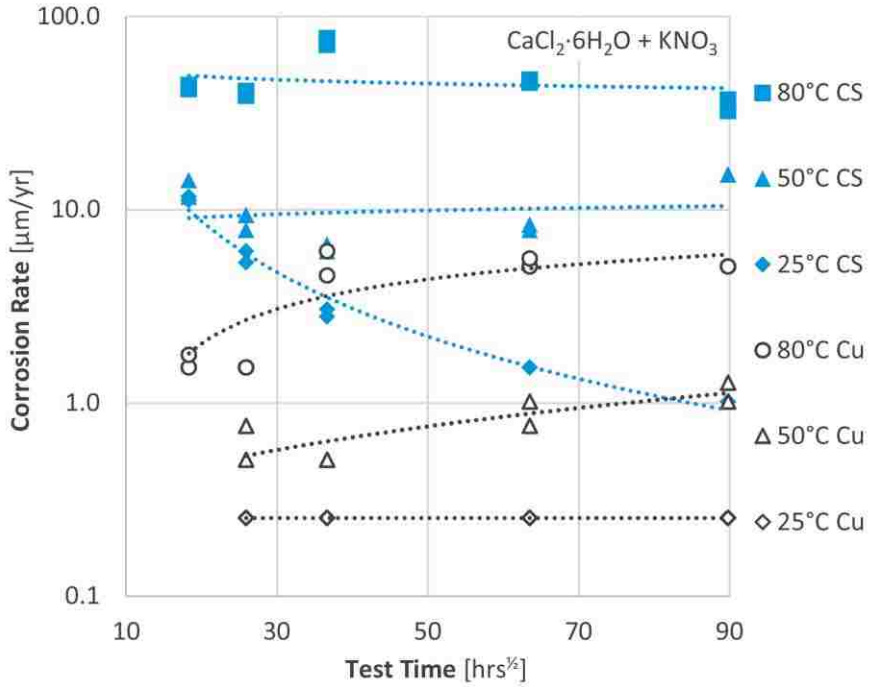

Figure 6.12: Isothermal Corrosion Rate of CS and Cu in CC6+KN

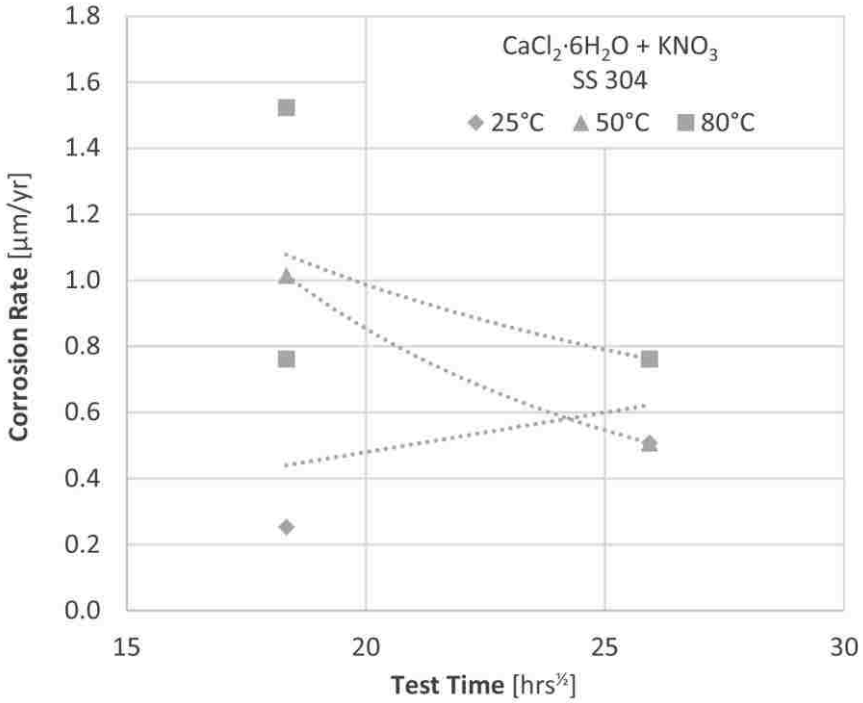

Figure 6.13: Isothermal Corrosion Rate of SS 304 in CC6+KN

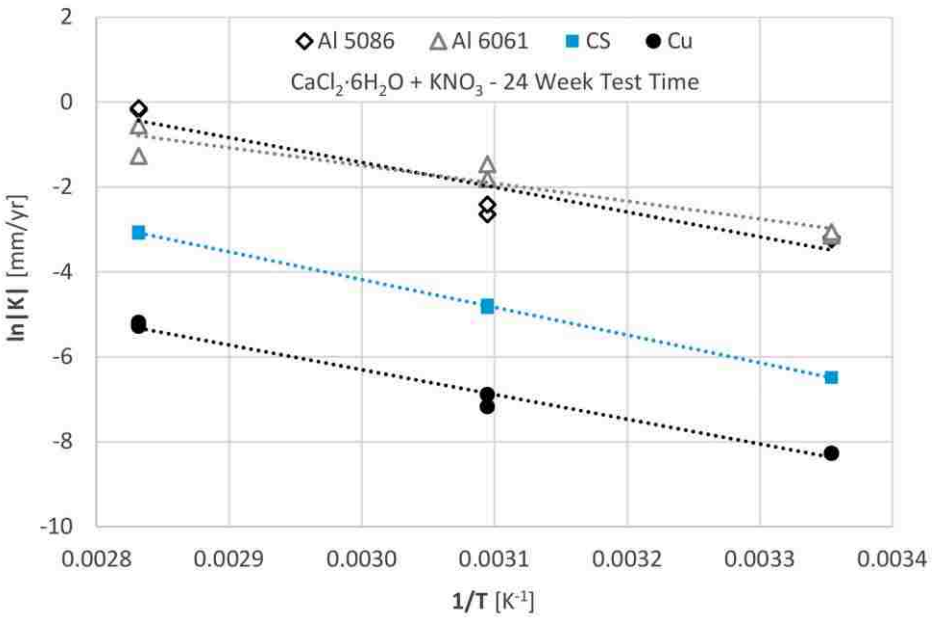

Figure 6.14: Arrhenius Curve Fits for Metals in CC6+KN

Table 6.6: Activation Energy for Metals Immersed in CC6+KN

Metal	E_a [kJ/mol]	R^2
Copper	14,448.60	0.985
CS	16,193.29	1.000
Al 5086	14,471.65	0.908
Al 6061	10,387.57	0.903

6.3.3 $CaCl_2 \cdot 6H_2O + MgCl_2 \cdot 6H_2O$ Corrosion Testing

Isothermal corrosion testing of the five metals in the CC6+MC6 PCM was also conducted at 25, 50 and 80°C, with the results presented in Figure 6.15 through Figure 6.17. As was the case for the other two PCMs, the corrosion rate was found to decrease with increasing test time for most of the metal/temperature combinations. Copper was found to not follow this trend at 50 and 80°C and SS 304 was found to increase in corrosion rate with increasing time for the 80°C condition. Overall, CS was found to have the highest corrosion rate after 1 year of testing at all

temperatures, although this corrosion rate was below 10 µm/yr at 80°C. Al 5086 and Al 6061 had comparable corrosion resistance with long-term corrosion rates of less than 5 µm/yr. These results suggest that either aluminum would serve well in long-term exposure to the CC6+MC6 PCM.

As with the other two PCMs, an Arrhenius relationship was used to quantify the dependence of corrosion rate in CC6+MC6 with temperature (Figure 6.18). The calculated activation energies and R^2 values for the linear regressions of all four metals are presented in Table 6.6.

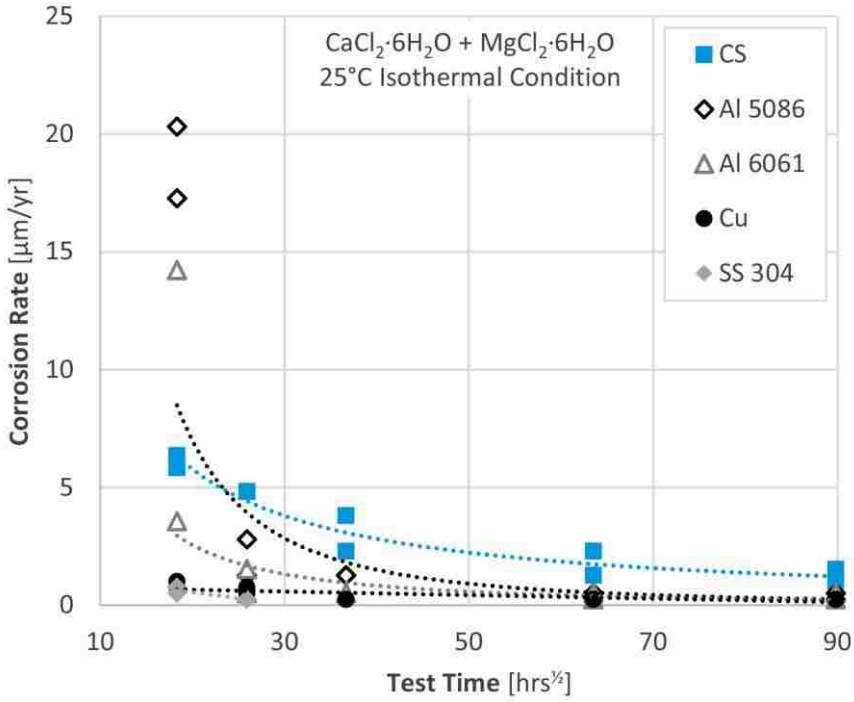

Figure 6.15: Isothermal Corrosion Test Results in CC6+MC6 at 25°C

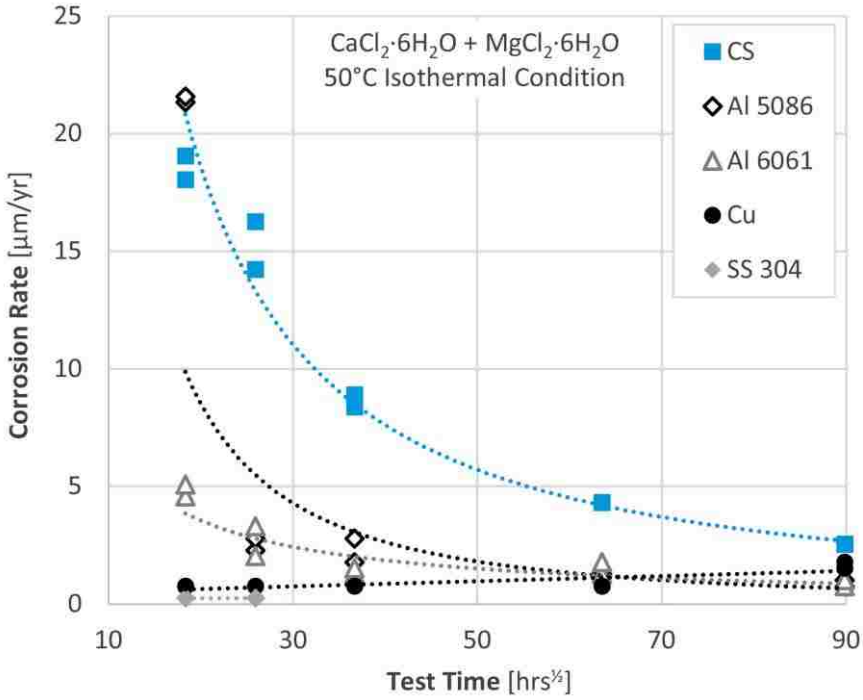

Figure 6.16: Isothermal Corrosion Test Results in CC6+MC6 at 50°C

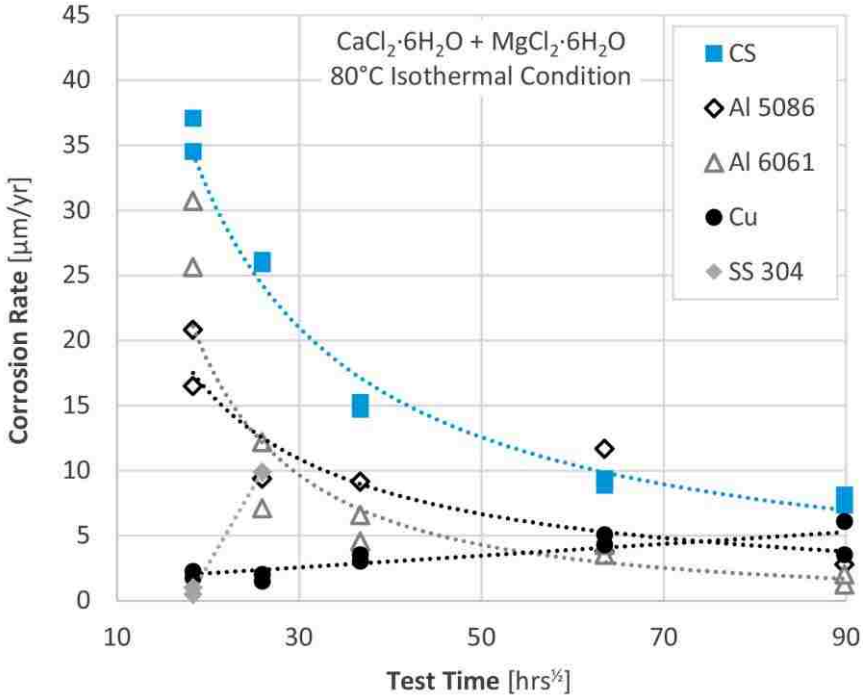

Figure 6.17: Isothermal Corrosion Test Results in CC6+MC6 at 80°C

Table 6.7: Activation Energy for Metals Immersed in CC6+MC6

Metal	E_a [kJ/mol]	R^2
Copper	13,838.53	0.980
CS	7,969.84	0.938
Al 5086	12,228.69	0.892
Al 6061	11,335.03	0.935

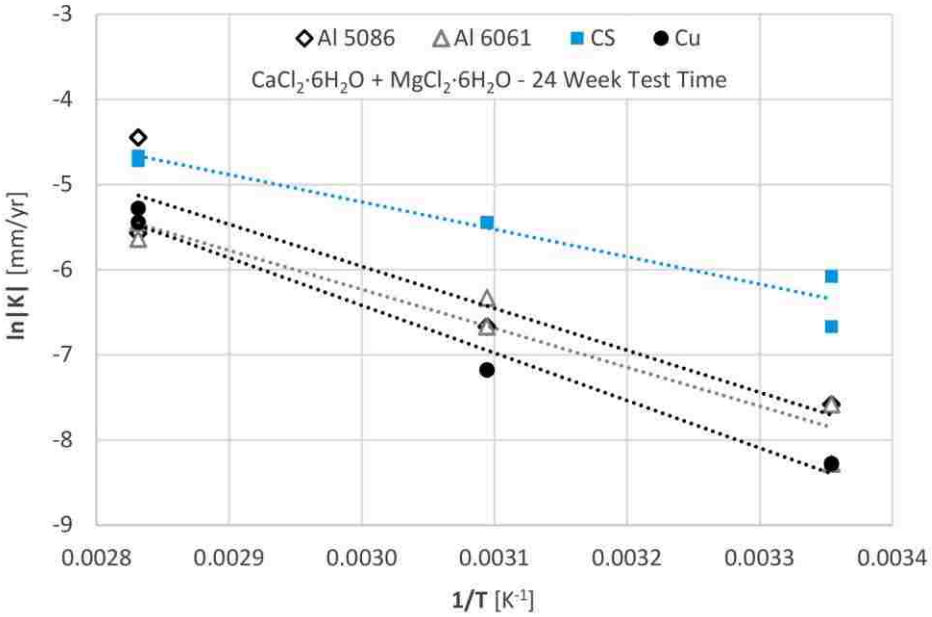

Figure 6.18: Arrhenius Curve Fits for Metals in CC6+MC6

6.3.4 Pitting

Since the ASTM-G1 method is based on a mass-loss principle, this method cannot accurately quantify non-uniform pitting of the coupons. This is a significant drawback as deep, localized pitting may only lead to marginal changes in mass, while severely impacting the integrity of the metal. For instance, consider the case of a deep pit, which leads to a pin-prick hole in a containment vessel. This pitting corrosion can often be hidden as the pits can form beneath what appears to be only surface-level corrosion. Pitting corrosion may be initiated by localized damage

to the oxide layer, a localized chemistry imbalance, or non-uniformities in the metal surface. Chlorine ions are known to be particularly problematic as they aggressively attack the protective oxide layer. Other factors, which influence pitting are pH, temperature and the dissolved oxygen. Aluminum alloys and stainless steels are known to have the most problems with pitting. If the oxide layer is locally breached and does not reestablish itself very quickly, corrosion at this location will proceed more rapidly than over the remainder of the metal, forming a corrosion pit.

After completing isothermal corrosion testing, the coupons were individually examined for pitting. This was strictly a visual observation. With the exception of the aluminum coupons in CC6+KN, where extensive corrosion took place, pitting was only observed on the aluminum coupons removed from the CC6. The nature of this pitting varied between the two alloys with pitting of the Al 5086 being less severe based on the size of the formed pits. Figure 6.19 presents Al 5086 and Al 6061 coupons at all three isothermal temperature conditions. Pits in these coupons appear as dark points or regions on the light surface of the coupons. It can be seen that at the higher temperatures the number and/or size of the pits increases for both metals. However, the pits formed in the Al 6061 are much larger with less uniformity than those in the Al 5086. While the number, size, and depth of these pits have not been quantitatively examined across all of the test coupons, these general trends have led to the recommendation that Al 5086 is more suited for used in CC6-based salts than Al 6061.

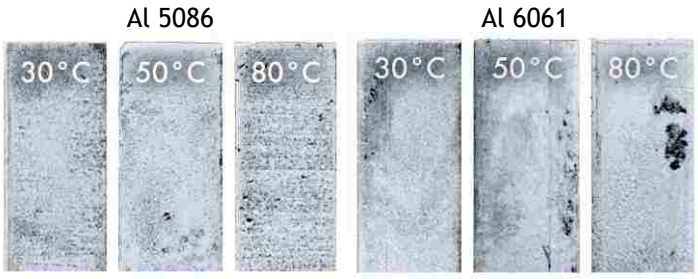

Figure 6.19: Pitting of Aluminum During Isothermal Corrosion Testing

6.4 Cycling Corrosion Testing

It was necessary to conduct comparable corrosion testing under cycling conditions. The phase transition between liquid and solid is capable of exerting considerable mechanical stresses on any surfaces in contact with the PCM. It was hypothesized that these stresses could decrease corrosion resistance of the metals through mechanical fracturing of the protective oxide layer formed on the surface of the metal. Cycling corrosion of stainless steel, carbon steel, two aluminum alloys, and copper in CC6 was examined by Porisini after up to 5650 cycles [P14]. Stainless steel was found to be resistant to corrosion, carbon steel and copper were slightly corroded, and the aluminum alloys experienced deep pitting [P14]. Besides this work my Porisini, cycling corrosion testing of metals in CC6 is largely absent from the literature. The current work builds on aspects of cycling not discussed by Porisini, namely the progression of corrosion during cycling (corrosion rate vs. number of cycles) and the relationship between corrosion rate and the cycling rate. In addition, the cycle corrosion results can be directly compared with the isothermal corrosion test results above.

Corrosion testing of CS, Al 5086 and SS 304 was conducted in CC6 at the two cycling rates of t = 0.5 hr. and 2.5 hrs. At t = 0.5 hr., testing for up to 1,200 complete cycles was conducted, while this number was reduced to 600 cycles for the t = 2.5 hr. condition. CS and Al 5086 were selected for cycling testing due to their low cost and ease of manufacturing. Also, these two metals showed good corrosion resistance during isothermal testing, and in the case of Al 5086, better resistance to pitting vs. Al 6061. Cycling of SS 304 was also conducted, but only at the t = 2.5 hr. condition. A summary of corrosion rate results under cycling is presented in Figure 6.20.

At the fast corrosion rate (t = 0.5 hr.), Figure 6.20 shows a relatively high (~10 μm/yr) corrosion rate for both CS and Al 5086 after 1,200 cycles, with Al 5086 performing worse. These results were not unexpected if the protective oxide layer were being mechanically damaged during

cycling. Interestingly, as the cycling rate was slowed to t = 2.5 hrs., the corrosion rate of both metals decreased significantly. In fact, it can be seen in Figure 6.20 that the corrosion rate of Al 5086 is less that of SS 304 during slow cycling.

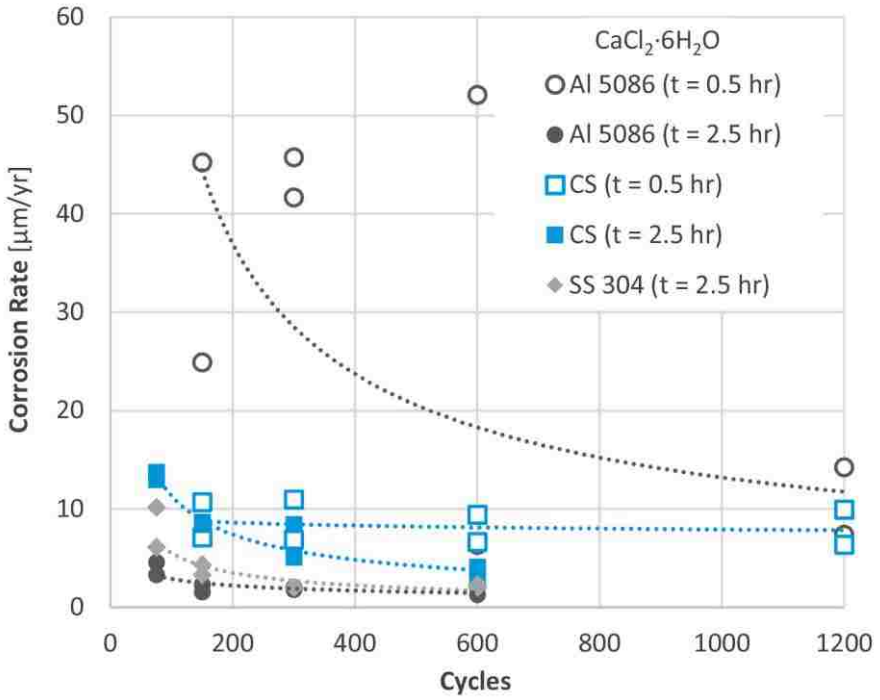

Figure 6.20: Cycling Corrosion Test Results

For better comparison, the corrosion rates for CS and Al 5086 under isothermal and cycling conditions are plotted in Figure 6.21 and Figure 6.22 respectively. These results were normalized to the square root of test time, with test time for the cycling cases being the real-world time required to complete the cycle duration examined. This is why the slow and fast cycling conditions have similar test times, despite the fact that the fast cycling samples completed twice as many cycles. When the corrosion rate of CS under fast cycling is compared to the isothermal condition in Figure 6.21, it can be clearly seen that while the corrosion rate decreases with increasing test time for the isothermal case, the same cannot be said for the fast cycling case.

Throughout fast cycling, the corrosion rate of CS remains virtually unchanged at close to 7.5 µm/yr, while the corrosion rate for the isothermal case is seen to continue to decrease through 1 year of testing. As mentioned by Bradshaw et al., a metal mass loss rate, which scales linearly with time (aka. a flat corrosion rate with time), implies that the protective oxide layer is porous and does not adequately protect against additional corrosion [B18]. In the case of cycling corrosion, it is suggested that increased oxide layer porosity may be due to mechanical damage to the layer.

Interestingly, when the cycling rate was slowed to t = 2.5 hrs., the corrosion rate of CS was once again found to decrease with increasing test time. In fact, the corrosion rate curves for the slow cycling and 50°C isothermal conditions are nearly identical, indicating cycling does not adversely impact the corrosion rate of CS in CC6 if the cycling rate is below a certain threshold.

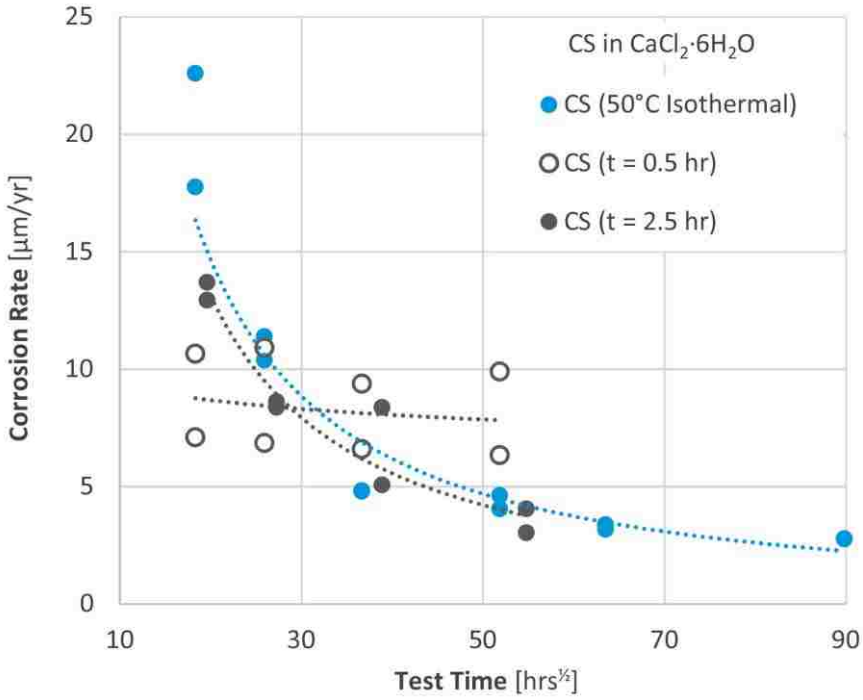

Figure 6.21: Corrosion Rate of CS in CC6 Under Isothermal and Cycling Conditions

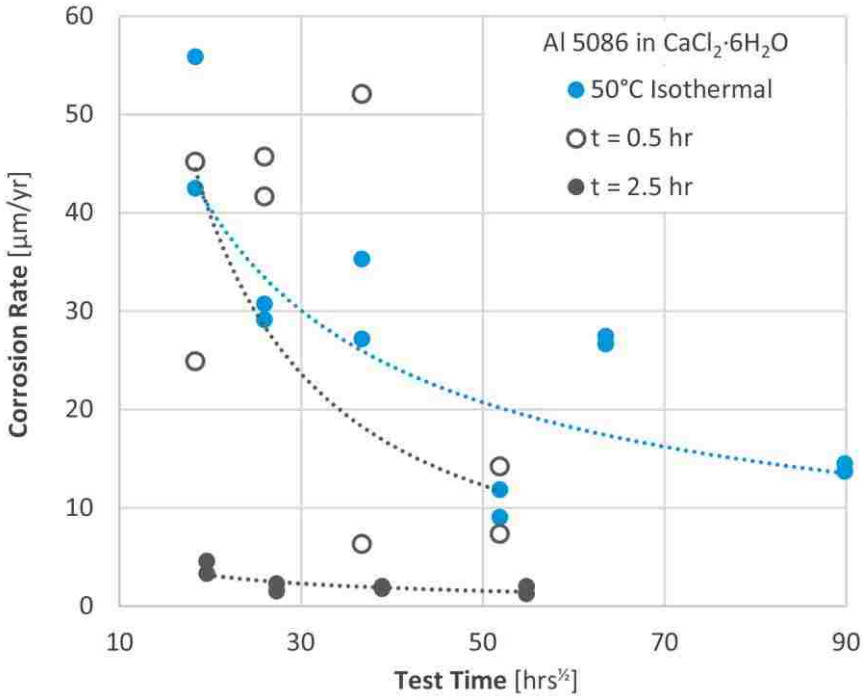

Figure 6.22: Corrosion Rate of Al 5086 in CC6 Under Isothermal Cycling Conditions

The comparison of isothermal and cycling conditions for Al 5086 in Figure 6.22 show that the corrosion rate of this metal always decreases with increasing test time – even during fast cycling. This indicates that the oxide layer formed on the surface of this metal is quite durable and is not easily disturbed by freezing and melting of the $CaCl_2 \cdot 6H_2O$. Still, an order of magnitude decrease in the corrosion rate was found when the cycling rate was slowed. This trend of a reduced corrosion rate at a slower cycling rate is promising as the cycling rate of most PCM-based thermal storage systems operate on even greater cycle timescales. For instance, the ACC cold-storage system proposed in Section 1.1 would operate on a 24 hr. cycle.

6.5 Anodized Aluminum

Later in the test regime, isothermal corrosion testing of anodized Al 5086 in $CaCl_2 \cdot 6H_2O$ was conducted at 50°C. Coupons were cut from sheets of Al 5086 before being anodized with a Type III coating (III Al 5086). Type III anodizing, also referred to as "Hard Coat", forms a harder and more abrasion resistant coating on the surface of the aluminum than the more typical Type II method. Ten coupons were placed into $CaCl_2 \cdot 6H_2O$ at 50°C and were removed after 2, 4, 8, 16, and 24 weeks.

Results from this testing are presented in Figure 6.23 alongside comparable corrosion test results for CS, Al 5086 and Al 6061. Anodized Al 5086 showed no weight loss during corrosion for the samples removed at 2, 4, and 8 weeks. The samples removed at 16 weeks had a corrosion rate close to, but slightly below that of the two non-anodized aluminums. As with the raw aluminum samples, the corrosion rate was seen to decrease after this initial increase (between 16 and 24 weeks). It is believed that the anodized coating prevented significant corrosion of the coupons for up to 8 weeks. After 8 weeks elapsed, the coating was no longer capable of preventing all corrosion and the coupons began to corrode. This corrosion rate decreased with time as a protective oxide layer accumulated on the surface of the coupon. The dashed black line in Figure 6.23 shows a potential path of the corrosion rate for the anodized Al 5086 samples. Overall, the corrosion rate of anodized Al 5086 at 24 weeks was found to be less than half the corrosion rate of raw Al 6061 and was an order of magnitude less than raw Al 5086.

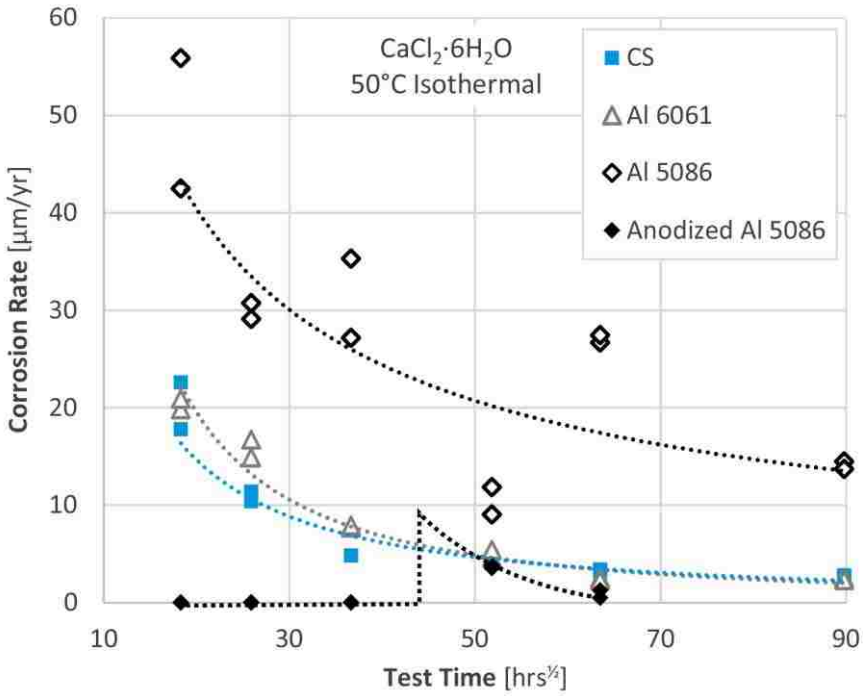

Figure 6.23: 50°C Isothermal Corrosion Test Results Including Anodized Al 5086

Anodized Al 5086 was also tested at 80°C isothermal, with these results presented alongside comparable isothermal results for the raw Al 5086 in Figure 6.24. As in the 50°C case, for the 80°C case the corrosion rate was found to jump, but this jump occurred at a shorter test time. This is to be expected as the jump is believed to correspond to the point where the anodization no longer perfectly protects the coupon from the salt. It is logical that this jump would occur at an earlier point at a higher test temperature. Still, the critical conclusion to be drawn from Figure 6.24 is that anodized Al 5086 has an order of magnitude greater corrosion resistance than raw Al 5086.

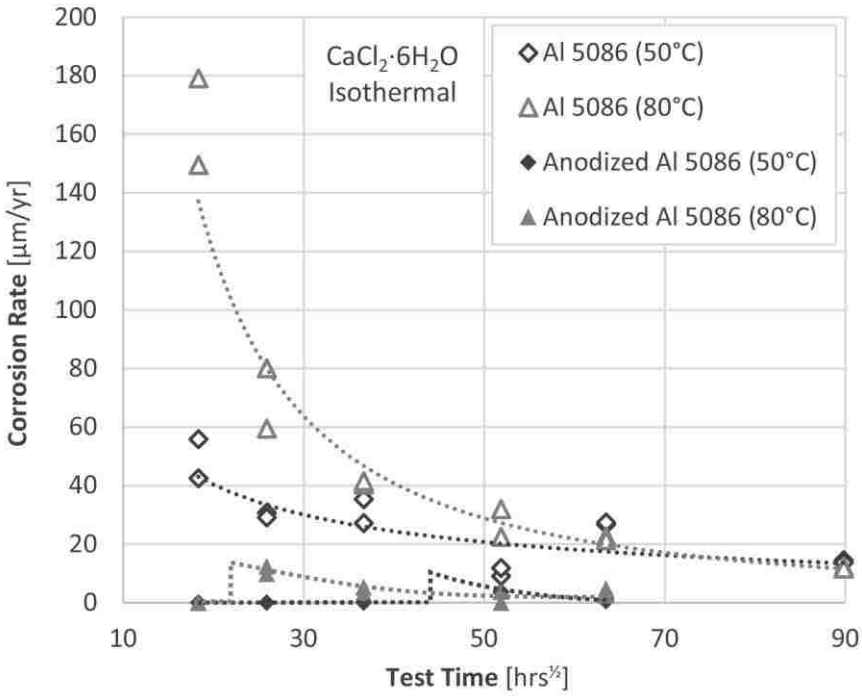

Figure 6.24: Comparison of Isothermal Testing of Anodized and Raw Al 5086

Anodized Al 5086 was also slow cycled alongside raw Al 5086 and CS (Figure 6.25). These results clearly show the benefit of anodization on preventing corrosion. At the longest test period of 600 cycles (~3000 hrs. of testing), CS was found to have a good corrosion rate of 4 µm/yr. At this condition, Al 5086 performed more than twice as well with a corrosion rate of less than 2 µm/yr. Through the addition of type III anodizing to the Al 5086, the corrosion rate was further suppressed by an order of magnitude to around 0.1 µm/yr.

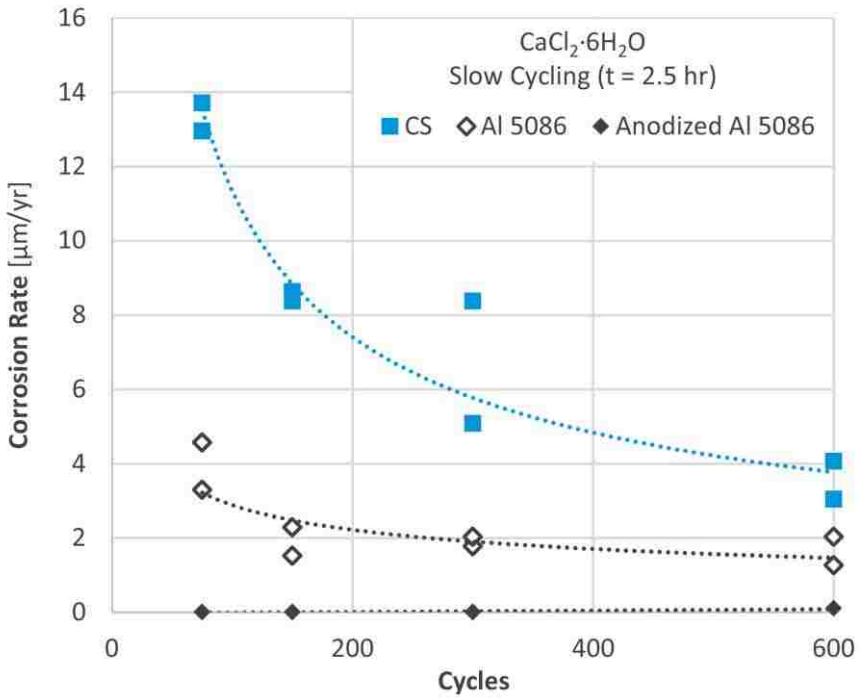

Figure 6.25: Corrosion Rate of CS, Al 5086 and Anodized Al 5086 Under Slow Cycling

6.6 Summary of Corrosion Test Results

Corrosion testing of PCM/metals pairs for the three $CaCl_2 \cdot 6H_2O$-based PCMs has produced info for long-term use of five common metals with the PCMs. A summary of these long-term corrosion test results is presented in Table 6.8.

Beginning with $CaCl_2 \cdot 6H_2O$, all of the metals tested were found to have an acceptable long-term corrosion rate (< 20 µm/yr) under all isothermal test temperatures. CS and Al 5086 were targeted for additional cycle testing due to their low cost and the improved pitting resistance of Al 5086 relative to Al 6061. Under fast cycling, CS experienced an increase in the corrosion rate relative to the isothermal cases. However, once the cycling rate was slowed, this corrosion rate fell by around 50%. For Al 5086, fast cycling did not appreciably change the long-term corrosion rate relative to the isothermal cases. However, under slow cycling the corrosion rate was found to be

even lower than for the lowest temperature isothermal condition. Finally, testing of Type III Anodized Al 5086 showed excellent corrosion resistance under both the isothermal and slow cycling conditions. This improvement is notable as the corrosion rate of III Al 5086 is an order of magnitude lower than that of Al 5086 under slow cycling. Since the cost of anodization is quite low, this is proposed as an effective and cost-effective method for reducing the corrosion rate of aluminum in long-term contact with $CaCl_2 \cdot 6H_2O$.

Table 6.8: Summary of Long-term Corrosion Rate Results for all PCM/Metal Pairs

PCM	Metal	$T_{m(l)}$ [μm/yr]	50°C [μm/yr]	80°C [μm/yr]	t = 0.5 hr Cycling [μm/yr]	t = 2.5 hr Cycling [μm/yr]
$CaCl_2 \cdot 6H_2O$	Cu	0.5	1.9	4.4		
	CS	0.8	2.8	2.4	8.1	3.6
	SS 304	0.3	0.3	0.3		2.2
	Al 5086	2.2	14.1	11.9	10.8	1.7
	Al 6061	1.7	2.4	7.9		
	III Al 5086		0.9	3.7		0.1
$CaCl_2 \cdot 6H_2O$ + 7% KNO_3	Cu	0.3	1.1	5.1		
	CS	1.0	15.2	34.8		
	SS 304*	0.6	0.5	0.8		
	Al 5086	25.9	52.6	525		
	Al 6061	35.2	212	238		
$CaCl_2 \cdot 6H_2O$ + 18% $MgCl_2 \cdot 6H_2O$	Cu	0.3	1.7	4.8		
	CS	1.3	2.5	7.8		
	SS 304*	0.3	0.1			
	Al 5086	0.4	0.9	2.8		
	Al 6061	0.4	0.9	1.7		

* Longest data was only at the 4 week test time.

For $CaCl_2 \cdot 6H_2O$ + 7% KNO_3 the long-term corrosion rate of most metals was found to be quite high during isothermal testing. Cu and SS 304 performed the best with the maximum corrosion rate of 5.1 μm/yr found for Cu at the 80°C test condition. Aluminum was found to be strongly incompatible with the CC6+KN PCM, with corrosion rates in excess of 500 μm/yr measured for Al

5086 at 80°C. Even at the $T_{m(l)}$ temperature, both aluminum alloys had corrosion rates in excess of 20 µm/yr, making them unsuitable for long-term use with CC6+KN. Carbon steel performed better in this PCM, but its use should be taken with caution as the 80°C isothermal condition was found to exceed the 20 µm/yr threshold.

$CaCl_2 \cdot 6H_2O$ + 18 $MgCl_2 \cdot 6H_2O$ was found to have similar material compatibility to $CaCl_2 \cdot 6H_2O$. As expected, SS 304 was found to have the best corrosion resistance at all three isothermal temperatures. Surprisingly, the aluminum alloys followed SS 304 with the second-best performance. In fact, for the 50°C condition, it can be seen in Table 6.8 that both aluminums have a corrosion rate of less than 1 µm/yr. Copper follows aluminum with CS having the highest corrosion rate at the longest test period of 1 year. Still, even as the worst performer in CC6+MC6, CS has a long-term corrosion rate of less than 8 µm/yr at up to 80°C isothermal. This indicates that any of the five metals tested would be a good candidate for use with this PCM.

7 $CaCl_2 \cdot 6H_2O$ PCMs at Scale

As mentioned in Chapter 1, the primary advantage to the use of hydrated salt PCMs is their low price. However, in order to realize this lost cost, industrial-grade salts must be used when the product is scaled-up. Up to this point, all of the test results in this report have been for laboratory-grade salts, which have a higher price tag ($42/kg for CC6 [F12]). With this higher cost comes a higher purity material (>97 wt% $CaCl_2 \cdot 6H_2O$). This does not mean that all industrial-grade salts have a low $CaCl_2$ purity. For instance, Table 7.1 presents the manufacturer supplied composition for Dow's Briners Choice anhydrous $CaCl_2$. As seen, the purity of this $CaCl_2$ is quite high (>94 wt%). When mixed with water to the hexahydrate composition (50.6 wt% $CaCl_2$), the purity of CC6 could be as high as 97.2 wt%, which is comparable to the low range of laboratory-grade salts. This Dow $CaCl_2$ retails around $1.25/kg in relatively small quantities of several hundred kilograms [A3].

Table 7.1: Dow Briners Choice $CaCl_2$ Composition

	wt%
$CaCl_2$	94.5
KCl	2.5
NaCl	1.6
$CaBr_2$	0.9
H_2O	0.5

The supercooling tests of Section 4.6.2 and stability testing in Section 5.5 have demonstrated the importance of adding small percentages of $SrCl_2 \cdot 6H_2O$ and KCl to $CaCl_2 \cdot 6H_2O$. These additives are available at the slightly greater prices of $6.28/kg ($SrCl_2 \cdot 6H_2O$) and $18/kg (KCl) [A3]. However, given the low required weight percentages of these additives, this higher cost does little to impact the low cost of the final PCM (Estimated at ~$1.74/kg [A3]). It should be noted

that these costs are for small-batch orders from United States suppliers. The project partner, Advanced Cooling Technologies (ACT), has received quotes for $CaCl_2$ from several Chinese suppliers, with prices as low as $0.22/kg [A3].

7.1 Characterization of Industrial-Grade CC6

Industrial-grade, anhydrous $CaCl_2$ was purchased from the Dow Chemical Company with a manufacturer-supplied composition seen in Table 7.1. This anhydrous $CaCl_2$ was mixed with water, $SrCl_2 \cdot 6H_2O$, and KCl at the weight percentages indicated in Table 7.2. During mixing, excess water was intentionally added to this mixture with the expectation that the PCM would self-stabilize to a eutectic composition where any excess water would end up in the supernatant liquid, which would be removed. This phenomenon was discussed more fully in Section 5.5.

Table 7.2: Component Mixture for Industrial-Grade CC6

Component	wt%	mol/mol_{CC}
$CaCl_2$	46.66	1
H_2O	48.34	6.38
$SrCl_2 \cdot 6H_2O$	3.00	0.03
KCl	2.00	0.06

Assuming that the added water fully hydrates the $CaCl_2$ to $xH_2O = 6$, the weight percentage of excess water (Ex. H_2O) for this mixture was calculated as seen in Table 7.3. After preparing this mixture in bulk (as will be discussed in Section 7.2), a few hundred grams were removed for testing via drop calorimetry and cycling. Four RTD-instrumented samples (1I, 4I, 7I, and 17I) of ~80 g each were prepared in the same shortened stainless steel cylinders used for slow cycling and drop calorimetry of the laboratory-grade PCM samples.

Table 7.3: Component Breakdown of Industrial-Grade CC6 Showing Excess H_2O

Component	wt%	mol/mol$_{CC}$
$CaCl_2 \cdot 6H_2O$	92.11	1
Ex. H_2O	2.89	0.38
$SrCl_2 \cdot 6H_2O$	3.00	0.03
KCl	2.00	0.06

Two additional samples (20I and 21I) were prepared from the same salts, where water was added to the $CaCl_2$ at the stoichiometric composition required for the formation of a 6-hydrate. In other words, a final composition of: 95 wt% CC6, 3 wt% SC6, and 2 wt% KCl. After these samples were prepared, they were frozen with any supernatant liquid being removed prior to testing. The final weights of these two samples are presented in Table 7.4 alongside the 4 other samples.

Table 7.4: Industrial-Grade CC6 Samples for Drop Calorimetry and Cycling

Sample	m_{ENC} [g]	m_{PCM} [g]	Ex. H_2O [wt%]
1I	247.2	74.2	2.89
4I	242.3	86.1	
7I	244.3	87.4	
17I	245.9	83.9	
20I	241.7	71.5	0
21I	241.0	72.3	

The samples in Table 7.4 were cycled in the water bath between 22 and 32°C with 1°C/hr. temperature ramps and 2 hour holds at both the hot and cold temperature extremes (a 24 hour cycle). The latent heat storage capacity of the samples was measured by drop calorimetry at 0, 10, 15, and 40 cycles (Figure 7.1).

Upon examination of Figure 7.1, the first thing that is evident is the significant difference in H_f between the samples with and without excess water. At 0 cycles, the 2.89 wt% excess water samples have an average H_f of 134 J/g, while the 0 wt% excess water samples average 149 J/g at 0 cycles. In addition to differences in H_f between the samples with different quantities of added H_2O, the drop calorimetry results were also used to estimate the melting temperatures of the PCMs. For the 2.89 wt% excess water samples, an average melting temperature of 26.0°C was found, while a slightly higher value of 28.5°C was found for the samples with no excess H_2O.

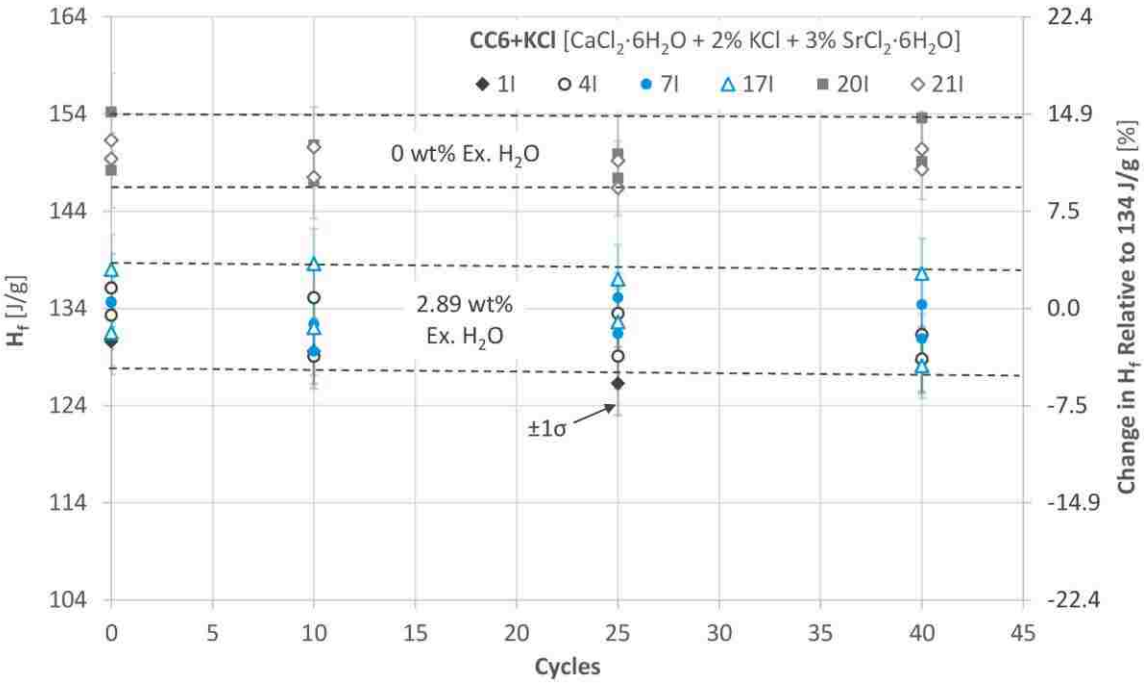

Figure 7.1: H_f During Slow Cycling of CC6+KCl PCM Made with Industrial-Grade Salts

These findings suggest that otherwise identical samples of $CaCl_2·6H_2O$, $SrCl_2·6H_2O$, and KCl can result in different stable forms depending on the quantity of excess water present in the samples. This agrees well with the modeled ternary phase diagram of the $CaCl_2$-H_2O-KCl system (Figure 7.2). The ternary phase diagram suggests that there are various eutectic mixtures of $CaCl_2$-H_2O-

KCl, which can be formed more or less along a line of constant KCl concentration. Because of this correlation between eutectic points and a line of constant KCl concentration, changing the quantity of H_2O in the mixture simply shifts the PCM along the constant KCl concentration line, forming a new eutectic mixture in the process. Figure 7.2 suggests that the primary difference between eutectics at different H_2O concentrations will be their phase transition temperature, with higher H_2O concentrations lowering the phase transition temperature. This agrees well with the finding of a lower melt temperature for the industrial-grade salt with 2.89 wt% excess water.

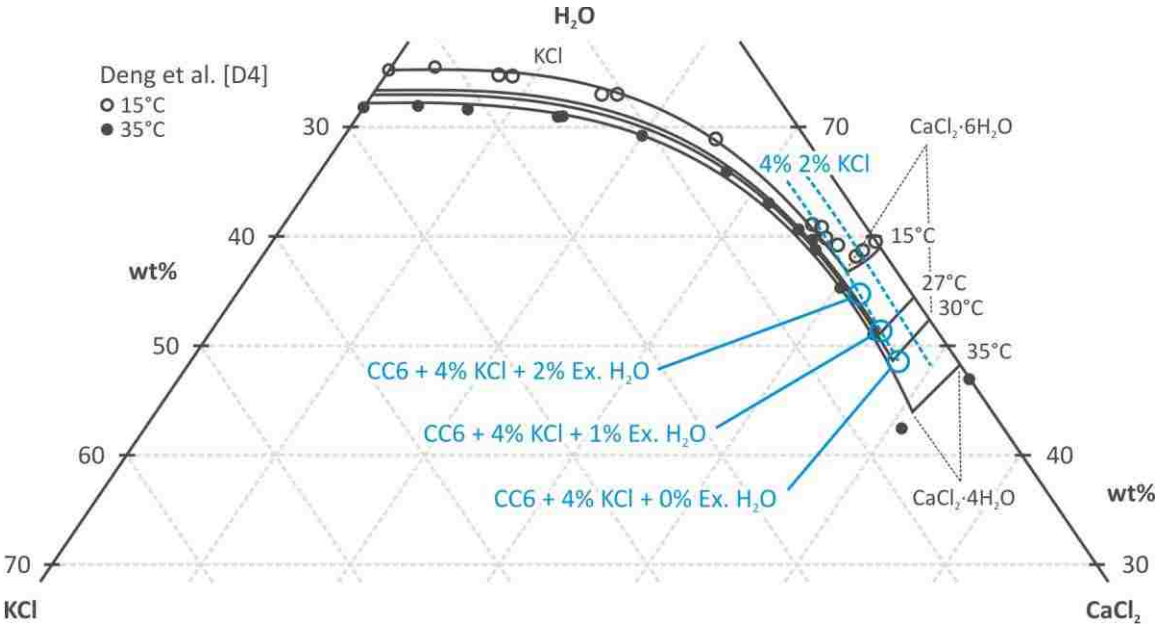

Figure 7.2: Modeled Ternary Phase Diagram of $CaCl_2$-H_2O-KCl System

Although Figure 7.1 shows good thermal stability with cycling, it is also suggesting that there is a slight decrease in thermal performance between 0 and 40 cycles, for the 2.89 wt% excess water samples (around a 2.9% decrease in H_f). While this change is only slightly greater than the average calorimeter sample standard deviation (±2.64%), it still appears significant as all of the 2.89 wt% excess water samples show this decreasing H_f trend with increasing cycle number. Longer-term

cycle testing should be conducted to determine if this trend continues with increasing cycle number.

7.2 Preparation of Medium-Scale Quantities of CC6 PCM

In order for the preceding PCM lab-scale experiments to be of use commercially, preparation of the developed PCM must be capable of being scaled up. Through work with ACT, experience was gained in the scaling of the PCM preparation process. The following is an attempt to briefly discuss how lab-scale experiments can be scaled to several hundred kilograms of PCM.

In preparation for medium-scale (several hundred kilograms) PCM preparation, 50 pound (22.7 kg) bags of Dow Briners Choice anhydrous calcium chloride pellets were ordered and shipped to ACT. This is the same anhydrous $CaCl_2$ presented in Table 7.1. The required quantities of $SrCl_2 \cdot 6H_2O$ and KCl were also sourced and delivered.

7.2.1 Considerations for Mixing of $CaCl_2$ and Water

The initial mixture made during the preparation of the CC6 is that of $CaCl_2$ and H_2O, which is made at the 1:6 molar ratio. Determining the quantity of water to be added to the $CaCl_2$ would be straightforward except that truly anhydrous $CaCl_2$ is very difficult to obtain since it is a strong desiccant. If the $CaCl_2$ contains an initial mass of water, m_{w0}, the following equation can be used to determine the quantity of water, which should be added to the $CaCl_2$:

$$m_{add} = (xH_2O - n_{ew})m_{CC+w}\left(\frac{M_{H2O}}{M_{CC} + n_{ew}M_{H2O}}\right) \tag{56}$$

Where xH_2O is the desired moles of water per mole of $CaCl_2$, m_{CC+w} is the mass of $CaCl_2$ plus any entrained moisture, n_{ew} is the moles of entrained water relative to 1 mole of $CaCl_2$, m_{add} is the mass of water to add, M_{H2O} is the molar mass of water (18.015 g/mol), and M_{CC} is the molar mass of $CaCl_2$ (110.978 g/mol).

The hydration of $CaCl_2$ is a highly exothermic process, which complicates the PCM preparation process. While internal heat generation helps promote complete mixing, higher PCM temperatures favor the evaporation of water from the salt, impacting the water balance of the PCM. Tetra Chemicals Europe [T8] provides the heat of hydration for the hydrates of $CaCl_2$ as presented in Table 7.5. For the hexahydrate ($xH_2O = 6$), the heat of hydration is seen to be -840 kJ/kg. Using this value, the total heat released during the hydration of CC to CC6 (Q_{hyd}) is given by the following equation:

$$Q_{hyd} = m_{CC6}\ 840\ kJ/kg \tag{57}$$

Assuming that all of this energy is transferred to the PCM, the following energy balance for heating of the PCM during mixing is found:

$$m_{CC6}\ 840\ kJ/kg = m_{CC6}\ Cp_{CC6}(T_2 - T_1) \tag{58}$$

Where T_1 and T_2 are the PCM temperatures before and after hydration respectively and Cp_{CC6} is the specific heat of CC6. Rearranging Equation (58), the end temperature (T_2) can be estimated by:

$$T_2 = \frac{840\ kJ/kg}{Cp_{CC6}} + T_1 \quad (59)$$

Table 7.5: Heats of Hydration for Hydrates of $CaCl_2$ [T8]

xH_2O	Heat of Hydration [kJ/kg]
0	-
1	-240
2	-295
4	-600
6	-840

7.2.2 Mixing of $CaCl_2$ and H_2O

Work by both the ERC and ACT has shown that industrial-grade $CaCl_2$ and H_2O can be easily mixed together to create $CaCl_2 \cdot 6H_2O$. Heating of the mixed PCM is a concern due to the high heat of hydration for the hexahydrate concentration; as presented in Table 7.4. Excessive heating of the PCM can be problematic as water more easily evaporates from the hydrated PCM – especially as the temperature approaches 100°C. To prevent excessive heating during mixing, it is recommended that the $CaCl_2$ be slowly mixed with the water. In order to more quickly mix the $CaCl_2$ and water, it is suggested that mixing occur in a container, which is designed with a cooling system capable of removing the heat generated during hydration. Despite the problems associated with heating during mixing, this generated heat is also beneficial as it helps to promote better mixing of the $CaCl_2$ and water. A minimum mixing temperature of 40°C is recommended.

The following best practices are suggested when mixing $CaCl_2$ and H_2O to create $CaCl_2 \cdot 6H_2O$:

- $CaCl_2$ should be added to the H_2O at a rate, which prevents the mixture temperature from exceeding 80°C.
- The mixture temperature should not fall below 40°C in order to promote mixing of the $CaCl_2$ and H_2O. Since the reaction of water and $CaCl_2$ is highly exothermic, this process is self-heating.
- During mixing, the PCM mixture should be contained in an atmospherically-sealed container in order to prevent water loss to the atmosphere. If sealing is impractical during all steps of the mixing process, the time periods when the mixture is exposed to the environment should be kept to a minimum – especially when temperatures are greater than 40°C.
- The mixture should be stirred to promote complete mixing.

7.2.3 Addition of Additives to CC6

Once the water and $CaCl_2$ are fully mixed, 2 wt% KCl can be added to the CC6. Note that 2 wt% is a percentage of the final PCM weight with all additives. Or in other words, the following holds:

$$m_{KCl} = (m_{CC+w} + m_{add}) \frac{w_{KCl}}{1 - w_{KCl} - w_{SC6}} \tag{60}$$

Where m_{KCl} is the mass of KCl added to the PCM, w_{KCl} is the desired weight fraction of KCl, and w_{SC6} is the desired weight fraction of SC6. After adding KCl to the mixture, the PCM should be fully mixed by stirring. Next, the 3 wt% SC6 can be added to the PCM. Care should be taken to ensure that the PCM temperature is less than 50°C before the addition of SC6. This temperature limit is to prevent SC6 from liquifying and dissolving into the CC6, at which point it will no longer function properly as a nucleating agent. The melting temperature of SC6 is approximately 60°C. The 3 wt% SC6 is added to the PCM according to the following equation:

$$m_{SC6} = (m_{ew} + m_{add}) \frac{w_{SC6}}{1 - w_{KCl} - w_{SC6}} \quad (61)$$

Where m_{SC6} is the mass of SC6 added to the PCM. After adding SC6, the PCM should be well mixed using a mechanical stirrer.

7.2.4 Prototype Test System

A 10 kWh prototype cold-storage system was constructed by ACT according to the design seen in Figure 7.3. The following results are a brief summary of ACT's findings during testing of this system. After construction of the prototype test system, the PCM heat exchanger was charged with around 200 L of pre-mixed PCM. The air-cooled radiator and steam evaporator were used to either heat or cool the heat transfer fluid running throughout the PCM heat exchanger. This setup allows for both melting and freezing of the PCM within the heat exchanger. Thermocouples at three vertical levels throughout the heat exchanger were used to record PCM temperatures throughout testing.

The prototype cold storage system was operated by ACT for around a six-month period with PCM temperatures, instantaneous power, and cumulative energy being either directly measured or calculated. During melting, power was directly measured using a Yokogawa analyzer, while during freezing it was calculated using a thermal resistance calculation. After 30 cycles, average power during melting was found to be reduced by approximately 7.7% from an initial value of 1.3 kW. While it is believed that this phenomenon may indicate the pretense of separation within the PCM, the current system design does not provide sufficient temperature information to conduct a complete energy balance. The differences in power with increased cycling should be examined further to determine what exactly they indicate. More importantly, future systems

should be designed such that complete material and energy balances can be conducted to determine cumulative energy transfer during melting and freezing.

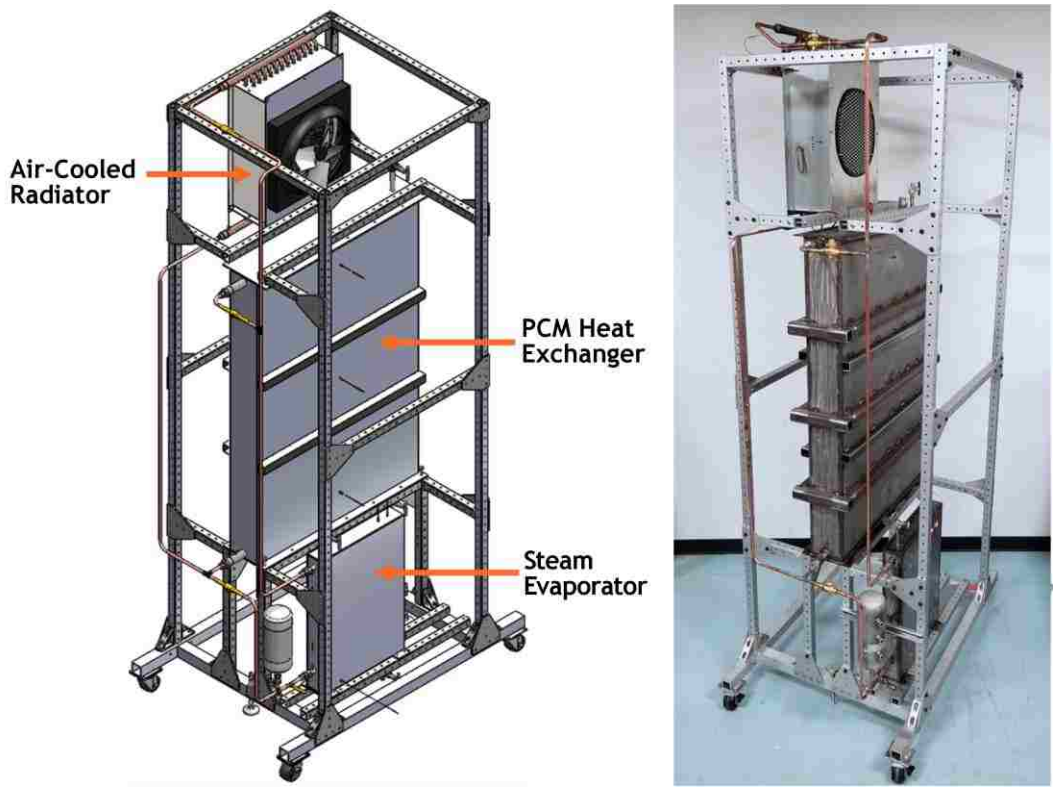

Figure 7.3: Design and Finished Prototype Cold Storage System

7.3 Summary of Experience with Industrial-Grade Materials

Industrial-grade formulations of $CaCl_2 \cdot 6H_2O$ + 3 wt% $SrCl_2 \cdot 6H_2O$ + 2 wt% KCl have shown good long-term stability under 24 hr. cycling. It was found that while this PCM self-stabilizes to a particular water content, this self-stabilized composition is dependent on the quantity of water initially present in the PCM. Stabilized PCMs were created with added water sufficient to meet the stoichiometric 6-hydrate condition as well as a case where 2.89 wt% excess water was added. For the 2.89 wt% excess water case, a lower heat of fusion and melt temperature was found

relative to the case with 0 wt% excess water above the 6-hydrate. When cycled, both of these industrial-grade salts were found to have good H_f stability up to 40 cycles. However, these results suggest a slight decrease in H_f for the 2.89 wt% Ex. water samples, while there was no observable change in H_f for the 6-hydrate stoichiometric samples. Given these results, it is suggested that care be taken during PCM preparation to ensure that the water added during $CaCl_2 \cdot 6H_2O$ preparation be sufficient and only sufficient in meeting the 6-hydrate condition.

It was found that $CaCl_2 \cdot 6H_2O$ could be effectively prepared in bulk (several hundred kg) by simple mixing of water and $CaCl_2$. Since heat removal during this process can be challenging, it is recommended that an appropriate heat rejection system be used during mixing. The required additives of KCl and SC6 are added to the mixed PCM after it has cooled. After 6 months of testing, the industrial-grade PCM in ACT's 10 kWh prototype cold storage system experienced a small decrease in measured average power, which may indicate separation within the PCM. Additional testing of this PCM at scale is required to determine its long-term thermal performance.

8 Conclusions and Recommendations

The research presented in this report summarizes work on the development of a low-temperature (T_m between 15 and 30°C) PCM. Throughout this research, the thermal properties, supercooling, stability, and corrosiveness of PCMs suited for the proposed applications were investigated and characterized. Three $CaCl_2 \cdot 6H_2O$-based PCMs were targeted for in-depth analysis, with potential solutions to uncovered issues being found and tested as required. Beginning with PCM characterization, the following is a summary of the key findings of this study:

- Two novel, low-temperature eutectic mixtures of $CaCl_2 \cdot 6H_2O$ (CC6)-based hydrated salts have been proposed; $CaCl_2 \cdot 6H_2O$ + 7 wt% KNO_3 (CC6+KN) and $CaCl_2 \cdot 6H_2O$ + 18 wt% $MgCl_2 \cdot 6H_2O$ (CC6+MC6). These PCMs have measured melt temperatures of 20 and 21°C, with H_f values of 120 and 149 J/g, respectively.
- While the literature has suggested a eutectic concentration of 66:33 wt. frac. for the CC6+MC6 mixture, a eutectic mixture of 82:18 wt. frac. was found experimentally. This result was supported by phase diagram modeling using the extended UNIQUAC model, as developed by Thomsen [T12]. It is recommended that additional experimental testing be conducted to provide empirical data, which can be compared to the modeled phase diagram results.
- $CaCl_2 \cdot 6H_2O$ was found to have good thermal performance with a measured T_m of 29°C and H_f of ~175 J/g.
- $SrCl_2 \cdot 6H_2O$ (SC6) was found to suppress supercooling of all $CaCl_2 \cdot 6H_2O$-based PCMs to within 2°C. While 1 wt% SC6 suppressed supercooling in CC6 at the beginning of cycling, it lost its effectiveness after 100 cycles. 3 wt% SC6 demonstrated good supercooling suppression in CC6 for up to 2,700 cycles. While using more than 3 wt% SC6 also suppressed supercooling during 2,700 cycles, the latent heat storage potential of the

PCM was reduced with increasing SC6 percentage. Because of this, is recommended that 3 wt% SC6 be used as it demonstrably suppresses supercooling for thousands of cycles, while not excessively decreasing the PCM's thermal storage capacity.

- The CC6+KN and CC6+MC6 eutectic mixtures were rapid-cycled for up to 2,700 cycles without significant changes in H_f as measured by drop calorimetry. It is believed that this good long-term performance is due to congruent melting and freezing of these eutectics.
- After rapid thermal cycling to 2,700 cycles, the H_f of CC6 was found to decrease by an average of 3.8% from 172.6 to 166.0 J/g. This result suggested that CC6 experienced phase separation during thermal cycling.

The phase stability of CC6 during repeated cycling was tested under different cycling conditions. With stability fully characterized, potential solutions to phase segregation (separation) were tested. The following key findings were found during stability testing of CC6:

- During phase separation, CC6 separates into three distinct layers, a supernatant $CaCl_2$ solution, CC6 and $CaCl_2{\cdot}4H_2O$ (CC4). The supernatant liquid is formed as a portion of the CC6 separates to form CC4 during freezing. After forty, 24-hour cycles, around 50% of the CC6 was found to have separated into CC4 and supernatant liquid.
- The cooling rate of CC6 was found to have a direct impact on separation with slower cooling rates corresponding to more separation. As the cooling rate approaches 0°C/hr, up to 5 wt% of the available CC6 was found to separate per cycle. Alternatively, at cooling rates of 20°C/hr, separation per cycle was found to approach 0%. When samples of CC6 were cycled at 1°C/hr, H_f was found to decrease by as much as 34% after 25 cycles. These results have important implications for rapid-cycling of CC6 as rapid cycling positively biases separation. This is problematic as the only feasible method for testing the long-term thermal performance of CC6 is

through accelerated cycling. It is recommended that additional testing be performed to determine a more accurate relationship between CC6 separation and the cycling rate. Using this relationship, accelerated cycling results can be adjusted such that they accurately reflect cycling under any desired rate.

- It was found that separated CC6 could be reconstituted as a homogenous PCM through heating to a temperature greater than the CC4 melt temperature (~45°C). This is useful as it offers a method for restoring the PCM to its original thermal performance if separation occurs. If a system using unstable CC6 regularly reaches temperatures in excess of ~45°C, these results suggest that the material will continue to regenerate itself and provide good long-term thermal storage performance.
- The addition of small percentages of KCl (1-2 wt%) to CC6 was found to form a stable eutectic. This mixture was found to self-stabilize with respect to the quantity of entrained water, with a supernatant liquid being formed when the mixture was frozen. In order for the CC6+KCl eutectic to maintain its stability during cycling, any supernatant liquid must be removed. After the supernatant liquid was removed, CC6 samples with 2% KCl and 3% SC6 were cycled up to 100 cycles without a measurable decrease in H_f. The mixture of 95% CC6, 2% KCl and 3% SC6 is recommended as a stable, congruently melting/freezing PCM with a phase transition temperature of ~25°C and H_f of ~170 J/g.
- Phase diagram modeling of the $CaCl_2$-H_2O-KCl system suggests that stable eutectics form along a line of approximately 4 wt% KCl. Since the eutectics form more or less along a line of constant KCl wt%, eutectics can form for H_2O concentrations from the hexahydrate to around 2-3 wt% in excess of the hexahydrate. As the water concentration increases, T_m and H_f will both decrease.
- It is recommended that additional cycle testing of the new CC6 + 2% KCl + 3% SC6 PCM be conducted to ensure long-term stability. This cycling can be conducted in a

rapid cycling system similar to that illustrated in Figure 3.6. However, before this cycling is conducted a correlation between cycling rate and separation should be sought for this PCM such that the rapid cycling results can be applied to the cycling rate desired.

- Additional phase diagram modeling of the $CaCl_2$-$SrCl_2$-H_2O-KCl system is recommended to determine $SrCl_2 \cdot 6H_2O$'s impact on the eutectic concentration of the mixture. It is also recommended that experimental testing be conducted to provide empirical data points for comparison with the modeled results.

In addition to thermal and stability testing of CC6-based salts, corrosion testing of several common metals in contact with these salts was conducted. The goal of this testing was to find inexpensive, common metals, which could be used to encapsulate the salts for over a decade of continuous use. In order to meet this specification, a maximum corrosion rate of 20 μm/yr was targeted. The following key findings resulted from this research:

- For $CaCl_2 \cdot 6H_2O$, carbon steel and Al 5086 were found to have good corrosion resistance during both isothermal testing up to 80°C and thermal cycling. Al 6061 is not recommended for use with this PCM due to significant pitting observed during isothermal testing.
- Both CS and Al 5086 are recommended for use with the CC6+MC6 eutectic. Corrosion rates of less than 10 μm/yr were measured for both of these metals during isothermal testing at 80°C.
- Aluminum is not recommended for used with the CC6+KN mixture due to severe corrosion.
- During CC6 cyclic corrosion testing at a reduced heat transfer rate, CS was found to have a good corrosion rate (3.6 μm/yr) after 600 cycles. Al 5086 was found to have

a better corrosion rate (1.7 μm/yr) under the same conditions. If a lower corrosion rate is required, it was found that anodized Al 5086 had excellent performance during cycling with a corrosion rate as low as 0.1 μm/yr after 600 cycles.

- Additional isothermal and cycling corrosion testing of the new CC6+KCl+SC6 PCM should be conducted to ensure that the metals which performed well in contact with CC6 continue to do so under this new formulation.

Industrial-grade CC6 was prepared in bulk quantities of up to 200 L for testing in a prototype test system constructed by Advance Cooling Technologies (ACT). This material was tested via drop calorimetry and slow cycling with the following key results being found:

- The industrial-grade formulations of CC6+KCl+SC6 have shown good stability during 24-hour cycling. This PCM was found to self-stabilize to a particular water content where excess water accumulates in the supernatant liquid, which must be removed to ensure stability during cycling.
- Adding water in excess of the hexahydrate results in both a lower melt temperature and latent heat of fusion. It is recommended that care be taken to ensure that the PCM is prepared with the current quantity of water needed for stoichiometric mixing at $xH_2O = 6$.
- It was found that CC6 could be successfully prepared in batches of several hundred kg through mixing in a large container.
- It is recommended that an automated system for preparation of large quantities of the CC6+KCl+SC6 PCM system be designed and tested. This system should be capable of mixing the $CaCl_2$, H_2O and additives before freezing the mixed PCM to facilitate removal of any supernatant liquid.

References

A1. Abhat, A. Low Temperature Latent Heat Thermal Energy Storage - Heat Storage Materials. *Solar Energy, 30(4),* 1983, 313-332.

A2. Aboul-Enein, S., Ramadan, M. Storage of Low Temperature Heat in Salt-Hydrate Melts for Heating Applications. *Solar & Wind Technology, 5(4),* 1988, 441-444.

A3. Advanced Cooling Technologies. Heat-Pipe PCM Based Cool Storage for ACC Systems: ARPA-E Progress Report (April, 2018). Internal Report.

A4. Agyenim, F., Hewitt, N., Eames, P., Smyth, M. A Review of Materials, Heat Transfer and Phase Change Problem Formulation for Latent Heat Thermal Energy Storage Systems (LHTESS). *Renewable and Sustainable Energy Reviews, 14*, 2010, 615-628.

A5. Ait Adine, H., El Qarnia, H. Numerical Analysis of the Thermal Behaviour of a Shell-and-Tube Heat Storage Unit Using Phase Change Materials. *Applied Mathematical Modelling, 33*, 2009, 2132-2144.

A6. Alderman, R. US 5770295 A. 1995.

A7. Alibaba. 2017. <http://www.alibaba.com> Accessed: 2016.

A8. ARPA-E. Advanced Research in Dry Cooling - ARID - Project Description. 2015.

A9. ARPA-E. ARID Program Overview. <https://arpa-e.energy.gov/sites/default/files/documents/files/ARID_ProgramOverview.pdf> Accessed: Nov. 2018.

A10. Assarson, G., Balder, A. Equilibria Between 18 and 114° in the Aqueous Ternary System Containing Ca^{2+}, Sr^{2+} and Cl^{-}. *Journal of Physical Chemistry, 57*, 1953, 717-722.

A11. ASTM G1-03: Standard Practice for Preparing, Cleaning, and Evaluating Corrosion Test Specimens. ASTM International, West Conshohocken, PA. 2011. <http://doi.org/10.1520/G0001-03R11>.

A12. Aydın, A., Aydın, A. High-Chain Fatty Acid Esters of 1-Hexadecanol for Low Temperature Thermal Energy Storage with Phase Change Materials. *Solar Energy Materials & Solar Cells, 96*, 2012, 93-100.

B1. Babich, M., Benrashid, R., Mounts, R. DSC Studies of New Energy Storage Materials. Part 3. Thermal and Flammability Studies. *Thermochimica Acta, 243*, 1994, 193-200.

B2. Babich, M., Hwang, S., Mounts, R. The Search for Novel Energy Storage Materials Using Differential Scanning Calorimetry. *Thermochimica Acta, 210*, 1992, 83-88.

B3. Bajnóczy, G. Reversibility Problems of Calcium Chloride Hexahydrate-Strontium Chloride Hexahydrate Heat Stores. *Applied Energy*, 16, 1984, 77-82.

B4. Barzin, R., Chen, J., Young, B., Farid, M. Application of PCM Energy Storage in Combination with Night Ventilation for Space Cooling. *Applied Energy, 158*, 2015, 412-421.

B5. Barzin, R., Chen, J., Young, B., Farid, M. Application of Weather Forecast in Conjunction with Price-Based Method for PCM Solar Passive Buildings - An Experimental Study. *Applied Energy, 163*, 2016, 9-18.

B6. Barzin, R., Chen, J., Young, B., Farid, M. Peak Load Shifting with Energy Storage and Price-Based Control System. *Energy, 92*, 2015, 505-514.

B7. Bassett, H., Barton, G., Foster, A., Pateman, C. The Ternary Systems Constituted by Mercuric Chloride, Water, and an Alkaline-earth Chloride or Cupric Chloride. *Journal of the Chemical Society, 0*, 1933, 151-164.

B8. Behunek, I., Bachorec, T., Fiala, P. Properties and Numerical Simulation of $CaCl_2 \cdot 6H_2O$ Phase Change. *PIERS Online, 2(6),* 2006, 667-671.

B9. Benson, D., Webb, J., Burrows, R., McFadden, J., Christensen, C. Materials Research for Passive Solar Systems: Solid-State Phase-Change Materials. *Solar Energy Research Institute*, 1985.

B10. Bentilla, E., Sterrett, K., Karre, L. (Northrop Space Laboratories, Northrop Corporation, Hawthorne, CA). Research and Development Study on Thermal Control by Use of Fusible Materials. Final Report. Huntsville (AL): George C. Marshall Space Flight Center, National Aeronautics and Space Administration; 1966 April. Report no.: N66-26691. Contract no.: NAS 8-11163. <http://ntrs.nasa.gov/search.jsp?R=19660017401>

B11. Bhatt, V., Gohil, K., Mishra, A. Thermal Energy Storage Capacity of Some Phase Changing Materials and Ionic Liquids. *International Journal of ChemTech Research, 2(3),* 2010, 1771-1779.

B12. Bielsa, P. Almacenamiento Térmico de Energía Mediante Cambio de Fase. *PhD Thesis, University of Zaragoza, Spain*, 2002.

B13. Bilen, K., Takgil, F., Kaygusuz, K. Thermal Energy Storage Behavior of $CaCl_2 \cdot 6H_2O$ During Melting and Solidification. *Energy Sources, Part A, 30*, 2008, 775-787.

B14. Biswas, D. Thermal Energy Storage Using Sodium Sulfate Decahydrate and Water. *Solar Energy, 19*, 1977, 99-100.

B15. Blaney, J., Neti, S., Misiolek, W., Oztekin, A. Containment Capsule Stresses for Encapsulated Phase Change Materials. *Applied Thermal Engineering, 50(1),* 2013, 555-561.

B16. Bo, H., Gustafsson, E., Setterwall, F. Tetradecane and Hexadecane Binary Mixtures as Phase Change Materials (PCMs) for Cool Storage in District Cooling Systems. *Energy, 24*, 1999, 1015-1028.

B17. Bouwman, I. PCM in the Built Environment. *Deerns*.

B18. Bradshaw, R., Goods, S. Corrosion Resistance of Stainless Steels During Thermal Cycling in Alkali Nitrate Molten Salts. *Sandia National Laboratories*, Sandia Report SAND2001-8518, Sept. 2001.

B19. Brandstetter, A. On the Stability of Calcium Chloride Hexahydrate in Thermal Storage Systems. *Solar Energy*, 41(2), 1988, 183-191.

B20. Butti, K., Perlin, J. A Golden Thread – 2500 Years of Solar Architecture and Technology. Cheshire Books, Palo Alto, CA. 1980.

C1. Cabeza, L., Castell, A., Barreneche, C., de Gracia, A., Fernández, A. Materials Used as PCM in Thermal Energy Storage in Buildings: A Review. *Renewable and Sustainable Energy Reviews, 15*, 2011, 1675-1695.

C2. Cabeza, L., Roca, J., Nogueés, M., Mehling, H., Hiebler, S. Long Term Immersion Corrosion Tests on Metal-PCM Pairs Used for Latent Heat Storage in the 24 to 29°C Temperature Range. *Materials and Corrosion, 56(1),* 2005, 33-38.

C3. Cantor, S. Applications of Differential Scanning Calorimetry to the Study of Thermal Energy Storage. *Thermochimica Acta, 26(1),* 1978, 39-47.

C4. Cantor, S. Salt Hydrates and Other Phase-Change Materials. *Oak Ridge National Laboratory Project, Oak Ridge, TN.*

C5. Carlsson, B. Phase Change Behaviour of Some Latent Heat Storage Media Based on Calcium Chloride Hexahydrate. *Solar Energy, 83*, 2009, 485-500.

C6. Carlsson, B., Stymne, H., Wettermark, G. An Incongruent Heat-of-Fusion System – $CaCl_2 \cdot 6H_2O$ – Made Congruent Through Modification of the Chemical Composition of the System. *Solar Energy, 23,* 1979, 343-350.

C7. Casarin, C., Ibanez, J. Experimental Demonstration of the Principles of Thermal Energy Storage and Chemical Heat Pumps. *Journal of Chemical Education, 70(2),* 1993, 158-162.

C8. Chan, C. W., & Russell, N. Thermal Energy Storage Technologies. *The University of Sheffield, Department of Chemical & Biological Engineering*. 2011.

C9. Chen, Z., Chen, G. Experimental Study on the Thermal Storage Performance and Preparation of Glycerin Mixtures Used in the Phase Change Wall. 2010 WASE International Conference on Information Engineering, 2010, 51-54.

C10. Chuah, T., Rozanna, D., Salmiah, A., Thomas, C., Sa'ari, M. Fatty Acids Used as Phase Change Materials (PCMs) for Thermal Energy Storage in Building Material Applications. *JURUTERA,* 2006, 8-15.

C11. Climator. Phase Change Materials. <https://beopt.nrel.gov/sites/beopt.nrel.gov/files/Harvard%20Group07.PhaseChangeMaterials.pdf> Accessed: Sept. 2015.

C12. Cohen, E. Die Bestimmung von Umwandlungspunkten auf Elektrischem Wege und die Elektromotorische Kraft bei Chemischer Zersetzung. *Zeitshrift für Physikalische Chemie, 14*, 1894, 53-92.

C13. Costa, M., Buddhi, D., Oliva, A. Numerical Simulation of a Latent Heat Thermal Energy Storage System with Enhanced Heat Conduction. *Energy Conversion and Management, 39(3/4)*, 1998, 319-330.

C14. Costello, V., Melsheimer, S., Edie, D. Heat Transfer and Calorimetric Studies of a Direct Contact-Latent Heat Energy Storage System. *Proceedings of the Winter Annual Meeting of the American Society of Mechanical Engineers, San Francisco, CA,* December 10-15, 1978.

C15. Cui, R. Effect of Selected Phase Change Materials Concentration and Manufacturing Process on the Properties of Plaster Mixture Systems. *Master's Thesis, Clemson University*, 2011.

D1. Danilin, V., Dolesov, A., Petrenko, R., Shaposhnikov, B., USSR Patent 568669, 1977.

D2. D'Ans, J., Tollert, H. Die Bestimmung Der Spezifishen Wärmen Konzentrierter Wässriger Salzlösungen. *Ztschr. Elektrochem, 43(2)*, 1937, 81-91.

D3. Demirbas, M., Thermal Energy Storage and Phase Change Materials: An Overview. *Energy Sources, Part B: Economics, Planning, and Policy. 1(1),* 2006, 85-95.

D4. Deng, T., Li, D., Wang, S. Metastable Phase Equilibrium in the Aqueous Ternary System (KCl-$CaCl_2$-H_2O) at (288.15 and 308.15) K. *Journal of Chemical Engineering Data, 53*, 2008, 1007-1011.

D5. Dimaano, M., Watanabe, T. Performance Investigation of the Capric and Lauric Acid Mixture as Latent Heat Energy Storage for a Cooling System. *Solar Energy, 72(3),* 2002, 205-215.

D6. Dinçer, İ., Rosen, M. Thermal Energy Storage, Systems and Applications, *John Wiley & Sons*, Chichster, England, 2002.

D7. Dong, O., Zeng, D., Zhou, H., Han, H., Yin, X., Du, Y. Phase Change Materials in the Ternary System NH_4Cl + $CaCl_2$ + H_2O. *CALPHAD: Computer Coupling of Phase Diagrams and Thermochemistry, 35*, 2011, 269-275.

D8. Dow Chemical Company. Calcium Chloride Handbook: A Guide to Properties, Forms, Storage and Handling. *Dow Chemical Company*, 2003.

D9. Dow Chemical Company. CARBOWAX Polyethylene Glycol (PEG) 600 Technical Data Sheet. 2011.

D10. Dubey, K., Mishra, R. (2014). A Review on Properties of Phase Change Material for Solar Thermal Storage System. *International Conference of Advance Research and Innovation,* 2014. ISBN: 978-93-5156-328-0.

D11. Dupont. Energain Product Datasheet. 2011.

D12. Dutil, Y., Rousse, D., Salah, N., Lassue, S., Zalewski, L. A Review on Phase-Change Materials: Mathematical Modeling and Simulations. *Renewable and Sustainable Energy, 15(1),* 2011, 112-130.

E1. EIA. Residential Energy Consumption Survey (RECS). U.S. Energy Information Administration. <https://www.eia.gov/consumption/residential/data/2015/index.php?view=consumption#by%20end%20uses> Accessed: 2015.

E2. EIA. What is U.S. Electricity Generation by Energy Source? U.S. Energy Information Administration. <https://www.eia.gov/tools/faqs/faq.php?id=427&t=3> Accessed: 2017.

E3. Efimova, A., Pinnau, S., Mischke, M., Breitkopf, C., Ruck, M., Schmidt, P. Development of Salt Hydrates Eutectics as Latent Heat Storage for Air Conditioning and Cooling. *Thermochimica Acta, 575*, 2014, 276-278.

E4. Esen, M., Ayhan, T. Development of a Model Compatible with Solar Assisted Cylindrical Energy Storage Tank and Variation of Stored Energy with Time for Different Phase Change Materials. *Energy Conversion and Management, 37(12)*, 1996, 1775-1785.

E5. Esen, M, Durmuş, A., Durmuş, A. Geometric Design of Solar-Aided Latent Heat Store Depending on Various Parameters and Phase Change Materials. *Solar Energy, 62(1)*, 1998, 19-28.

E6. Van Essen, V., Bleijendaal, L., Kikkert, B., Zondag, H., Bakker, M., Bach, P. Development of a Compact Heat Storage System Based on Salt Hydrates. *The International Conference on Solar Heating, Cooling and Buildings*, Graz, Austria, 2010.

E7. Van Essen, V., Gores, J., Bleijendaal, L., Zondag, H., Schuitema, R., Van Helden, W. Characterization of Salt Hydrates for Compact Seasonal Thermochemical Storage. *Energy Research Center of the Netherlands,* 2009.

F1. Farid, M., Hamad, F., Abu-Arabi, M. Phase Change Cool Storage Using Dimethyl-Sulfoxide. *Energy Conversion and Management, 39 (8)*, 1998, 819-826.

F2. Farid, M., Khalaf, A. Performance of Direct Contact Latent Heat Storage Units with Two Hydrated Salts. *Solar Energy, 52(2),* 1994, 179-189.

F3. Farid, M., Khudhair, A., Razack, S., & Al-Hallaj, S. A review on phase change energy storage: materials and applications. *Energy Conversion and Management, 45(9-10),* 2004, 1597-1615.

F4. Farid, M., Yacoub, K. Performance of Direct Contact Latent Heat Storage Unit. *Solar Energy, 43(4),* 1989, 237-251.

F5. Feilchenfeld, H., Fuchs, J., Kahana, F., Sarig, S. The Melting Point Adjustment of Calcium Chloride Hexahydrate by Addition of Potassium Chloride or Calcium Bromide Hexahydrate. *Solar Energy, 34(2),* 1985, 199-201.

F6. Feilchenfeld, H., Fuchs, J., Sarig, S. A Calorimetric Investigation of the Stability of Stagnant Calcium Chloride Hexahydrate Melt. *Solar Energy*, 32(6), 1984, 779-784.

F7. Feilchenfeld, H., Sarig, S. Calcium chloride hexahydrate: a phase-changing material for energy storage. *Industrial & Engineering Chemistry Product Research and Development, 24(1),* 2985, 130-133.

F8. Feldman, D., Banu, D. DSC Analysis for the Evaluation of an Energy Storing Wallboard. *Thermochimica Acta, 272*, 1996, 243-251.

F9. Feldman, D., Banu, D., Hawes, D. Development and Application of Organic Phase Change Mixtures in Thermal Storage Gypsum Wallboard. *Solar Energy Materials and Solar Cells, 36*, 1995, 147-157.

F10. Feldman, D., Shapiro, M., Banu, D., Fuks, C. J. Fatty Acids and Their Mixtures as Phase-Change Materials for Thermal Energy Storage. *Solar Energy Materials, 18*, 1989, 201-216.

F11. Feldman, D., Shapiro, M., Banu, D. Organic Phase Change Materials for Thermal Energy Storage. *Solar Energy Materials, 13,* 1986, 1-10.

F12. Fisher Scientific. Calcium Chloride Hexahydrate, for Analysis, ACROS Organics. <https://www.fishersci.com/shop/products/calcium-chloride-hexahydrate-analysis-acros-organics-3/AC389260010#?keyword=calcium+chloride+hexahydrate> Accessed: Nov. 5, 2018.

F13. de Forcband, M. Les Hydrates du Fluorure de Potassium. *Chimie Minérale, 152(17),* 1911, 1073-1077.

F14. Fouda, A., Despault, J., Taylor, J., Capes, C. Solar Storage Systems Using Salt Hydrate Latent Heat and Direct Contact Heat Exchanger – II Characteristics of Pilot System Operating with Sodium Sulfate Solution. *Solar Energy, 32(1),* 1984, 57-65.

F15. Furbo, S. Heat Storage Units Using a Salt Hydrate as Storage Medium Based on the Extra Water Principle. Report EUR 8169 EN, Commission of the European Communities, Luxembourg, 1983.

F16. Furbo, S. Heat Storage with an Incongruently Melting Salt Hydrate as Storage Medium Based on the Extra Water Principle. Thermal Insulation Laboratory, Technical University of Denmark, Lyngby, 1980.

F17. Furbo, S. Investigation of Heat Storages with Salt Hydrate as Storage Medium Based on the Extra Water Principle. Report EUR 6646 EN. Part 2, Commission of the European Communities, Luxembourg, 1980.

G1. Gang, L., Zhang, B., Li, X., Zhou, Y., Sun, Q., Yun, Q. The Preparation, Characterization and Modification of a New Phase Change Material: $CaCl_2 \cdot 6H_2O$-$MgCl_2 \cdot 6H_2O$ Eutectic Hydrate Salt. *Solar Energy Materials & Solar Cells, 126,* 2014, 51-55.

G2. Gao, D., Deng, T. Energy Storage - Preparations and Physiochemical Properties of Solid-Liquid Phase Change Materials for Thermal Energy Storage. *Materials and Processes for Energy: Communicating Current Research and Technological Developments. Formatex.*, 2013, 32-44.

G3. García-Romero, A., Diarce, G., Ibarretxe, J., Urresti, A., Sala, J. Influence of the Experimental Conditions on the Subcooling of Glauber's Salt When Used as PCM. *Solar Energy Materials & Solar Cells, 102,* 2012, 189-195.

G4. Garg, H., Mullick, S., Bhargava, A. *Solar Thermal Energy Storage*. D. Reidel Publishing Company, Dordrecht, Holland. 1985.

G5. Gawron, K., Schröder, J. Properties of Some Salt Hydrates for Latent Heat Storage. *Energy Research, 1,* 1977, 351-363.

G6. Ghoneim, A. Comparison of Theoretical Models of Phase-Change and Sensible Heat Storage for Air and Water-Based Solar Heating Systems. *Solar Energy, 42(3)*, 1989, 209-220.

G7. Gök, Ö., Yilmaz, M., Paksoy, H. Stabilization of Glaubers Salt for Latent Heat Storage.

G8. Greenberg, J., Reeder, B. Phase Change Thermal Energy Storage and the Model Building Codes. *U.S. Department of Commerce, National Bureau of Standards, Gaithersburg, MD*, 1984.

G9. Güerisoli, C. Development and Characterization for New Materials Incorporating Phase Change Materials (PCM) for Thermal Energy Storage (TES) Applications in Buildings. *PhD Thesis, University de Barcelona*, 2013. <http://hdl.handle.net/10803/123749>

G10. Gumus, M. Reducing Cold-Start Emission from Internal Combustion Engines by Means of Thermal Energy Storage System. *Applied Thermal Engineering, 29*, 2009, 652-660.

G11. Gu, X., Niu, J., Qin, S. Antarcticite: A Phase Change Material for Thermal Energy Storage – Experiments and Simulation. Proceedings of the 11th International Congress for Applied Mineralogy (ICAM), Mianyang, China, 2013, 125-135.

H1. Haghighat, F. (Operating Agent) State of the Art Review: Applying Energy Storage in Building of the Future, Subtask A&B Report, Annex 23. Iea Energy Technology Network, 2013.

H2. Haillot, D., Bauer, T., Kröner, U., Tamme, R. Thermal Analysis of Phase Change Materials in the Temperature Range 120-150°C. Thermochimica Acta, 513, 2011, 49-59.

H3. Hale, D., Hoover, M., O'Neill, M. Phase Change Materials Handbook. Technical Report. Huntsville (AL): National Aeronautics and Space Administration; 1971 September. Report no.: NASA-CR-61363. Contract no.: NAS8-25183. <http://dx.doi.org/2060/19720012306>.

H4. Hamdan, M., Elwerr, F. Thermal Energy Storage Using a Phase Change Material. Solar Energy, 56(2), 1996, 183-189.

H5. Hamada, Y., Ohtsu, W., Fukai, J. Thermal Response in Thermal Energy Storage Material Around Heat Transfer Tubes: Effect of Additives on Heat Transfer Rates. Solar Energy, 75, 2003, 317-328.

H6. Hasan, A. Phase Change Material Energy Storage System Employing Palmitic Acid. Solar Energy, 52(2), 1994, 143-154.

H7. Hasan, A., Sayigh, A. Some Fatty Acids as Phase-Change Thermal Energy Storage Materials. Renewable Energy, 4(1), 1994, 69-76.

H8. Hasan, A. Thermal Energy Storage System with Stearic Acid as Phase Change Material. Energy Conversion and Management, 35(10), 1994, 843-856.

H9. Hasnain, S. Review on Sustainable Thermal Energy Storage Technologies, Part I: Heat Storage Materials and Techniques. Energy Conversion and Management, 39(11), 1998, 1127-1138.

H10. Hasnain, S. Review on Sustainable Thermal Energy Storage Technologies, Part II: Cool Thermal Storage. Energy Conversion and Management, 39(11), 1998, 1139-1153.

H11. Hawes, D., Feldman, D., Banu, D. Latent Heat Storage in Building Materials. Energy and Buildings, 20, 1993, 77-86.

H12. Heckenkamp, J., Baumann, H. Latentwärmespeicher (Latent Heat Storage Systems). Nachrichten aus Chemie, Technik und Laboratorium / Herausgegeben von der Gesellschaft Deutscher Chemiker, 45(11), 1997, 1075-1081.

H13. Heinz, A., Streicher, W. Application of Phase Change Materials and PCM-Slurries for Thermal Energy Storage. Institute of Thermal Engineering, Graz University of Technology, Austria.

H14. He, M., Yang, L., Yang, L., Zhang, Z. Experimental Studies on Cycling Stable Characteristics of Inorganic Phase Change Material $CaCl_2 \cdot 6H_2O$-$MgCl_2 \cdot 6H_2O$ Modified with $SrCl_2 \cdot 6H_2O$ and CMC. *IOP Conf. Series: Earth and Environmental Science, 108*, 2018.

H15. Herrmann, U., Kearney, D. Survey of Thermal Energy Storage for Parabolic Trough Power Plants. Journal of Solar Energy Engineering, 124, 2002, 145-152.

H16. Himran, S., Suwono, A., Mansoori, G. Characterization of Alkanes and Paraffin Waxes for Application as Phase Change Energy Storage Medium. Energy Sources, 16, 1994, 117-128.

H17. Hirata, T., Nishida, K. An Analysis of Heat Transfer Using Equivalent Thermal Conductivity of Liquid Phase During Melting Inside an Isothermally Heated Horizontal Cylinder. International Journal of Heat and Mass Transfer, 32(9), 1989, 1663-1670.

H18. Hittle, D. Phase Change Materials in Floor Tiles for Thermal Energy Storage. Colorado State University, Fort Collins, CO, 2002. Award No. DE-FC26-00NT40999.

H19. Hong, Y., Xin-shi, G. Preparation of Polyethylene-paraffin Compound as a Form-Stable Solid-Liquid Phase Change Material. Solar Energy Materials & Solar Cells, 64, 2000, 37-44.

H20. Howe, H. Sun Furnace in Your Attic. *Popular Science, 154 (3)*, March, 1949. 106-112.

H21. Huang, M., Eames, P., Norton, B. Thermal Regulation of Building-Integrated Photovoltaics Using Phase Change Materials. International Journal of Heat and Mass Transfer, 47, 2004, 2715-2733.

I1. Iliuta, M., Thomsen, K., Rasmussen, P. Extended UNIQUAC Model for Correlation and Prediction of Vapour-Liquid-Solid Equilibria in Aqueous Salt Systems Containing Non-Electrolytes. Part A. Methanol-Water-Salt Systems. *Chemical Engineering Science, 55*, 2000, 2673-2686.

I2. Ingole, P., Mohod, T., Gaddamwar, S. Use of Phase Change Materials in Construction of Buildings: A Review. *International Journal of Engineering Research and General Science, 2(4),* 2014, 624-628.

J1. Jankowski, N., McCluskey, F. A Review of Phase Change Materials for Vehicle Component Thermal Buffering. *Applied Energy, 113*, 2014, 1525-1561.

J2. Jeon, J., Jungki, S., Jeong, S., Kim, S. PCM Application Methods for Residential Building Using Radiant Floor Heating Systems. *Building Environment & Materials Lab, School of Architecture, Soongsil University, Seoul, Korea.*

J3. Ji, H., Sellan, D., Pettes, M., Kong, X., Ji, J., Shi, L., Ruoff, R. Enhanced Thermal Conductivity of Phase Change Materials with Ultrathin-Graphite Foams for Thermal Energy Storage. *Energy & Environ. Sci., 7*, 2014, 1185-1192.

J4. Juárez, D., Balart, R., Ferrándiz, S., Peydró, M. Classification of Phase Change Materials and His Behaviour in SEBS/PCM Blends. *Proceedings of the 5th Manufacturing Engineering Society International Conference, Zaragoza,* 2013.

K1. Kalnæs, S., & Jelle, B. Phase change materials and products for building applications: A state-of-the-art review and future research opportunities. *Energy and Buildings, 94*, 2015, 150-176.

K2. Kanimozhi, B., Ramesh Bapu, B., Pranesh, V. Thermal Energy Storage System Operating with Phase Change Materials for Solar Water Heating Applications: DOE Modeling. *Applied Thermal Engineering, 123*, 2017, 614-624.

K3. Kauranen, P., Peippo, K., Lund, P. An Organic PCM Storage System with Adjustable Melting Temperature. *Solar Energy, 46(5),* 1991, 275-278.

K4. Kaygusuz, K. Experimental and Theoretical Investigation of Latent Heat Storage for Water Based Solar Heating Systems. *Energy Conservation and Management, 36(5),* 1995, 315-323.

K5. Kaygusuz, K. The Viability of Thermal Energy Storage. *Energy Sources, 21(8),* 1999, 745-755.

K6. Keleş, S., Kaygusuz, K., Sarı, A. Lauric and myristic acids eutectic mixture as phase change material for low-temperature heating applications. *International Journal of Energy Research, 29(9),* 2005, 857-870.

K7. Kenisarin, M. High-Temperature Phase Change Materials for Thermal Energy Storage. *Renewable and Sustainable Energy Reviews, 14*, 2010, 955-970.

K8. Kenisarin, M., Mahkamov, K. Salt Hydrates as Latent Heat Storage Materials: Thermophysical Properties and Costs. *Solar Energy Materials & Solar Cells, 145,* 2016, 255-286.

K9. Kenisarin, M., Mahkamov, K. Solar energy storage using phase change materials. *Renewable and Sustainable Energy Reviews, 11(9),* 2007, 1913-1965.

K10. Kenisarin, M. Short-Term Storage of Solar Energy. 1. Low Temperature Phase-Change Materials. *Applied Solar Energy, 29(2),* 1993, 48-65.

K11. Kimura, H. Impurity Effect on Growth Rates of $CaCl_2 \cdot 6H_2O$ Crystals. *Journal of Crystal Growth*, 73, 1985, 53-62.

K12. Kimura, H., Kai, J. Mixtures of Calcium Chloride Hexahydrate with Some Salt Hydrates or Anhydrous Salts as Latent Heat Storage Materials. *Energy Conversion and Management, 28(3)*, 1988, 197-200.

K13. Kimura, H., Kai, J. Phase Change Stability of $CaCl_2 \cdot 6H_2O$. *Solar Energy, 33 (6),* 1984. 557-563.

K14. Kobe, K., Anderson, C. The Heat Capacity of Saturated Sodium Sulfate Solution. *The Journal of Physical Chemistry, 40*(4), 1936, 429-433.

K15. Kolokolov, D., Glaznev, I., Aristov, Y., Stepanov, A., Jobic, H. Water Dynamics in Bulk and Dispersed in Silica $CaCl_2$ Hydrates Studied by ^2H NMR. *Journal of Physical Chemistry*, 112, 2008, 12853-12860.

K16. Krane, R. Storage of Thermal Energy by Change of Phase. *Energy Storage Systems, Chapter 1.*

K17. Kuznik, F., David, D., Johannes, K., Roux, J. A review on phase change materials integrated in building walls. *Renewable and Sustainable Energy Reviews, Elsevier, 15 (1*), 2011, 379-391.

L1. Lacroix, M. Numerical Simulation of a Shell-and-Tube Latent Heat Thermal Energy Storage Unit. *Solar Energy, 50(4)*, 1993, 357-367.

L2. Lane, G. Adding Strontium Chloride or Calcium Hydroxide to Calcium Chloride Hexahydrate Heat Storage Material. *Solar Energy*, 27, 1981, 73-75.

L3. Lane, G. Hydrated $CaCl_2$ Reversible Phase Change Compositions with Nucleating Additives. European Patent EP 0013569A1, 1980.

L4. Lane, G. Low Temperature Heat Storage with Phase Change Materials. *The International Journal of Ambient Energy, 1,* 1980, 155-168.

L5. Lane, G. Phase Change Materials for Energy Storage Nucleation to Prevent Supercooling. *Solar Energy Materials and Solar Cells, 27,* 1992, 135-160.

L6. Lane, G., Rossow, H. Reversible Phase Change Compositions of Calcium Chloride Hexahydrate with Potassium Chloride. U.S. Patent US 4613444 A, 1986 [cited December 6, 2016], Available from: www.google.com/patents/US4613444.

L7. Lane, G. (ed.) Solar Heat Storage: *Latent Heat Materials, Volume I: Background and Scientific Principles.* CRC Press, Boca Raton, FL. 1983.

L8. Lane, G. (ed.) Solar Heat Storage: *Latent Heat Materials, Volume II: Technology.* CRC Press, Boca Raton, FL. 1986.

L9. Leenhardt & Boutaric. Cryoscopie Dans les Sels Hydratés Fondus. *Bulletin de la Société Chimique de France, 13*, 1913, 651-657.

L10. Lele, A., Kuznik, F., Rammelberg, H., Schmidt, T., Ruck, W. Thermal Decomposition Kinetics of Salt Hydrates for Heat Storage Systems. *Applied Energy*, 154, 2015, 447-458.

L11. Levitskij, E., Aristov, Y., Tokarev, M., Parmon, V. "Chemical Heat Accumulators": A New Approach to Accumulating Low Potential Heat. *Solar Energy Materials and Solar Cells*, 44, 1996. 219-235.

L12. Li, D., Zeng, D., Yin, X., Han, H., Guo, L., Yao, Y. Phase Diagrams and Thermochemical Modeling of Salt Lake Brine Systems. II. $NaCl+H_2O$, $KCl+H_2O$, $MgCl_2+H_2O$ and $CaCl_2+H_2O$ Systems. *Computer Coupling of Phase Diagrams and Thermochemistry, 53,* 2016, 78-89.

L13. Li, G., Zhang, B., Li, X., Zhou, Y., Sun, Q., Yun, Q. The Preparation, Characterization, and Modification of a New Phase Change Material: $CaCl_2 \cdot 6H_2O$-$MgCl_2 \cdot 6H_2O$ Eutectic Hydrate Salt. *Solar Energy Materials & Solar Cells, 126,* 2014, 51-55.

L14. Limited, P. C. M. P. PlusICE Phase Change Materials - 2013.

L15. Linnow, K., Niermann, M., Bonatz, D., Posern, K., Steiger, M. Experimental Studies of the Mechanism and Kinetics of Hydration Reactions. *Energy Procedia, 48,* 2014, 394-404.

L16. Liu, Z., Chung, D. Calorimetric Evaluation of Phase Change Materials for Use as Thermal Interface Materials. *Thermochimica, 366,* 2001, 135-147.

L17. Li, X., Zhou, Y., Nian, H., Zhang, Z., Dong, O., Ren, X., Zeng, J., Hai, C., Shen, Y. Advanced Nanocomposite Phase Change Material Based on Calcium Chloride Hexahydrate with Aluminum Oxide Nanoparticles for Thermal Energy Storage. *Energy & Fuels, 31*, 2017, 6560-6567.

L18. Lorsch, H., Kauffman, K., Denton, J. Thermal Energy Storage for Solar Heating and Off-Peak Air Conditioning. *Energy Conversion, 17*, 1975, 1-8.

L19. Lu, D., Di, Y., Tan, Z., & Dou, J. Low-temperature heat capacities, and thermodynamic properties of solid–solid phase change material bis (1-octylammonium) tetrachlorocuprate. *Journal of Thermal Analysis and Calorimetry, 111(1),* 2012, 213-218.

M1. Madessa, H. A Review of the Performance of Buildings Integrated with Phase Change Material: Opportunities for Application in Cold Climate. *Energy Procedia, 62*, 2014, 318-328.

M2. MakeItFrom.com ASTM A36 (SS400, S275) Structural Carbon Steel. < https://www.makeitfrom.com/material-properties/ASTM-A36-SS400-S275-Structural-Carbon-Steel> Accessed: November, 2018.

M3. Marcus, Y., Minevich, A., Ben-Dor, L. Solid-Liquid Phase Diagrams of Binary Salt Hydrate Mixtures Involving Magnesium Nitrate and Acetate, Magnesium and Aluminum Nitrates,

Ammonium Alum and Sulfate, and Ammonium Alum and Aluminum Sulfate. *Thermochimica Acta, 412,* 2004, 163-170.

M4. Marín, J., Zalba, B., Cabeza, L. Mehling, H. Determination of Enthalpy-Temperature Curves of Phase Change Materials with the Temperature-History Method: Improvement to Temperature Dependent Properties. *Measurement Science and Technology, 13*, 2003, 184-189.

M5. Marks, S. An Investigation of the Thermal Energy Storage Capacity of Glauber's Salt with Respect to Thermal Cycling. *Solar Energy, 25,* 1980, 255-258.

M6. Marliacy, P., Solimando, R., Bouroukba, M., Schuffenecker, L. Thermodynamics of Crystallization of Sodium Sulfate Decahydrate in H_2O-NaCl-Na_2SO_4: Application to $Na_2SO_4 \cdot 10H_2O$-based Latent Heat Storage Materials. *Thermochimica Acta, 344,* 2000, 85-94.

M7. Matweb. ASTM A36 Steel Bar. <http://www.matweb.com/search/DataSheet.aspx?MatGUID=d1844977c5c8440cb9a3a967f8909c3a&ckck=1> Accessed: November 2018.

M8. McMaster-Carr. <http://www.mcmaster.com> Accessed: Sept. 19, 2018.

M9. McMullin, M., Ben-Abdallah, N. An Investigation of Low-Temperature Phase-Change Materials for Short-Term Energy Storage in Greenhouses. *Canadian Agricultural Engineering, 30*, 1988, 65-68.

M10. Mehling, H., Cabeza, L. Heat and Cold Storage with PCM: An up to Date Introduction into Basics and Applications. *Springer*. 2008. ISBN: 978-3-540-68556-2.

M11. Murray, R., Desgrosseilliers, L., Stewart, J., Osbourne, N., Marin, G., Safatli, A., Groulx, D., White, M. Design of a Latent Heat Energy Storage System Coupled with a Domestic Hot Water Solar Thermal System. *World Renewable Energy Congress, Linköping, Sweden,* 2001.

N1. Nagano, K., Mochida, T., Takeda, S., Domański, R., Rebow, M. Thermal Characteristics of Manganese (II) Nitrate Hexahydrate as a Phase Change Material for Cooling Systems. *Applied Thermal Engineering, 23*, 2003, 229-241.

N2. Naumann, R., Emons, H. Results of Thermal Analysis for Investigation of Salt Hydrates as Latent Heat-Storage Materials. *Journal of Thermal Analysis, 35*, 1989, 1009-1031.

N3. Ng, K., Gong, Z., Mujumdar, A. Heat Transfer in Free Convective-Dominated Melting of a Phase Change Material in a Horizontal Annulus. *International Communications in Heat and Mass Transfer, 25(5)*, 1998, 631-640.

N4. N'Tsoukpoe, K., Rammelberg, H., Lele, A., Korhammer, K., Watts, B., Schmidt, T., Ruck, W. A Review of the Use of Calcium Chloride in Applied Thermal Engineering. *Applied Thermal Engineering, 75*, 2015, 513-531.

N5. N'Tsoukpoe, K., Schmidt, T., Rammelberg, H., Watts, B., Ruck, W. A Systematic Multi-Step Screening of Numerous Salt Hydrates for Low Temperature Thermochemical Energy Storage. *Applied Energy, 124,* 2014, 1-16.

O1. Occidental Chemical Corporation (OXY). Calcium Chloride: A Guide to Physical Properties. <http://www.oxycalciuMC6loride.com> Accessed: Nov. 2016.

O2. Oró, E., de Gracia, A., Castell, A., Farid, M., Cabeza, L. Review on Phase Change Materials (PCMs) for Cold Thermal Energy Storage Applications. *Applied Energy, 99,* 2012, 513-533.

O3. Oró, E., Miró, L., Barreneche, C., Martorell, I., Farid, M. Corrosion of Metal and Polymer Containers for Use in PCM Cold Storage. *Applied Energy, 109.* 2013, 449-453.

P1. Pan, C., Charles, J., Vermaak, N., Romero, C., Neti, S., Zheng, Y., Chen, C., Bonner, R. Experimental, Numerical and Analytic Study of Unconstrained Melting in a Vertical Cylinder with a Focus on Mushy Region Effects. *International Journal of Heat and Mass Transfer, 124*, 2018, 1015-1024.

P2. Paris, J., Falardeau, M., Villeneuve, C. Thermal Storage by Latent Heat: A Viable Option for Energy Conservation in Buildings. Energy Sources, 15, 1993, 85-93.

P3. Pasupathy, A., Athanasius, L., Velray, R., Seeniraj, R. Experimental Investigation and Numerical Simulation Analysis on the Thermal Performance of a Building Roof Incorporating Phase Change Material (PCM) for Thermal Management. *Applied Thermal Engineering, 28*, 2008, 556-565.

P4. Pasupathy, A., Velraj, R. Phase Change Material Based Thermal Storage for Energy Conservation in Building Architecture. *International Energy Journal, 7(2),* 2006.

P5. Pathak, A., Nedea, S., Zondag, H., Rindt, C., Smeulders, D. A DFT-based Comparative Equilibrium Study of Thermal Dehydration and Hydrolysis of $CaCl_2$ Hydrates and $MgCl_2$ Hydrates for Seasonal Heat Storage. *Phys. Chem. Chem. Phys.*, 18, 2016, 10059-10069.

P6. Peippo, K., Kauranen, P., Lund, P. A Multicomponent PCM Wall Optimized for Passive Solar Heating. *Energy and Buildings, 17(4),* 1991, 259-270.

P7. Perman, E., Urry, W. The Dissociation of Sodium Sulphate Decahydrate. *Transactions of the Faraday Society, 24*, 1928, 337-343.

P8. Perron, G., Roux, A., Desnoyers, J. Heat Capacities and Volumes of NaCl, $MgCl_2$, $CaCl_2$, and $NiCl_2$ up to 6 Molal in Water. *Canadian Journal of Chemistry*, 59, 1981, 3049-3054.

P9. Phase-Change-Material. *n.d. In Wikipedia*. <https://en.wikipedia.org/wiki/Phase-change_material> Accessed: 2016.

P10. Phase Change Materials. Power Point Presentation from Harvard University Archives.

P11. Pielichowska, K., & Pielichowski, K. Phase change materials for thermal energy storage. *Progress in Materials Science, 65*, 2014, 67-123.

P12. Pitzer, K., Coulter, L. The Heat Capacities, Entropies, and Heats of Solution of Anhydrous Sodium Sulfate and of Sodium Sulfate Decahydrate. The Application of the Third Law of Thermodynamics to Hydrated Crystals. *Journal of the American Chemical Society, 60*, 1938, 1310-1313.

P13. Plazanet, M., Glaznev, I., Stepanov, A., Aristov, Y., Jobic, H. Dynamics of Hydration Water in $CaCl_2$ Complexes. *Chemical Physics Letters*, 419, 2006, 111-114.

P14. Porisini, F. Salt Hydrates Used for Latent Heat Storage: Corrosion of Metals and Reliability of Thermal Performance. *Solar Energy, 41(2),* 1988, 193-197.

P15. Potong, W., Sookkumnerd, T., Rattanaphanee, P. Analysis of Phase Transformation of Pure Fatty Acids and Its Mixtures by Differential Scanning Calorimetry. *TIChE International Conference, Hatyai, Songkhla Thailand,* 2011.

P16. Prutton, C., Tower, O. The System Calcium Chloride-Magnesium Chloride-Water at 0, -15 and -30°. Journal of the American Chemical Society, 54(8), 1932, 3040-3047.

R1. Rady, M., Arquis, E., Le Bot, C. Characterization of Granular Phase Changing Composites for Thermal Energy Storage Using the T-History Method. *Int. J. Energy Res., 34*, 2010, 333-344.

R2. Rammelberg, H., Myrau, M., Schmidt, T., Ruck, W. An Optimization of Salt Hydrates for Thermochemical Heat Storage. *International Symposium on Innovative Materials for Processes in Energy Systems*, Fukuoka, Japan, 2013. Paper No. IMPRES2013-117.

R3. Rammelberg, H., Osterland, T., Priehs, B., Opel, O., Ruck, W. Thermochemical Heat Storage Materials – Performance of Mixed Salt Hydrates. *Solar Energy*, 136, 2016, 571-589.

R4. Rammelberg, H., Schmidt, T., Ruck, W. Hydration and Dehydration of Salt Hydrates and Hydroxides for Thermal Energy Storage - Kinetics and Energy Release. *Energy Procedia, 30*, 2012, 362-369.

R5. Randell, J. Storing Heat at a Steady Temperature. European Patent EP 0011357A1, 1979.

R6. Rathod, M., Banerjee, J. Thermal Stability of Phase Change Materials Used in Latent Heat Energy Storage Systems: A Review. *Renewable and Sustainable Energy Reviews, 18,* 2013, 246-258.

R7. Ren, S., Charles, J., Wang, X., Nie, F., Romero, C., Neti, S., Zheng, Y., Hoenig, S., Chen, C., Cao, F., Bonner, R., Pearlman, H. Corrosion Testing of Metals in Contact with Calcium Chloride Hexahydrate Used for Thermal Energy Storage. *Materials and Corrosion, 68*, 2017, 1046-1056.

R8. Reznitskii, L., Filippova, S. Potassium Fluoride Tetrahydrate as a Reversible Heat Accumulator at Room Temperature. Moscow University Chemistry Bulletin, 52(3), 1997, 43-45.

R9. Robaidi, A. Development of Novel Polymer Phase Change Material for Heat Storage Application. *International Journal of Materials Science and Applications, 2(6),* 2013, 168-172.

R10. Roozeboom, H. Experimentelle und Theoretische Studien über die Gleichgewichtsbedingungen Zwischen Festen und Flüssigen Verbinungen von Wasser min Salzen, Besonders mit dem Chlorcalcium. *Zeitschrift f. Physik. Chemie. 4*, 1889, 31-65.

R11. Roxas-Dimaano, M., Watanabe, T. The Capric and Lauric Acid Mixture with Chemical Additives as Latent Heat Storage Materials for Cooling Applications. *Energy, 27*, 2002, 869-888.

R12. Ryu, H., Woo, S., Shin, B., Kim, S. Prevention of Supercooling and Stabilization of Inorganic Salt Hydrates as Latent Heat Storage Materials. *Solar Energy Materials and Solar Cells, 27*, 1992, 161-172.

S1. Salunkhe, P., Krishna, D. Investigations of Latent Heat Storage Materials for Solar Water and Space Heating Applications. *Journal of Energy Storage, 12*, 2017, 243-260.

S2. Saman, W., Vakilaltojjar, S. Evaluation of a Thermal Storage System Employing Multiple Phase-Change Materials. *Proceedings of Solar '97, Australian and New Zealand Solar Energy Society*, 1997.

S3. Sarı, A., Kaygusuz, K. Some Fatty Acids Used for Latent Heat Storage - Thermal Stability and Corrosion of Metals with Respect to Thermal Cycling. *Renewable Energy, 28*, 2003, 939-948.

S4. Sarı, A., Kaygusuz, K. Thermal and Heat Transfer Characteristics in a Latent Heat Storage System Using Lauric Acid. *Energy Conversion and Management, 43*, 2002, 2493-2507.

S5. Sarı, A., Kaygusuz, K. Thermal Energy Storage System Using Some Fatty Acids as Latent Heat Energy Storage Materials. *Energy Sources, 23(3),* 2001, 275-285.

S6. Sarı, A., Kaygusuz, K. Thermal Performance of Myristic Acid as a Phase Change Material for Energy Storage Application. *Renewable Energy, 24,* 2001, 303-317.

S7. Sarı, A. Thermal Reliability Test of Some Fatty Acids as PCMs Used for Solar Thermal Latent Heat Storage Applications. *Energy Conversion and Management, 44(14)*, 2003, 2277-2287.

S8. Sasaguchi, K., Viskanta, R. Phase Change Heat Transfer During Melting and Resolidification of Melt Around Cylindrical Heat Source(s)/Sink(s). *Journal of Energy Resources Technology, 111*, 1989, 43-49.

S9. Schossig, P. Phase Change Materials for Cold Storage Applications. *Peheat Workshop at CETIAT*. 2006.

S10. Seong, Y., Lim. J. Energy Saving Potentials of Phase Change Materials Applied to Lightweight Building Envelopes. *Energies, 6,* 2013, 5219-5230.

S11. Shabgard, H., Hu, H., Rahman, M., Boettcher, P., McCarthy, M., Cho, Y., Sun, Y. Indirect Dry Cooling of Power Plants Using Spray-Freezing of Phase Change Materials. *Drexel University*. 2015.

S12. Shahbaz, K., AlNashef, I., Lin, R., Hashim, M., Mjalli, F., Farid, M. A Novel Calcium Chloride Hexahydrate-Based Deep Eutectic Solvent as a Phase Change Materials. *Solar Energy Materials & Solar Cells, 155*, 2016, 147-154.

S13. Shamberger, P., O'Malley, M. Heterogeneous Nucleation of Thermal Storage Material $LiNO_3 \cdot 3H_2O$ from Stable Lattice-Matched Nucleation Catalysts. *Acta Materialia, 84*, 2015, 265-274.

S14. Shamberger, P., Reid, T. Thermophysical Properties of Lithium Nitrate Trihydrate from (253 to 353) K. *Journal of Chemical & Engineering Data, 57*, 2012, 1404-1411.

S15. Shamberger, P., Reid, T. Thermophysical Properties of Potassium Fluoride Tetrahydrate from (243 to 348) K. *Journal of Chemical & Engineering Data, 58,* 2013, 294-300.

S16. Sharma, A., Chen, C. Solar Water Heating System with Phase Change Materials. *International Review of Chemical Engineering (I.RE.CH.E.) 1(4),* 2009, 297-307.

S17. Sharma, A., Shukla, A., Chen, C., Wu, T. Development of Phase Change Materials (PCMs) for Low Temperature Energy Storage Applications. *Sustainable Energy Technologies and Assessments, 7*, 2014, 17-21.

S18. Sharma, A., Tyagi, V., Chen, C., Buddhi, D. Review on Thermal Energy Storage with Phase Change Materials and Applications. *Renewable and Sustainable Energy Reviews*, 13, 2009, p.318-345.

S19. Sharma, A., Won, L., Buddhi, D., Park, J. Numerical Heat Transfer Studies of the Fatty Acids for Different Heat Exchanger Materials on the Performance of a Latent Heat Storage System. *Renewable Energy, 30*, 2005, 2179-2187.

S20. Sharma, S., Buddhi, D., Sawhney, R. Accelerated Thermal Cycle Test of Latent Heat-Storage Materials. *Solar Energy, 66(6)*, 1999, 483-490.

S21. Sharma, S., Kitano, H., Sagara, K. Phase Change Materials for Low Temperature Solar Thermal Applications. *Res. Rep. Fac. Eng. Mie Univ., 29*, 2004, 31-64.

S22. Sharma, S., Sagara, K. Latent Heat Storage Materials and Systems: A Review. *International Journal of Green Energy, 2,* 2005, 1-56.

S23. Shatikian, V., Ziskind, G., Letan, R. Numerical Investigation of a PCM-based Heat Sink with Internal Fins. *International Journal of Heat and Mass Transfer, 45,* 2005, 3689-3706.

S24. Shilei, L., Neng, Z., Guohui, F. Eutectic Mixtures of Capric Acid and Lauric Acid Applied in Building Wallboards for Heat Energy Storage. *Energy and Buildings, 38,* 2006, 708-711.

S25. Shukla, A., Buddhi, D., Sawhney, R. Thermal Cycling Test of Few Selected Inorganic and Organic Phase Change Materials. Renewable Energy, 33, 2008, 2606-2614.

S26. Siemens, P., Giauque, W. The Entropies of the Hydrates of Sodium Hydroxide. II. Low-Temperature Heat Capacities and Heats of Fusion of $NaOH{\cdot}2H_2O$ and $NaOH{\cdot}3.5H_2O$. *The Journal of Physical Chemistry, 73(1),* 1969, 149-157.

S27. Sinke, G., Mossner, E., Curnutt, J. Enthalpies of Solution and Solubilities of Calcium Chloride and its Lower Hydrates. *J. Chem. Thermodynamics, 17*, 1985, 893-899.

S28. Socaciu, L. Thermal Energy Storage with Phase Change Material. *Leonardo Electronic Journal of Practices and Technologies, (20),* 2012, 75-98.

S29. Solé, A., Miró, L., Barreneche, C., Martorell, I., Cabeza, L. Review of the T-History Method to Determine Thermophysical Properties of Phase Change Materials (PCM). *Renewable and Sustainable Energy Reviews, 26*, 2013, 425-436.

S30. Solomon, A. Melt Time and Heat Flux for a Simple PCM Body. *Solar Energy, 22*, 1979, 251-257.

S31. Solomon, L. The Use of Sodium Chloride & Aluminum as Phase Change Materials for High Temperature Thermal Energy Storage Characterized by Calorimetry. Master's Thesis. *Lehigh University Lehigh Preserve*. 2013.

S32. Solomon, L., Zhao, W., Zheng, Y., Sabol, J., Tuzla, K., Neti, S., Oztekin, A., Chen, J. High Temperature Thermal Energy Storage Using Sodium Chloride as an Encapsulated Phase Change Material. *Internal Report.*

S33. Stritih, U. An Experimental Study of Enhanced Heat Transfer in Rectangular PCM Thermal Storage. *International Journal of Heat and Mass Transfer, 47*, 2004, 2841-2847.

S34. Sun, Y., McCarthy, M., Cho, Y. I., Boettcher, P., Hu, H., Shi, B., & Xie, Q. US 20150204612 A1. 2015.

S35. Suppes, G., Goff, M., & Lopes, S. Latent heat characteristics of fatty acid derivatives pursuant phase change material applications. *Chemical Engineering Science, 58(9),* 2003, 1751-1763.

S36. Swanson, H., McMurdie, H., Morris, M., Evans, E., Paretzkin, B., Groot, J., Carmel, S. Standard X-ray Diffraction Powder Patterns: Section 11-Data for 70 Substances. *NIST*, Washington, D.C. 1974.

T1. Tanveer, S., Chen, C. Thermodynamic Modeling of Aqueous Ca^{2+} - Na^{+} - K^{+} - Cl^{-}. *Fluid Phase Equilibria, 409*, 2016, 193-206.

T2. Telkes, M. Nucleation of Supersaturated Inorganic Salt Solutions. *Industrial and Engineering Chemistry*, 1952, 1308-1310.

T3. Telkes, M. Storage of Solar Heating/Cooling. *Papers Presented at the Symposium on Solar Energy Applications at the ASHRAE Annual Meeting*, 1974, Montreal, Canada.

T4. Telkes, M., Raymond, R. Storing Solar Heat in Chemicals – A Report on the Dover House. *Heating and Ventilating, 46*, 1949, 80-86.

T5. Telkes, M. Thermal Energy Storage in Salt Hydrates. *Solar Energy Materials, 2,* 1980, 381-393.

T6. Telkes, M. Thermal Storage for Solar Heating and Cooling. *Proceedings of the Workshop on Solar Energy Storage Subsystems for the Heating and Cooling of Buildings,* Charlottesville, VA, 1975, 17-23.

T7. Telkes, M. Thixotropic Mixture and Method of Making Same. U.S. Patent US 3986969, 1975 [cited Sept. 2018], Available from: www.google.com/patents/US3986969.

T8. Tetra Chemicals Europe. Solids Properties of $CaCl_2$. Available from: <http://www.tetrachemicalseurope.com/resources/physical_properties/solids.aqf> Accessed: Sept. 5, 2018.

T9. ThermoFisher Scientific. Hydrofluoric Acid Safety Data Sheet. Rev. Jan., 2018. Available from: <https://www.fishersci.com/msdsproxy%3FproductName%3DA463500%26productD

escription%3DHYDROFLUORIC%2BACID%2BOPTIMA%2B500ML%26catNo%3DA463-500%2B%26vendorId%3DVN00033897%26storeId%3D10652> Accessed: Oct. 12, 2018.

T10. ThermoFisher Scientific. Potassium Fluoride Safety Data Sheet. Rev. May, 2018. Available from: <https://www.fishersci.com/store/msds?partNumber=AC390810250&productDescription=POTASSIUM+FLUORIDE%2C+40+W+25GR&vendorId=VN00032119&countryCode=US&language=en> Accessed: Oct. 12, 2018.

T11. Thomsen, K., Iliuta, M., Rasmussen, P. Extended UNIQUAC Model for Correlation and Prediction of Vapor-Liquid-Liquid-Solid Equilibria in Aqueous Salt Systems Containing Non-Electrolytes. Part B. Alcohol (Ethanol, Propanols, Butanols)-Water-Salt Systems. *Chemical Engineering Science, 59*, 2004, 3631-3647.

T12. Thomsen, K. Phase Diagram Software. Aqueous Solutions Aps., Denmark. Available from: <http://www.phasediagram.dk>.

T13. Tong, W., Tong, A. Solar-Absorbing Metamaterial Microencapsulation of Phase Change Materials for Thermo-Regulating Textiles. *Journal of Smart and Nano Materials, 6(2),* 2015, 105-112.

T14. Trausel, F., Jong, A., Cuypers, R. A Review on the Properties of Salt Hydrates for Thermochemical Storage. *Energy Procedia, 48,* 2014, 447-452.

T15. Trp, A., Lenic, K., Frankovic, B. Analysis of the Influence of Operating Conditions and Geometric Parameters on Heat Transfer in Water-Paraffin Shell-and-Tube Latent Thermal Energy Storage Unit. *Applied Thermal Engineering, 26*, 2006, 1830-1839.

T16. Tunçbilek, K., Sari, A., Tarhan, S., Ergüneş, G., Kaygusuz, K. Lauric and Palmitic Acids Eutectic Mixture as Latent Heat Storage Material for Low Temperature Heating Applications. *Energy, 30*, 2005, 677-692.

T17. Tyagi, V., Buddhi, D. PCM Thermal Storage in Buildings: A State of Art. *Renewable and Sustainable Energy Reviews, 11(6),* 2007, 1146-1166.

T18. Tyagi, V., Buddhi, D. Thermal Cycle Testing of Calcium Chloride Hexahydrate as a Possible PCM for Latent Heat Storage. *Solar Energy Materials & Solar Cells, 92,* 2008, 891-899.

T19. Tyagi, V., Kaushik, S., Pandey, A., Tyagi, S. Experimental Study of Supercooling and pH Behavior of a Typical Phase Change Material for Thermal Energy Storage. *Indian Journal of Pure & Applied Physics, 49,* 2011, 117-125.

U1. Ugurlu, A., Gokcol, C. A Review on Thermal Energy Storage Systems with Phase Change Materials in Vehicles. *Electronic Journal of Vocational Colleges,* 2012, 1-15.

V1. Vakilaltojjar, S. Phase Change Thermal Storage System for Space Heating and Cooling. *PhD Thesis, University of South Australia, Australia*, 2000.

V2. Verner, C. Phase Change Thermal Energy Storage. *Thesis, Brighton University* (See http://freespace.virgin.net/m.eckert/carl vener's dissertation.htm), May, 1997.

W1. Wada, T., Kimura, F., Yamamoto, R. Studies of Salt Hydrate for Latent Heat Storage, II. Eutectic Mixture of Pseudo-Binary System $CH_3CO_2Na{\cdot}3H_2O$-$CO(NH_2)_2$. *Bulletin of the Chemical Society of Japan, 56*, 1983, 1223-1226.

W2. Wada, T., Tamamoto, R., Matsuo, Y. Heat Storage Capacity of Sodium Acetate Trihydrate During Thermal Cycling. *Solar Energy, 33(3),* 1984, 373-375.

W3. 王维, 张慧洁, 张哲明, 陈海滨, 吴景深. Phase Change Material and Preparation Method. Chinese Patent CN 104419381 A, 2015 [cited Aug. 9, 2018] (Translated from Chinese), Available from: <https://patents.google.com/patent/CN104419381A/en?oq=CN104419381A>.

W4. Wang, Y., Zhang, Y., Yang, W., & Ji, H. Selection of Low-Temperature Phase-Change Materials for Thermal Energy Storage Based on the VIKOR Method. *Energy Technology, 3(1),* 2015, 84-89.

W5. Phase-Change-Material. n.d. In Wikipedia. <https://en.wikipedia.org/wiki/Phase-change_material> Accessed: 2016.

X1. Xiaoqin, Z., Hu, J., Zhao, H., Li, W. Phase Transformation Temperature Adjustment of Calcium Chloride Hexahydrate. *Trans Tech Publications, Switzerland.* 2012, 512-515.

X2. Xie, N., Huang, Z., Luo, Z., Gao, X., Fang, Y., Zhang, Z. Inorganic Salt Hydrate for Thermal Energy Storage. *Appl. Sci., 7*, 2017, 1317-1334.

X3. Xing, L., Hongyan, L., Shujun, W., Lu, Z., Hua, C. (2006). Preparation and Thermal Properties of Form Stable Paraffin Phase Change Material Encapsulation. *Energy Conversion and Management, 47,* 2006, 2515-2522 (Retracted Article).

X4. Xu, X. Dong, Z., Memon, S., Bao, X., Cui, H. Preparation and Supercooling Modification of Salt Hydrate Phase Change Materials Based on $CaCl_2 \cdot 2H_2O/CaCl_2$. *Materials, 10*, 2017, 691-701.

Y1. Yamaguchi, T., Hayashi, S., Ohtaki, H. X-ray Diffraction Study of Calcium (II) Chloride Hydrate Melts: $CaCl_2 \cdot RH_2O$ (R = 4.0, 5.6, 6.0, 8.6). *Inorganic Chemistry, 28*, 1989, 2434-2439.

Y2. Yinping, Z., Yi, J., Yi, J. A Simple Method, the T-history Method of Determining the Heat of Fusion, Specific Heat and Thermal Conductivity of Phase-Change Materials. *Measurement Science Technology, 10*, 1999, 201-205.

Y3. Yuan, K., Zhou, Y., Sun, W., Fang, X., Zhang, Z. A Polymer-Coated Calcium Chloride Hexahydrate/Expanded Graphite Composite Phase Change Material with Enhanced Thermal Reliability and Good Applicability. *Composites Science and Technology, 156*, 2018, 78-86.

Z1. Zalba, B., Marín, J., Cabeza, L., Mehling, H. Review on Thermal Energy Storage with Phase Change - Materials Heat Transfer Analysis and Applications. *Applied Thermal Engineering, 23*, 2003, 251-283.

Z2. Zhang, J., Zhang, J., He, S., Qu, K., Liu, X. Thermal Studies of the Solid-Liquid Phase Transition in Binary Systems of Fatty Acids. *Thermochimica Acta, 369*, 2001, 157-160.

Z3. Zhang, Y., Zhou, G., Lin, K., Zhang, Q., Di, H. Application of latent heat thermal energy storage in buildings: State-of-the-art and outlook. *Building and Environment, 42(6),* 2007, 2197-2209.

Z4. Zhao, C., Zhang, G. Review on Microencapsulated Phase Change Materials (MEPCMs): Fabrication, Characterization and Applications. *Renewable and Sustainable Energy Reviews, 15*, 2011, 3813-3832.

Z5. Zhao, W. Heat Transfer Analysis of Encapsulated Phase Change Materials. 2009.

Z6. Zheng, Y. Thermal Energy Storage with Encapsulated Phase Change Materials for High Temperature Applications. *Lehigh University Lehigh Preserve*. 2015.

Z7. Zhou, D., Zhao, C., Tian, Y. Review on thermal energy storage with phase change materials (PCMs) in building applications. *Applied Energy, 92*, 2012, 593-605.

Z8. Zivkovic, B., Fujii, I. An Analysis of Isothermal Phase Change of Phase Change Material Within Rectangular and Cylindrical Containers. *Solar Energy, 70(1)*, 2001, 51-61.

Z9. Zondag, H., Kikkert, B., Smeding, S., Boer, R., Bakker, M. Prototype Thermochemical Heat Storage with Open Reactor System. *Applied Energy*, 109, 2013. 360-365.

Vita

Joshua Charles was born in 1986 in Lancaster, Pennsylvania before his family moved to north-central Pennsylvania, while he was in elementary school. Upon graduation from high-school, Josh worked as a graphic designer for a year before attending Mansfield University of Pennsylvania, where he earned a Bachelor of Science degree in Physics. After graduating from Mansfield in 2009, Josh enrolled at Lehigh University, completing a Masters of Science of Mechanical Engineering in 2011.

Between 2011 and 2018 Josh has worked as a research scientist for the Lehigh University Energy Research Center, conducting research into a variety of energy topics from power plant emissions and CO_2 capture to ash and solid fuels handling. He has managed DOE and industry-funded projects and has extensive experience in thermodynamics systems modeling. During his time at the Energy Research Center, Josh has authored or co-author over a dozen journal articles and/or conference presentations. In 2016 he was the winner of the Mid-Atlantic States Section of the Air & Waste Management Association's (MASS-A&WMA) Air Pollution Educational and Research Grant (APERG).

Josh resides in Bethlehem, Pennsylvania with his wife Megan and works as a research scientist for the Lehigh University Energy Research Center.